

Particle Image Velocimetry Experiments on Surf-Zone Breaking Waves

Narumon Emarat



A thesis submitted in fulfilment of the requirements
for the degree of Doctor of Philosophy
to the
University of Edinburgh
2000



TO MY PARENTS

Abstract

An experimental study on kinematics and turbulent structures in surf-zone breaking waves has been carried out in laboratory wave flumes. Particle Image Velocimetry (PIV) was used as a measurement technique to obtain the full field, instantaneous velocity throughout the breaking process. The experiments were performed on a single plunging breaker, a train of weak plunging breakers and a train of spilling breakers; all of which were generated on a 1/13 plane sloping beach. Measurements were carried out in a way which would allow mean flow and turbulent characteristics to be determined. The PIV velocity data were post-processed by means of an ensemble average (for the single plunging breaker) and a phase average (for the trains of breakers). The spatial distributions of mean velocity, mean vorticity and turbulent intensity, for each type of breaking wave, are presented. The results obtained from the single plunging breaker experiments are also compared to those predicted by a numerical model based on a Navier-Stokes solver. Furthermore, turbulent kinetic energy transportation is examined, based on the k -equation. The turbulent advection and production are calculated directly from the PIV data while the turbulent diffusion and dissipation are estimated. By this means the turbulent transport process for different types of the surf-zone breaker is investigated. The influence of wave and turbulence characteristics on successive waves is also determined. Comparisons are made with the results of other researchers; some of which were carried out with different optical measuring techniques.

Acknowledgements

First of all I would like to thank my supervisor, Professor Clive Greated, for his invaluable guidance and encouragement throughout.

My friends both inside and outside the Fluids group have made an excellent and friendly environment in the department. Particular thanks should go to Frank Morris for the many times he gave me technical help and for his endless jokes which cheered me up when I was in trouble, both at Edinburgh and on a trip to Denmark. I thank Jianhong Wang and Thomas Haydon who assisted me during my first year. Thanks also to John & Lisa, Alix, all the Alistairs, John Cullen and Susan's gang for their beautiful friendship. Special thanks must go to David, not only for his great help with my research and thesis, but also for his understanding and companionship. I would also like to thank his family (Brian, Heather, Joan, Bob & Kirstie and John & Lynne) for their continual kindness over the last three years.

Outside the lab-life, my Thai friends, who are in the same situation as me (being the overseas students in Edinburgh); I thank them for the enjoyable badminton games and the Thai cooking. I am also very grateful to my landlord Martin. I would have had many more problems, apart from work ones, and I would not have felt that Edinburgh was like my second home, if it had not been for his warmth and kind-heartedness.

I owe a greatest debt of thanks to my family: Mum, Dad, P-Palm and Pum. Their love and patient support are beyond compare.

Part of my PhD research has been included in the European project called Surf

and Swash Zone Mechanics (SASME). It was funded by the Commission of the European Communities Directorate General for Science Research and Development, under the contract number MAST3-CT97-0081. Some of the experiments were carried out at ISVA, Technical University of Denmark. I would therefore like to thank Associate Professor B. Mutlu Sumer, Professor Jørgen Fredsøe and the technical staff at ISVA for their immense help. I would also like to thank Dr Erik Christensen from DHI Water and Environment for his enthusiastic collaboration with me.

Finally, the scholarship for my PhD studies was from the Ministry of Education, Thai Government. Their support is greatly acknowledged.

Declaration

I declare that this thesis was composed by myself and that the work contained therein is my own, except where explicitly stated otherwise in the text.

Table of Contents

Dedication	i
Abstract	ii
Acknowledgements	iii
Declaration	v
List of Figures	xi
List of Tables	xvii
Chapter 1 Introduction	1
1.1 Aim of Thesis	2
1.2 Experimental Methodology	5
1.3 Thesis Outline	6
Chapter 2 Surf-Zone Breaking Waves	8
2.1 Wave Deformation	8
2.2 Wave Breaking Criteria	9
2.3 Breaking Wave Classification	12
2.4 Physical Dynamics during Breaking	15
2.5 Surf-Zone Breaker-Generated Turbulence	20

2.6	A Review of Optical Studies on Breaking Waves	23
2.6.1	Deep-Water Breaking Waves	23
2.6.2	Surf-Zone Breaking Waves	27
2.7	Summary of Chapter 2	35
Chapter 3 Particle Image Velocimetry		36
3.1	Introduction	36
3.2	Outline of the Technique	37
3.3	Image Acquisition	39
3.3.1	Illumination System	39
3.3.2	Seeding Particles	41
3.3.3	CCD Cameras & Lens	42
3.3.4	Image Calibrations	46
3.4	Image Analysis	47
3.4.1	Autocorrelation	48
3.4.2	Crosscorrelation	51
3.5	Image Shifting	52
3.5.1	Errors in Image Shifting	54
3.6	Accuracy of PIV	55
3.6.1	Errors Introduced during Image Acquisition	56
3.6.2	Errors Introduced during Image Analysis	58
3.7	Summary of Chapter 3	60
Chapter 4 Experimental Facilities		62
4.1	Flumes & Wave Generation	62
4.1.1	UEDIN Wave Flume	62
4.1.2	ISVA Wave Flume	66

4.2	Beach Construction	72
4.2.1	UEDIN Beach	72
4.2.2	ISVA Beach	74
4.3	Wave Gauges	76
4.4	Summary of Test Parameters	78
4.5	Summary of Chapter 4	80
Chapter 5 Experimental Data Analysis		82
5.1	PIV Data Validation	82
5.2	Estimation of Wave & Turbulent Quantities	86
5.2.1	Vorticity	86
5.2.2	Mean Flow & Turbulence Characteristics	87
5.2.3	Turbulent Kinetic Energy Transportation	89
5.2.4	Computing Programs	93
5.3	Summary of Chapter 5	94
Chapter 6 Single Breaking Wave Experiments		95
6.1	Experimental Set-up	95
6.1.1	Problems with the Experiments	98
6.2	Results & Discussion	100
6.2.1	Velocity Vector Maps	101
6.2.2	Isovelocity Contours	105
6.2.3	Vorticity	108
6.2.4	Turbulent Intensity	113
6.2.5	Turbulence Transport Mechanisms	118
6.3	Summary of Chapter 6	129

Chapter 7	Trains of Breaking Waves Experiments	132
7.1	Experimental Set-up	132
7.1.1	Problems with the Experiments	135
7.2	Weak Plunging Breaker	137
7.2.1	Velocity Vector Maps	137
7.2.2	Isovelocity Contours	141
7.2.3	Vorticity	143
7.2.4	Turbulent Intensity	147
7.2.5	Turbulence Transport Mechanisms	151
7.3	Spilling Breaker	161
7.3.1	Velocity Vector Maps	161
7.3.2	Isovelocity Contours	165
7.3.3	Vorticity	167
7.3.4	Turbulent Intensity	171
7.3.5	Turbulence Transport Mechanisms	175
7.4	Summary of Chapter 7	181
Chapter 8	Comparison with Numerical Results	185
8.1	Introduction	185
8.2	Numerical Model	186
8.2.1	Input Conditions	187
8.3	The Comparisons	189
8.3.1	Free-Surface Elevation	189
8.3.2	Velocity Vector Maps	191
8.3.3	Velocity-Magnitude Contours	195
8.4	Summary of Chapter 8	200

Chapter 9	Conclusions & Further Work	202
9.1	Conclusions	202
9.2	Suggestions for Further Work	206
Appendix A	List of Publications	209
Appendix B	List of Symbols	211
Bibliography		214

List of Figures

1.1	A natural surf-zone breaking wave. Santamonica beach, California.	1
2.1	The transformation of a wave in different regions of the surf zone.	9
2.2	A diagram of some basic wave terminology and their definitions. .	11
2.3	The overturning of the jet in a plunging breaker on a natural beach.	16
2.4	Three possibilities of splash-up mechanisms.	17
2.5	A surface roller and plunger vortex are forming after the splash at the plunge point.	18
2.6	A sketch of the plunger vortex and the surface roller being formed at the plunge point	19
2.7	A series of plunger vortices generated from jet-splash motions. . .	20
2.8	The structure of large-scale eddies under breaking waves.	21
2.9	Different regions of turbulence generated under a breaking wave. .	22
3.1	Two main steps in achieving a PIV velocity vector map.	38
3.2	Scanning beam illumination system.	40
3.3	Timing diagrams for PIV recordings.	44
3.4	Two-CCD array system [17].	45
3.5	The autocorrelation analysis process.	49
3.6	The crosscorrelation analysis process.	51
3.7	Set-up of the image shifting system (plan view).	53

4.1	A schematic diagram of the wave flume at UEDIN.	63
4.2	Wave spectrum for producing a single plunging breaker in the UEDIN wave flume.	67
4.3	A photograph of the ISVA wave flume.	68
4.4	A schematic diagram of the ISVA wave flume.	68
4.5	Free-surface elevations of the waves generated in the ISVA wave flume.	71
4.6	UEDIN wave flume when fitted with the beach.	73
4.7	ISVA wave flume when fitted with the beach.	74
4.8	Cross-section of the beach in the ISVA wave flume.	75
4.9	Calibration lines for the wave gauges.	77
5.1	Raw velocity vector map of an instantaneous flow field under a weak plunging breaker.	83
5.2	Velocity vector map first shown in figure 5.1, after validation and interpolation.	85
6.1	The PIV set-up for the experiments carried out at UEDIN.	96
6.2	PIV measurements taken at 3 positions within the middle section of the UEDIN wave flume.	97
6.3	Two PIV images of the plunging breaker taken at the same position and time but from different experiments.	99
6.4	Mean velocity of the plunging breaker.	102
6.5	Mean velocity of the plunging breaker, continued from figure 6.4.	103
6.6	The perpendicular of two isolines.	105
6.7	Isovelocity contours of the plunging breaker.	107
6.8	Mean vorticity of the plunging breaker.	109

6.9	Mean vorticity of the plunging breaker, continued from figure 6.8.	110
6.10	The turbulent intensity against the number of repeated experiments.	114
6.11	Turbulent Intensity of the plunging breaker.	115
6.12	Turbulent Intensity of the plunging breaker, continued from figure 6.11.	116
6.13	The control volumes for the plunging breaker in which the mean value of each term in the k -equation is calculated.	120
6.14	Mean velocities, turbulent kinetic energy and turbulent trans- port terms of the plunging breaker, calculated in the area $-0.089 \leq (x - x_b)/h_b \leq 0.090$ and $-0.401 \leq z/h_b \leq -0.222$ (area I of figure 6.13).	121
6.15	Similar to figure 6.14 but in the area $-0.089 \leq (x - x_b)/h_b \leq 0.090$ and $-0.939 \leq z/h_b \leq -0.760$ (area II of figure 6.13).	122
6.16	Similar to figure 6.14 but in the area $1.028 \leq (x - x_b)/h_b \leq 1.207$ and $-0.411 \leq z/h_b \leq -0.232$ (area III of figure 6.13).	123
6.17	Similar to figure 6.14 but in the area $1.028 \leq (x - x_b)/h_b \leq 1.207$ and $-0.859 \leq z/h_b \leq -0.680$ (area IV of figure 6.13).	124
6.18	Similar to figure 6.14 but in the area $2.043 \leq (x - x_b)/h_b \leq 2.222$ and $-0.431 \leq z/h_b \leq -0.252$ (area V of figure 6.13).	125
6.19	Similar to figure 6.14 but in the area $2.043 \leq (x - x_b)/h_b \leq 2.222$ and $-0.744 \leq z/h_b \leq -0.565$ (area VI of figure 6.13).	126
6.20	Similar to figure 6.14 but in the area $2.625 \leq (x - x_b)/h_b \leq 2.804$ and $-0.431 \leq z/h_b \leq -0.252$ (area VII of figure 6.13).	127
6.21	Similar to figure 6.14 but in the area $2.625 \leq (x - x_b)/h_b \leq 2.804$ and $-0.744 \leq z/h_b \leq -0.565$ (area VIII of figure 6.13).	128
7.1	The PIV set-up for the experiments carried out at ISVA.	133

7.2	Two PIV images of the weak plunging breaker taken at the same position and phase but from different cycles.	135
7.3	Mean velocity of the weak plunger.	138
7.4	Mean velocity of the weak plunger, continued from figure 7.3. . . .	139
7.5	Isovelocity contours of the weak plunger.	142
7.6	Mean vorticity of the weak plunger.	144
7.7	Mean vorticity of the weak plunger, continued from figure 7.6. . .	145
7.8	Turbulent intensity of the weak plunger.	148
7.9	Turbulent intensity of the weak plunger, continued from figure 7.8.	149
7.10	The control volumes for the weak plunging breaker in which the mean value of each term in the k -equation is calculated.	152
7.11	Mean velocities, turbulent kinetic energy and turbulent transport terms of the weak plunging breaker, calculated in the area $-0.112 \leq (x - x_b)/h_b \leq 0.087$ and $-0.615 \leq z/h_b \leq -0.416$ (area I of figure 7.10).	153
7.12	Similar to figure 7.11 but in the area $-0.112 \leq (x - x_b)/h_b \leq 0.087$ and $-0.864 \leq z/h_b \leq -0.665$ (area II of figure 7.10).	154
7.13	Similar to figure 7.11 but in the area $0.883 \leq (x - x_b)/h_b \leq 1.082$ and $-0.615 \leq z/h_b \leq -0.416$ (area III of figure 7.10).	155
7.14	Similar to figure 7.11 but in the area $0.883 \leq (x - x_b)/h_b \leq 1.082$ and $-0.814 \leq z/h_b \leq -0.615$ (area IV of figure 7.10).	156
7.15	Similar to figure 7.11 but in the area $1.914 \leq (x - x_b)/h_b \leq 2.112$ and $-0.705 \leq z/h_b \leq -0.508$ (area V of figure 7.10).	157
7.16	Similar to figure 7.11 but in the area $2.900 \leq (x - x_b)/h_b \leq 3.097$ and $-0.705 \leq z/h_b \leq -0.508$ (area VI of figure 7.10).	158

7.17	Similar to figure 7.11 but in the area $3.438 \leq (x - x_b)/h_b \leq 3.633$ and $-0.649 \leq z/h_b \leq -0.454$ (area VII of figure 7.10).	159
7.18	Mean velocity of the spilling breaker.	162
7.19	Mean velocity of the spilling breaker, continued from figure 7.18.	163
7.20	Isovelocity contours of the spilling breaker.	166
7.21	Mean vorticity of the spilling breaker.	168
7.22	Mean vorticity of the spilling breaker, continued from figure 7.21.	169
7.23	Turbulent intensity of the spilling breaker.	172
7.24	Turbulent intensity of the spilling breaker, continued from figure 7.23.	173
7.25	The control volumes for the spilling breaker in which the mean value of each term in the k -equation is calculated.	176
7.26	Mean velocities, turbulent kinetic energy and turbulent trans- port terms of the spilling breaker, calculated in the area $1.341 \leq (x - x_b)/h_b \leq 1.531$ and $-0.540 \leq z/h_b \leq -0.350$ (area I of figure 7.25).	177
7.27	Similar to figure 7.26 but in the area $1.341 \leq (x - x_b)/h_b \leq 1.531$ and $-0.778 \leq z/h_b \leq -0.588$ (area II of figure 7.25).	178
7.28	Similar to figure 7.26 but in the area $2.339 \leq (x - x_b)/h_b \leq 2.530$ and $-0.683 \leq z/h_b \leq -0.492$ (area III of figure 7.25).	179
7.29	Similar to figure 7.26 but in the area $2.800 \leq (x - x_b)/h_b \leq 2.989$ and $-0.603 \leq z/h_b \leq -0.413$ (area IV of figure 7.25).	180
7.30	Similar to figure 7.26 but in the area $3.275 \leq (x - x_b)/h_b \leq 3.465$ and $-0.603 \leq z/h_b \leq -0.413$ (area V of figure 7.25).	181
8.1	Experimental set-up to record wavemaker angle and free-surface elevation.	188

8.2	Free-surface elevations of the plunging breaker from the experiments, BIM and Navier-Stokes solver.	190
8.3	Comparisons between the numerical and PIV vector maps of the plunging breaker at $(t - t_b)/T = 0, 0.184, 0.368$ and 0.551	192
8.4	Continuing from figure 8.3: at $(t - t_b)/T = 0.735, 0.919, 1.103$ and 1.287	193
8.5	Comparisons between the numerical and PIV results for the plunging breaker at $(t - t_b)/T = 0$ and 0.184 . Velocity vector maps are shown overlapping velocity-magnitude contours.	196
8.6	Continuing from figure 8.5: at $(t - t_b)/T = 0.368$ and 0.551	197
8.7	Continuing from figure 8.6: at $(t - t_b)/T = 0.735$ and 0.919	198
8.8	Continuing from figure 8.7: at $(t - t_b)/T = 1.103$ and 1.287	199

List of Tables

2.1	Breaker types and their definitions.	12
2.2	Transition values between breaker types.	13
2.3	Comparison of wave steepnesses, surf similarity parameters and breaker type for different experiments.	14
3.1	Specification of the cameras and the corresponding frame-grabbers used in this study.	43
3.2	Lens and other parameters using with the corresponding cameras in this study.	46
3.3	Systematic and random errors introduced during image acquisition.	56
4.1	Wave parameters for producing a single plunging breaker in the UEDIN wave flume.	66
4.2	Wave parameters used in the ISVA wave flume and the correspond- ing breaker types.	70
4.3	Summary of all the test parameters used in this study.	79

Chapter 1

Introduction

People do not go to the beach on their holidays only to enjoy sun and sand; sea waves are also another important factor that attracts them. Many enjoy riding on the waves using a surfboard, while others only want to watch and listen to the waves when they break. Transformation of the waves on the beach includes wave steepening, overturning (in some cases), breaking and trapping the air which can be seen as foamy water riding along the surface towards the shore (see figure 1.1). This wave transformation can hardly fail to attract people, especially

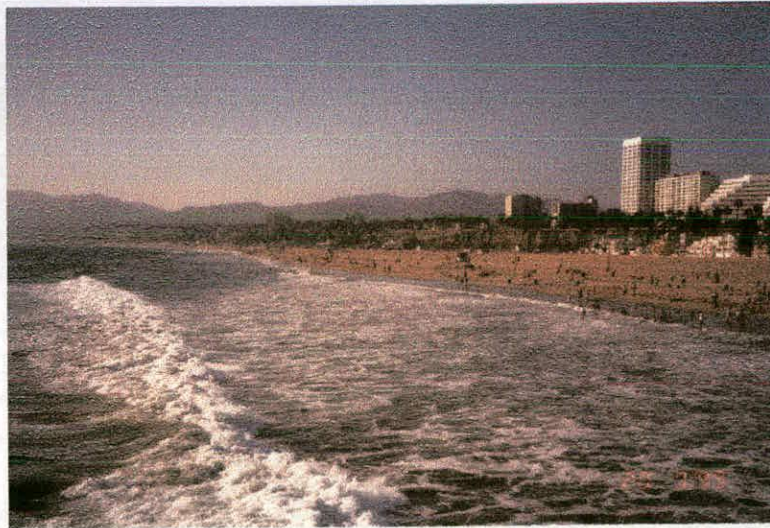


Figure 1.1: A natural surf-zone breaking wave with entrained air bubbles along the surface. Photograph taken by the author from the pier at Santamonica beach, California (September 1999).

coastal scientists. However, it is not only these phenomena that interest them. For years, coastal engineers have been interested in the influence and impact of breaking waves on coastal structures. Sediment transport and erosion or deposition of a coastline are also of important environmental concern. Fluid dynamicists have been trying to solve the problems of wave dynamics throughout the breaking process. Several analytical approaches have been applied to the flow but these break down when the waves become steep and therefore cannot be used to study breaking. As a result, numerical approaches must be employed and several of these have successfully used the fact that the flow is essentially irrotational up until breaking. After breaking the flow becomes more complex due to the generation of vorticity and turbulence. Consequently, new numerical methods have been developed to study the dynamics of surf-zone waves throughout the breaking process. However, to solve the equations of turbulent flow, some flow characteristics and/or conditions are required. These details are normally approximated from experimental results. In fact, experiments have been the principle investigation technique used to study surf-zone breaking waves. The experimental approach not only acts as a guide to the development of numerical models; it also provides an immediate picture of the flow in reality. The present study shows how to achieve this.

1.1 Aim of Thesis

Most of the early experimental studies on breaking waves were carried out qualitatively [4, 56]. The only quantitative measurements that could be done was to study the variation of the free-surface profile by using simple wave gauges [73, 75]. This all changed about two decades ago when non-intrusive optical techniques became available and as a result quantitative measurements of wave

kinematics could then be carried out comprehensively.

The most common optical technique that has been used to measure the fluid velocity at a fixed point is Laser Doppler Anemometry (LDA) [14, 54, 63, 78]. Although this technique provides a high sampling rate, it has the disadvantage that simultaneous spatial distributions of velocity can not be obtained. A technique that can overcome this disadvantage is the Particle Image Velocity (PIV) technique. The PIV technique provides full-field velocity vector maps and consequently, in recent years, it has been widely used to study breaking wave kinematics [8, 9, 35, 57, 60, 68]. However, all of these PIV applications present only instantaneous velocity information.

This thesis is concerned with investigating the kinematics of, and the turbulence transport in, surf-zone breaking waves.

Chang & Liu [8] and Haydon *et al.* [36] were among the first researchers who used PIV to study turbulence under breaking waves. However, Chang & Liu [8] investigated intermediate (constant) depth breaking waves rather than surf-zone breaking waves. Haydon *et al.* [36] studied turbulence under both deep-water and surf-zone breaking waves but they used a rather different technique (when compared to the standard method) to extract turbulent quantities from the PIV data. This will be explained in more detail in the literature review (see section 2.6).

A study of the turbulence transport processes in surf-zone breaking waves was made by Ting & Kirby [79, 80]. They employed the LDA technique to measure velocities under spilling and plunging breakers. They then used the results to examine turbulence production, advection, dissipation and diffusion using the transport equation for the turbulent kinetic energy (the k -equation). However, due to the above mentioned shortcomings of LDA, only a limited number of points

were used, and so the large number of spatial derivatives in the k -equation could not be calculated directly. Instead, these spatial derivatives were estimated from an empirical formula.

In the present study the PIV technique is employed and therefore these spatial derivatives can be calculated directly from the data.

Another interesting aspect of the study of breaking waves is the comparison between experimental and numerical results. This kind of comparison has been made in the past but, to the author's knowledge, none of the previous studies have: (i) matched experimental and numerical conditions exactly; (ii) compared full flow fields and (iii) compared the flow after breaking.

All of the above discussion provides the motivation for, and aims of, the present study. That is, **the aims of this thesis** are to employ the PIV technique to quantitatively investigate

- mean velocity and vorticity fields
- turbulence structures and
- turbulence transport mechanisms,

under surf-zone breaking waves. An additional aim is to perform a comparison with numerical results which satisfies the above three numbered criteria.

Very recently (during the time this thesis was written up), Chang & Liu [10] also attempted to investigate turbulence transport mechanisms using PIV. However, as before they studied breakers generated over a horizontal bottom in water of intermediate depth, rather than over a beach. Furthermore, Chang & Liu [10] did not compare their PIV results against numerically predicted results, as is done here. Having said that, the method used by Chang & Liu [10] is similar to that used by Ting & Kirby [79, 80], and that used here. It is therefore worthwhile

to compare the results obtained from the three studies.

1.2 Experimental Methodology

The experiments were carried out in two laboratory wave flumes, one at the Fluid Dynamics Group, University of Edinburgh (UEDIN) and the other at the Department of Hydrodynamics and Water Resources (ISVA), Technical University of Denmark. The experiments done at the latter place were part of the EU sponsored Marine Science and Technology (MAST-III) programme: Surf and Swash Zone Mechanics (SASME) project. The comparison between experimental results and numerical results was also part of this project. For this comparison, only the experiments undertaken at UEDIN were used.

At UEDIN, the experiments were performed on a single plunging breaker. Due to the limited length of the flume, trains of shallow-water regular waves could not be properly generated. These experiments were carried out in order to try to understand the initial breaking kinematics and the turbulence structures during and after breaking. The measurements were compared with the results found by a numerical model based on a Navier-Stokes solver. The model was developed by Dr. Erik Christensen [12] at DHI Water and Environment, Denmark.

At ISVA, the train of breaking waves experiments were carried out. Weak plunging breakers and spilling breakers were generated. These experiments were carried out to study the wave kinematics and turbulence characteristics in a more realistic situation. The influence of these turbulence parameters between wave cycles was also investigated.

The measurement of wave kinematics at both institutes was carried out by means of the PIV technique. The technique was developed at UEDIN and a complete system was taken over to ISVA. Different types of PIV systems were

used at the two institutes. However, they were based on the same principles and were both suitable for water wave studies.

1.3 Thesis Outline

The outline of the rest of this thesis is given as follows.

Chapter 2 gives a review of the general knowledge of surf-zone breaking waves. The process of wave deformation and breaking into different types of breaker is explained. A physical description of breaking-wave dynamics and turbulence generation is given. Finally in chapter 2, the experimental studies related to breaking waves, both in deep-water and in surf-zone regions, are reviewed. The purpose of this is to give a picture of the advances in optical measuring techniques applied to the breaking wave research, particularly in the past ten years.

In chapter 3, the Particle Image Velocimetry technique used in the present study is described in detail. An outline of the technique is first given followed by a more detailed explanation of the apparatus used and the procedures of the method. The accuracy of the PIV approach, as applied to water wave studies, is assessed at the end of chapter 3.

Chapter 4 describes the experimental facilities used at UEDIN and ISVA. Details of the wave flumes, wave generation and beach construction are given. The structure and operation of the wave gauges, which are used to measure the free-surface elevation, is also explained. Chapter 4 ends with a summary of all the wave parameters used in this study.

Chapter 5 deals with two aspects of the post-processing of PIV data. Firstly, the methods of “spurious”-vector elimination and interpolation are explained. Secondly, the procedures for extracting vorticity, and mean and turbulent quantities from the PIV data are given. The method of using PIV data to calculate

each term of the k -equation is then discussed. Therefore, this chapter explains how the first three aims of this thesis are achieved. That is, it shows how the PIV data can be used to investigate the above quantities in surf-zone breaking waves.

In chapters 6 and 7, the results from the two sets of experiments are presented and discussed. These are the results from the single breaking wave experiments (done at UEDIN) and the trains of breaking waves experiments (done at ISVA), respectively. In each of these two chapters, the experimental set-up is first described, including the problems that occurred during the experiments. Then, the maps of mean velocity, isovelocity, vorticity and turbulent intensity are displayed and discussed. Finally, the turbulence transport of each breaker type is investigated.

In chapter 8, the results obtained from the single breaking wave (UEDIN) experiments are compared against the results predicted by a numerical model. After a brief explanation of the (hybrid) numerical model and the input conditions, comparisons are made between free-surface elevations, velocity fields and velocity-magnitude contours.

Finally, in chapter 9 the main findings of the study are summarised and suggestions for further work are made.

Chapter 2

Surf-Zone Breaking Waves

Many coastal researchers have devoted much of their research to studying breaking waves in the surf zone. The behaviour of such waves has been investigated theoretically, numerically and experimentally over the last few decades. This chapter will give a review of the research in relation to the physical processes and dynamics of surf-zone breaking waves. The chapter will then go on to discuss the turbulent structures induced by such waves and the related experimental studies, specifically the progress on optical measuring techniques that have been applied to the study of breaking waves during the past ten years.

2.1 Wave Deformation

When a wave starts to travel onto a beach the effect of the bottom begins to appear. The influence of the bottom causes the wave profile to deform and become asymmetric. As the water depth decreases, the wave becomes slower, shorter and its height increases. This is known as the *shoaling* effect. However, the wave cannot continue like this. Instead, as the wave moves into progressively shallower water it becomes unstable, the wave crest starts to topple and finally the wave breaks.

Once the wave breaks, it will normally trap and mix air into the water body

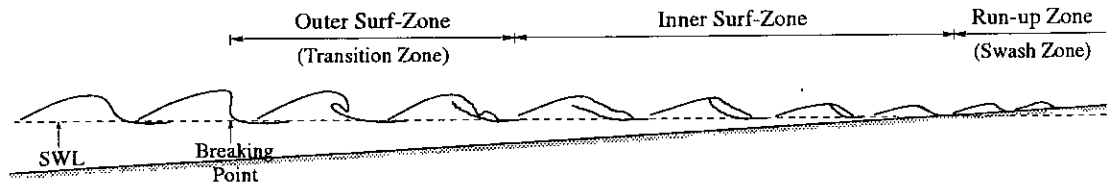


Figure 2.1: The transformation of a wave in different regions of the surf zone, following Svendsen *et al.* [75].

along the surface. This however, depends on the type and dynamics of the particular breaker as will be explained in section 2.3. Such a process produces air bubbles which then propagate with the wave front as a bore. The surf zone is the area along the coastline that contains these shoaling and breaking processes of waves. Svendsen *et al.* [75] split the surf zone into three different regions associated with the process of breaking, as shown in figure 2.1. The *outer surf-zone* is where there is a rapid deformation of the wave shape. It starts from the breaking point and takes place over a horizontal distance in which complicated wave patterns occur above the wave trough. This region ends where the wave starts to form a propagating bore. It is also called the *transition zone*. The *inner surf-zone* contains a slower rate of wave deformation and a quasi-steady wave profile. The entrained-air, or the bore-like wave front, appears mostly in this region, hence it is also termed the *bore region*. As the bore-like wave approaches the shoreline, above the still water level, it continues to travel onto the beach until it reaches the maximum point before travelling back as the *backwash*. This motion is termed the *swash*. The region which contains this rushing up and down water motion is called the *run-up zone* or the *swash zone*.

2.2 Wave Breaking Criteria

Wave breaking is known as a sudden, violent transition from irrotational to rotational motion which then generates a complex flow structure and hence a turbu-

lent flow field. A wave breaks when it reaches a critical state. There are different proposed conditions for a wave to break. Generally, breaking is defined to start where the front of the wave becomes vertical. However, this vertical wave front does not appear in every type of breaking wave. Another possible condition for wave breaking is that breaking will occur when the horizontal velocity of the water at the wave crest exceeds the wave speed. The recent work done by Chang & Liu [9] supports this condition. They carried out laboratory experiments and found that the fluid particle velocity at the tip of the overturning wave crest reached 1.68 times the phase velocity. Moreover, they also found that the overturning wave crest enters the water surface at the front with an acceleration of 1.1 times that of gravity.

A useful parameter that can be used to determine whether waves break or not is that demonstrated by Munk & Wimbush [53], and later discussed by Peregrine [56] and Battjes [5, 6]. This criterion parameter consists of the beach slope α and the deep-water wave steepness of the incident (periodic) wave $a_o\omega^2/g$. Here a_o is the deep-water amplitude of the wave and ω is the incident wave frequency. Munk & Wimbush derived the parameter as $a_o\omega^2/g\alpha^2$, with the criterion value of 1 for wave breaking. They obtain this parameter by taking the ratio of the water acceleration downslope ($a_o\omega^2/\alpha$) to the downslope component of gravitational acceleration (αg).

Another proposed criterion for wave-breaking is that a surf-zone breaking wave will occur when the ratio of the wave height to the local water depth (H_b/h_b) is 0.78 (determined by McCowan [49] in 1894 while Fredsøe & Deigaard [26] have given the ratio to be 0.8). This ratio was in fact estimated for mild slopes. If the slope is greater than about 1:40 the ratio will increase [16]. There also seems to be agreement that the breaking point should refer to the point where the ratio

between wave height and water depth is maximum. Svendsen & Buhr-Hansen [73] performed laboratory experiments which show that plunging-type breaking occurs when this ratio is maximum.

Before giving further explanation of the wave-breaking regimes, it is worthwhile to present, here, the definitions of some basic wave terminology that appear in this chapter and elsewhere in this thesis. Referring to figure 2.2, L is the wave length and H is the *local wave height*, which is the distance between *wave crest* and *wave trough*. The *local (or mean) water depth* is termed h , which is the distance from the bottom to the *mean water level* (MWL). On the other hand, the *still water depth*, d , is the distance from the bottom to the *still water level* (SWL). The mean water level separates equal areas between that under the wave crest and that above the wave trough [74]. The MWL can be the same as the SWL, such as in small waves where linear theory can be applied, but in shoaling waves this is not necessarily true. η is the *free-surface elevation*, which is measured from the SWL. The subscript b indicates the value at breaking point. The determination of the breaking point has already been analysed and will be mentioned more in the next section. Finally, β is an angle between the beach and the horizontal bottom.

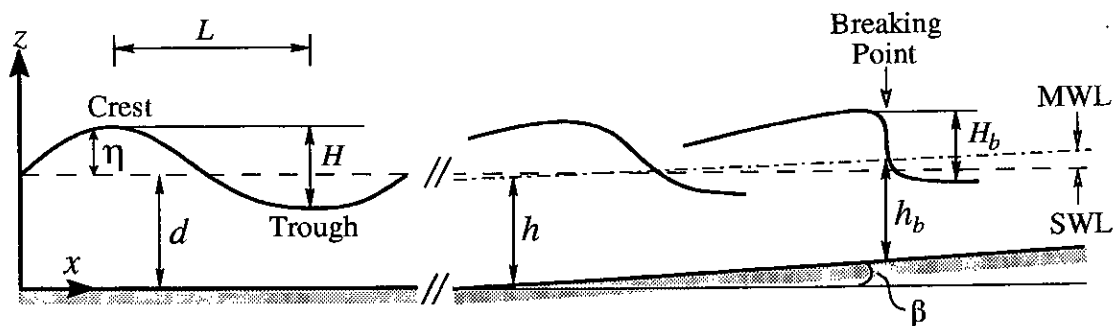


Figure 2.2: A diagram of some basic wave terminology and their definitions.

2.3 Breaking Wave Classification

Breaking waves can appear in different forms depending on the wave steepness and beach slope. Breakers are generally classified into four types: spilling, plunging, collapsing and surging. This classification has been the accepted way of distinguishing between breaker types in experiments for many years. There are many published papers and textbooks that have given a clear definition of each breaker type (see Fredsøe & Deigaard [26], Galvin [27], Sawaragi [66] and Svendsen & Jonsson [74]). A summary of all breaker type definitions is given in table 2.1.





Breaker Type	Definition
 <p><i>Spilling breaker</i></p>	<p><i>Spilling breakers</i> occur when the wave crest becomes unstable at the top and spills down the front face of the wave generating foamy “white” water. The air bubbles slide down the front and travel with the wave. A small-scale curling crest is also observed before the air-bubbles begin.</p>
 <p><i>Plunging breaker</i></p>	<p><i>Plunging breakers</i> occur when the wave crest curls over the front face. The overturning jet then normally entraps air as it falls onto the base at the front of the wave. Following this, there is usually a sequence of splashes which then develops into a propagating bore.</p>
 <p><i>Collapsing breaker</i></p>	<p><i>Collapsing breakers</i> occur in the lower part of the front face instead of at the crest. Bubbles and foamy water are formed and slide up the beach without a splash-up. This is an intermediate type of breaking, between plunging and surging.</p>
 <p><i>Surging breaker</i></p>	<p><i>Surging breakers</i> occur when the wave crest remains unbroken but the foot of the front face rushes up the beach causing the wave crest to decrease and disappear. There is a minor breaking in this type.</p>

Table 2.1: Breaker types and their definitions.

The classification of breaker types can be done visually from the physical appearance of the breakers. The first attempt to classify breaker types from laboratory observations was made by Galvin [27] in 1968 (he also gave the definition of a collapsing breaker). Galvin gave the classifying parameters in terms of the beach slope (m) and the wave steepness (wave height to wave length ratio), which can be either the deep-water wave steepness H_o/L_o or the breaker steepness H_b/gT^2 . Note that the subscript o indicates deep-water value. As defined in the previous section, the subscript b indicates the value at the breaking point. Here the breaking point was defined to be the location where the bore-like shape began to appear at the crest for the spilling breaker, or where the wave front was vertical for the plunging breaker, or where the water reverses for the surging breaker. The classifying parameters which Galvin proposed are the deep-water wave steepness H_o/L_o , the *offshore parameter* $H_o/(L_o m^2)$ and the *inshore parameter* $H_b/(gmT^2)$. Transition values for these parameters are shown in table 2.2. The results are based on laboratory experiments on beach slopes of 1/5, 1/10 and 1/20. It was observed that the inshore parameter seems to classify the breaker type better than the offshore parameter.

Parameter	Surge-Plunge	Plunge-Spill
H_o/L_o (slope 1/10)	0.0015	0.05
H_o/L_o (slope 1/20)		0.01
Offshore $H_o/(L_o m^2)$	0.090	4.80
Inshore $H_b/(gmT^2)$	0.003	0.068

Table 2.2: Transition values between breaker types for the deep-water steepness, the offshore parameter and the inshore parameter (from Galvin [27]).

These breaker classifying parameters were later re-analysed by Battjes [5], in 1974, and he renamed them as the *surf similarity parameters*. Galvin's offshore parameter was then re-written in the form of the deep-water surf similarity parameter $\xi_o = \tan \beta / \sqrt{(H_o/L_o)}$ and the inshore parameter was replaced by

the breaker surf similarity parameter $\xi_b = \tan \beta / \sqrt{(H_b/L_o)}$, which then gives¹

Spilling breaker:	$0.5 > \xi_o$	or	$0.4 > \xi_b$
Plunging breaker:	$0.5 < \xi_o < 3.3$	or	$0.4 < \xi_b < 2.0$
Surging or Collapsing breaker:	$\xi_o > 3.3$	or	$\xi_b > 2.0$.

To summarise, spilling, plunging, collapsing and surging breakers occur in that order for decreasing wave steepness and/or increasing beach slope.

Battjes's surf similarity parameters have been widely used to classify breaker types [14, 70, 78]. Table 2.3 shows a comparison of the wave steepnesses, the surf similarity parameters and the breaker type for different experiments including those parameters used in the present study. It can be seen that the relationship between the surf similarity parameters and the breaker type can vary between experiments. However, most of the relations agree with those proposed by Battjes [5]. This shows that the surf similarity parameters can be used as a standard criterion to classify the breaker type.

Work done by	slope	H_o/L_o	ξ_o	H_b/L_b	ξ_b	type
Stive [70]	1/40	0.032	0.140	0.036	0.132	spilling
Cox <i>et al.</i> [14]	1/35			0.023	0.190	spilling
Ting & Kirby [78]	1/35	0.020	0.202			spilling
Nadaoka <i>et al.</i> [54]	1/20	0.041	0.248			spilling
present study	1/13	0.047	0.354	0.054	0.331	spilling
Stive [70]	1/40	0.010	0.250	0.016	0.198	plunging
present study	1/13	0.028	0.461	0.053	0.333	plunging
Ting & Kirby [78]	1/35	0.0023	0.596			plunging

Table 2.3: Comparison of wave steepnesses, surf similarity parameters and breaker type for different experiments.

As a result of much comprehensive research on spilling and plunging breakers during the past two decades, it may be possible to say that the physical processes and dynamics of such breaking waves are now very well understood. However,

¹Note that the beach slope m is now written as $\tan \beta$.

the turbulent structures generated under them is still an ongoing and interesting research topic.

The following section will give a detailed explanation of the physical dynamics of waves during breaking. The discussion will concentrate on spilling and plunging breakers as these are the types which occur most frequently on natural beaches. Spilling and plunging breakers are also the most commonly generated breakers in laboratory wave flumes. These are the types of breakers that are studied in this thesis. Attention will also be paid to the turbulence generated during the breaking process but it will be focused more in section 2.5.

2.4 Physical Dynamics during Breaking

Wave breaking in the outer surf-zone was the most interesting subject for coastal researchers over the past twenty years. This was due to the fact that it contains a violent transformation of the wave shape as well as other dramatic phenomena that can be observed on natural beaches.

The definition of each breaker type was introduced in the previous section. Although the plunger's initial state of breaking is more obvious than that of the spiller, they both actually contain a similar process of breaking. Wave breaking starts at the vertical front of the wave, the crest then curls up and overturns as a *jet* falling into the water in front. This phenomenon occurs in both types of breaker but it is observed to be at a very much smaller scale in the spilling type. After the jet impacts the front of the wave, at the *plunge point*, there is a splashing up of water which then forms another jet and the subsequent jet-splash cycles are regenerated. Figure 2.3 shows the overturning of the jet in a plunging breaker. (This photograph was taken on the beach in front of the conference centre where the author was attending the 3rd International workshop



Figure 2.3: The overturning of the jet in a plunging breaker on a natural beach. A smaller wave is also breaking in the foreground as a spiller.

on PIV in Santa Barbara, California, September 1999.) The overturning of the plunging jet is obvious as well as the splash up of water after the impact of the jet. Interestingly, there is also a small wave breaking as a spiller closer to the shoreline at the same time as the bigger plunger is breaking behind it. This shows the irregularity of waves on a natural beach.

Very good introductions to the features of these processes can be found in several review papers of the 1980's, such as Peregrine [56] in 1983 and Battjes [6] in 1988. These reviews are often referenced by many of the recent papers and they are aimed towards obtaining an understanding of the dynamics of surf-zone breaking waves.

Peregrine [56] gives a review of the dynamical processes of breaking waves, with special emphasis on wave steepening, overturning and splashing. He reveals

the important features of the wave face prior to the overturning motion. These features include the fact that, in the crest region, the water-particle velocities exceed the wave velocity. This is the well known criterion for wave breaking. Another interesting feature is that water in a thin region on the front of the wave accelerates faster than gravity. This is thought to be necessary to project forward the overturning jet.

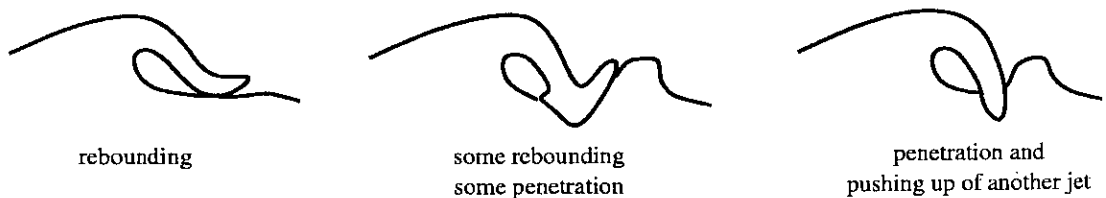


Figure 2.4: Three possibilities of splash-up mechanisms suggested by Peregrine [56]

Peregrine suggested three possible models for the splash-up mechanism which occurs at the plunge point (that is, where the overturning jet touches or impacts onto the water surface in front). Figure 2.4 shows these three models. These mechanisms at the plunge point were later studied and described qualitatively by Basco [4] in 1985. He observed that once the overturning jet penetrated into the frontal trough air was trapped and bubbles as well as vortex motion were formed. This vortex motion is called the *plunger vortex*. The impact of the jet causes the water surface to splash up and then fall forwards to form a *surface roller* (see figure 2.5 and the sketch in figure 2.6). It has been shown that the fluid in the surface roller moves with a velocity equal to the wave celerity [70]. Basco has given an interesting hypothesis; according to his observations the plunger vortex translates horizontally and generates a secondary wave disturbance similar to that generated by a piston-type wavemaker. This is why a secondary wave crest is sometimes observed.

There have been experimental investigations performed in the aerated region



Figure 2.5: A surface roller and plunger vortex are forming after the splash at the plunge point. Photograph courtesy of Peter Tuffy and David Skyner.

in the upper part of breaking waves. The results were found to support the phenomena during the breaking process that are described above. These experimental studies include Jansen [39] in 1986 and recently Lin & Hwung [44] in 1992. Both studies employed ultraviolet light to illuminate fluorescent tracer particles which were fed into the air-bubble region. This was found to be the most efficient way of reducing the light reflection from the bubbles on the images. By studying the photographic and video images from both experiments the sequence of jet-splash motions in both plunging and spilling breakers was revealed. A number of jet-splash cycles was found for plunging breakers and an even larger number was found in spilling breakers [39]. Furthermore, the sequence of these motions was found to be reproduced in each individual wave (in a regular wave train). These motions seem to continue into the inner surf-zone as well. However, the subsequent jet-splash and vortex formations decrease rapidly in strength due to dissipation and transfer of wave energy to the turbulent motion in the air-bubble field [44]. In Jansen's [39] results, smooth trajectories of the particles inside the jet-splash motions suggested so-called coherent motions in the flow. This was, however, determined in the absence of significant turbulence. In Lin & Hwung's [44] results, the main mechanism that drives the motion in the bubble zone was found to be the vortex system that was generated from the jet-splash

cycles. Vortex-stretching was also found to occur due to the interaction between the jets, the vortices and the effect of the rising buoyant bubbles. The vortices finally collapse under the influence of the backwash.

The process of jet-splash motions, surface roller generation and plunger vortex formation can be found in both plunging and spilling breakers. The only differences are the rates and scales. In the plunging breaker the plunger vortex is stronger than in the spilling breaker, whose front face is dominated by the surface roller (whitecap or foamy water) generated after the smaller scale overturning jet has impacted. The production of turbulence in both breakers comes from the same sources. The strong shear at the toe beneath the surface roller and at the border of the rotating plunger vortex are thought to be the primary sources of turbulence generation in the outer surf-zone [4] (see figure 2.6). Again, the turbulence generated in the different types of breaker and in different places differs in terms of the rates and the scales.

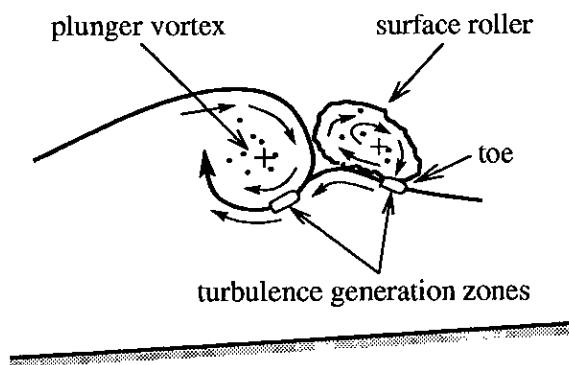


Figure 2.6: A sketch of the plunger vortex and the surface roller being formed at the plunge point, following Basco [4].

After the surface roller is generated on the steep front face, it proceeds shorewards into the inner surf-zone and transforms into a turbulent bore. This motion was reviewed by Battjes [6]. Once the surface roller is formed it generates another falling jet and hence another plunger vortex with the same direction of rotation

as the previous one but with a smaller size. These large-scale organised vorticities finally decrease in strength and degenerate into small-scale and disordered vortices until finally they turn into turbulent motion. At this stage, the breaking wave (both spilling and plunging) is treated as a turbulent bore. The beginning of the inner surf-zone is where this turbulent bore starts to form.

2.5 Surf-Zone Breaker-Generated Turbulence

Turbulence under breaking waves emerges when the vortices degenerate into smaller scales and become disordered. The high intensity of turbulence is associated with the loss of wave energy during breaking.

As mentioned in the previous section, the strong shear at the toe of the surface roller and at the border of the plunger vortex are treated as the sources of turbulence. Jansen [39] and Lin & Hwung [44] both show a series of plunger vortices (see figure 2.7) generated from the sequence of jet-splash motions mentioned earlier. These vortices have the same direction of rotation (clockwise

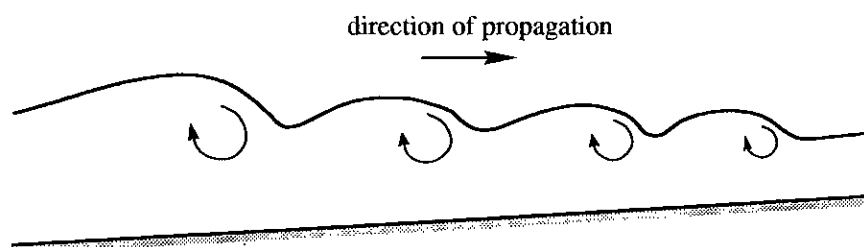


Figure 2.7: A series of plunger vortices generated from jet-splash motions.

and with horizontal rotational axes) but the later generated vortices are weaker and smaller. This sequence of horizontal vortices is also observed by Nadaoka *et al.* [54]. They called them the *horizontal eddies*. They also postulated that another vortex system develops after the wave-breaking front has passed. These vortices, however, have their rotational axes inclining relative to the vertical di-

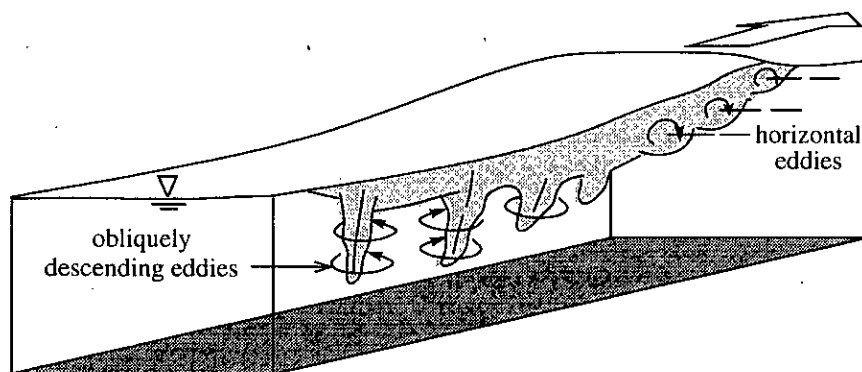


Figure 2.8: The structure of large-scale eddies under breaking waves as observed by Nadaoka *et al.* [54].

rection (see figure 2.8). They are termed as the *obliquely descending eddies* and they cause the three dimensional flow. The author suggests that these eddies are developed from the rising of air bubbles, observed by Lin & Hwung [44], which were previously trapped in the plunger vortices (horizontal eddies).

These organised horizontal eddies gradually reduce in strength and scale while they are proceeding shorewards into the inner surf-zone and they are generally located close to the water surface. They finally become disordered and so small in size that they can be treated as turbulence. The intensity of this turbulence then decreases gradually due to spreading and dissipation until it slowly dissipates into heat.

Turbulence in the surf zone can be split into different regions as suggested by Fredsøe & Deigaard [26]. Each region is dominated by distinct turbulence characteristics. The first region is the area near the surface roller where there is very intense production of turbulence due to the strong shear between water in the surface roller and water in the main flow. This region is treated as the source of the turbulence. The second region is the area where the turbulence remaining from the production zone spreads downwards and gradually dissipates until a new wave front breaks and produces another batch of intense turbulence.

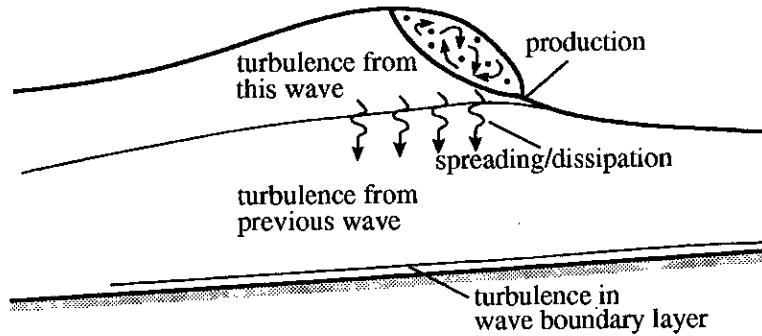


Figure 2.9: A schematic diagram showing different regions of turbulence generated under a breaking wave (adapted from Fredsøe & Deigaard [26] and Svendsen [72]).

Svendsen [72] illustrated the process of the spreading of the turbulence towards the bottom in the inner surf-zone. This is shown in figure 2.9 together with a schematic diagram of the different turbulence regions. The final region is where the turbulence is influenced by the bed, including the wave boundary layer. In this region turbulence is generated by the shear stress in the oscillating wave boundary layer. It has been argued that the externally generated turbulence (*e.g.* turbulence generated from near the surface roller) and the shear-generated turbulence from the wave boundary layer are statistically independent [26]. However, little information is available on the variation of the turbulence and the effect of the interaction between the turbulence generated from the two sources.

The process of turbulence production, spreading and dissipation occurs in each individual cycle of wave breaking. In some cases the turbulence dissipates before a new breaking-wave produces new turbulence, while in other cases a significant level of turbulence from the previous wave remains and even interacts with the new turbulence.

2.6 A Review of Optical Studies on Breaking Waves

This section follows closely a review paper written by the author and Professor Greated at the University of Edinburgh (see Greated & Emarat [32]). This paper describes different optical techniques and their practical applications to wave and current interaction, breaking waves, internal waves, wave boundary layers and the motion of bed sediments. However, only the breaking wave part is adapted (and rewritten) here. This part illustrates recent advances in experimental techniques and tools applied to gain more knowledge of such complicated waves.

Particular attention is given to laboratory experiments that have been undertaken in the last ten years. Among the techniques used, the point measuring method of Laser Doppler Anemometry (LDA; sometimes referred to as Laser Doppler Velocimetry (LDV)) and the whole field approach known as Particle Image Velocimetry (PIV) are applied to most of the measurements. The next chapter is devoted to giving a detailed description of PIV which is the technique that is used for the present experimental study. Explanation of the LDA technique will not be given here because it is beyond the scope of this thesis. Reader who are interested in this technique can consult other references, such as Durst [18] and Watraswicz & Rudd [83] for the basic principles and some applications, and Goldstein [28] (see chapter 4 by R. J. Adrian) for a more recent review on the technical theory.

2.6.1 Deep-Water Breaking Waves

Over the past decade, there are a number of researchers who have focused their studies on wave breaking, particularly in deep water. These include the comprehensive and detailed laboratory observations carried out by Rapp & Melville [63],

whose experiments employed the laser-Doppler anemometry technique. Recently, particle image velocimetry has shown itself to be a preferable technique, as can be seen in Haydon *et al.* [36], Skyner [68], Perlin *et al.* [57] and Chang & Liu [8, 9].

One of the first attempts to study the turbulent structures under broken waves using velocity flow fields obtained from PIV measurements was that of Haydon *et al.* [36], in 1996. The PIV system they used was similar to the system developed and reviewed in 1992 by Greated *et al.* [33] but with additional improvements to the image shifting technique [1, 52]. By placing a mirror that rotates about a vertical axis in front of the camera, a large dynamic range of velocity in turbulent flow can be obtained. Instead of photographic film, a CCD (Charge Coupled Device) camera was employed to capture a sequence of flow images after breaking. The camera was moved to different positions in order to cover the full region of broken wave turbulence and vorticity.

The PIV results of Haydon *et al.* [36] only showed vorticity information for a period long enough after the initial breaking in order to avoid air bubble influences. From observations, vorticity was concentrated soon after breaking and was seen to get weaker as it moved down to deeper regions. They also used PIV data to extract the mean and turbulent flow components by a method of local-averaging. This is a different method from the common theoretical methods of moving-averaging and phase-averaging which are generally applied to the data recorded by LDA. This is due to the fact that their PIV system could not provide high frequency velocity records owing to the limitation of the camera capture rate and frame grabbing memory (the use of phase-averaging with PIV data was developed later; see Emarat & Greated [22] and chapter 5 of this thesis). Haydon *et al.* [36] applied the local-averaging technique to the PIV data by using nearby velocities to calculate an average at each point and then subtracted this averaged

value from the original velocity to obtain the turbulent component. The size of the averaging area was determined from spectral information measured by wave gauges (see the detailed description in Haydon [35]). The results from using this averaging method were then used to determine turbulence characteristics such as its intensity and energy profile. It was shown that in deep-water broken waves there is a strong decay of the turbulence level with depth.

One of the disadvantages of using LDA to measure kinematics in breaking waves is that such a technique cannot easily be applied in the region beneath the breaking crest. To overcome this, recent researchers prefer to use the PIV measurement technique which can yield simultaneous velocity measurement over a wide region of the flow including the breaking crest. Such measurements can be seen, for example, in Skyner [68], Perlin *et al.* [57] and Chang & Liu [9].

In 1996, Skyner [68] used PIV to study the internal kinematics of a particular deep-water, plunging breaker, especially in the plunging tip. Later the experimental results were carefully compared with the results from a time-stepping numerical model based on the Boundary-Integral Method. The waves were first generated numerically and then replicated in the physical wave flume by matching wave gauge records to numerical predicted wave amplitude time-series. Numerical predictions for the internal kinematics were found to be in good agreement with the PIV measurements. Although there were some discrepancies at the vertical front of the water surface, which is a region of very high acceleration, they were within the limits of experimental error.

That same year, Perlin *et al.* [57] reported results on deep-water plunging breakers using three different experimental techniques including nonintrusive surface elevation measurement, PIV and *Particle Tracking Velocimetry* (PTV; see [62]). Their results concentrated on the wave crest region. The main finding

was that there are parasitic capillaries generated on the lower front face of the plunger when the front face becomes approximately vertical and the jet develops. The PIV and PTV experiments gave agreeing results. These results show that there was insignificant vorticity on the leeside of the wave which suggested that the flow was irrotational prior to breaking. Perlin *et al.* [57] concluded that potential flow theory is valid outside the surface boundary layer.

Another attempt to measure kinematics in the breaking crest was recently performed by Chang & Liu [9] in 1998. In their experiments the particle velocities and accelerations in the overturning jet of a plunging wave were measured for the first time, as claimed, as well as the vertical component of vorticity on a horizontal plane behind a broken wave. The PIV technique they used employed a pulsed laser system which was set on top of the tank in order to project a vertical light sheet into the flow. An image shifter was placed in front of the CCD camera. To measure the velocity and the acceleration in the overturning jet, fluorescent dye was mixed in with the water. The camera was then set at 45° to the normal of the vertical plane, in order to avoid blocking of the light sheet by the water surface near the tank wall. This then required a correction procedure in the analysis process to eliminate the effects of angled images.

The PIV data revealed that the fluid particle velocity at the overturning jet reaches 1.68 times the phase velocity which, they claimed, was in the range predicted by numerical methods (this is also referred to in section 2.2 when explaining the wave breaking criteria). Moreover, Chang & Liu [9] also used the PIV data to calculate fluid particle acceleration around the tip of the jet and found that it was almost 1.1 times the gravitational acceleration.

By setting the camera on top of the tank and directing the laser from the side to produce a horizontal light sheet, Chang & Liu [9] were able to measure the

vertical component of vorticity after the wave had broken and the air bubbles had passed the test section to avoid erroneous data. Using the PIV velocity data, vorticity distributions can be calculated directly. It was shown that the vortices are random in number and location. This generation of vertical vortices after wave breaking supports the presence of the obliquely descending eddies studied by Nadaoka *et al.* [54], which will be explained in the following subsection (also some of their findings were already mentioned in the previous section). Furthermore, Chang & Liu [9] showed that there was a non-zero transverse component of mean velocity which suggests a three-dimensional flow structure during the breaking process.

2.6.2 Surf-Zone Breaking Waves

Most of the early laboratory studies of breaking waves in the surf zone employed the laser-Doppler velocimetry technique, notably Nadaoka *et al.* [54], Pedersen *et al.* [55] and Ting & Kirby [78, 79, 80].

One of the comprehensive studies of surf-zone breaking waves was carried out by Nadaoka *et al.* [54]. This study was aimed at investigating the structure of the turbulent flow field in a spilling breaker. Nadaoka *et al.* investigated the intrinsic characteristics of large-scale eddies under breaking waves by means of a fibre-optic LDA system as well as several flow visualisation techniques. In their velocity measurements, a two-component fibre-optic laser Doppler velocimeter, operating in the backscattered fringe mode (FLV), was developed. The horizontal and vertical velocity components could be measured simultaneously with two-colour laser beams. Their FLV system has the advantage that it is not affected much by entrained air bubbles, hence it can be applied to the region above the trough level of the waves. Bragg cells were used to shift the frequencies to solve the ambiguity in the particle direction. The data derived from the measurements was used to

obtain the phase averages of velocity components and turbulence intensities.

Nadaoka *et al.* [54] paid special attention to the deformation structure in the air bubble region around the wave crest. This was observed from photographs on a movie film taken by a cinecamera. By close examination of sequential photographs, Nadaoka *et al.* postulated that around the wave crest there are two dimensional dominant eddies with their axes parallel to the crest line (the so-called horizontal eddies). Then there is a quick transformation from the two-dimensional eddy structure at the wave front to the oblique eddy structure behind the wave crest which stretches obliquely downwards to almost reach the bottom (this structure was then termed the “obliquely descending eddies”, see figure 2.8).

Nadaoka *et al.* [54] also investigated the Lagrangian behaviour of the water particles both in and under the air bubble region. To visualise the particle movements, particle tracking techniques were carried out with different kinds of particles in different regions of interest. They observed that there was a regular orbital motion of particles in the region around the wave crest under the air bubbles. On the other hand, near the water surface there was a shoreward movement with relatively high speed, and at mid-depths the water particles show orbital motion combined with the undertow (offshore flow). Nadaoka *et al.*'s most important findings, however, related to the obliquely descending eddies which are of direct relevance to the sediment transport mechanism.

To validate the visualisation study results, Nadaoka *et al.* [54] used the laser-Doppler velocimetry technique to measure velocity components and then post-processed the data to get flow characteristics such as phase-averaged velocity field, Reynolds stress, shear-strain rate, vorticity and turbulence information. The measurements revealed the responsibility of large-scale eddies for the generation of Reynolds stress in the upper layers of the water. Nadaoka *et al.* used a

rather different method of extracting the fluctuating components from their velocity records. They considered that the velocity field consists of irrotational and rotational components and by separating them they could examine several effects of breaking wave vorticity dynamics associated with the large-scale eddies. It was shown that the generation of the mean rotational component causes considerable increase in mass and momentum transport.

Another important turbulence characteristic in breaking waves is the turbulent length scale. It is an important characteristic because it is useful in determining other parameters such as the eddy viscosity and the turbulent diffusion rate. Pedersen *et al.* [55] are among those investigators who made an effort to measure the turbulent length scales under breaking waves. The experimental technique they used incorporated two laser Doppler anemometers in order to make a spatial correlation between two vertical turbulent velocity components recorded simultaneously at different positions. This was achieved by setting up one laser at a fixed position above the sloping bottom while the other, set at the opposite side of the wave flume, was moved vertically with varying distance relative to the first one. The signals recorded from the two LDAs were ensemble averaged to extract the turbulent components from the instantaneous velocities. From these turbulent components the spatial correlation coefficient between two signals could be determined and therefore the integral length scale. It was found that close to the bed the length scale increases linearly away from the bottom and in the upper regions it remains constant due to the vanishing influence of the bottom.

In Ting & Kirby [78], undertow and turbulence in laboratory surf-zone breakers were investigated. They obtained velocity measurements in different types of breakers on a uniformly sloping beach by using a two-component fibre-optic laser-Doppler anemometer. The system was a backscatter one with four laser beams.

There is a slight disadvantage with this system in that only one velocity component can be measured at a time. Different components were obtained by running the same experiment twice. Moreover, because LDA can measure velocities at just one point, to gain a complete velocity field the measurement probe had to be moved to successive points across the flow field while the same experiment was repeated. This was done by mounting the LDA fibre-optic probe on a carriage which slid along the top of the tank while the probe was submerged in the water throughout the experiment. Another problem that occurred when trying to use LDA to measure velocity above the trough level in breaking waves was that the air bubbles caused the signal to “drop-out”. Ting & Kirby solved this problem by producing a lock detector signal to distinguish between a valid Doppler signal and noise. They also checked Doppler signals by using the measured water surface level as a validation criterion that will discard the signal if the probe was above or at the water surface.

Through further study, Ting & Kirby also used the same measurement techniques to investigate, in more details, the turbulence characteristics in a strong plunging breaker [79] and in a spilling breaker [80]. Unlike Nadaoka *et al.* [54], Ting & Kirby [78, 79, 80] extracted the turbulent velocity fluctuations by phase-averaging the velocity signal over many successive waves and then subtracting the phase-averaged velocity from the original velocity signal. They then analysed the correlation between the mean (or wave-induced) flow and the turbulence in both the spilling and the plunging breakers to infer the different mechanisms for sediment transport between the different breakers. It was found that in spilling breakers the correlations are seawards and dominated by the undertow current which then becomes the main factor for the cross-shore sediment transport in the offshore direction. On the other hand, in plunging breakers the correlations are

shorewards and dominated by the orbital wave motion. This suggests that the net transport of turbulent kinetic energy is onshore and so is the movement of suspended sediment. The other interesting result was that the turbulent kinetic energy under the spilling breaker dissipated slowly and not before a new breaker arrived, whereas in the plunging breaker the dissipation appeared quickly, within one wave cycle between the breakers. These results show the important fundamental difference in the dynamics of turbulence between different types of breaker in the surf zone.

Although point measuring techniques such as laser Doppler anemometry have produced useful results in experimental investigations, they do not provide the spatial structures of the flow that could be used to determine vorticity and energy dissipation which are the important characteristics in breaking waves. Hence, in recent years, several investigators have carried out laboratory experiments on surf-zone breaking waves using imaging techniques, especially PIV, to produce full field instantaneous flow information. These experiments include those of Lin & Rockwell [45], Dabiri & Gharib [15], Quinn [60] and Emarat & Greated [22]. Most of them focused on a spilling breaking wave, as it is the most commonly occurring breaker.

Lin & Rockwell [45] investigated the initial and intermediate stages of the breaking. In particular, they studied the distributions of velocity and vorticity relative to the distortions of the free surface during these stages of breaking. They generated their spilling breaker by accelerating the fluid above a hydrofoil which was located some distance beneath the free surface. The breaker they generated was quasi-steady as it showed unsteadiness about the equilibrium state of the breaker. It was suggested by Svendsen & Putrevu [76] that the velocities close to the free surface under hydrofoil-generated breakers resemble those in a deep-

water breaking wave. Additionally, the velocities are quite different from those in a surf-zone breaker when looking at the flow further down from the surface.

The form of hydrofoil-generated breakers is controlled by the Froude number. By changing the Froude number the breaker can be changed from a small-scale capillary pattern to a large-scale separated region beneath a distorted free surface. The capillary pattern is formed along the wave crest at the initial stage of development of a spilling breaker. The fully evolved breaker occurs when there is an abrupt change in the slope of the surface along with a sudden increase in elevation. This revealed a separation of the flow beneath the curved free surface. Lin & Rockwell [45] investigated the evolution of these characteristics: from the onset of the capillary pattern to the fully evolved breaking wave, by using a high-image-density PIV technique.

In their PIV experiments, Lin & Rockwell [45] employed a high-speed scanning laser system to generate pulsed sheets across the flow field of interest. The laser they used was a very high intensity Argon-Ion laser which illuminated each particle with full intensity in order to optimise the image acquisition. Six images of each of the seeding particles were recorded on to photographic film. The directional ambiguity of the particle velocities was solved by using an image shifting system. The image shifting system used a rotating mirror placed in front of the camera lens to impose a bias vertical velocity. A single frame crosscorrelation technique, described by Meinhart *et al.* [50], was used to determine the velocity vector in each interrogation area. In addition, to supplement the PIV, a high-resolution video camera was used to record a large number of multiple images of the wave patterns. This allowed the capillary wave patterns to be related to the flow structure beneath it.

By employing these visualisation techniques, the velocity and vorticity pat-

terns relative to the distortions of the free surface, at different stages of breaking, were revealed (see figure 5 and 6 in the paper). Lin & Rockwell [45] suggested that the sharp free-surface curvature plays an important role as the source of the vorticity. It was shown that there exists a concentration of vorticity beneath the troughs of the capillary patterns. Once the breaker is fully evolved, the large-scale vorticity concentrations are formed by flow separation from the sharp curvature of the free surface. This separation region is expected to resemble the dividing streamline between the surface roller and the fluid body beneath it in a breaking wave [76].

A similar investigation of the vorticity generation within a spilling breaker has recently been investigated by Dabiri & Gharib [15]. Their purpose was to search in more detail for the origins of the source of vorticity in a spilling breaking wave. Instead of using a hydrofoil (as in Lin & Rockwell [45]), Dabiri & Gharib used a honeycomb and a mesh screen placed in front of the test section. When the fluid passes through this honeycomb/screen section the free-surface elevation decreases due to the drop in pressure and as a result the fluid accelerates. This accelerated fluid then cause the free-surface to rise again sharply and a spilling breaker is formed. Similar to Lin & Rockwell's experiment [45], the breaker height and wave pattern can be controlled by changing the the Reynolds number and the Froude number.

To view the wave phenomenon through the breaking process, the shadowgraph technique along with a Digital Particle Image Velocimetry (DPIV) system was used. One image of each seeding particle was captured in each exposure allowing crosscorrelation to be possible to determine the particle displacements. Dabiri & Gharib [15] also developed a technique to deal with free-surface reflections in the image analysis stage. By replacing the intensity by a constant value above

and at the free surface, the area below the free surface can be separated and used to generate the accurate velocity and vorticity data over the different positions and types of wave. Dabiri & Gharib concluded from their results that in the honeycomb/screen-generated spilling breaker, the source of vorticity is due to the deceleration of the free-surface, just prior to breaking, rather than the sharp free-surface curvature as concluded by Lin and Rockwell [45]. They suggested further that this free-surface deceleration also generates a sharp slip velocity which grows into a shear layer, convecting the vorticity downstream and injecting the vorticity into the fluid from the free surface. Moreover, the experimental results indicate that the spilling breaker can be modelled by a shallow water hydraulic jump.

Very recent PIV experiments on laboratory surf-zone breaking waves were reported in Quinn [60] and Emarat & Greated [22]. Quinn [60] used PIV to study the hydrodynamics of wave breaking on mildly sloping beaches as well as on the profiled beaches. The Boussinesq- and Serre-type models were used to predict the depth-averaged horizontal velocity and compared with PIV data. The predictions agree quite well with the measured values especially near the bed but it was over-estimated in the crest region. PIV velocity data was also used to calculate the radiation stress, mean energy flux and mean momentum flux.

The paper by Emarat & Greated [22] describes the experimental study carried out as part of this thesis. Consequently, it will not be reviewed in detail. The main thing to be pointed out here is that these last two papers [22, 60] show the capability of PIV in obtaining detailed velocities under surf-zone breaking waves. However, this measuring technique suffers from the problem introduced by the aeration of the water during breaking which limits the region of measurement.

2.7 Summary of Chapter 2

This chapter reviews the general knowledge of surf-zone breaking waves, in particular the process by which breaking waves develop and deform. The criteria to determine whether, and where, a wave will break as well as to classify different types of breakers were presented. The definition of each of the breaking wave types: spilling, plunging, collapsing and surging, was given.

The physical dynamics during breaking was discussed in detail. It was shown that the physical process from initial to after breaking of spilling breakers is similar to that of plunging breakers. Only the smaller scale vortices and turbulence structures in spilling breakers are different. Turbulence generated by surf-zone breaking waves during and after breaking was explained. The process and regions of turbulent production, spreading and dissipation were pointed out.

Finally, the last section contains a literature review on optical techniques involved in measuring breaking waves kinematics, both in deep-water regions and surf-zone regions. The review was focused on the experimental studies that have been carried out in the past decade in order to illustrate the recent advances on optical measurements. Emphasis was placed on the use of the full-field measuring technique: Particle Image Velocimetry (PIV), together with the point measuring technique: Laser Doppler Anemometry (LDA). The discussion of their advantages and disadvantages when applied to breaking waves experiments was also given.

Chapter 3

Particle Image Velocimetry

This chapter contains a description of Particle Image Velocimetry (PIV), a whole field experimental technique used to obtain velocity measurements. In this study it is used to investigate the kinematics of, and turbulence generated by, breaking waves in the surf zone. The principles, methodology, analysis methods and the accuracy of the technique are given.

3.1 Introduction

With the advent of the laser in the 1960's, it has been possible to develop non-intrusive measurement techniques using sophisticated optical and electronic instruments. PIV is one such technique applied to experimental fluid mechanics for the measurement of whole velocity fields. It is a relatively new technique introduced with its own name in the early 1980's after it was developed from the earlier technique of *Laser Speckle Photography* [58]. During the last two decades, the technique has undergone rapid development and is used extensively now in research ranging from water wave studies, including offshore and coastal dynamics, to aerodynamic and acoustic studies. As a result, there are a very large number of publications relating to the subject. Background theory can be found in the review paper by Adrian [2]. Other good introductions can be found in the form

of journal papers [3, 42, 84, 86], conference papers [30, 33], course notes [20], and even textbooks, some having been published very recently (see Raffel *et al.* [62] and Stanislas *et al.* [69]). A review of the application of the technique to the study of wave kinematics outside the current investigation, such as wave and current interaction, internal waves, wave boundary layers and the motion of bed sediment, can be found in the review paper by Greated & Emarat [32]. Since PIV is now well documented a detailed description of the technique in its entirety is not given here, rather it is detailed as is relevant to its application in the current investigation. Details of the PIV set-up for each experiment are given in sections 6.1 and 7.1. A brief outline of the technique is given with further details in the following sections.

3.2 Outline of the Technique

PIV is a quantitative form of photographic flow visualisation. In principle it is a technique that is used to measure the velocity of *tracer particles* which follow the flow faithfully. To achieve this, the flow is seeded with small particles and illuminated with a two-dimensional sheet of laser light. The illuminated flow region is then photographed from the side by either conventional wet-film based camera or the digital camera.

After the images are captured they are then analysed to generate a quantitative map of 2-D velocity vectors. The velocity is obtained by a simple determination. That is, the velocity is a ratio of the particle displacement to the time taken for the particle to travel this distance. The image analysis procedure mainly consists of determining the particle displacements. It can be done by dividing a whole image into small areas known as the *interrogation areas*. Each single interrogation area, after being analysed using a *correlation* technique with

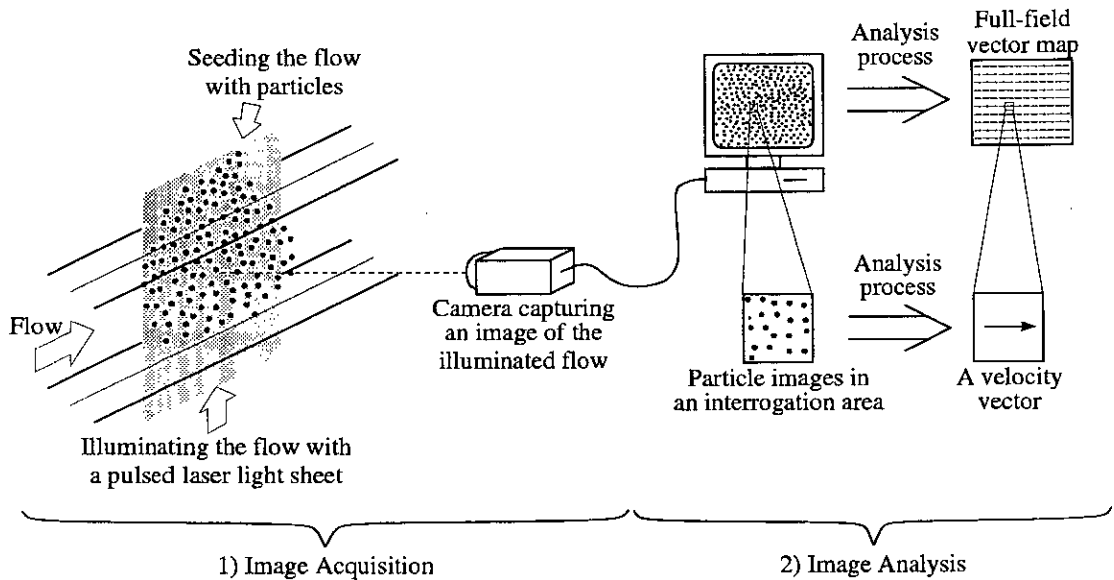


Figure 3.1: Two main steps in achieving a PIV velocity vector map.

the knowledge of magnification and time scales, gives a local average velocity vector. A whole map of the velocity vectors is composed of these interrogations. The velocity vector map may be further processed to give maps of parameters such as vorticity, kinetic energy and shear rate.

Although there are now a number of companies that manufacture commercial systems, the current investigation has made use of an “in-house” system initially developed within the Fluid Dynamics Group at the University of Edinburgh (UEDIN) in the late 1980’s by Gray [29] and Skyner [67]. At that time the conventional system, including wet photography and the Young’s fringe analysis technique, was still used. Since then the system has been gradually developed and used by many research students and staff in the group [19, 52, 59, 60, 82]. The system is nowadays dominated by the digital techniques throughout the image capture and analysis procedures [17, 23, 35]. It is often referred to as Digital Particle Image Velocimetry (DPIV) and is used throughout this study.

PIV can be broadly sectioned into two main categories, *image acquisition*

(which includes illuminating, seeding and capturing the flow) and *image analysis*, as shown in Figure 3.1. Full details of the individual components of these categories are now given.

3.3 Image Acquisition

The image acquisition procedure employs practically all of the hardware used in PIV measurements. It consists of the laser light source, the method of generating the light sheet, the seeding material, the camera, lenses and other sundry optics used. The apparatus adopted for this water wave study is based on the principles suggested by [20], [33] and [61]. The exception is the digital camera which has just been used and developed within the Fluids Group in the last 4–5 years [17, 35]. These items are now explained in more detail, beginning with the illumination system.

3.3.1 Illumination System

The two most appropriate methods for illuminating the relatively large areas in coastal engineering experiments are pulsed and scanning beam systems. Pulsed lasers are used to generate short bursts of laser light and is most suitable for relatively high speed flows, greater than 10 ms^{-1} or so. In the laboratory wave flume, the scanning beam method lends itself more naturally to the lower velocity water waves (a few metres per second) and the relatively large measurement areas. The scanning beam method adopted here was initially developed by Gray *et al.* [31].

Light Sheet Generation for the Scanning Beam System

In the scanning beam illumination method, a continuous wave (CW) laser is used. An Argon-Ion CW laser (manufactured by *Spectra Physics*) is used throughout this study which gives powers of up to 15W. It produces light in the blue-green

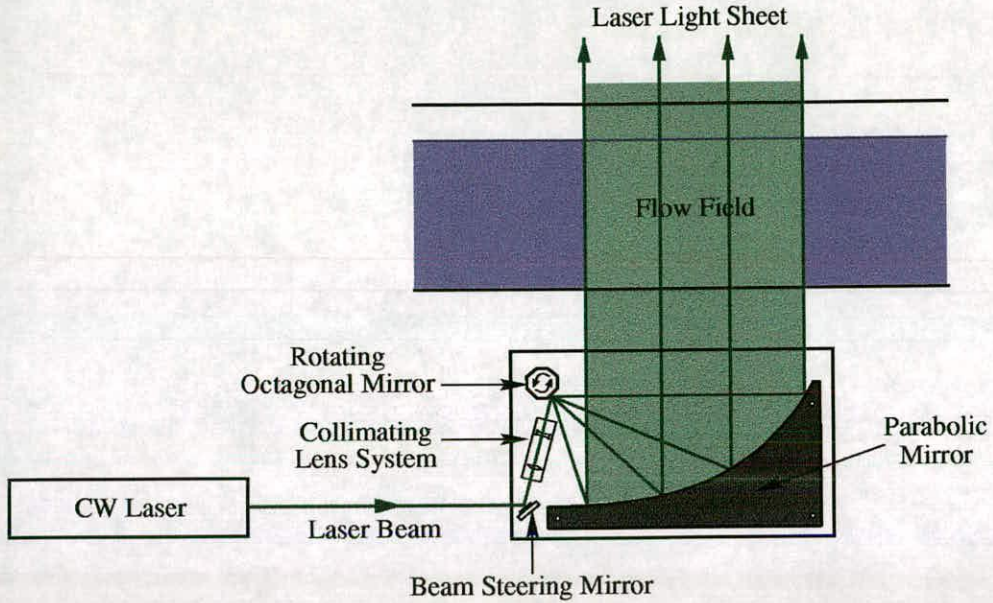


Figure 3.2: Scanning beam illumination system.

wavelength range (457–514 nm). Green light (488 nm) is used here with a power of 8–10W. A diagram of the scanning beam illumination system is shown in figure 3.2. The whole system, excluding the laser, is installed in a so called *scanning beam box*. The box is made from 8 mm thick black Aluminium sheets which serve to hold all the equipment in fixed positions and also to provide protection from hazardous high power laser reflections. The equipment inside the box includes a beam steering mirror, a beam collimating lens system, a rotating octagonal mirror and a parabolic mirror. The parabolic mirror is composed of silver-coated perspex strip attached onto a 20 mm thick Aluminium plate which is cut into a parabolic curve.

Entering from one side and at the bottom of the scanning beam box, the directed laser beam is deflected off a rotating octagonal mirror and the static parabolic mirror is employed to collimate the beam into the flow as a two-dimensional pseudo-sheet of light. This method gives a relatively even illumination intensity over a large area which is suitable for experiments in a water

wave tank [31]. The extent of the laser light sheet depends on the size of the parabolic mirror. At UEDIN the light sheet is normally 1 m wide and approximately 1.5–2.0 mm thick. The light sheet is usually produced from below a wave tank entering vertically upwards into the flow in the middle of the tank. Side illumination can be used if the tank has an opaque bottom.

Illumination Interval & Exposure Time

The rotating mirror can be adjusted very accurately to give rotational speeds in the range 12–250 revolutions per second. The beam is then reflected by the rotating mirror onto the parabolic mirror and into the flow as a light sheet with a scan period of 0.5–10 ms. Each seeding particle within the flow region is illuminated for a very short period of time and is then re-illuminated upon the following scan of the beam. Thus the scan period determines the interval between exposures and is an important factor for accurate particle velocity determination. The interval should be set to allow the largest displacement of particle images (corresponding to the largest velocities) to be within the resolvable range chosen for the analysis system [33]. It is also important that the large majority of particles remain within the illuminated plane during the scan interval, otherwise excessively large errors due to particle drop-out are introduced into the analysis process.

3.3.2 Seeding Particles

PIV relies on the fact that the fluid medium is seeded with tracer particles. It is the motion of these tracers that is measured, not the fluid motion itself. It is therefore crucial that the seeding particle used should be small enough to follow the flow faithfully yet big enough to scatter the laser light effectively. A comprehensive and detailed study on tracer particles and seeding for PIV can be found in Melling [51].

Conifer pollen was found to be the most suitable seeding particle and has been used preferentially in the water wave studies at UEDIN. Its mean diameter is in the range 50–70 μm and its density is very close to that of water when wet which renders it close to neutrally buoyant. It has a very small tendency to rise giving an error of about 0.025% to the measured velocities [61].

An alternative option for water wave studies is to seed the flow with silver coated hollow glass spheres. In the experiments performed at UEDIN, these particles with an average diameter of approximately 40 μm were chosen. The scattered light intensity is higher than that from pollen and hence glass spheres are more suitable when the distance between the camera and the illumination plane needs to be increased. Additionally, if experiments with a long duration are performed, pollen tends to coagulate and degrade and therefore glass spheres are more suitable in this case as they have neither of these drawbacks.

After making the decision as to which particle is going to be used to seed the flow, the seeding density needs to be determined. The optimum seeding density for PIV should give the resulting image in a way that each interrogation area contains about 3–6 images of each particle (for autocorrelation analysis) and about 10 different particles [20]. The illumination interval and camera exposure time also play an important part in achieving the optimum seeding density.

3.3.3 CCD Cameras & Lens

Advances in the technology of scientific digital cameras have improved PIV into a relatively fast and robust technique. In fact, real-time commercial systems are available which produce vector maps of a measurement region. Regardless of whether a system is real time or not, most commercial PIV systems employ *Charge Coupled Device* (CCD) cameras for image capture. Wet-film photography may be used when single shot high resolution velocity maps are required to capture a

Specification	Kodak Megaplug ES 1.0/SC (used at UEDIN)	Pulnix TM-9701 (used at ISVA)
Array Size	1008(H) × 1018(V) pixels	768(H) × 484(V) pixels
Pixel Size	9.0 × 9.0 μm	11.6 × 13.3 μm
Array Type	Non-interlace	Full-frame interline transfer
Scanning	progressive scan	progressive scan
Frame Rate	15 fps	30 fps
Frame-Grabber	OCULUS-F/64 board (CORECO INC.) used with a PC under Windows 3.11™	DT3157 board (DATA TRANSLATION®) used with a Pentium based PC under Windows NT™

Table 3.1: Specification of the cameras and the corresponding frame-grabbers used in this study. (See [62] for a detailed explanation of the array types and the scanning of CCD sensors.)

single event in fine detail.

Before CCD cameras were introduced to the Edinburgh PIV system by Haydon [35], wet-film based cameras were used extensively [19, 29, 52, 60, 67, 82]. However digital cameras have important advantages over the traditional wet film in terms of image capture, storage and analysis. The main advantage is the evident time efficiency of the digital technique over wet-film and optical correlations. Furthermore, digitally stored images do not degrade with time as is the case with wet-film images. Finally, it is also easier to optimise the experimental set-up using the digital camera.

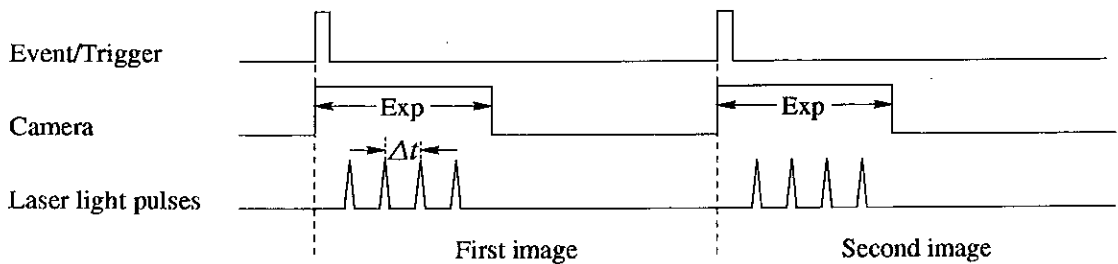
A CCD camera typically consists of semi-conductor sensor arrays. Each individual sensor element is called a *pixel* and a large number of pixels are arranged in a rectangular array giving a CCD array. A detailed description of the different types of CCD sensors and their application to PIV can be found in Dewhurst [17] and Raffel *et al.* [62].

Table 3.1 shows the specification of the cameras and the corresponding frame-grabbers used in this study. The reasons for using different types of cameras are mainly due to the progress in development and the availability of the cameras for

the PIV system.

While the two-CCD array PIV system was still under the development process, the Kodak Megaplus ES 1.0/SC (single channel mode) camera was used in the experiments done at UEDIN. The software used with this camera was developed by Thomas Haydon [35]. It allows the contiguous acquisition of up to 30 images at a time, storing them in the frame grabber memory. These stored images can then be transferred onto hard disc. Because of its high resolution but low frame rate, the camera was used to capture single frames of multiple exposed particle images. A timing diagram for PIV recording using this CCD camera is given in figure 3.3(a). It was used along with the image shifting system in order to remove the ambiguity of the particle directions which occurs during the autocorrelation analysis process. This is explained in section 3.5.

(a) Kodak Megaplus ES 1.0/SC



(b) Pulnix TM-9701 (2-CCD Array)

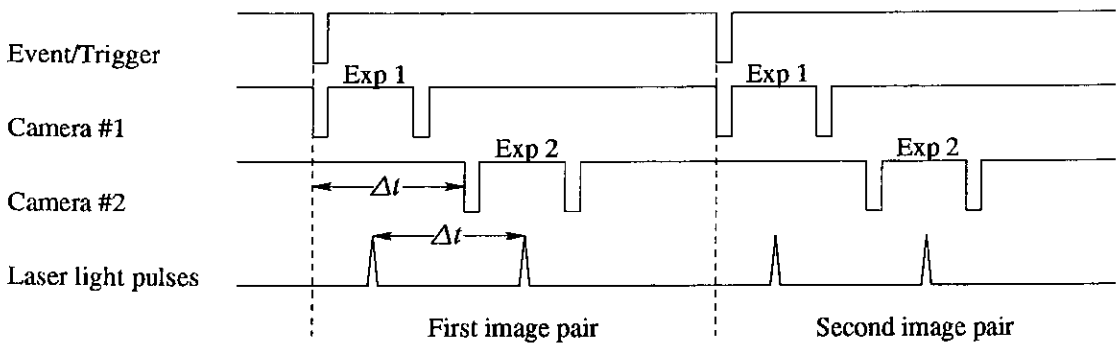


Figure 3.3: Timing diagrams for PIV recordings using (a) Kodak Megaplus ES 1.0/SC and (b) Pulnix TM-9701 (2-CCD Array). “Exp” is the exposure time of the camera and Δt is the time between illuminations.

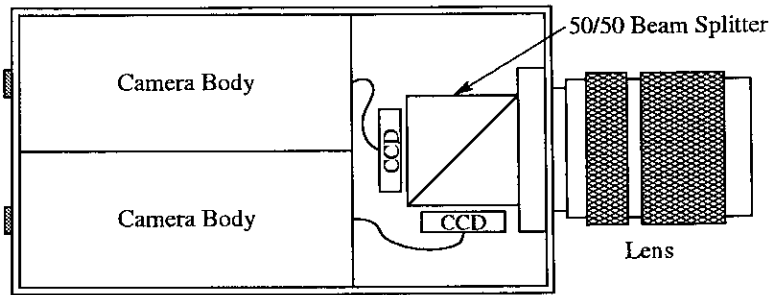


Figure 3.4: Two-CCD array system [17].

In order to avoid errors introduced from using the image shifter (see section 3.5) the two-CCD camera system was used for the experiments carried out at ISVA. This system is based on using two CCD arrays, each of which captures a frame of single exposed particle images. A pair of frames (one from each CCD) can be captured at the different times separated by a very short duration (Δt , see figure 3.3(b)). This method allows a relatively large dynamic range of velocities to be measured, including zero and near-zero velocities, using crosscorrelation analysis. Consequently, there is no need to use image shifting with this system. The two-CCD system composes of two Pulnix TM-9701 cameras. It was developed by Tim Dewhurst [17]. Both cameras can capture images at the same spatial coordinate in the flow, using an unpolarised 50/50 beam splitter placed before the arrays as shown in figure 3.4. A detailed description of this two-camera system can be found in [17].

The frame grabber (DT3157) software used with the two-camera system was developed by Thomas Haydon and John Cosgrove at UEDIN. Each frame grabber board is installed in a separate computer. With this system a pair of images can be captured with separations (Δt) as small as μs [17]. Furthermore, a sequence of contiguous images can be captured into computer memory (RAM) and these can later be transferred to hard disc or compact disc. Both CCD array types have a dynamic range of 8 bits or 0–255 grey levels (0 is black and 255 is white).

Lens

The choice of lens and aperture are important aspects governing the quality of the PIV images. It is essential that the images of the individual particles are sharp in order to obtain high quality PIV records. To achieve this, a relatively large aperture (small f -number¹) lens must be used. This has the advantage of maximising the amount of light collected on the CCD arrays. However, it has the effect of giving a poor depth of field making focusing less easy. This problem may be overcome by increasing the distance between the camera and the laser sheet but the light intensity must also be increased. A high quality flat-field lens is needed when using the large aperture in order to minimise the image distortions due to lens aberration. A summary of lens, aperture and other parameters used with each camera are shown in table 3.2.

Parameter\Used with	Kodak Megaplug ES 1.0/SC	Pulnix TM-9701 (2-CCD Array)
Lens	50 mm Micro-Nikkor	55 mm Micro-Nikkor
Aperture (f -Number)	$f/2.8$ (max.)	$f/2.8$ (max.)
Camera distance	1.90 m (approx.)	1.30 m (approx.)
Laser power	8–10 W	10 W
Light sheet width	1.0 m	0.5 m

Table 3.2: Lens and other parameters using with the corresponding cameras in this study.

3.3.4 Image Calibrations

One of the particular problems in optical studies using a flume is the distortion caused by refractive index changes. The effects become more significant if the laser light sheet is far from the flume wall. A correction for this effect must then be applied. In practice, a regular white plastic grid is carefully placed in the water at the position where the light sheet is transmitted. The image of the grid is then

¹ f -number is defined as the ratio of focal length to aperture diameter.

taken with the image capture system that is used for the PIV recordings. This procedure is useful for obtaining the magnification which is necessary for velocity determination. Moreover, the grid image is also used to align the camera so that it is horizontal and perpendicular to the light sheet. It is then essential that calibration (or grid) images are taken prior to commencing PIV measurements whenever the camera position is changed.

In the two-CCD array system the two arrays can become misaligned due to handling and transit of the camera. The first step in dealing with this misalignment is to try to correct it by using adjustment screws attached to the arrays. To do this a picture of a grid is taken simultaneously by the two arrays. The resultant images are then examined for misalignment and adjustments are made accordingly. This process is repeated until, by eye, the alignment is considered satisfactory. However, there will still be an error and the next step in dealing with this is as follows. A sheet of A4-paper “sprayed” with black dots is printed out [13]². A picture of this sheet is then taken simultaneously by the two arrays. The two resulting images are then crosscorrelated to produce a vector field which represents the misalignment. Following this, a linear least-squares fit was used to produce a function which describes the vector at each interrogation location. Finally, this function is used at the main analysis stage to remove the misalignment (see [17] for more details of this process).

3.4 Image Analysis

Velocities are obtained by correlating the displacements of particle images in the raw image frames. To achieve this, the whole image frame is divided into small, normally square, interrogation areas. Each interrogation area can be analysed

²This can be done using simple graphics software on a computer.

by performing a 2-D spatial correlation. It is important that the flow is approximately uniform within each of these areas. That is, the velocity gradients should be fairly low ($< 3\text{--}5\%$) [84]. The effect of these velocity gradients will be explained in section 3.6.

Throughout these experiments, the PIV analysis is carried out purely digitally using the analysis software developed by Tim Dewhurst [17]. This software is called “EdPIV” and it is run on a Unix based PC.

3.4.1 Autocorrelation

If a PIV image is taken as a single frame of multiply exposed particle images, then the autocorrelation analysis technique is used to extract the displacement information. The most basic routine for this method is to correlate each interrogation area with itself. If the intensity distribution function³ in an Interrogation Area (IA) is represented by $I(x, y)$, the autocorrelation function $A(x, y)$ is of the form

$$A(x, y) = \int \int_{\text{IA}} I(x', y') I(x' - x, y' - y) dx' dy'. \quad (3.1)$$

Because the images are recorded digitally onto pixel arrays, $A(x, y)$ is calculated from the discrete summation:

$$A(x, y) = \sum_0^N \sum_0^N I(x', y') I(x' - x, y' - y) \Delta x' \Delta y', \quad (3.2)$$

where $N \times N$ is the size of the interrogation area in pixels. Normally, 64×64 pixels, or 32×32 pixels, is used depending on the particle density and the image resolution.

It is, however, less time consuming if the computational process is carried out by employing a Fourier Transform (FT). According to the correlation theorem or

³The intensity of an individual particle is best described by a Gaussian-like profile [86]. $I(x, y)$ used here represents the image intensity field of the whole interrogation area.

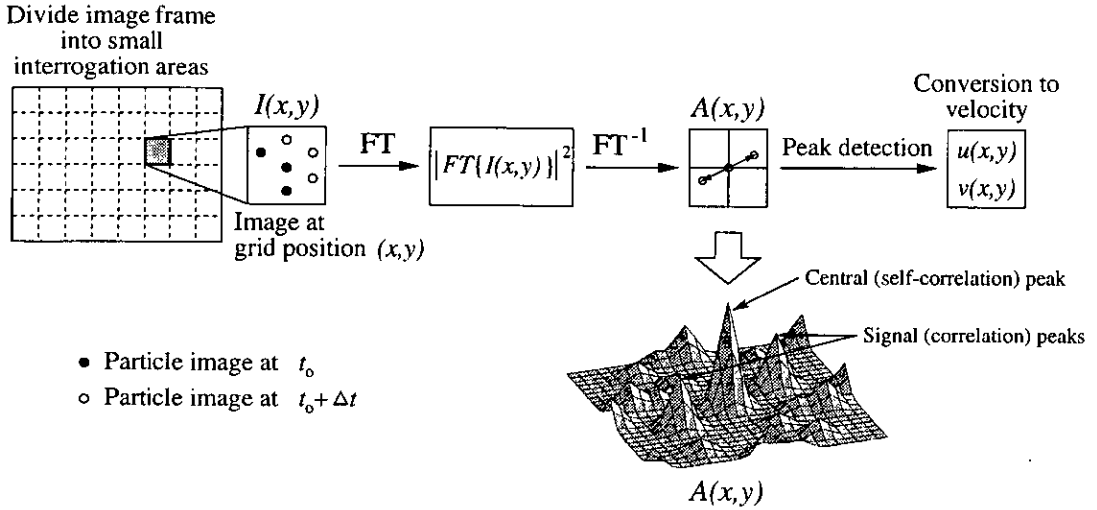


Figure 3.5: The autocorrelation analysis process for a single frame/double or multiple exposure recordings. $A(x,y)$ is the autocorrelation plane.

the *Wiener-Khintchine theorem*, the FT of equation (3.1) gives

$$FT\{A(x,y)\} = FT\{I(x,y)\}FT^*\{I(x,y)\}, \quad (3.3)$$

where $*$ denotes the complex conjugate. The autocorrelation function can now be written as

$$A(x,y) = FT^{-1}\{|FT\{I(x,y)\}|^2\}, \quad (3.4)$$

where FT^{-1} denotes the inverse Fourier Transform. The form of an $A(x,y)$ plane is shown in figure 3.5, along with the autocorrelation analysis process.

Nowadays the autocorrelation analysis technique is usually carried out totally digitally but in the past it was done partially optically. In the UEDIN conventional system, a developed PIV negative is probed, at each interrogation area, by a low power laser beam (normally a He-Ne beam of 1mW). The light is then diffracted by the series of particle images and a Young's fringe pattern is produced behind a lens. This is the result of the first FT. The intensity distribution of this pattern is recorded digitally on a CCD array. The inverse FT is then carried out numerically to reveal the autocorrelation plane. With the current system,

all of the Fourier Transform calculations are done numerically by using a 2-D Fast Fourier Transform (FFT) algorithm and as a result the correlation plane is produced much faster.

The autocorrelation plane contains the main and tallest peak at the centre, secondary peaks placed around this tallest peak and small peaks which appear randomly in the plane (see figure 3.5). The *central peak* (or *self-correlation peak*) is formed from the correlation of the particle images with themselves, therefore its value is the highest and positioned at the centre (giving zero displacement). The secondary peaks located symmetrically around the central peak are “mirror peaks” of each other. These *signal peaks* (or *correlation peaks*) are the result of the correlation between images of the same particle at different positions. The small *random peaks* represent the unwanted noise which results from random correlations: between different particle images, particle images that are moving off the interrogation area and particle images that are disappearing out of the illumination plane.

The signal peaks are of the most interest because their positions give the required displacement. There can be more than two signal peaks depending on the number of times that the particles were exposed. By performing *peak detection* the signal peaks can be found, and from their positions the displacement and the resulting velocity vector can be obtained. However, if it is not known which particle image appears first in the interrogation area, it is difficult to tell which one of the signal-peak pair is the right one. Consequently, the well known problem of the 180-degree ambiguity in the particle direction emerges. In addition, if the particle velocity is zero or near-zero, the exposed images overlap and the analysis fails. These problems can be overcome by incorporating the image shifting method during the image capture procedure which will be explained in

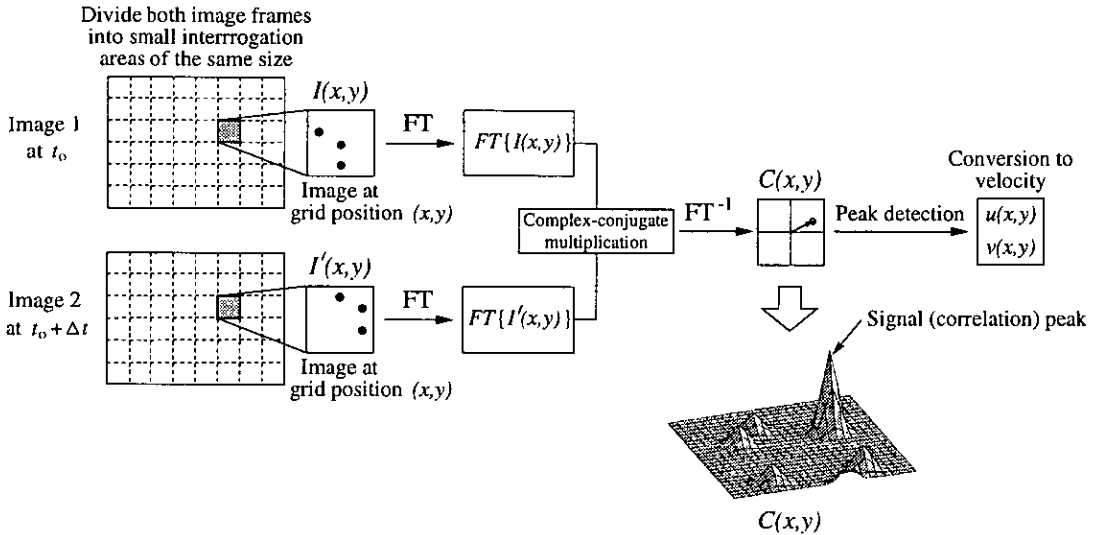


Figure 3.6: The crosscorrelation analysis process for double frame/single exposure recordings. $C(x,y)$ is the crosscorrelation plane.

section 3.5.

3.4.2 Crosscorrelation

When PIV images are taken as double frames of single exposed particle images, crosscorrelation analysis is used. A pair of image frames are divided into small interrogation areas with the same size. The interrogation area of the first frame is then crosscorrelated with the corresponding interrogation area of the second frame to extract the displacement information.

The crosscorrelation function is derived in the same way as the autocorrelation function, and is written as

$$C(x,y) = FT^{-1} \{ FT\{I(x,y)\} FT^* \{ I'(x,y) \} \}, \quad (3.5)$$

where $I(x,y)$ and $I'(x,y)$ are the intensity distribution functions in the interrogation area of the first frame and the second frame, respectively. The flow-chart in figure 3.6 explains the crosscorrelation analysis process which also shows the form of the $C(x,y)$ plane.



Because there is only one image of the individual particles on each frame, the correlation between them gives only one signal peak on the crosscorrelation plane. There is also random background noise but its level is lower than that in the autocorrelation plane. This is because there are typically a smaller number of the particle images in a crosscorrelation interrogation area and there is also less possibility of overlapping images. The *signal to noise* ratio (S/N) can be used as a factor to determine whether the resulting correlation is meaningful. That is, the higher the S/N ratio, the better the result is. This is one of the reasons why crosscorrelation is the preferable analysis technique in PIV. In addition, since there is only one correlation peak, the directional ambiguity problem is automatically resolved and so there is no need to employ image shifting. Furthermore, a large dynamic range of zero and near-zero velocities up to high speed flows can be measured using the crosscorrelation analysis technique.

3.5 Image Shifting

To resolve the problem of the directional ambiguity as well as the small and zero velocities in the autocorrelation analysis technique, the image shifting method is applied during the image capture process. The method was first introduced by Adrian [1]. The system used here was developed by Morrison [52] and has been extensively used [19, 35, 82] before the crosscorrelation system was developed at UEDIN.

In principle, the directional ambiguity will not be a problem if the first and the second or subsequent particle images can be identified [1]. It is, however, more useful if the image capture can be done in such a way that the resulting frame contains particle images that are moving in the same direction. Image shifting can help to achieve this. By rotating a flat mirror about its central vertical axis in

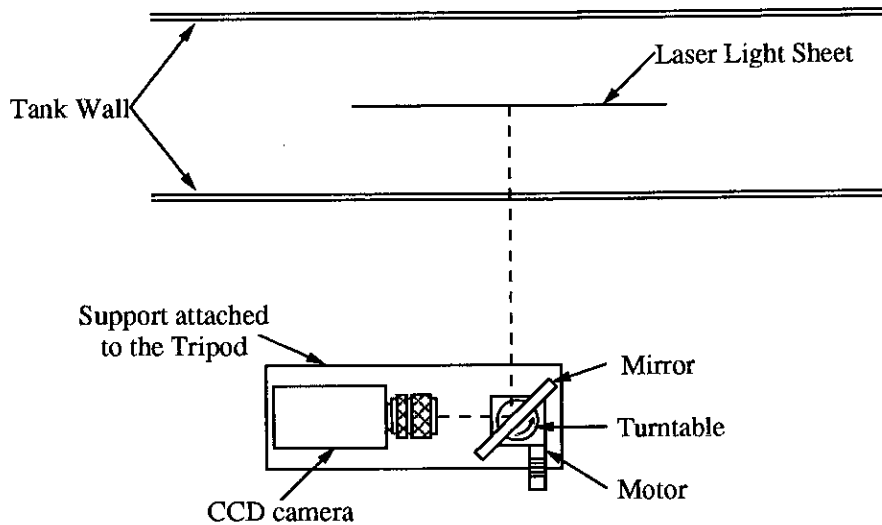


Figure 3.7: Set-up of the image shifting system (plan view).

front of, and at 45° , to the camera during exposure (see figure 3.7), the subsequent images of each particle are shifted horizontally with respect to the previous image. For the set-up shown in figure 3.7, the imposed shifting velocity points towards the right and therefore positive horizontal direction. If this shifting velocity is much greater than the most negative horizontal particle velocity then all the particles in the resultant image will have positive horizontal velocity which is not close to zero. This resolves all the problems mentioned above.

The shifting velocity depends on the angular velocity of the mirror and the distance between the mirror and the measurement zone. The required angular velocity is used as input for the computer which controls the turntable. This computer also sends the signal to trigger the camera when the mirror is at 45° . The shifting velocity can be simply determined by capturing an image of still water seeded with particles. The same experimental set-up is then used to perform the PIV measurements of the actual experiments. After the measurements have been taken, autocorrelation analysis is carried out with the knowledge of the shifting direction. At each interrogation position the resulting velocity vector is

composed of the actual particle velocity and the shifting velocity. The shifting velocity calibration map is then removed from the PIV records, revealing the actual flow.

3.5.1 Errors in Image Shifting

A disadvantage of using image shifting in a PIV system is that the associated apparatus is difficult to set up and use. However, a more important disadvantage of image shifting is that it introduces errors.

Random errors occur when the turntable, mirror or the camera vibrate. The angular velocity of the turntable may also vary during exposure. By using a high quality turntable, carefully constructed and set up, those errors can be minimised and made negligible.

Systematic errors include the variation of the shifting velocity across the frame, the flatness of the mirror and the angle of the mirror during exposure. The errors due to the latter two sources can again be reduced to a minimum by using a very high quality mirror, which is carefully set up and accurately aligned. Of most importance, however, is the systematic error of the non-constant shifting velocity across the field. Due to image distortion effects, the rotating mirror image shifting system gives a greater shift at the edges of the CCD array than at the centre. The error is increased if the camera to measurement zone distance is decreased. This effect was demonstrated by Morrison [52], who showed that the horizontal shift speed may vary across the measurement zone by up to 10%. The same effect was also shown by Haydon [35]. In that study, Haydon corrected the horizontal and vertical velocities by using a quadratic fit and a linear fit to the data, respectively.

In this study, the error due to the distortion in image shifting was corrected by performing ensemble averaging of a number of still-water shift-velocity calibration

maps. The camera to measurement zone distance was also kept fairly large so as to reduce the effect of this error. The averaged shifting velocity was then subtracted from the recorded PIV maps. This technique was previously used by Earnshaw [19].

3.6 Accuracy of PIV

Error analysis of the PIV technique has been an interesting and important subject for a number of researchers. It is essential to show whether or not the measured velocities are accurate and reliable. For water wave studies, the accuracy of, and the errors found in, the velocity measurements made using PIV have been discussed by Gray [29] and Quinn *et al.* [61]. Their discussions were aimed towards the accuracy of the conventional technique, where wet-film photography and the optical autocorrelation analysis were employed. It was found that such a system gave an error in the measured velocities of up to a few percent in extreme cases. In the work of Keane & Adrian [40, 41] an attempt was made to minimise the errors in autocorrelation analysis when double and multiple pulsed PIV systems were used. Recent research [17, 38, 84] has been aimed at the accuracy of the DPIV technique, where the key errors have been suggested to stem from the digital analysis process and especially from the peak detection algorithm.

A brief discussion of the main errors relevant to the PIV technique used in this study is given here. Since the technique consists of two main steps, namely image acquisition and image analysis, the errors due to these steps will be dealt with separately. Particular problems associated with the measurement of velocity fields under breaking waves will be considered in the individual experiment chapters (chapters 6 and 7).

3.6.1 Errors Introduced during Image Acquisition

The errors inherent in this step of the PIV are mainly due to the characteristics of the optical recording system. These errors can be divided into the two classes of systematic and random errors [61], as shown in table 3.3. The effects of the systematic errors remain constant between measurements. Most of the errors can be minimised by using high quality equipment and setting it up with great care.

Systematic Errors	Random Errors
<ul style="list-style-type: none"> • light sheet intensity and flatness • seeding buoyancy • geometric distortion of camera lens • refractive index changes between water-glass-air interface • out-of-plane velocity components 	<ul style="list-style-type: none"> • illumination interval • light sheet thickness • random distribution of seeding particles • focus and alignment of camera • magnification measurement

Table 3.3: Systematic and random errors introduced during image acquisition.

A few problems arise when using the scanning beam system to illuminate the flow. The illumination intensity is not perfectly constant [31] but this effect is rather minimal. There is light loss due to reflection at every optical component in the beam path as well as due to light absorption by the seeded water. By using a high powered laser, blocking out the external light and cleaning the tank regularly, a high contrast image of bright particles on a dark background can be achieved.

The laser light sheet may not be perfectly flat due to small deformations in the reflecting parabolic mirror. Typically, the flatness of the light sheet is within ± 3 mm, and for a light sheet of around 2 mm thick this gives a random magnification error of about 0.1% [61].

Another problem which stems from using the scanning beam method is the small uncertainty in the illumination interval. This is due to the fact that particles

in different regions are not illuminated at precisely the same instant of time. However, if the interrogation areas are much smaller than the total width of the light sheet, this error is very small [31].

It has been pointed out that the choice of seeding particles is crucial. They need to precisely follow the flow and scatter the light well. Conifer pollen and silver coated hollow glass spheres were adopted in this study, where the first one has a small tendency to rise and the latter has a slight tendency to sink. In addition to these systematic errors, random errors occur due to the fact that the seeding particles are distributed randomly throughout the water. That is, the continuous flow field is represented by a random sample of points across the measurement region [2].

The resulting PIV images may appear curved, especially at the edges. This is caused by refractive index changes. Fortunately however, this problem is almost counter balanced by the distortion due to lens aberration, which has the opposite effect [29]. Nevertheless, it is still necessary to check the total distortion from the image of a grid, to see whether the effect is negligible.

Because the PIV used here is a two-dimensional technique, the out-of-plane velocity components cannot be measured and, moreover, this can result in significant errors. It is suggested that because the experiments were carried out in a 2-D wave flume, the out-of-plane component is minimal [61]. However, when measurements are made of the turbulent flow field under breaking waves, this conclusion cannot be made. The effect of this error is minimised when the camera shutter is only opened for a very short time, so that the flow does not change significantly during exposure.

Misalignment of the camera causes problems with focusing and magnification and result in poor image quality. This then gives errors in the measured velocities.

These errors can be reduced to a minimum by patiently and accurately setting up the camera. This philosophy is also applied to the rest of the apparatus.

3.6.2 Errors Introduced during Image Analysis

The most important thing to be considered during the analysis process is the accuracy of the particle displacement measured from the correlation plane. The quality or resolution of particle images recorded by a CCD camera plays a major part in the accuracy of particle displacements. The main source of error is the uncertainty in the detection of the correlation peak, which is influenced by the following:

- particle image size
- seeding concentration/particle image density
- velocity gradients.

With the current DPIV system, the position of the correlation peak can be measured to sub-pixel accuracy. There are three well known possible routines for calculating the sub-pixel particle displacements [17, 62]. They are referred to as *three-point estimators* and they are the centroiding or centre-of-mass peak fit, the parabolic peak fit and the Gaussian peak fit. Because it is the best performing and most frequently implemented approach, the Gaussian peak fit is used in this study to detect the correlation peak. This good performance is based on the fact that the particle images are well approximated by a Gaussian intensity distribution and so the resulting correlation peak will also have the same distribution profile. These three-point estimators, however, give the best results when the correlation peak is relatively narrow. If the fitted peak does not agree with the actual correlation peak, a *bias error* can occur.

The form and size of the correlation peak is dependent on the diameter of the particle images. If the particle images are too small, there is not sufficient information in the correlation peak compared to that of the noise. If the particle images are too large, the correlation peak becomes wide, and so an uncertainty in the peak detection is introduced. There has been much work done on improving the displacement estimation [17, 62, 84]. It has been shown that for 32×32 pixel crosscorrelation, the optimum particle image should be approximately 2 pixels in diameter, in order to achieve the minimum error [84].

The seeding density should not be too high because this causes particle images to overlap and distorts the peaks in the correlation plane. This will then introduce the bias error in the peak detection. On the other hand, very low seeding densities are also unsuitable as there are generally not enough particle images to achieve an acceptable signal to noise ratio. The optimum particle image density is recommended to be around 10–15 particle pairs per interrogation area for autocorrelation analysis [41, 61]. For crosscorrelation analysis it is suggested that the number of particle images should be greater than 7 in an interrogation area [42].

Although the camera exposure is chosen to be a very short period of time, so that the flow is constant, in water waves it is hard to avoid regions of high acceleration or vorticity within the flow. As a result, the individual particle images are irregularly spaced, introducing displacement gradients or velocity gradients in some interrogation areas. This effect causes the correlation peak to be spread over a wider area and reduces the peak height so that the random error in the peak displacement is increased. In addition to this, a bias error also occurs. This is because smaller displacements are measured more than larger displacements, due to the loss of faster moving particles between exposures. Keane & Adrian [41] reported that for high peak detection probabilities, the velocity variation should

be less than 5% across the whole interrogation area. This however is also dependent on the in-plane and out-of-plane displacements, which should be less than one quarter of the interrogation area width and the light sheet thickness, respectively. For breaking wave measurements, Quinn *et al.* [61] estimated that the random error, relative to the maximum velocity, can be as much as 3.0% for the extreme displacement gradient of 0.05.

There are a number of ways to remove the bias errors caused by the above effects (see further details in [17], [38] and [62]). In this study the method known as *re-interrogation* is applied during the analysis. This method involves performing the correlation at each interrogation location twice. In practice, the first correlation is made as normal. However, before performing the second correlation, the interrogation area of the second image is moved by the integer number of pixels closest to the displacement known from the first correlation. This means that the largest displacement in the second correlation should be ± 0.5 pixels. It was found by Westerweel *et al.* [85] (with a 32×32 pixel interrogation area and a 2 pixel particle image size) that if the particle displacement is less than 0.5 pixels, the rms (root mean square) error is very small. Therefore, with the re-interrogation method explained above, the bias effects are reduced and the S/N ratio is also increased.

3.7 Summary of Chapter 3

This chapter explains the full-field 2-D velocity measurement technique known as Particle Image Velocimetry (PIV). The principles and methodology of the technique were given. The current system applied to this study is a totally digital technique. That is, the image capture is carried out by using a CCD camera and the image analysis is performed computationally. All of the instruments involved

Chapter 3 — Particle Image Velocimetry

in the current PIV system were described. The inherent errors in PIV due to several effects and the techniques to minimise these errors were discussed. It was pointed out that PIV can give accurate and reliable results if care is taken throughout the processes of experimental set-up, image acquisition and image analysis.

Chapter 4

Experimental Facilities

This chapter contains the description of experimental facilities including the wave flumes, wave generation and the beach construction. In addition to the velocity measurements, the free-surface elevations have been recorded using wave gauges. The structures and operation of these devices are explained. Finally, all the test parameters used in the experiments are summarised.

4.1 Flumes & Wave Generation

It has already been introduced in the first chapter that the experiments were conducted in two different flumes. The experiments using a single plunging breaker were carried out in a short wave flume at the Fluid Dynamics Group, University of Edinburgh (UEDIN). The experiments using a train of breaking waves were carried out in a large wave flume at the Department of Hydrodynamics and Water Resources (ISVA), Technical University of Denmark. The details of wave flume and wave generation at each place are now given.

4.1.1 UEDIN Wave Flume

At The University of Edinburgh, the wave flume used is known locally as the “Green tank”. It is 9.75 m in length, 0.40 m in width, 1.00 m in height and the

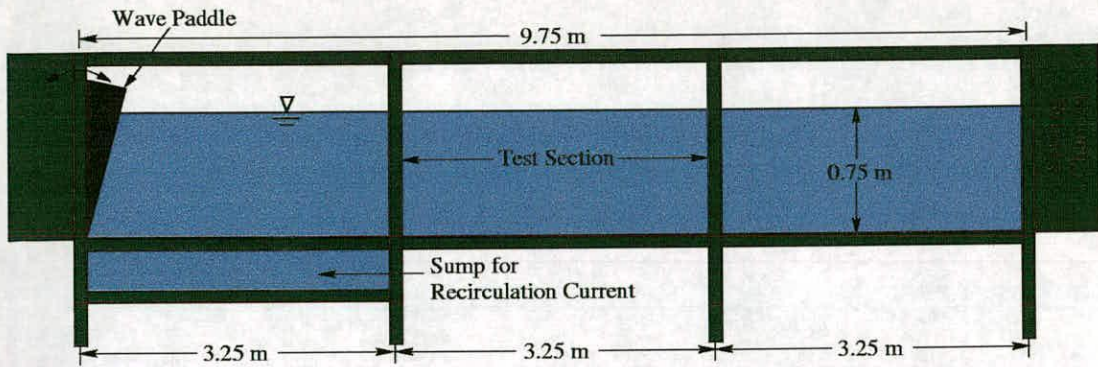


Figure 4.1: A schematic diagram of the wave flume at UEDIN.

working water depth is 0.75 m. The supporting frame of the flume is steel. The base and side walls of the flume are of 25 mm thick glass in order to allow optical access for flow visualisation. Figure 4.1 shows a schematic diagram of this wave flume without the beach set-up. A wavemaker is located at one end of the flume and the settling chamber is at the opposite end. The flume has three sections, each 3.25 m in length, and the experiments were conducted in the middle section where the initial breaking occurred.

The flume is designed not only for the study of water waves, but currents also. These can be generated by pumping the water into the flume at the base of the wavemaker end and out at the chamber end. More information about current generation as well as the detailed flume construction can be found in Skyner [67] who designed and built the flume.

Wave Generation at UEDIN

The wavemaker installed in the Green tank is the hinged-paddle (or a flap) type, which also acts as an active wave absorber. The paddle and its controlling software were made by *Edinburgh Designs Ltd*, developed from a design of Prof. Stephen Salter in the Department of Mechanical Engineering, University of Edinburgh. There are force and velocity transducers built within the wavemaker

so that reflections can be sensed and absorbed by the paddle whilst waves are being generated. A variety of wave spectra can be produced.

The wave paddle is controlled, through an interface box, by a PC. In addition to sending the drive signal to the paddle, the wavemaker controller can also output signals to trigger other devices, such as cameras, as well as sample signals from external devices such as wave gauges and position transducers. The software used to perform the present experiments was version 3.61 of **Ocean** compiler, developed by Rogers & Bolton-King [65].

With the existence of the beach in a wave flume of such limited length, it is very difficult to generate breaking waves from a train of regular waves. Consequently in this study, a single plunging breaker was generated by superimposing a number of wave fronts and focusing them to break at the desired time and position in the flume. However, it transpired that the actual breaking position and time were not exactly what had been programmed into the wavemaker controller. This was due to shoaling of the wave as it travelled up the beach; the wave generation software and paddle controller are designed to focus waves in a constant water depth over the whole flume and do not account for the effect of shoaling on breaking position. The breaking point was then determined from the free-surface profiles measured by wave gauges. It is determined as a point where wave height to water depth ratio H/d is maximum (see section 2.2).

A detailed explanation of the generation of focused waves in the Green tank is given as follows. The free surface displacement η at position x and time t can be described by

$$\eta(x, t) = \sum_{n=1}^N a_n \cos(k_n x - 2\pi f_n t + \phi_n), \quad (4.1)$$

with

$$\omega_n = 2\pi f_n \quad (4.2)$$

and

$$\omega_n^2 = gk_n \tanh(k_n h). \quad (4.3)$$

Here a_n is the amplitude of the n th frequency component, ϕ_n is the corresponding phase and h is the undisturbed water depth. Equation (4.3) is a well known dispersion relation for the gravity water waves, it relates the wave number k_n with the radian frequency ω_n .

In the user program, the wave amplitude and frequency range are specified [65]. The controlling software for the paddle has a built-in function that creates multiple wave fronts by distributing the wave amplitude across the frequency range, modified by a slope factor (see figure 4.2).

The amplitude a_n for a front n in the wave is specified as:

$$a_n = \frac{a f_{\text{base}}}{f_{\text{max}} - f_{\text{min}}} \left(1 + \frac{s(f_n - f_{\text{mean}})}{f_{\text{max}} - f_{\text{min}}} \right), \quad (4.4)$$

where

a	=	total amplitude (given amplitude),
f_{min}	=	minimum frequency,
f_{max}	=	maximum frequency,
s	=	slope factor in range $[-1,1]$,
f_{mean}	=	$(f_{\text{min}} + f_{\text{max}}) / 2$,
f_{base}	=	the base frequency determined by the frequency of the wavemaker and
f_n	=	frequency corresponding to front n .

The next step is to focus all the wave fronts at the desired position and time in the flume. This is done by setting the start phases of all the fronts in a wave group so that they will have equal phase at a particular time and location. The start phase of each front is set to the value of:

$$k_n x_b - 2\pi f_n t_b + \phi_n = 2\pi m \quad (m = 0, \pm 1, \pm 2, \dots), \quad (4.5)$$

where x_b and t_b are position and time of the focused event respectively. Then the

free surface displacement from equation (4.1) becomes:

$$\eta(x, t) = \sum_{n=1}^N a_n \cos [k_n (x - x_b) - 2\pi f_n (t - t_b)]. \quad (4.6)$$

By specifying x_b and t_b in the software function, *i.e.* equation (4.6), the paddle can be controlled to generate a focused wave. The type of focused wave is dependent on the size of the specified amplitude. By gradually increasing this, the wave produced can vary from a non-breaking steep wave, through spilling breaker, to a violent, plunging breaker. In this study, a single plunging breaker was chosen. The input parameters for the wave generation functions are shown in table 4.1 and its spectrum is shown in figure 4.2.

Parameters		Chosen Values	
amplitude	a	0.08	m
minimum frequency	f_{\min}	0.4375	Hz
maximum frequency	f_{\max}	1.3750	Hz
slope factor	s	-0.70	
focused position	x_b	4.20	m
focused time	t_b	15.00	sec

Table 4.1: Wave parameters for producing a single plunging breaker in the UEDIN wave flume. Note that in the controlling program, $x = 0$ is at the paddle pivot.

4.1.2 ISVA Wave Flume

Since the wave flume at UEDIN is (a) limited in length and (b) not suitable for shallow-water wave generation, a different, larger scale of wave flume was required for experiments using a train of breaking waves. Therefore PIV experiments were performed at ISVA in a flume 28 m in length, 0.60 m in width and 0.80 m in height, the flume being made by *Armfield* of England. The actual depth of water in the flume for the experiments was 0.51 m. Figure 4.3 is a photograph of the ISVA wave flume, taken before the PIV apparatus was installed, and its schematic

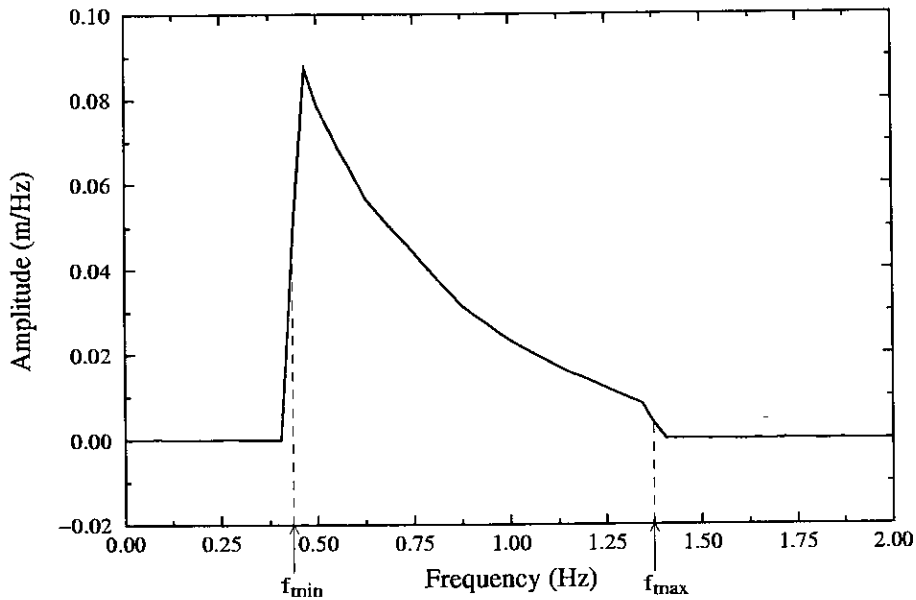


Figure 4.2: Wave spectrum for producing a single plunging breaker in the UEDIN wave flume.

diagram is shown in figure 4.4. The side walls of the flume are made of thick glass and supported by a steel frame, similar to the flume at UEDIN. However, the base of the ISVA flume is opaque and consequently the illumination for PIV was introduced through a side wall of the flume. Further details of the PIV set-up will be given in section 7.1.

The flume consists of three main sections: the wavemaker section at one end, the middle section ($0.60 \text{ m} \times 28.0 \text{ m}$) which is used for flow visualisation experiments and the reservoir section at the other end. The middle section is connected to the reservoir by a large diameter pipe under the laboratory floor, not only for the purpose of current generation, but also to minimise the filling time for such a large flume. As can be seen in figure 4.4, a breakwater and sand bank in front of the reservoir were in place throughout the present experiment. They were used in other experiments performed prior to this study and were not removed before the beach was set up. Thus, to prevent the fine sand particles



Figure 4.3: A photograph of the ISVA wave flume. A piston-type wavemaker is located at the far end (on the left hand side of the picture, unseen).

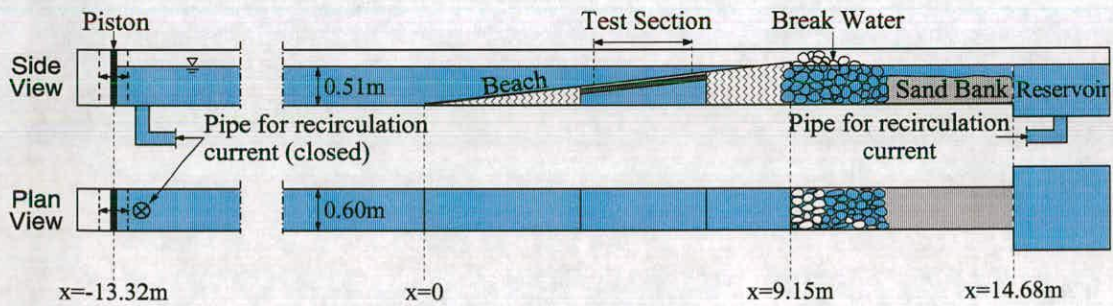


Figure 4.4: A schematic diagram of the ISVA wave flume.

mixed in the reservoir coming into the test section, the connection was closed and the flume was instead filled with tap water. This was a very time-consuming procedure but it was the best solution to prevent particulate contamination of the test section.

Wave Generation at ISVA

A piston-type wavemaker was used in the ISVA flume. It is driven in the horizontal direction in figure 4.4 by two hydraulic pistons, an electrical servo system being used to control the movement with a maximum stroke of ± 0.30 m within a two second period. The motion control signal is generated from a PC with a built-in digital to analog converter. The PC contains a program that can calculate a number of wave types: sinusoidal movement of the piston, regular waves (based on 2nd order cnoidal or Stokes theory), or irregular waves (based on a first-order Biesel transfer function). The program was written by Eskholm *et al.* [24].

In this experiment, a train of regular waves based on the 2nd-order Stokes theory was generated in the flume. As the waves travel up the beach, the deformation and shoaling effects occur before the waves break. If the shallow-water waves were produced by a simple sinusoidal motion of the piston wave generator, an almost unavoidable *free second harmonic wave* would normally appear. This secondary wave is suggested as a smaller and slower wave that travels down the flume and superimposes on the main wave [7, 27]. It causes the generated waves to become irregular in form. In such case, the surface elevation can be written in terms of the superposition of a second order Stokes' wave and a free second harmonic wave:

$$\eta(x, t) = a_1 \cos(\omega t - kx) + a_2 \cos 2(\omega t - kx) + a_{22} \cos(2\omega t - k_{22}x + \alpha_{22}), \quad (4.7)$$

where ω is the wave frequency and is related to the wave number k by the dispersion relations:

$$\omega^2 = gk \tanh(kh) \quad (4.8)$$

and

$$(2\omega)^2 = gk_{22} \tanh(k_{22}h). \quad (4.9)$$

On the right hand side of equation (4.7), the first two terms are a 2nd order Stokes wave and the last term represents a free second harmonic wave. α_{22} is the phase angle between the main wave and the free second harmonic wave at the generator. The period of the free second harmonic wave was approximately half of the main wave period.

In order to reduce the unwanted free second harmonic wave, but leaving the waves of constant form, a non-sinusoidal motion was introduced to the piston wave generator instead of a simple sinusoidal motion. The translation of the piston is written as

$$\xi(t) = e_1 \sin(\omega t) + e_{22} \sin(2\omega t + \beta_{22}), \quad (4.10)$$

where e is the amplitude of the piston translation and β_{22} is the phase angle between the two components of the piston motion.

This method was introduced by Buhr Hansen & Svendsen [7] (see also Svendsen & Buhr Hansen [73]). It is found to be an efficient way to generate the waves of constant form which can minimise the effect of the free second harmonic wave down to 2% of the main wave height.

The basic wave parameters that need to be given as input to the controlling programme are wave height (H), water depth (h), wave period (T) and wave length (L). Then the command signal is computed based on the 2nd order Stokes theory taking into account the need to reduce the free second harmonic wave.

The wave parameters chosen in this experiment are shown in table 4.2 including the resulting 2nd order Stokes wave height (H_2) and free second harmonic

Breaking wave type	H (m)	h (m)	T (s)	L (m)	H_2/H	H_{22}/H_2
Weak plunging	0.105	0.51	1.20	2.06	0.1132	0.3319
Spilling	0.105	0.51	1.08	1.73	0.1156	0.3928

Table 4.2: Wave parameters used in the ISVA wave flume and the corresponding breaker types.

wave height (H_{22}), relative to the main wave height (H) and H_2 , respectively. Two types of breaking wave are generated on the beach depending on the initial wave steepness. Figure 4.5 shows the resulting measured free surface elevations and their Fourier Transforms of the two generated waves at the same x position over the horizontal bed. Figure 4.5(a) and (b) correspond to a train of weak plunging breakers and figure 4.5(c) and (d), to a train of spilling breakers. It can be seen that the records show the constant form of the waves with almost no free second harmonic components.

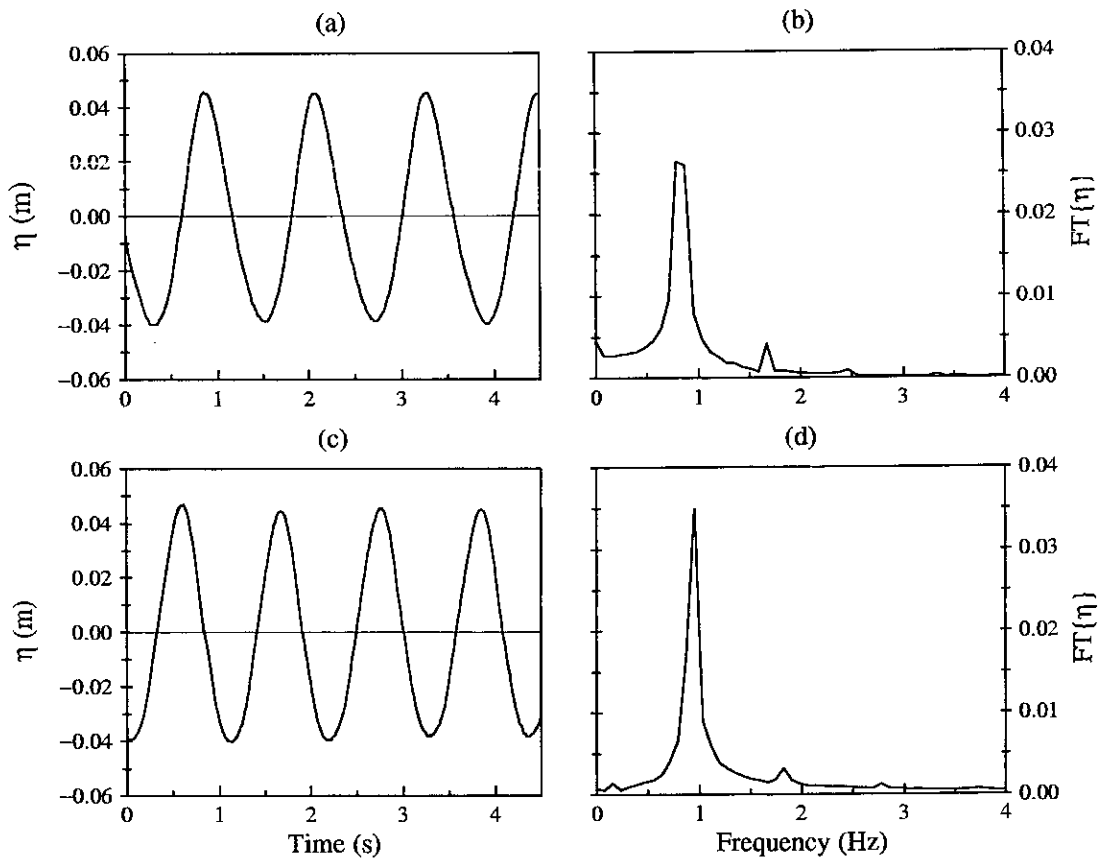


Figure 4.5: Free-surface elevations measured over the horizontal bed (at 12.45 m from the piston wavemaker) in the ISVA wave flume; the records show waves of constant form. (a) is a record of a wave train before breaking as plunging breakers; its Fourier Transform is shown in (b) and (c) is a record of a wave train before breaking as spilling breakers; its Fourier Transform is shown in (d).

4.2 Beach Construction

The experiments carried out at UEDIN and ISVA employed an artificial beach fitted into the flume to represent a surf-zone region. In both cases, the beach slope was $1/13$. This was agreed for comparison with a numerical model [12]. This is relatively steep but was preferred in order to reduce the amount of computational points and time steps needed in the numerical model [11]. Although the beaches used at both institutions had the same slope, their construction was different due to the different flume and wave scales.

4.2.1 UEDIN Beach

At UEDIN a smooth impermeable beach, made from 8.5 mm thick perspex plates, was fitted into the flume as shown in figure 4.6. Another reason to use a $1/13$ slope was that reasonable depths could be maintained at the breaking point, within the limited flume length available. Note that there is a sudden change of slope in the beach at the end of the first bay in figure 4.6(a). Due to the paddle wavemaker it is necessary to keep the water depth at 0.75 m at the paddle. It is impossible to install a $1/13$ slope beach and achieve this in the Green tank due to its limited length. Consequently, two separate slopes were used. The steeper section of beach (a “ramp”) is a wooden plate which would normally be laid horizontally above the sump, for deep-water wave experiments.

Using perspex plates for the beach allows the laser illumination to enter the measurement zone through the bottom of the flume. It was adapted from the method of Quinn [60] who used very thin transparent plastic to cover a small gap between two thick plastic beaches running longitudinally along the sides of the Green tank. It was found that after running many waves over such a beach type, the thin plastic started to flap up and down under wave motion until it detached

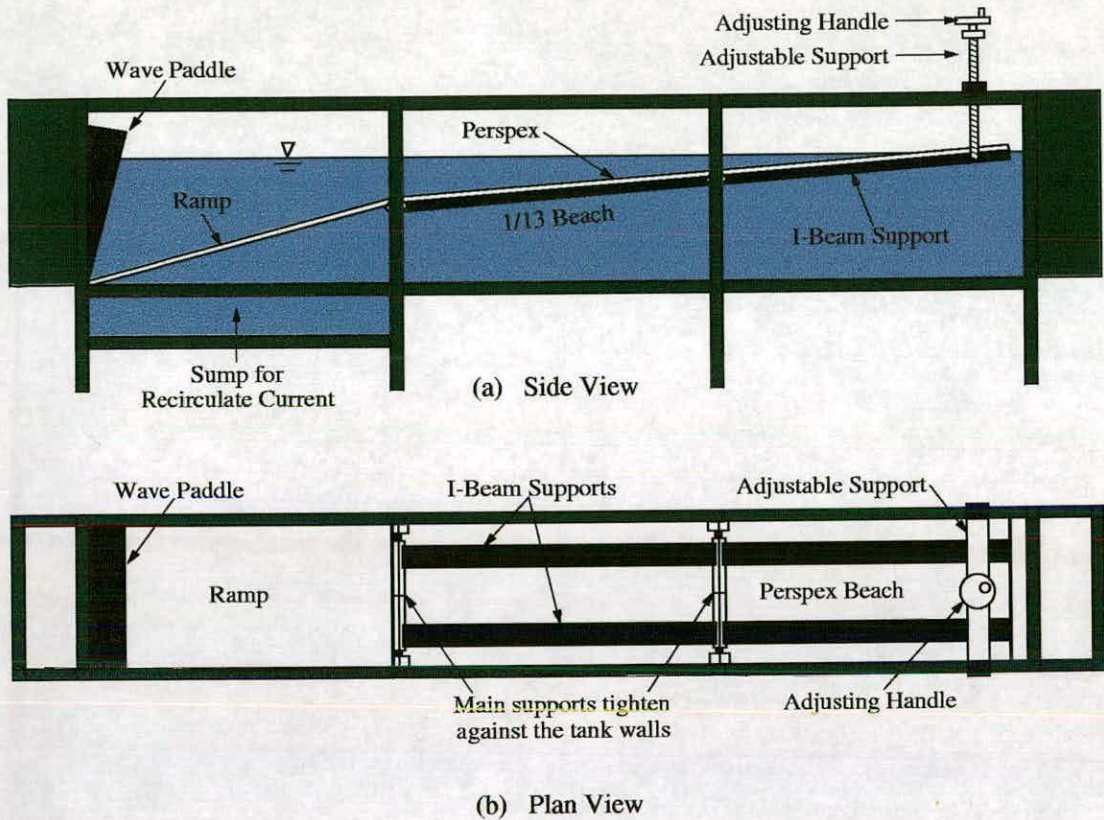


Figure 4.6: UEDIN wave flume when fitted with the beach; side view is shown in (a) and plan view is shown in (b).

from the beach. Because the beach used here was going to be constant in shape and slope throughout the experiments, a more-robust, solid-perspex beach was a suitable choice for the job. The installation of this beach is very similar to that of Quinn's plane sloping beach, and detailed information on the support structures and their installation can be found in [60]. A brief description is given here.

Three perspex plates were used, the overall length being about 6 m. They were screwed directly onto the fibre-glass "I" beam supports. In the plan view, the I-beams were set at about 0.15 m apart, leaving a gap between them for the PIV illumination. The I-beams were supported by three main supports, two of which can be tightened against the tank walls (see figure 4.6(b)). One of these supports was located at the toe of the 1/13 beach and the other at the mid-point

of the beach. The top of the beach, at the chamber end of the tank, was attached to a support resting on top of the tank. This was used to adjust the height of that end of the beach to achieve the correct slope.

4.2.2 ISVA Beach

The beach at ISVA was installed with its toe at 13.32 m from the rest position of the piston wavemaker. Due to the large scale of the flume and the larger waves, the beach need to be relatively robust. It was built up from two different kinds of material. In the test section, where PIV measurements were conducted, the beach was made from 15 mm thick perspex plates. The rest of the beach was made from concrete.

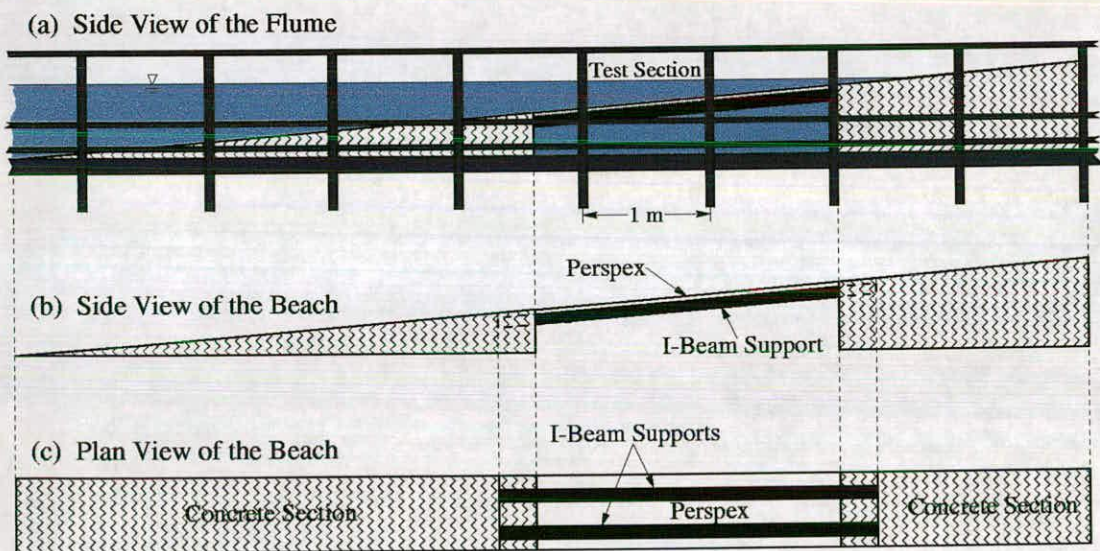


Figure 4.7: (a) ISVA wave flume when fitted with the beach. (b) side view and (c) plan view of the perspex beach attached to the concrete beaches.

Figure 4.7 shows the structure of the beaches when fitted into the flume. The perspex plates and the I-beam supports were prepared at UEDIN and taken over to ISVA, together with all PIV equipment. The concrete sections were prepared and fitted into the flume by technical staff at ISVA. Due to the size of the cargo

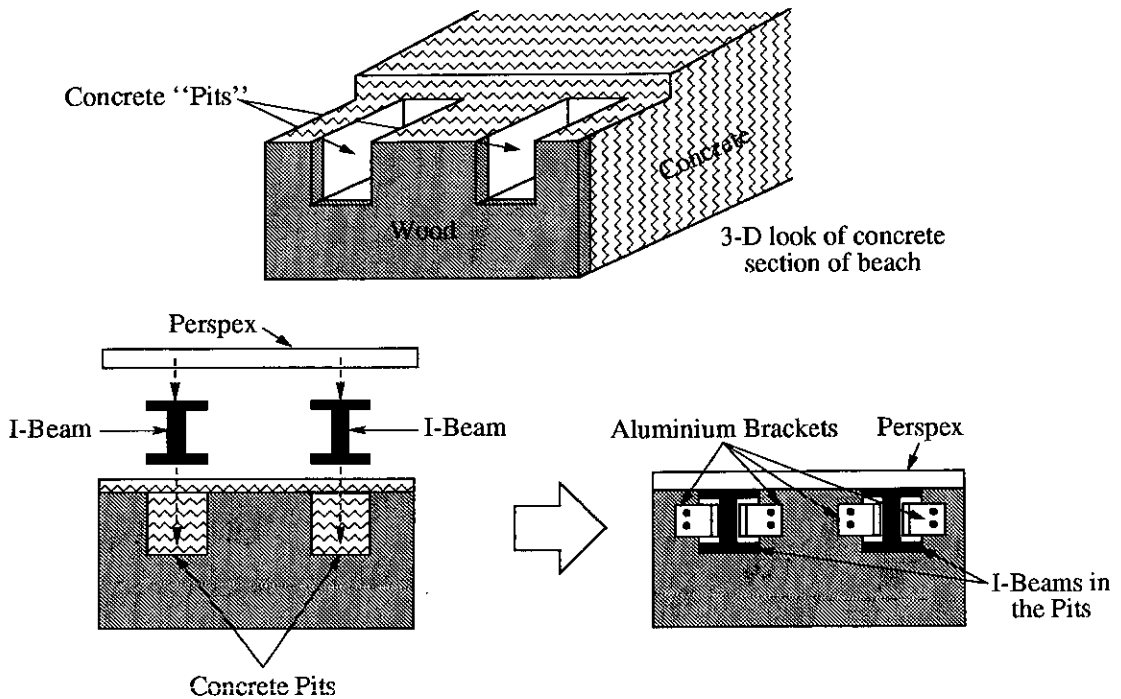


Figure 4.8: Cross-section of the beach in the ISVA wave flume: (top) the three-dimensional look of the concrete section and (bottom) the attachment between the perspex plate, the I-beams and the concrete section.

area of the vehicle used to transport the equipment, the perspex beach could not be made as one long section. Instead it was fabricated in 2 sections, one of which was about 2 m long and the other, about 1 m long. The process of perspex beach construction is similar to that done for the beach at UEDIN. Two pairs of I-beams were used, each pair being joined using Aluminium webbing plates and bolting them through, to create 2 longer beams. The perspex plates were then screwed directly onto the I-beam supports. The completed beach was now ready to fit between the concrete sections. The test section end of each of the concrete sections contains two “pits” for the I-beams to fit in and be bolted in place, see figure 4.8. To stop the I-beams from moving under the wave motion, Aluminium right-angled brackets were used to fasten the I-beams onto the wooden plate attached to the front of the concrete.

4.3 Wave Gauges

Wave gauges were used to measure the free-surface elevation from the still water level. These measurements were carried out in addition to the PIV measurements at both institutions. At UEDIN, the free-surface measurements are useful in testing the repeatability of the waves from one focused event to the next. Additionally, the record of free-surface displacement can be used to determine the breaking point, wave length and crest speed of each breaker.

The wave gauges used at both places have similar structures and functions. They consist of two parallel steel rods partly-immersed vertically in the flume. The operation of the gauges is based on conductivity, *i.e.* the signal from the rods depends on their submerged distance in the water and some other variable factors: the salinity and temperature of the water. In the well-controlled, laboratory wave flume conditions, these unwanted parameters can be kept fairly constant. A sinusoidal signal carrier is supplied to the gauges, the returned signal basically then depends on the submersion. The signal is then amplified to produce an analog ± 5 Volt output. The gauges at UEDIN were recorded at 16 Hz by the wavemaker controller at the same time as a wave is being generated. The data were then transferred onto a PC. At ISVA, the gauges were sampled at 66.67 Hz. The sample rates of the ISVA wave gauges can be easily adjusted by a controlling PC which is connected to the signal amplifier.

The data recorded from the wave gauges are initially units of volts. In order to convert into a physical length unit, a calibration procedure needs to be carried out. This can be achieved, when the water is still, by sampling the gauge at different submersion distances. As conductivity is linearly proportion to the submersion (with constant salinity and temperature) the calibration graph should be a straight line, as shown for example in figure 4.9. By using linear regression with

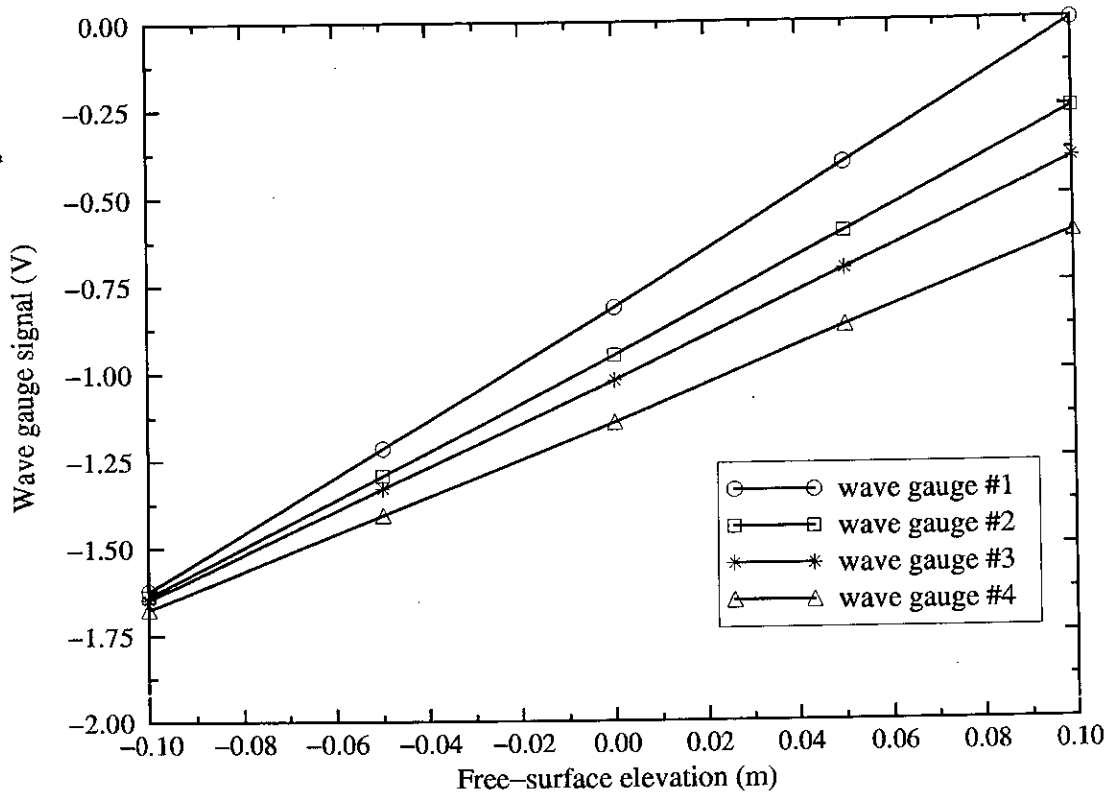


Figure 4.9: Calibration lines for the wave gauges.

a least-square fit method, the conversion from voltage to physical length unit can be done.

Camera-Trigger Signal Generator

At ISVA it was not possible to generate signals from the wavemaker to trigger the camera at the desired wave phases. Thus, a specially-designed wave gauge was constructed and positioned on top of the flume. It was made by Jørgen Christensen, a member of the technical staff at ISVA.

A simple wave-trigger consisting of two steel rods similar to those in a normal wave gauge, spaced 10 mm apart, was used as a trigger source. It was positioned in the flume such that each wave crest just touched the tip of the rods. In air, the resistance between them is infinite, but when a water wave crest travels past, it

shorts the electrodes. This was used to trigger a TTL pulse for 100 milliseconds, every time a wave crest travels past the rods, this in turn being used to trigger the camera. By locating this signal-generating wave gauge at different positions along the wave flume, covering one wave length, different phases of each wave cycle can be captured (see also section 7.1).

4.4 Summary of Test Parameters

Here, a summary of all the test parameters used in this study is given, the method of wave generation having been explained in section 4.1. These parameters are shown in table 4.3.

For the single plunging breaker experiments, the starting wave height at the paddle $H_o = 0.08$ m steepening up to the height at breaking point $H_b = 0.154$ m. Because a single breaking wave was generated from the superposition of many wave fronts, the central frequency that represents the breaking wave needs to be determined. This can be found from the wave spectrum such as that shown in figure 4.2. The central wave frequency can be calculated from the spectrum using the following weighing method:

$$f_c = \frac{\sum_{n=1}^N a_n f_n}{\sum_{n=1}^N a_n}, \quad (4.11)$$

where $f_1 = f_{\min}$ and $f_N = f_{\max}$ (see equation 4.4). The central frequency is then used as the characteristic frequency of a generated single breaker. The corresponding characteristic wave period was then calculated as $T_c = 1/f_c$ and the characteristic wave length as $L_c = g/2\pi f_c^2$ using a linear deep-water wave theory. Their values are shown in table 4.3. A wave breaks as a plunger over the beach at 1.66 m from the toe of the 1/13 slope and at the water depth d_b of 0.228 m. The

Test	d_h (m)	H_o (m)	H_b (m)	L_o (m)	T (s)	ξ_o	Breaker type	x_b (m)	d_b (m)	C_b (m/s)
UEDIN		0.080	0.154	2.87*	1.36*	0.461	plunger	1.66	0.228	1.60
ISVA	0.510	0.084	0.105	2.25	1.20	0.398	weak plunger	5.33	0.100	1.22
ISVA	0.510	0.086	0.098	1.82	1.08	0.354	spilling	5.28	0.104	1.21

Table 4.3: Summary of all the test parameters used in this study. C =crest speed, H =wave height, L =wave length, T =wave period, ξ =surf similarity parameter, x =horizontal position and d =still water depth. The subscripts o , h , b and the superscript * denote the deep-water parameter, horizontal bed section, breaking point and characteristic parameter respectively.

breaking type corresponds to a deep-water surf similarity parameter ξ_o of 0.461 which was just below the classified range proposed by Galvin [27] and Battjes [5] (see section 2.3). The speed of the wave crest at breaking, C_b , was 1.60 ms^{-1} , which is about 1.07 times the phase velocity. The crest speed was estimated by using two wave gauges recording the same wave at different positions within the breaking region.

For the ISVA experiments, two types of breakers: weak-plunging and spilling, were generated from the regular wave trains. The water depth was kept at 0.51 m throughout the experiments for both waves. The main wave parameters (H , L and T) of both breakers have been chosen after much trial and error of wave generation. The waves used in the experiments were those that broke over the perspex section of beach. PIV experiments were also carried out for the case of strong plunging breakers. Unfortunately, over nearly the whole wave period, the images contained a large amount of air bubbles generated during breaking. It is not possible to analyse the images where this exists and it was decided not to present the experiments for this wave here. As a result, the wave parameters of the weak plungers used here were close to that of the spilling breakers so as to avoid the large quantity of the bubbles. The differences in their physical

appearances at initial breaking, however, enables the waves to be categorised into two different types.

The deep-water wave length shown in table 4.3 of both breakers at ISVA were estimated by linear deep-water wave theory. The surf similarity parameters can then be calculated. Such a parameter for the weak plunger is smaller than the classified value of Battjes's [5]. It falls in the spilling breaker type, but the wave is labelled as a plunging breaker here judged by its appearance. The deep-water wave height was approximately equal to the wave height in the horizontal bed section. This is because the water depth to wave length ratio, d/L , in the horizontal bed section falls into the intermediate-depth regime [74]. The crest speed of both breaking waves were again estimated from the free surface profiles recorded using two wave gauges positioned at different locations. The crest speeds in table 4.3 of the weak plunger and the spilling breaker are 1.23 and 1.20 times their respective phase velocities.

4.5 Summary of Chapter 4

This chapter describes the experimental facilities used at two institutes. Experiments were carried out in two scales of laboratory wave flume, one at The University of Edinburgh (UEDIN) and the other at ISVA, Technical University of Denmark. Details of the wave flumes, wave generation and beach construction were given. In the UEDIN short wave flume, the single plunging breakers were generated by the hinged-paddle wavemaker which controls the multiple wave fronts to be focused at the desired position and time. In the ISVA large scale wave flume, the trains of regular waves were controlled by a non-sinusoidal translation of the piston-type wavemaker. The weak plunging and spilling breakers were generated. The beaches used in both wave flumes had the same slope of

1/13 and were made from the solid perspex plates so that the laser light sheet can be transmitted through.

Another measurement done apart from the PIV is that of the free-surface elevation. Such values are measured by using the wave gauges. The wave gauge structure and operation were explained along with the calibration method. These measurements are of important in calculating the crest speed of waves and also providing the information of the wave repeatability, wave length and breaking point. Finally, the summary of all the wave parameters used in this study was shown in the last section.

Chapter 5

Experimental Data Analysis

The main objective of this study is to gain knowledge of wave and turbulence characteristics under surf-zone breaking waves from PIV measurements. This chapter deals with the post-processing of PIV data and explains the method of extracting wave and turbulent quantities from instantaneous velocity vector fields. Before the data can be analysed to provide those quantities, it needs to be validated. The following section describes the validation method used.

5.1 PIV Data Validation

After the image analysis, explained in chapter 3, the output data contains two-dimensional instantaneous velocity on a regular grid in the flow field. Each data file contains velocity information in 5-column ascii form $(x, z, u, w, S/N)$, where x and z are the horizontal and vertical coordinates, respectively, u and w are the instantaneous velocity components in the x and z direction, respectively, and S/N is the signal to noise ratio.

If poor correlations occur, due to several effects explained in chapter 3, then “spurious” vectors or “outliers” can appear on a velocity map. These vectors are considered invalid and should be eliminated from the map before further data processing is done. The outliers can normally be quite readily detected visually on

a displayed map by comparing their magnitude and direction with their nearest neighbours. Figure 5.1 shows an example of the raw data for an instantaneous flow field under a weak plunger. Some of the spurious vectors can be seen clearly, especially along the edge of the field near the free-surface.

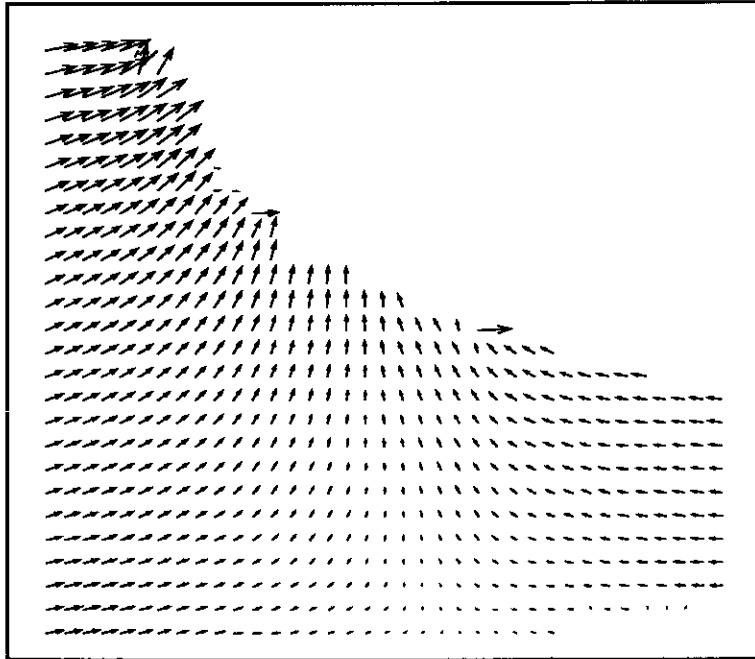


Figure 5.1: Raw velocity vector map of an instantaneous flow field under a weak plunging breaker. Some incorrect vectors can be observed.

It is a time-consuming task to detect and remove incorrect vectors manually, especially when there are a very large number of PIV images such as in the present experiments. In order to avoid this, an automatic validation algorithm for detecting incorrect data on a raw flow field was required.

The validation algorithm used in this study was developed by David Hann [34]. It was written in C and run under a Unix based PC. The algorithm not only detects the incorrect vectors, but removes and replaces them with new vectors that are generated from an interpolation algorithm. These algorithms are explained below.

Validation Algorithm

The validation method applied to raw PIV data is based on the *median* filtering technique. At each (x, z) position on the flow field, the program will find a median values of the u and w components over a number of neighbours, the size being specified by the user. Here, a 3×3 or 5×5 grid size with eight or twenty-four nearest neighbours, respectively, was selected. The median value is taken as the central value of the sorted order of these neighbours with respect to the magnitude of their u and w components. The velocity vector at position (x, z) is then considered invalid and removed if the absolute difference between its value and the median is above a specified threshold, that is

$$|u_i(\text{median}) - u_i(x, y)| > \epsilon_{\text{thresh}}, \quad (5.1)$$

where u_i is the i -component of the velocity vector. The threshold ϵ_{thresh} can be determined experimentally from the flow and varied until the incorrect vectors are removed.

Interpolation Algorithm

After the incorrect vectors have been removed by the median filtering method, the PIV data will contain gaps. This incomplete data field is not suitable for further data-processing algorithms, such as calculating the vorticity or other gradient quantities. As a consequence, the gaps need to be filled using interpolation. The interpolation used here is based on a *smoothing* algorithm. That is the missing data is estimated using a weighted average of the surrounding data with the Gaussian window technique.

At the (x, z) position on the flow field, the program will replace the velocity

components with the smoothed values:

$$u_i(x, z) = \frac{\sum_{m=-10}^{10} \sum_{n=-10}^{10} \alpha(m, n) u_i(x + m\Delta x, z + n\Delta z)}{\sum_{m=-10}^{10} \sum_{n=-10}^{10} \alpha(m, n)}, \quad (5.2)$$

where

$$\alpha(m, n) = \exp\left(\frac{-2(m^2 + n^2)}{\sigma_s^2}\right), \quad (5.3)$$

in which Δx and Δz are the distance between the grids on the vector map along the x and z direction respectively. In the present case $\Delta x = \Delta z$. σ_s is a smoothing factor specified by the user which is best set in the range 1.0–2.0, although it can take any value [34].

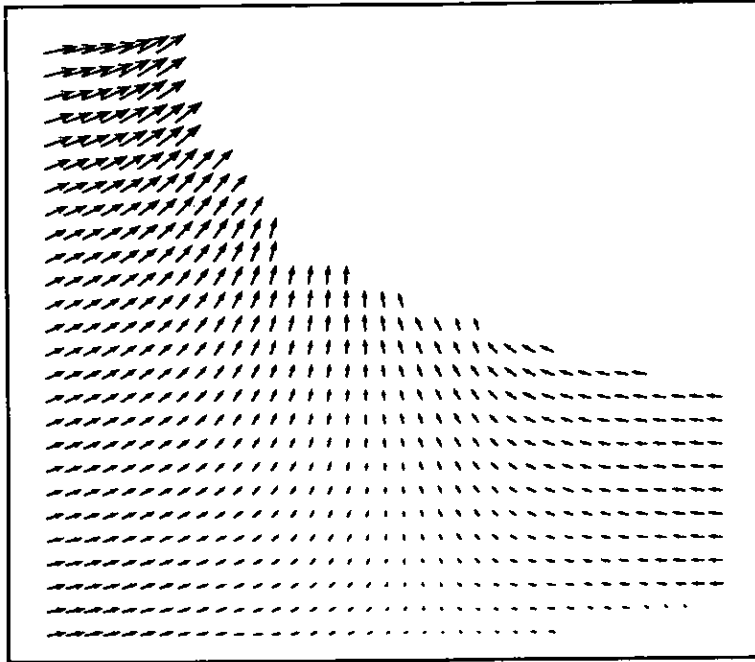


Figure 5.2: Velocity vector map of the instantaneous flow field under a weak plunging breaker first shown in figure 5.1, after validation and interpolation.

Figure 5.2 shows a result after using the validation and interpolation algorithms on the velocity vector map shown in figure 5.1. It can be seen that all the incorrect vectors are removed and replaced by new ones which seem to agree

well with the surrounding vectors. When the interpolation routine is applied to vectors at the edges, such as along the free surface, the number of points in the summation in equation (5.2) will be reduced since the velocity is not measured at points outside the edges.

This technique is used, not only to fill in missing vectors, but also to smooth the whole flow field. This is useful to reduce the noise which affects the experimental data [62]. However, in order to prevent small scale turbulence from being smoothed away, a smoothing factor $\sigma_s = 1.0$ is considered sufficient.

5.2 Estimation of Wave & Turbulent Quantities

Once PIV data is validated, it is ready to be used to extract flow information. This section explains the procedure for obtaining wave and turbulent quantities from the validated PIV data, in order to detect structures in the flow.

5.2.1 Vorticity

Vorticity is one of the important features of the flow. Vorticity maps can be used as a flow-visualisation tool in addition to the most commonly and easily presented tool: velocity field plots. In this study, vorticity is useful for considering the coherent structure and the rotational flow under breaking waves. Additionally, vorticity magnitudes and dynamics can, perhaps, suggest the pattern of sediment transport.

The vorticity $\vec{\omega}$ of a fluid motion is defined as the curl of the velocity vector $\vec{u} = (u, v, w)$ [81]. In the case of a two-dimensional PIV velocity map, only one component of vorticity, which is along the y -axis (normal to the light sheet), can

be determined:

$$\omega_y = \frac{\partial w}{\partial x} - \frac{\partial u}{\partial z}. \quad (5.4)$$

Vorticity at each grid point on a PIV map is calculated using a C-program written by the author. The differentiation operator was based on the method used by Earnshaw [19]. The program fits a 4th order polynomial to the velocity at the calculating point and its four nearest neighbours. The velocity gradients are then calculated from the fitted polynomial functions and hence the y -component of the vorticity, according to equation (5.4), can be estimated. This differentiation method is also applied to determine other differential quantities which are discussed in section 5.2.3. It was suggested that this method provides better results than other differentiation schemes, such as those based on finite differences [62].

5.2.2 Mean Flow & Turbulence Characteristics

In order to investigate turbulent structures under the surf-zone breaking waves, the PIV data needs to be analysed in a statistical way. This requires many measurements of each situation. The procedure for obtaining these records is explained in sections 6.1 and 7.1. The method for extracting mean flow and turbulence parameters from the PIV data is described here.

Mean Velocity

There are several methods for calculating the average value of the measured velocities. Each averaging method can only be carried out if certain conditions are satisfied [37]. Here the *ensemble-average* and *phase-average* method are applied to the PIV velocity maps.

For the UEDIN experiments on single-plunging breakers the same experiment was repeated 20 times. The mean velocity at a fixed point (x, z) and time t was

calculated by an ensemble average:

$$\langle u_i(x, z, t) \rangle = \frac{1}{N} \sum_{n=1}^N u_i^{(n)}(x, z, t), \quad (5.5)$$

where the symbol $\langle \rangle$ indicates averaging operator, $u_i^{(n)}$ is the i -component of the instantaneous velocity measured from the n th experiment and N is the number of repeated experiments, in this case $N = 20$.

For the ISVA experiments on trains of weak plunging and spilling breakers where PIV data were taken at the same phase of each wave cycle, the mean velocity at a fixed point (x, z) and phase ωt can be calculated by means of a phase average:

$$\langle u_i(x, z, \omega t) \rangle = \frac{1}{N} \sum_{n=0}^{N-1} u_i(x, z, \omega(t + nT)), \quad (5.6)$$

where ω is the wave angular frequency and T is the wave period. N is the number of wave cycles, here 60 cycles of the wave were measured.

Turbulence Characteristics

To yield information on turbulence characteristics such as turbulent intensities or turbulent kinetic energy, the turbulent fluctuation need to be separated from the mean flow. This can be done by subtracting the averaged value from the original instantaneous velocity:

$$u'_i = u_i - \langle u_i \rangle. \quad (5.7)$$

Thus the averaged value, $\langle u_i \rangle$, is treated as the wave component which is repeated from wave to wave and u'_i is the turbulent (fluctuating) velocity component.

Since the PIV technique used here can only measure two velocity components, the *turbulent intensity* is defined, following Chang & Liu [10], as

$$I = \langle u'u' + w'w' \rangle^{1/2}, \quad (5.8)$$

where u' and w' are the turbulent fluctuations in the x and z directions, respectively.

Another important turbulent quantity is the *turbulent kinetic energy*, k . By definition k is

$$k = \langle k' \rangle = \left\langle \frac{1}{2} u'_i u'_i \right\rangle, \quad (5.9)$$

where k' is the turbulent kinetic-energy fluctuation and summation over the repeated index is assumed. However, as for the determination of the turbulent intensity, only the x and z components of the velocity were measured. k is therefore approximated as

$$k \approx \frac{1.33}{2} \langle u'u' + w'w' \rangle = \frac{1.33}{2} I^2. \quad (5.10)$$

This approximation was obtained by Svendsen [72] under the assumption that the turbulence under breaking waves resembles that in a plane wake. It has previously been used by several researchers [10, 79, 80].

5.2.3 Turbulent Kinetic Energy Transportation

There has been little application of the turbulence theory in the studies of breaking waves in the surf zone. Only the qualitative features of turbulent flows and their effects on surf-zone dynamics are understood from the early studies (see sections 2.4 and 2.5). It has only recently been possible to carry out quantitative studies using complicated non-intrusive measuring instruments, such as LDA and PIV. Some researchers studied turbulence transport in a systematic manner, for example Chang & Liu [10] and Ting & Kirby [79, 80]. They examined the distribution of the turbulence in time and space.

Chang & Liu [10] also used PIV, as in the present study, to investigate the turbulent structure, however, their study was of spilling breakers in an intermediate water depth with a horizontal bed. Although Ting & Kirby [79, 80] also

conducted the experiments on surf-zone breaking waves similar to the present study, they used the LDA technique. It is worthwhile to note here again that this study is aimed towards the understanding of turbulent structures under surf-zone breaking waves using the PIV technique. The motivation for this aim is provided from the above studies. The technique for investigating the turbulence and its transport process is carried out following Chang & Liu [10] and Ting & Kirby [79, 80] for comparison purposes.

The distribution of turbulent kinetic energy is described by the energy transport equation (the k -equation) [77] as

$$\frac{\partial k}{\partial t} + \langle u_j \rangle \frac{\partial k}{\partial x_j} = -\langle u'_i u'_j \rangle S_{ij} - 2\nu \langle s_{ij} s_{ij} \rangle - \frac{\partial}{\partial x_j} \left(\frac{1}{\rho} \langle u'_j p' \rangle + \langle k' u'_j \rangle - 2\nu \langle u'_i s_{ij} \rangle \right), \quad (5.11)$$

(rate of change – advection = production – dissipation + diffusion)

where p' is the pressure fluctuation, ρ is the fluid density and ν is the kinematic viscosity. S_{ij} and s_{ij} are the mean rate of strain and the fluctuating rate of strain, respectively. They are defined by

$$S_{ij} = \frac{1}{2} \left(\frac{\partial \langle u_i \rangle}{\partial x_j} + \frac{\partial \langle u_j \rangle}{\partial x_i} \right), \quad s_{ij} = \frac{1}{2} \left(\frac{\partial u'_i}{\partial x_j} + \frac{\partial u'_j}{\partial x_i} \right). \quad (5.12)$$

The terms in equation (5.11) are identified as follows:

- The two terms on the left hand side are the local rate of change and the *advective* transport of k . The advection is affected by the mean flow.
- The first term on the right hand side describes the *production* of the turbulent kinetic energy when the Reynolds stresses, $-\langle u'_i u'_j \rangle$, are working against the mean flow gradient. It represents the exchange of the energy between the mean flow and turbulence.

- The second term on the right hand side represents the energy *dissipation* when viscous stresses perform deformation work against the fluctuating strain rate. This term is treated as a drain of energy [77]. The turbulent energy is transferred through a cascade process, where large eddies break down into smaller scales, and eventually dissipate as heat.
- The last long term on the right hand side is the net *diffusive* transport of the turbulent kinetic energy. It consists of the *pressure diffusion* transport due to pressure-gradient work, the *turbulent diffusion* transport by turbulent velocity fluctuation and the *viscous diffusion* transport by viscous stresses. The last diffusion term is usually much smaller than the other diffusion terms [26].

It is perhaps reasonable to assume¹ that the mean flow is two-dimensional when the measurements are taken at the vertical plane along the centreline of the 2-D wave flume [10]. As a consequence, the mean velocity $\langle v \rangle$ (normal to the light sheet) and $(\partial \langle \rangle / \partial y)$ terms vanish. For a large Reynolds number, the viscous diffusion term is very small compared to the other diffusion terms and can be neglected. If the viscous dissipation term is written as ϵ , the k -equation now reads

$$\begin{aligned}
 \frac{\partial k}{\partial t} + \overbrace{\langle u \rangle \frac{\partial k}{\partial x} + \langle w \rangle \frac{\partial k}{\partial z}}^{\text{advection, } -A} = & \\
 & \overbrace{-\langle u'^2 \rangle \frac{\partial \langle u \rangle}{\partial x} - \langle u'w' \rangle \left(\frac{\partial \langle u \rangle}{\partial z} + \frac{\partial \langle w \rangle}{\partial x} \right) - \langle w'^2 \rangle \frac{\partial \langle w \rangle}{\partial z} - \text{dissipation}}^{\text{production, } P} \\
 & \underbrace{- \left(\frac{\partial}{\partial x} \langle k'u' \rangle + \frac{\partial}{\partial z} \langle k'w' \rangle \right)}_{\text{turbulent diffusion, } \mathcal{I}_t} \underbrace{- \frac{1}{\rho} \left(\frac{\partial}{\partial x} \langle u'p' \rangle + \frac{\partial}{\partial z} \langle w'p' \rangle \right)}_{\text{pressure diffusion, } \mathcal{I}_p}. \quad (5.13)
 \end{aligned}$$

¹This assumption is not absolutely correct when three-dimensional flow occurs after a wave has broken, as observed by many researchers [9, 35, 54]. However, to apply the k -equation to the 2-D PIV data, this assumption is used here.

The simplified transport equation can be written as

$$\frac{\partial k}{\partial t} = \mathcal{A} + \mathcal{P} + \mathcal{J} - \epsilon, \quad (5.14)$$

where \mathcal{A} , \mathcal{P} , \mathcal{J} and ϵ represent the advection, production, diffusive transport and dissipation, respectively. The diffusive transport term \mathcal{J} is the sum of \mathcal{J}_t and \mathcal{J}_p . Note that Chang & Liu [10] excluded the normal-stress production terms (the first and last terms of \mathcal{P} in equation (5.13)).

Considering equation (5.13), every term except \mathcal{J}_p and ϵ can be calculated directly from the PIV measurements. Since the pressure field is not measured, the diffusive transport term, \mathcal{J} , needs to be approximated. Chang & Liu [10] suggested two approaches for the approximation: (i) \mathcal{J}_p can be neglected if $\mathcal{J}_p \ll \mathcal{J}_t$; or (ii) \mathcal{J} can be calculated by using a gradient-diffusion hypothesis which says that the diffusion flux of k is assumed proportional to the gradient of k :

$$-\left(\frac{1}{\rho}\langle u'_j p' \rangle + \langle k' u'_j \rangle\right) = \frac{\nu_t}{\sigma_k} \frac{\partial k}{\partial x_j}, \quad (5.15)$$

where σ_k is an empirical diffusion constant (≈ 1.0 ; see Rodi [64]). ν_t is the eddy viscosity and is proportional to a velocity scale and a length scale of the large eddies:

$$\nu_t \approx \ell \sqrt{k}, \quad (5.16)$$

in which ℓ is the turbulent length scale. Svendsen [72] suggested that for a breaking wave ℓ is about 0.2–0.3 times the water depth h . Measurements done by Pedersen *et al.* [55] also confirm this range for the length scale. Ting & Kirby [80], however, suggested that ℓ is in the range $0.1h$ to $0.2h$. In this study $\ell = 0.2h$ is used. Consequently, the diffusion term can be calculated:

$$\mathcal{J} = \frac{\partial}{\partial x} \left(\ell \sqrt{k} \frac{\partial k}{\partial x} \right) + \frac{\partial}{\partial z} \left(\ell \sqrt{k} \frac{\partial k}{\partial z} \right). \quad (5.17)$$

Using the above approximations, each term in equation (5.14), except ϵ , can now be calculated from the PIV velocity maps. If the local rate of change of

turbulent kinetic energy ($\partial k/\partial t$) can be calculated, then the dissipation, ϵ , can be estimated from the transport equation. However, because the PIV system used in these experiments could not provide a high enough frequency record, it is difficult to calculate a reasonable value for $\partial k/\partial t$. Consequently, the dissipation is estimated from the two approximation approaches shown below.

1. ϵ can be approximated using the classical turbulent model [64, 72]:

$$\epsilon = \frac{C_D}{\ell} k^{3/2}, \quad (5.18)$$

where C_D is an empirical constant and is equal to 0.09.

2. ϵ can be measured directly from the horizontal velocity fluctuations using the isotropic theory of turbulence:

$$\epsilon = 2\nu \langle s_{ij} s_{ij} \rangle = 15\nu \left\langle \left(\frac{\partial u'}{\partial x} \right)^2 \right\rangle. \quad (5.19)$$

This model is based on the fact that the dissipation takes place at the smallest-scale eddies, whose turbulent structure tends to be isotropic [64, 77]. This approximation was also used by Ting and Kirby [79].

With the above techniques for post-processing the PIV data, the turbulence transport process can be examined.

5.2.4 Computing Programs

It has been shown that PIV data can not only be used to present velocity vector fields but it can also be extracted to provide other wave and turbulent quantities. The computation of those quantities was carried out using C programs which run on a UNIX based machine. Some of the calculations need additional UNIX scripts. All of the computing programs for the data analysis described in section 5.2.1 to section 5.2.3 were written by the author. As already mentioned, the

differentiation scheme, based on a 4th order polynomial fit, was developed from a code originally written by Earnshaw [19]. It is used to calculate the differential quantities that appear in the vorticity formula (equation (5.4)), the turbulent energy transport equation (equation (5.13)), the diffusion transport approximation (equation (5.17)) and the dissipation approximation (equation (5.19)).

5.3 Summary of Chapter 5

This chapter describes the post-processing of experimental data. Before the PIV data can be analysed to extract flow information, it needs to be validated. The validation method based on the median filtering technique was explained. After the incorrect vectors have been removed by this technique, they were replaced by new values which are determined by interpolation. It was shown that the smoothing algorithm with the Gaussian window technique can be used to interpolate the missing vectors.

After validation, wave and turbulent quantities can now be estimated from the PIV data. The procedures for obtaining those quantities were given. Vorticity and other differential quantities can be calculated using a 4th order polynomial fit. Ensemble-average and phase-average techniques are applied to experimental data in order to extract the information about the mean flow and its fluctuations. Finally, the turbulent kinetic energy transportation is examined by using the energy equation. Each term, except the diffusion and dissipation, in the k -equation can be calculated directly from the PIV data. The diffusion can be estimated by employing the gradient-diffusion hypothesis and the dissipation is approximated by the models.

Chapter 6

Single Breaking Wave Experiments

In this and the next chapter the experiments carried out at UEDIN and ISVA are described respectively. Results from those experiments are also presented and discussed. The explanation of the experimental set-ups, contained in these two chapters, concentrates mainly on the PIV systems and measurement procedures. All of the facilities used at both institutes (which include: the wave flumes; wave generation; beach construction and wave gauges), along with a summary of the test parameters, have already been described in chapter 4. Detailed description of the individual equipment used in the PIV systems can be found in chapter 3. However, some descriptions of the experimental facilities and equipment may be repeated in certain situations in order to provide clear explanation.

6.1 Experimental Set-up

The single breaking wave experiments were carried out in the Green tank (9.75 m) at UEDIN. A single wave (group) was generated by a paddle-type wavemaker and broke as a plunger over a 1/13 beach. The PIV set-up can be seen in figure 6.1. The scanning beam system was set beneath the glass-bottomed flume so that a laser light sheet, about 1 m wide, could be reflected vertically upwards into the

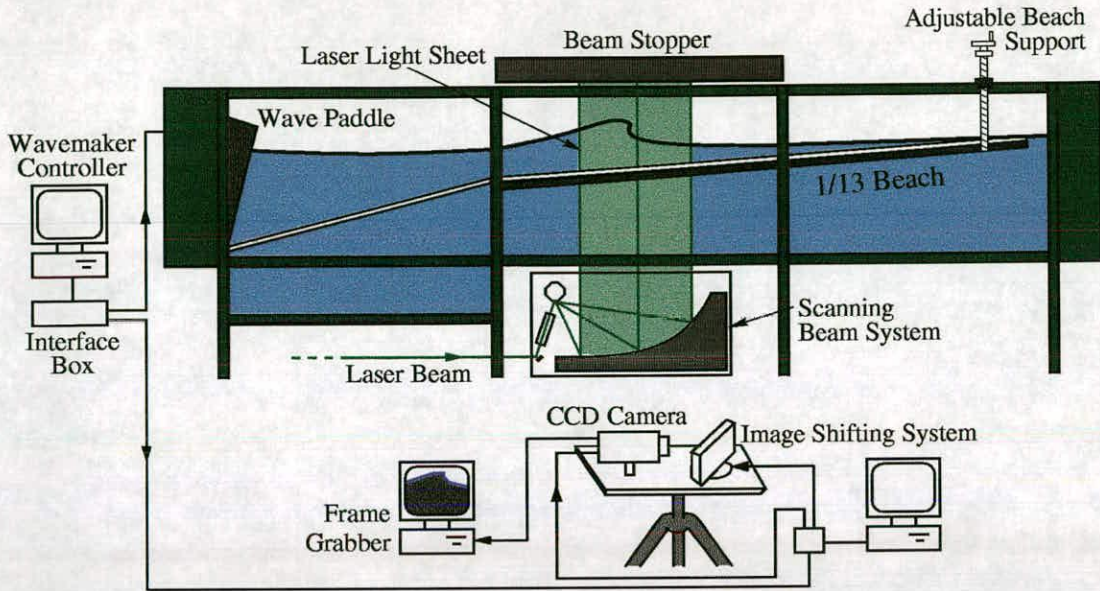


Figure 6.1: The PIV set-up for the experiments carried out at UEDIN.

flow along the centreline of the flume. An Argon-Ion CW laser was used with its output power set to 8 W. For safety reason the laser was kept in another room away from the measurement area. The beam was then covered and directed along the laboratory floor until it was exposed as the light sheet in the flume by the scanning beam system. A beam stopper was placed on top of the flume. The back wall of the flume (opposite to the side where the camera was set up) was covered with black paper in order to reduce reflection as well as to enhance the sharpness of the images.

Silver-coated hollow glass spheres were used as the seeding particles. Four images of each of the particles were recorded by the CCD camera (a Kodak Megaplus ES 1.0/SC). To resolve the ambiguity in the particle directions, an image shifting system was employed. The image shifter was activated and the camera was triggered by a signal sent from an interface box that was used to control the wavemaker. By this means an image could be taken at a desired phase. Due to the time delay of the image-shifting device, only two frames per

second could be captured. The autocorrelation technique was used to analyse the PIV images. With the knowledge of the image magnification, exposure time and shifting velocity, a velocity vector in each interrogation area (64×64 pixels, or around 10×10 mm) could be determined.

The PIV measurements were conducted in the middle section of the flume and were taken at 3 positions, as shown in figure 6.2. These positions cover the breaking point and the transition zone. The breaking point, $x_b = 1.656$ m, was where the wave height to water depth ratio was maximum. Note that the reference point ($x = 0, z = 0$) was at the free surface above the toe of the 1/13 slope. This reference was also applied to the experimental system in the ISVA wave flume.

In total, 40 phases of the wave were recorded (at each position) with 0.25 s time interval between each phase. The first phase was taken at 11.375 s after the wavemaker was activated, corresponding to the time when the wave broke. The experiments were repeated 20 times, thus a total of 2400 PIV images were taken. Each image contained approximately 900 velocity vectors but once the region above the free surface, the region below the beach and the region of air bubbles were excluded, the images contained only around half that number.

With the above PIV recording procedure, the mean and fluctuating velocity components at different phases throughout the breaking process of the plunger

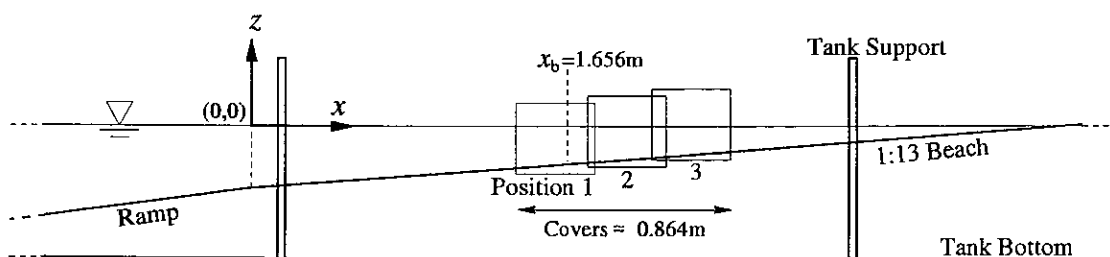


Figure 6.2: PIV measurements taken at 3 positions within the middle section of the UEDIN wave flume.

could be obtained using an ensemble-averaging technique, as explained in section 5.2.2.

6.1.1 Problems with the Experiments

Apart from the problems which occurred during the PIV measurements and analysis, as explained in section 3.6, other problems also occurred during the experimental set-up and execution. The problems that occurred in the single plunging breaker experiments were mainly due to air bubbles and wave repeatability. These are explained in the following.

Air Bubbles

Air bubble generation and entrainment are some of the most important features of breaking waves, especially in plunging and spilling breakers. Unfortunately, these phenomena cannot be studied using the current PIV measurement technique. This is because the air bubbles scatter the light sheet and produce bright patches on the PIV image. This then results in an error during the image analysis stage, due to the fact that individual particles in those patches cannot be detected. As a consequence, the velocity in the aerated region cannot be measured. However, if the air bubbles are small enough (close to the size of the seeding particles), the velocity in that region can be measured. It needs to be noted that these velocities represent the kinematics of the air bubbles, not that of the water particles.

Other problems occurred when air bubbles and seeding particles collected under the perspex beach. These air bubbles were not generated from the breaking wave but were produced when the tank was filled up. If these air bubbles and seeding particles moved into the beam path then the light sheet could be refracted/reflected and its intensity reduced. However, it was easy enough to resolve these problems. Since the beach was made up from three perspex plates,

they were fitted one after another, while the tank was being filled up. Once one section of perspex plate was fitted, the air bubbles under it were removed by wiping them out with a metre stick and then the next section was fitted. This procedure was repeated until, more or less, all of the air bubbles were removed and every perspex section was fitted in place. Furthermore, every time the tank was emptied and refilled, the tank walls and the perspex plates were cleaned thoroughly to remove old seeding particles.

Wave Repeatability

In order to apply the ensemble-averaging method to the PIV data it was essential that the waves were repeatable. Additionally, because PIV images were taken at different positions along the beach and these images were to be joined together, the waves in different experiments were required to be identical. Although images were taken at the same time for each experiment, there could be some occasions when the images appeared different. The unrepeatability of the waves was caused

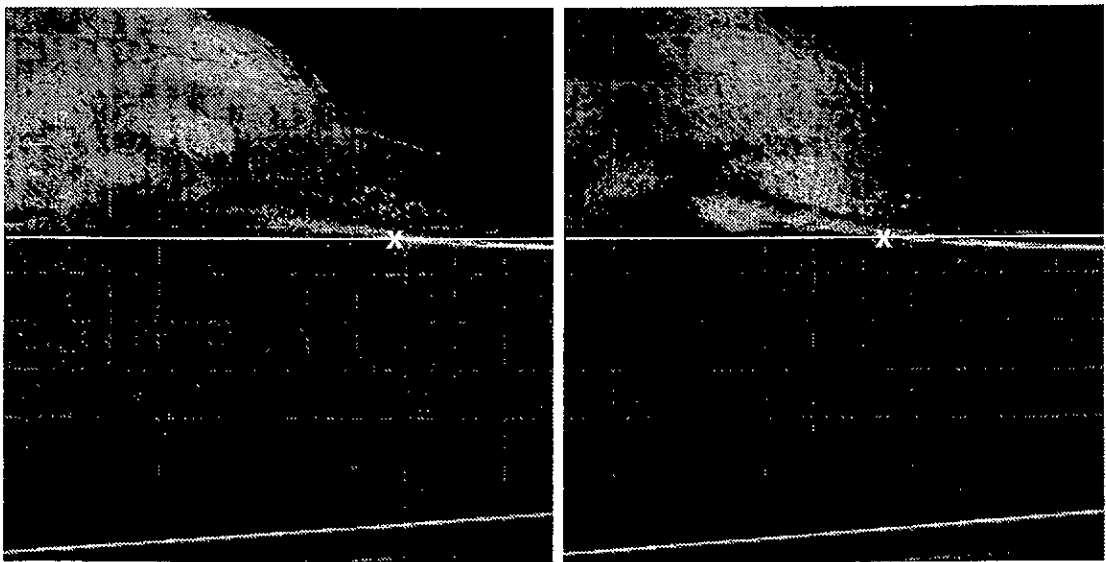


Figure 6.3: Two PIV images of the plunging breaker taken at the same position and time ($(t - t_b)/T = 0.184$) but from different experiments. The chosen horizontal line and its intersection with the free-surface are shown in both images.

by wave reflection. To test the repeatability of the single plunging breakers, the x -position of the intersection between the free-surface in front of the overturning jet and a chosen horizontal line, for each of the 20 experiments, was compared. Figure 6.3 shows the most extreme case of discrepancy between the PIV images. These two images were taken at the same position and exactly the same time but from different experiments. The standard deviation of the location described above was found to be 0.008 m, which is small when compared to the field of view of the images (~ 0.32 m). It was also reported by Quinn *et al.* [61] that with similar experiments on waves on beaches and using the same wave flume and wavemaker, the maximum horizontal velocity component in waves of identical phase differed by only 1.5%. According to these results and the examination of individual images, the repeatability of the single plunging breaker in these experiments was reasonably acceptable. This indicates good absorption of the reflected waves by the wavemaker.

6.2 Results & Discussion

Results from the single plunging breaker experiments are presented in this section. The following four subsections (section 6.2.1 to section 6.2.4) display the results in the form of maps of wave and turbulent quantities: mean velocity, isovelocity, mean vorticity and turbulent intensity. The investigation of turbulence transport will be given in section 6.2.5 .

All the maps of each quantity are arranged so that all the positions are displayed for each phase. For example, figure 6.4 shows the mean velocity maps at four phases (four rows) and at each phase three positions (three columns) are displayed. The plots of the same quantity for the next four phases are then continued in the next figure (figure 6.5). It is considered unnecessary to present the

maps for all 40 phases, therefore a sequence of 8 phases, beginning at breaking $(t - t_b)/T = 0$, with an interval of 0.184, is displayed for each quantity. An exception to the above rule is for the isovelocity contours where only the first 4 phases are displayed.

In every map, the horizontal coordinate $((x - x_b)/h_b)$ is the distance from the breaking point normalised by the undisturbed water depth at breaking and the vertical coordinate (z/h_b) is the distance from the still water level (SWL), which runs positively upwards (see a diagram in figure 6.2), normalised by the same value. The beach and free-surface lines are also drawn in each map. In some cases, such as in figure 6.4(b), (c) and (d), the aerated regions are indicated, most of which do not contain any velocity vectors. This form of displaying the results is also used in the next chapter.

6.2.1 Velocity Vector Maps

A typical method to present the PIV data is by using a vector plot. It gives an immediate picture of the internal kinematics of the flow. A sequence of ensemble-averaged velocity fields under the plunging breaker is shown in figure 6.4 and continues in figure 6.5. The velocity in these plots is normalised by C where C is the speed of the wave crest at breaking (160 cm/s). The reference vector, shown at the corner of the map, is $0.5C$.

Figure 6.4(a) shows the mean velocity fields at the time of breaking where the wave front is vertical. The wave crest is out of the measurement region, in position 1. However, it can be seen that there is a strong forward movement under the crest region. There the horizontal velocity magnitude is greater than $0.5C$ and gradually decreases in the deeper region towards the beach. A backwash movement can be seen in position 3. This interacts with the incoming breaker causing the “stagnation” of the horizontal velocity under the wave trough which

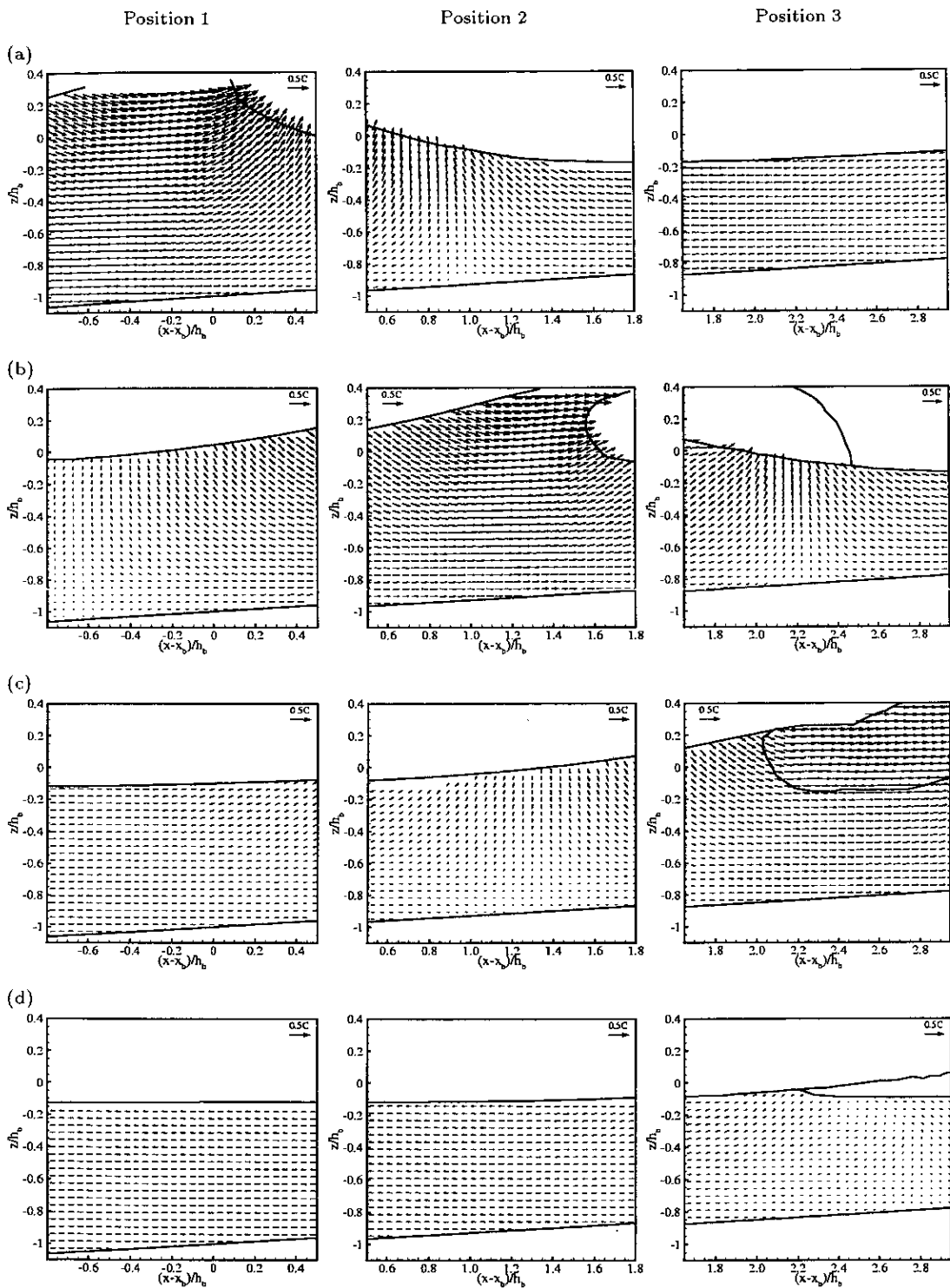


Figure 6.4: Mean velocity of the plunging breaker at $(t-t_b)/T =$ (a) 0, (b) 0.184, (c) 0.368 and (d) 0.551.

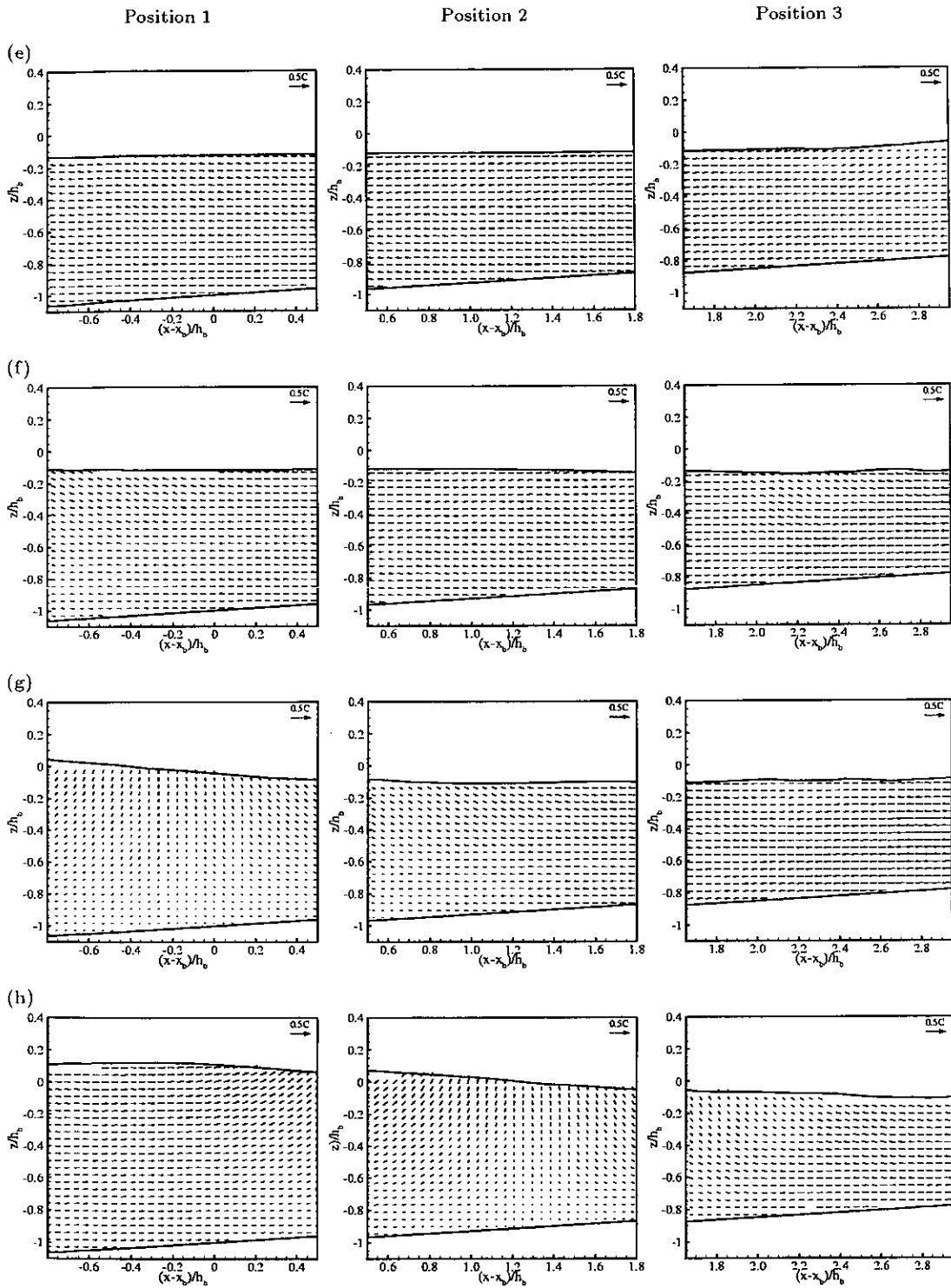


Figure 6.5: Mean velocity of the plunging breaker, continued from figure 6.4, at $(t - t_b)/T =$ (e) 0.735, (f) 0.919, (g) 1.103 and (h) 1.287.

can be seen in position 2. Lin & Hwung [44] called this a “dividing region” and suggested that this may cause the formation of a sand bar near the breaking point on a sandy bed.

Figure 6.4(b) is the phase at which the overturning jet has impacted the water surface at the front. The region just under the crest can now be seen in position 2. The horizontal velocity magnitude there is around 100 cm/s which is about $0.63C$. This result can be seen more clearly with the isovelocity contour plots shown later. There is a downward movement at the leeside of the wave, in position 1, and the flow on the far left begins to reverse. The stagnation of the horizontal velocity under the trough can also be observed in position 3.

In the third phase ($(t - t_b)/T = 0.368$, in figure 6.4(c)) the overturning jet has passed the measurement region and has left the generated air bubbles behind. This aerated region is indicated in position 3. Although there is an appearance of the air bubbles, an attempt to measure the velocity was made. Therefore, it should be noted that the signal to noise ratios of the measured velocities in that region is very low. However, the measured velocity and the vorticity (shown later) give quite useful results because they supply supporting evidence that the plunger vortex is generated from the overturning jet. The larger scale of the positive horizontal velocities ($\approx 0.4C$) can be seen in the aerated region which are different from those ($\approx 0.16C$) just outside it. The backward movement can now be observed in positions 1 and 2.

By phase 4 ($(t - t_b)/T = 0.551$, in figure 6.4(d)) the backward movement within position 1 and 2 is fully developed and the flow in position 3 begins to reverse. The rotational flow can be seen under the free surface in position 3. This is thought to be affected by the plunger vortex generated in the previous phase. This effect should be more obvious in the vorticity contour plot. The

flow continues to move backwards (see figure 6.5(e) and (f)) until the next small-amplitude wave arrives as seen in position 1 of figure 6.5(g). This wave is a member of the generated wave group and does not break. The new forward movement (of smaller scale than that in the plunging breaker) then begins and again interacts with the backwash.

6.2.2 Isovelocity Contours

It is known that flow under breaking waves is initially irrotational. That is, the flow is potential prior to breaking. It is possible to use PIV data to study the transition from potential flow to rotational flow. A convenient way to visualise this is through plots of isovelocity contours. If the contours of the two velocity components are perpendicular at a point then the flow is irrotational there (assuming two-dimensional flow). This can be shown as follows.

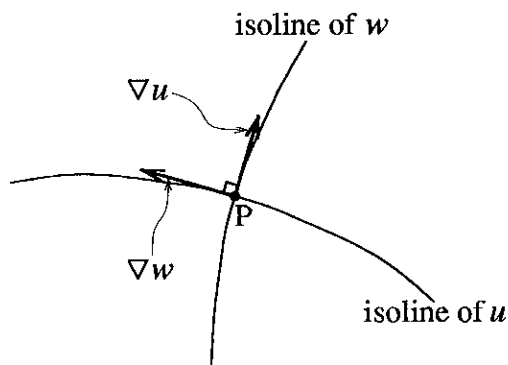


Figure 6.6: The perpendicular of two isolines.

An isovelocity contour (sometimes referred to as *isoline*) is the curve that is drawn through the positions which have equal value of the velocity component. Consider a point P, as shown in figure 6.6. Suppose the isoline of u is perpendicular to the isoline of w at P. Then the gradient of u at P is perpendicular to the

gradient of w at P. Therefore

$$\begin{aligned}\nabla u \cdot \nabla w &= \left(\frac{\partial u}{\partial x}, \frac{\partial u}{\partial z} \right) \cdot \left(\frac{\partial w}{\partial x}, \frac{\partial w}{\partial z} \right) \\ &= \frac{\partial u}{\partial x} \frac{\partial w}{\partial x} + \frac{\partial u}{\partial z} \frac{\partial w}{\partial z} = 0,\end{aligned}\tag{6.1}$$

at P. However, the flow is incompressible and so in two-dimensional flow

$$\frac{\partial w}{\partial z} = -\frac{\partial u}{\partial x}.\tag{6.2}$$

Substituting equation (6.2) into equation (6.1):

$$\frac{\partial u}{\partial x} \left(\frac{\partial w}{\partial x} - \frac{\partial u}{\partial z} \right) = 0.\tag{6.3}$$

Hence the flow is irrotational at P, unless $\frac{\partial u}{\partial x} = 0$ ¹.

Figure 6.7 shows the isovelocity contours of the mean velocity components. The solid lines represent the mean horizontal velocity components $\langle u \rangle$ and the dashed lines represent the mean vertical velocity components $\langle w \rangle$. It can be seen that at the time of breaking (figure 6.7(a)) there is an organised pattern of the contour lines in all positions. The contours of $\langle u \rangle$ are approximately perpendicular to those of $\langle w \rangle$. This then suggests that the flow at breaking is irrotational. Moving on to the next phase (figure 6.7(b)), when the overturning jet has impacted the water surface, in position 3, the organised and perpendicular contours can still be observed in the main flow. However, in the small region around the free surface underneath the overturning, the rotation of the fluid begins to form. This is thought to be affected by the rolling jet. This effect can be seen clearer in the contour plots of the vorticity. Figure 6.7(c) is the phase at which the overturning jet has just passed the measurement region. It can be seen that the isovelocity contours of the two velocity components are no

¹If $\frac{\partial u}{\partial x} = 0$ then the isoline of u is horizontal at P. Consequently, if at P the isoline of u is not horizontal and the isoline of u is perpendicular to the isoline of w then the flow is irrotational at P.

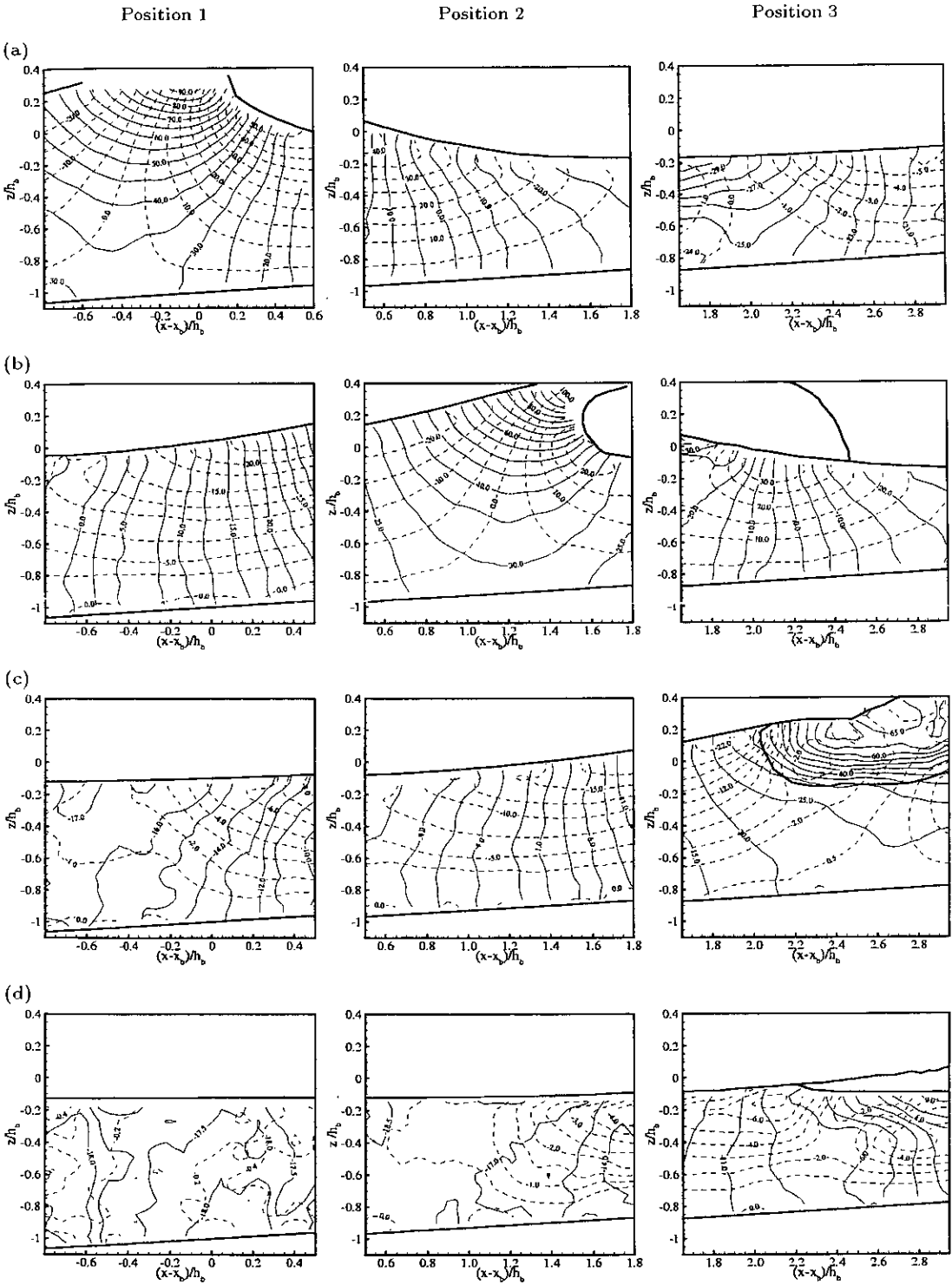


Figure 6.7: Isovelocity contours of the plunging breaker at $(t - t_b)/T =$ (a) 0, (b) 0.184, (c) 0.368 and (d) 0.551. The solid lines represent $\langle u \rangle$ and the dashed lines represent $\langle w \rangle$.

longer perpendicular, especially in the aerated region in position 3. Finally, in figure 6.7(d) it is now obvious that the flow becomes rotational, as indicated by the complexity of the contour lines.

These results support the knowledge that potential flow theory is valid up to breaking. In fact, it is perhaps possible to say that the flow is irrotational until the vertical front of the wave overturns and impacts the water surface in front. The flow then becomes rotational with a complex structure affected by the vorticity and turbulence generated after the wave has broken.

6.2.3 Vorticity

In this section the investigation of mean vorticity dynamics under the plunging breaker is made from the PIV data. The results will be compared with the qualitative studies reviewed in sections 2.4 and 2.5 as well as with the numerical study made by Lin & Liu [47].

Figures 6.8 and 6.9 show a sequence of mean vorticity contour plots. The mean vorticity is calculated using equation (5.4) but the instantaneous velocity components were replaced with the ensemble-average velocity components. The vorticity is normalised by $(C/h)_b$ where C_b and h_b are the crest speed and water depth at the breaking point, respectively. The negative (clockwise) vortices appear in the blue-coloured region while the positive (counter-clockwise) vortices appear in the red-coloured region.

Figure 6.8(a) shows the contour maps at the time of breaking. There is no significant vorticity appearing in the interior domain of the flow at this phase which supports the previous results from the isoline plots that the flow is potential. A small exception to this is at the location near the free surface in front of the vertical wave front where the negative vorticity occurs. This is treated as the free-surface vorticity which is generated due to the zero shear stress on the free

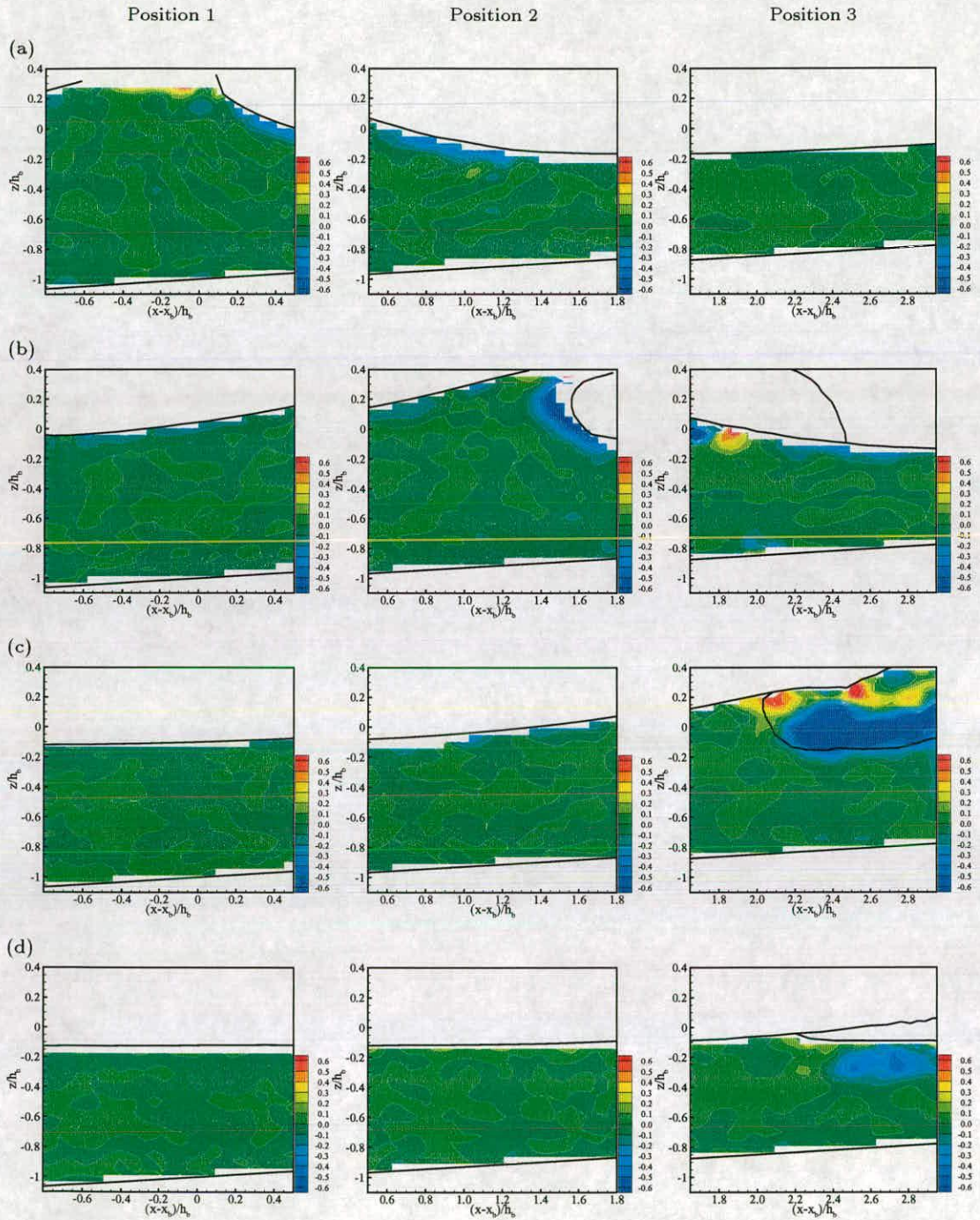


Figure 6.8: Mean vorticity of the plunging breaker at $(t - t_b)/T =$ (a) 0, (b) 0.184, (c) 0.368 and (d) 0.551.

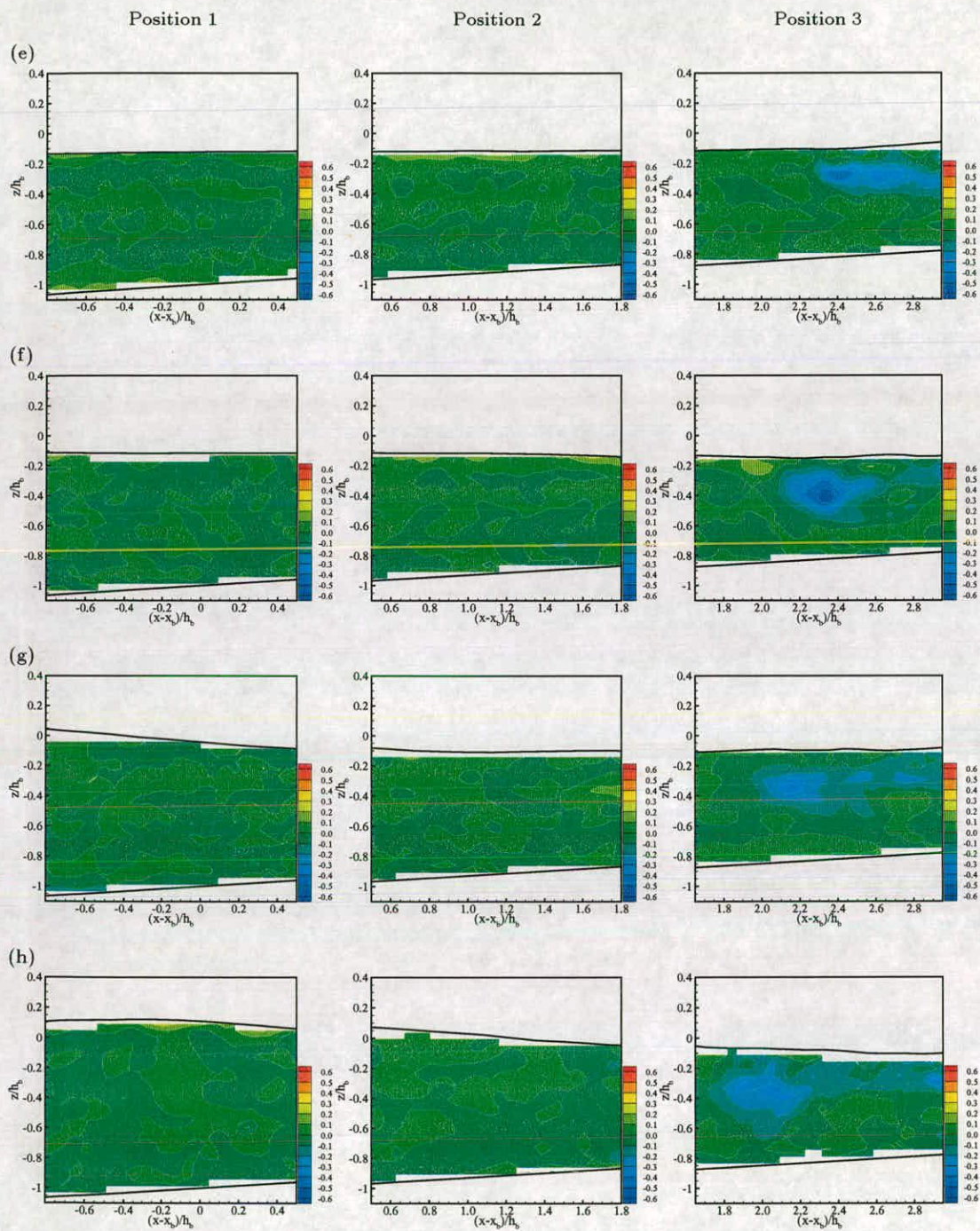


Figure 6.9: Mean vorticity of the plunging breaker, continued from figure 6.8, at $(t - t_b)/T =$ (e) 0.735, (f) 0.919, (g) 1.103 and (h) 1.287.

surface and the positive free-surface curvature [47]. However, this free-surface vorticity appears only in a thin boundary layer and does not affect the main flow. The maximum mean vorticity within such an area is found to be -4 s^{-1} which is about $-0.57(C/h)_b$.

In the next phase, figure 6.8(b), the overturning jet was formed and has impacted the water surface at the front. It is seen that the vorticity is generated mostly around the overturning front. This vorticity rotates in the same direction as that of the overturning jet which is a clockwise rotation. The maximum mean vorticity is -7 s^{-1} which appears to be roughly $-(C/h)_b$. This order of magnitude of the mean vorticity was also reported by Nadaoka *et al.* [54] and Chang & Liu [10]. It can also be observed that there are both negative vorticity and positive vorticity at the free surface beneath the overturning jet. However, the magnitude of positive vorticity ($\approx 0.57(C/h)_b$) is smaller than the negative ones and it is not observed in the subsequent plots. This is perhaps due to the fact that the positive vorticity is carried away out of the measurement region by the shoreward movement of the surface roller. The coexistence of these two different rotational-direction vortices was also observed from the numerical results of Lin & Liu [47]. They reported that the region of the vortices coexistence exists after the initial breaking only for a very short duration.

Moving onto the next phase, figure 6.8(c), the overturning jet has passed the measurement region and the generated air bubbles were left behind in position 3. As pointed out earlier, in section 6.2.1, an attempt was made to measure the velocity in the aerated region and hence the vorticity could also be calculated. Although the results may contain large errors, they give supporting evidence that the plunger vortex does exist. It can be seen that such a region is dominated by a large-scale negative vorticity ($\approx -10 \text{ s}^{-1} = -1.4(C/h)_b$). The rotational direction

of this vorticity suggests that its generation is caused by the overturning jet as reported by many researchers. This negative vorticity may well resemble the *plunger vortex* as observed by Basco [4] and the *horizontal eddy* as observed by Nadaoka *et al.* [54].

The positive vortices of smaller scales can also be seen, in position 3 of figure 6.8(c), along the wave crest which disappear in the next phase. Lin & Liu [47] suggested that these positive vortices were caused by the negative curvature of the free surface near the crest. The subsequent jet-splash features cannot be observed in these experiments since the measurement region covers only the breaking position and the transition zone. However, in the later plots the second smaller-scale plunger vortex can be observed. This will be discussed later.

After the plunger vortex was generated from the overturning jet it was then diffused into the flow domain. This mechanism can be visualised in figure 6.8(d). The “core” (the region which contains the maximum value) of the vortex is moving shorewards ahead of its “tail”. The maximum mean vorticity at this phase is approximately -3.5 s^{-1} ($\approx -0.5(C/h)_b$) which is much smaller than when the vortex was just generated in the previous phase. This is thought to be caused by the energy cascade from the large vortices to the small-scale vortices.

In figure 6.9(e) when the flow is now moving offshore (according to the vector plots in figure 6.5(e)) the core of the vorticity is now on the left of its tail. The maximum mean vorticity is still roughly the same as in the previous phase. This vortex then seems to move away from the free surface and is advected offshore as can be seen from the subsequent plots in figure 6.9(f) – (h). This suggests that the advection of the vorticity is mainly correlated with the mean flow.

In the last vorticity plots, figure 6.9(h), the second vortex locating near the free surface on the far right of position 3 can be observed. It is, however, of smaller

scale than the first one. It is suggested that this second vortex is generated from the jet-splash motion.

By observing these vortices in the subsequent phases (not displayed here) it is found that the second vortex disappears quickly. This is perhaps due to the cascading process of the vortex into smaller scales which cannot be observed with the resolution of the available PIV data. The first plunger vortex can still be seen. It starts to move forwards and then backwards with the influence from the main flow after the new small-amplitude wave has arrived into the region. The magnitude of mean vorticity then becomes smaller and the first vortex remains in position 3 until it later disappears.

6.2.4 Turbulent Intensity

Turbulent intensity I is calculated using equation (5.8) for the twenty repeated experiments. Before looking at the spatial distribution of I under the plunging breaker it is perhaps worthwhile to check the effect of a different number of repeated experiments N on the ensemble-average approach. Because such an averaging method requires a large number of repetitions to obtain stable statistical values, it is necessary to verify that 20 is a sufficient number for the current experiments. One way of doing this is by investigating the variation of I against N as shown in figure 6.10. This method was suggested by Sumer [71] and was also used in Chang & Liu [10].

Figure 6.10 shows the turbulent intensity (normalised by C) calculated at four positions, and for two phases at each position. From the figure it can be seen that for N greater than around 15 or 16 there is only a small variation in I . Chang & Liu [8, 10] also reported the same effect for N greater than 15. Consequently, it was decided that $N = 20$ would be sufficient to perform the ensemble average. Furthermore, as the number of repeats is increased the rms error only reduces

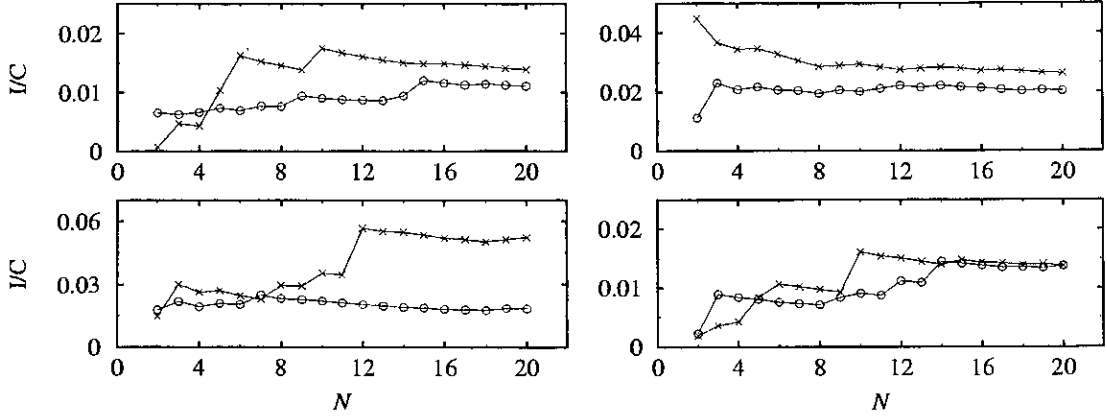


Figure 6.10: The turbulent intensity against the number of repeated experiments at $((x - x_b)/h_b, z/h_b) =$ (a) (1.774,-0.431), (b) (2.177,-0.431), (c) (2.625,-0.431) and (d) (1.774,-0.655). \circ — and \times — are at $(t - t_b)/T = 0.551$ and 0.919, respectively.

slowly. This is due to the fact that the rms error is inversely proportional to \sqrt{N} . Therefore, in order to reduce the rms error by, say, a half, N needs to be four times larger. In practice, a high number of images is difficult to obtain with the PIV system used for the UEDIN experiments.

Figures 6.11 and 6.12 show a sequence of turbulent intensity plotted in the spatial domains. The turbulent intensity in these plots is normalised by C and the higher value appears towards the red-coloured region while the smaller value appears towards the blue-coloured region. By close investigation and comparison with the mean vorticity plots shown in the previous section, it can be seen that, interestingly, the distribution of the turbulent intensity has the same pattern as that of the mean vorticity. That is, the strong turbulence region seems to locate at approximately the same region where the dominant plunger vortex (negative vorticity) occurs.

Throughout the breaking process, the strongest turbulent intensity is found to be generated in position 3 of figure 6.11(b), under the free surface after having been impacted by the overturning jet. The maximum value is about 26.56 cm/s

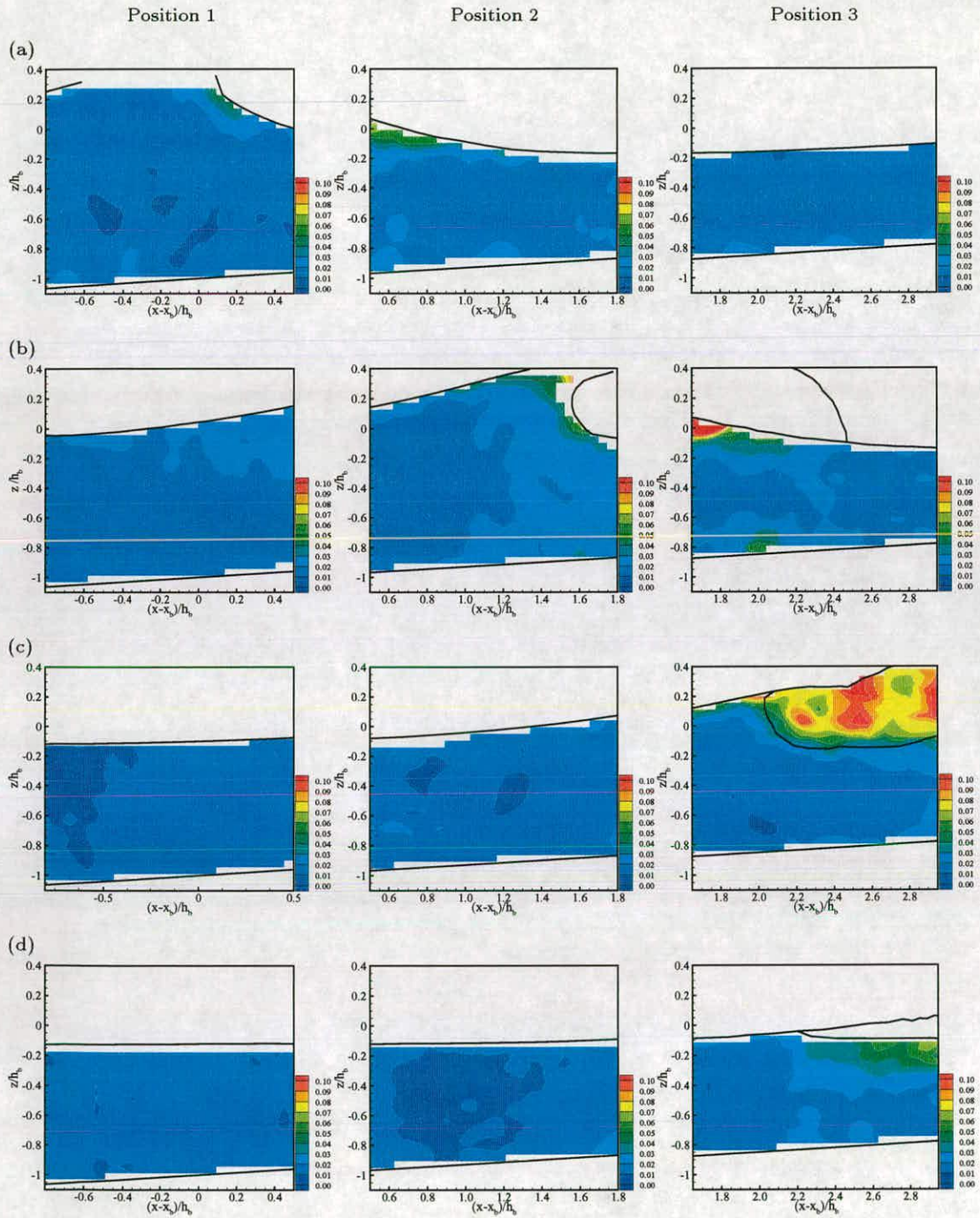


Figure 6.11: Turbulent Intensity of the plunging breaker at $(t - t_b)/T =$ (a) 0, (b) 0.184, (c) 0.368 and (d) 0.551.

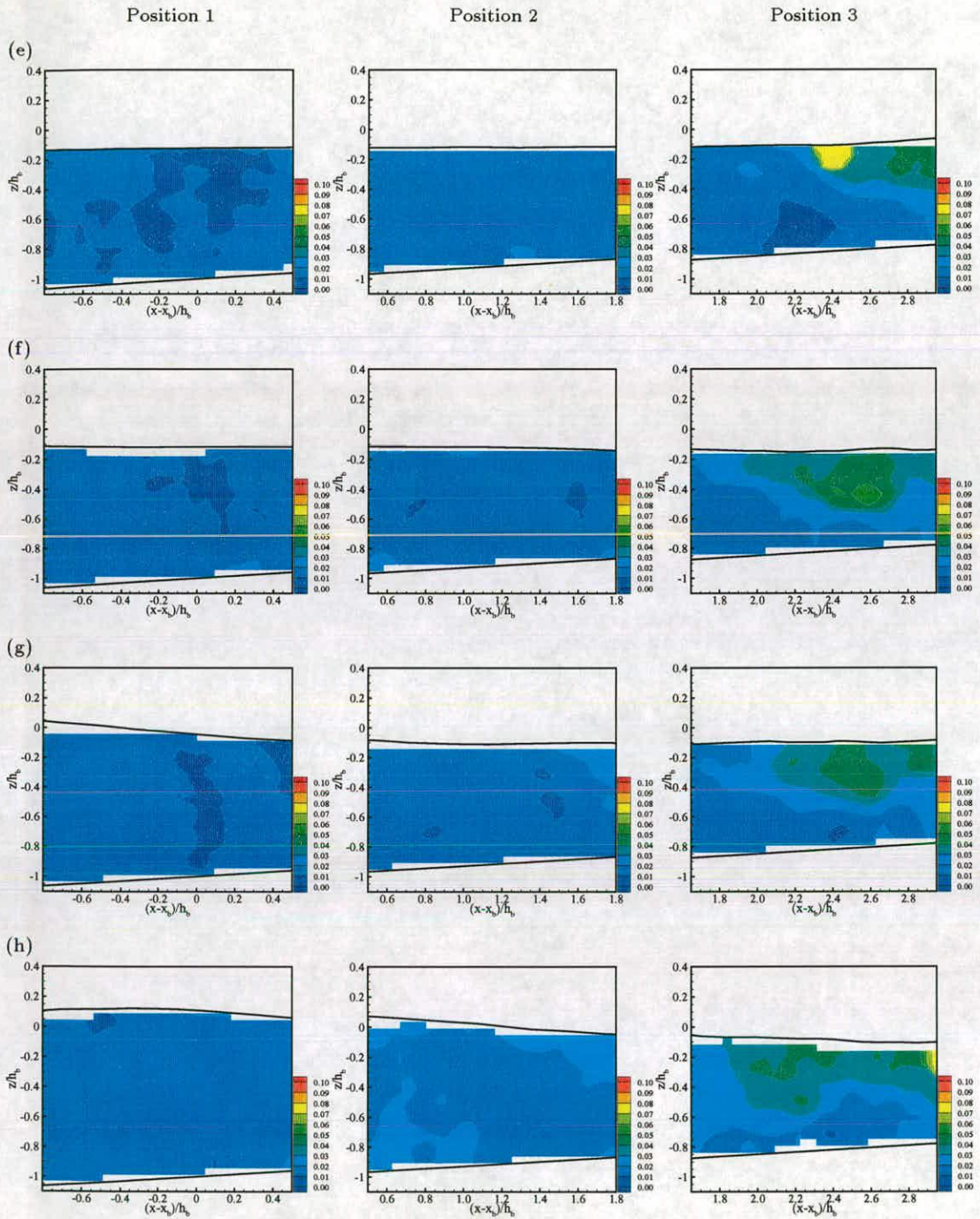


Figure 6.12: Turbulent Intensity of the plunging breaker, continued from figure 6.11, at $(t - t_b)/T =$ (e) 0.735, (f) 0.919, (g) 1.103 and (h) 1.287.

($\approx 0.17C$). The result shown here supports the knowledge of the turbulence source that the intense production of turbulence is due to the strong shear between the surface roller and water in the main flow. Lin & Liu [47] reported from their numerical results that the strongest turbulence is generated instantaneously when the plunging jet touches the water surface at the front. In their case the maximum value of turbulent intensity generated at that instant was very high: 1.2 times the phase velocity of the wave.

In the next phase, figure 6.11(c), the high intensity of turbulence (with a maximum value of about 18.81 cm/s $\approx 0.12C$) is mostly located within the aerated region. This plot corresponds to the mean vorticity plot shown in figure 6.8(c) where the aerated region is dominated by the strong negative vorticity. Once this vorticity is diffused into the interior domain of the flow, as seen in figure 6.8(d), the turbulence seems to be transported into the flow as well. This can be seen in figure 6.11(d) where the maximum value of the turbulent intensity is about 10.42 cm/s ($\approx 0.07C$).

From figure 6.12(e)–(f), the high-intensity turbulence region follows the region where the plunger vortex appears. The maximum value of the turbulent intensity, however, decreases gradually when moving onto the subsequent phases: $\approx 0.08C$, $0.05C$, $0.05C$ and $0.04C$ in figure 6.12(e), (f), (g) and (h), respectively. It is suggested that the decreasing of the turbulent intensity is due to advection and dissipation. This will be investigated more in the next section.

The main interesting result obtained from the plots of spatial distribution of the turbulent intensity here is that it supports the knowledge of turbulence sources as proposed by Basco [4] (see section 2.4). The strong turbulence found under the surface roller suggests that the strong shear within such a region is a source of turbulence generation in the transition zone. The synchronous regions

of the maximum negative vorticity and the high turbulent intensity suggests that the rotating plunger vortex is also a source of turbulence generation.

6.2.5 Turbulence Transport Mechanisms

In this section, turbulence transport in the single plunging breaker is investigated. In order to achieve this, each term of the k -equation (equation (5.13)) is first calculated at every point on the PIV map. A 5×5 grid area is then used as a so-called “control volume” to average the above quantities. This approach of using the mean value inside the control volume is adopted from Chang & Liu [10]. They suggested that by averaging the value over the control volume, the bias errors and other random errors can be smoothed out.

The investigation is carried out for 8 control-volume areas under the trough level of the wave. Figure 6.13 shows PIV vector maps indicating the locations of these areas. The results are presented in the following format: 8 sets (corresponding to 8 areas) of seven graphs are displayed in which each graph shows the time variation of the following normalised values:

graph (a) : mean horizontal velocity $\langle u \rangle$

graph (b) : mean vertical velocity $\langle w \rangle$

graph (c) : turbulent kinetic energy k

graph (d) : rate of change of turbulent kinetic energy $\partial k / \partial t$

graph (e) : turbulence production \mathcal{P} ,

horizontal advection $-\langle u \rangle (\partial k / \partial x)$ and

vertical advection $-\langle w \rangle (\partial k / \partial z)$

graph (f) : net diffusive transport \mathcal{J} ,

horizontal turbulent diffusion $-\partial \langle k' u' \rangle / \partial x$ and

vertical turbulent diffusion $-\partial \langle k' w' \rangle / \partial z$

graph (g) : modelled dissipation $\epsilon = C_D (k^{3/2}/l)$ and
 measured dissipation $\epsilon = 15\nu \langle (\partial u'/\partial x)^2 \rangle$.

The mean velocity components were calculated using an ensemble average as shown in equation (5.5). An attempt was made to calculate the time derivative of k . However, because the k data is significantly scattered the calculation of $\partial k/\partial t$ is made indirectly. A cubic smoothing spline, with a smoothing parameter λ , was fitted to the data and then differentiated to obtain an approximation to $\partial k/\partial t$. The smoothing parameter was chosen so that the smoothing spline best followed the trend in the data when observed visually. The rest of the terms in the k -equation were calculated using the approaches which are explained in section 5.2.3. The production \mathcal{P} is shown together with the horizontal and vertical advection. The net diffusive transport \mathcal{J} , estimated using equation (5.17), is shown together with the horizontal and vertical turbulent diffusion. Finally, the dissipation ϵ , calculated from the two different approaches, are shown in the last graph of each set. All of the above quantities are normalised: $\langle u \rangle$ and $\langle w \rangle$ are normalised by C , k by C^2 and all of the transport terms by C^2/T , where C is the crest speed measured at the breaking point and T is the wave period (see table 4.3). This method of displaying the results is adapted from that of Ting & Kirby [80] and Lin & Liu [46, 47].

In the following, eight sets of graphs (corresponding to eight areas) are displayed and the analysis and discussion for these plots are made in order to determine the turbulence transport mechanisms at different locations within the surf zone. The selected control volumes, as shown in figure 6.13, cover the locations around the breaking point and the transition zone (or the outer surf-zone):

- Area I : upper region around the breaking point (results in figure 6.14)
- Area II : lower region around the breaking point (results in figure 6.15)

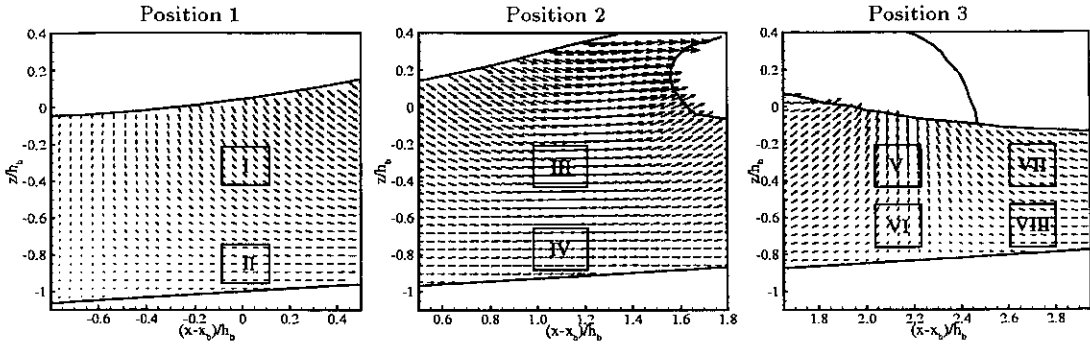


Figure 6.13: The control volumes for the plunging breaker in which the mean value of each term in the k -equation is calculated.

Area III : upper region in the initial transition zone (results in figure 6.16)

Area IV : lower region in the initial transition zone (results in figure 6.17)

Area V : upper region in the transition zone (results in figure 6.18)

Area VI : lower region in the transition zone (results in figure 6.19)

Area VII : upper region further in the transition zone (results in figure 6.20)

Area VIII : lower region further in the transition zone (results in figure 6.21).

Discussions on Turbulence Transport in the Single Plunging Breaker

Consider the first four sets of graphs (figures 6.14 – 6.17) which correspond to the locations around the breaking point and in the initial part of the transition zone. It can be seen that, when comparing with the other sets, the turbulent kinetic energy is relatively small and does not vary much. Also k is not correlated with the passage of the broken wave. Note that the free-surface elevation is not shown in the plots but it can be suggested by the temporal variation of the mean horizontal velocity.

In the location around the breaking point, the fluctuation of the rate of change of turbulent kinetic energy is small (see figures 6.14(d) and 6.15(d)). The effects of almost all of the transport terms in these areas are also insignificant. In the upper region (figure 6.14) there are slight effects of turbulence production, advection and

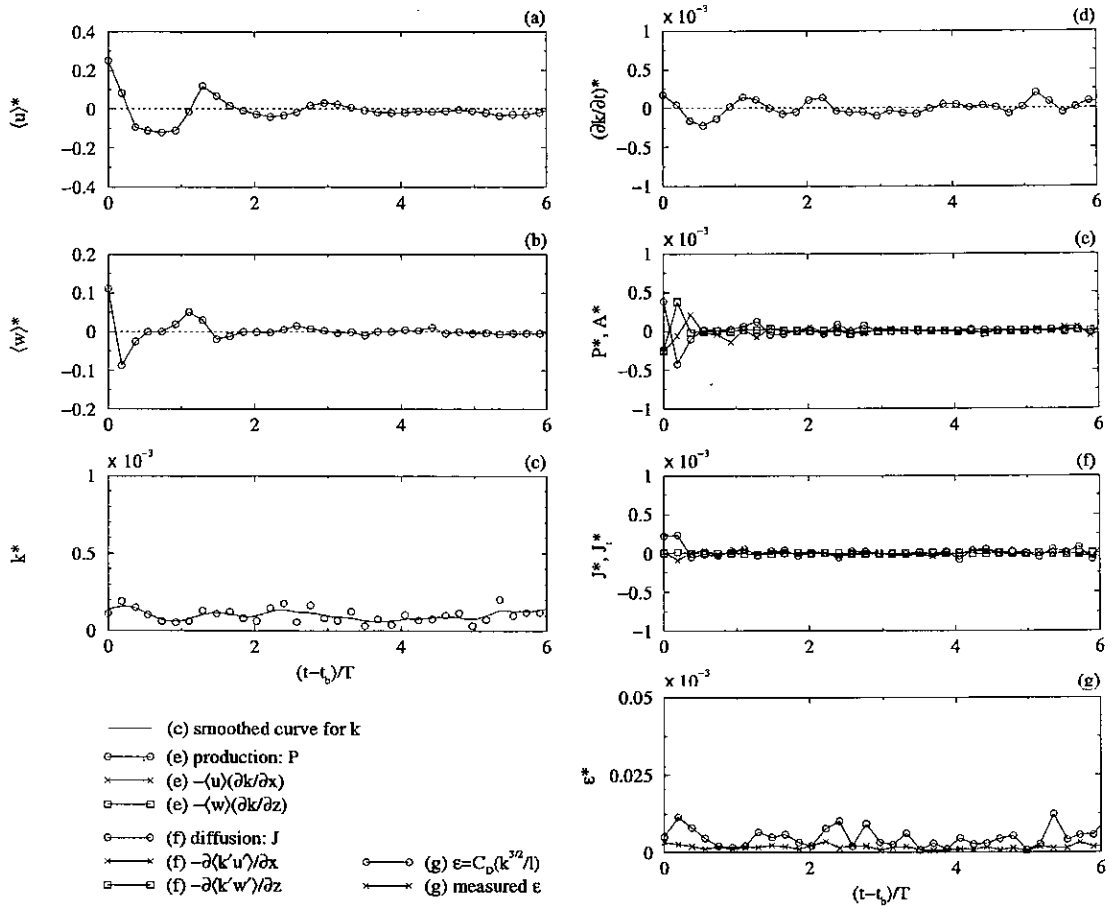


Figure 6.14: Mean velocities (a & b), turbulent kinetic energy (c) and turbulent transport terms (d – g) for k in equation (5.13), of the plunging breaker, calculated in the area $-0.089 \leq (x - x_b)/h_b \leq 0.090$ and $-0.401 \leq z/h_b \leq -0.222$ (area I of figure 6.13). The symbol * indicates normalised quantities: $\langle u \rangle$ and $\langle w \rangle$ are normalised by C , k by C^2 and all of the transport terms by C^2/T .

diffusion during the first half of the wave period. During that period the wave breaks, its crest appears and then passes the measurement section. After that none of the transport terms are effective. In the lower region (figure 6.15) the only obvious, although small, turbulent transport mechanism seems to be the horizontal advection. The production in the lower region is smaller than that in the upper region. In both regions the dissipation rate is tiny (two order of magnitude smaller) compared to the rate of change of k . These analyses indicate

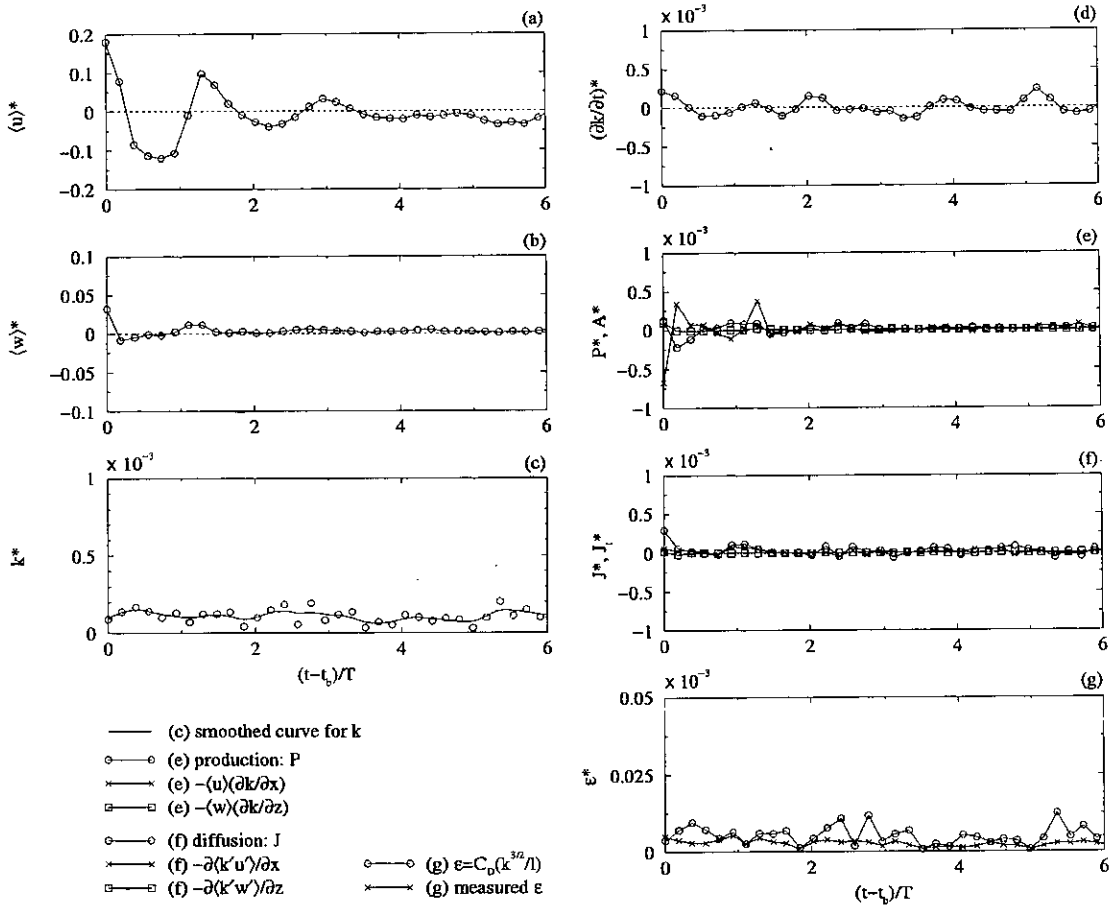


Figure 6.15: Similar to figure 6.14 but in the area $-0.089 \leq (x - x_b)/h_b \leq 0.090$ and $-0.939 \leq z/h_b \leq -0.760$ (area II of figure 6.13).

that at the breaking point, there is no dominant turbulence transport mechanism, regardless of vertical region.

It should be noted here that the predicted dissipation rate is found to be much smaller than the rate of change of k in every plot. A reasonable explanation for this was given by Ting & Kirby [79]:

“...because the rate of dissipation is governed by the rate of energy transfer from the large eddies to the small scale turbulence and is proportional to $k^{3/2}/\ell$, where k and ℓ represent the turbulent kinetic energy and length scale of the large eddies, respectively. On the other

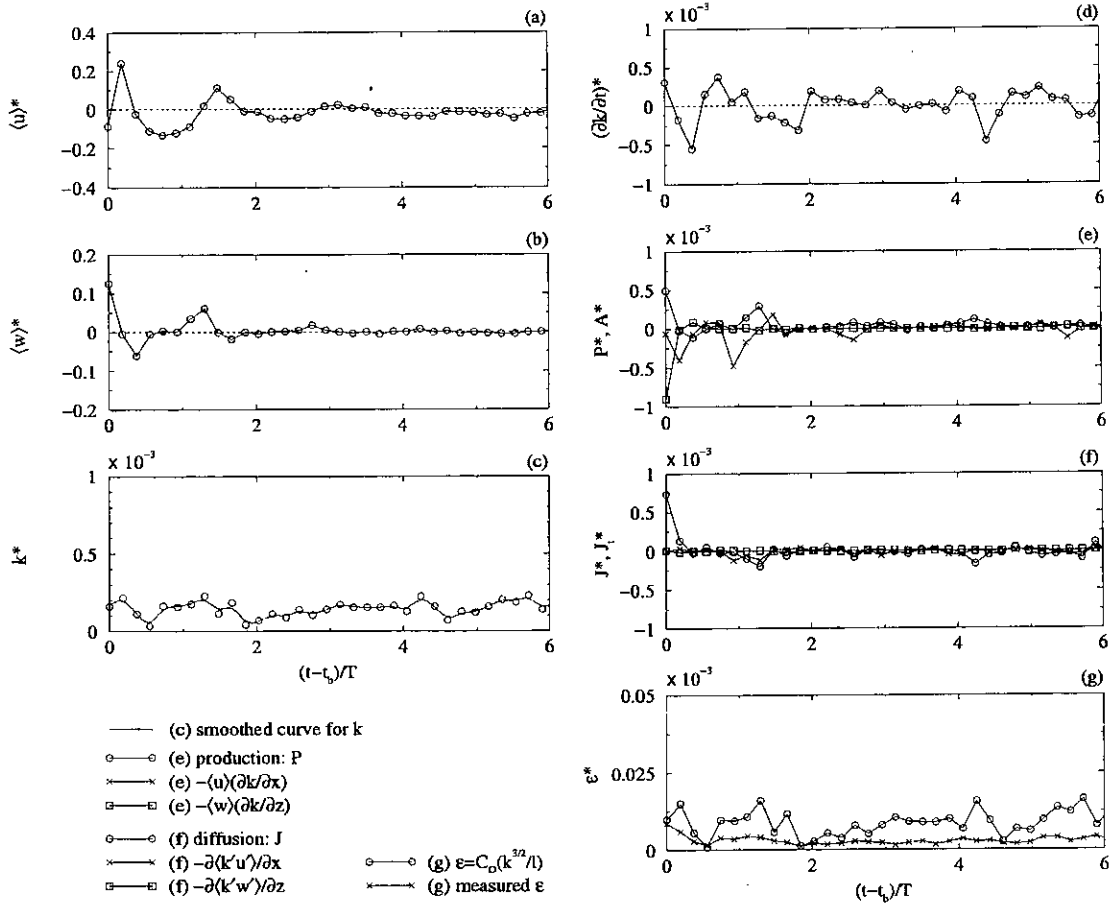


Figure 6.16: Similar to figure 6.14 but in the area $1.028 \leq (x - x_b)/h_b \leq 1.207$ and $-0.411 \leq z/h_b \leq -0.232$ (area III of figure 6.13).

hand, the time rate of change of k is mostly produced by turbulence structure blowing past the probe rather than by changes in the turbulence structure itself. Thus, it is not surprising that $\partial k/\partial t$ should be much larger than ϵ .”

The measured dissipation rates are also very low, even lower than the predicted dissipation rates. This is because the only contribution to the measured dissipation is the horizontal turbulent fluctuations u' and the calculation is based on the isotropic theory, that is, the dissipation takes place in the smallest-scale eddies (see section 5.2.3). However, in most cases the trends of the measured energy

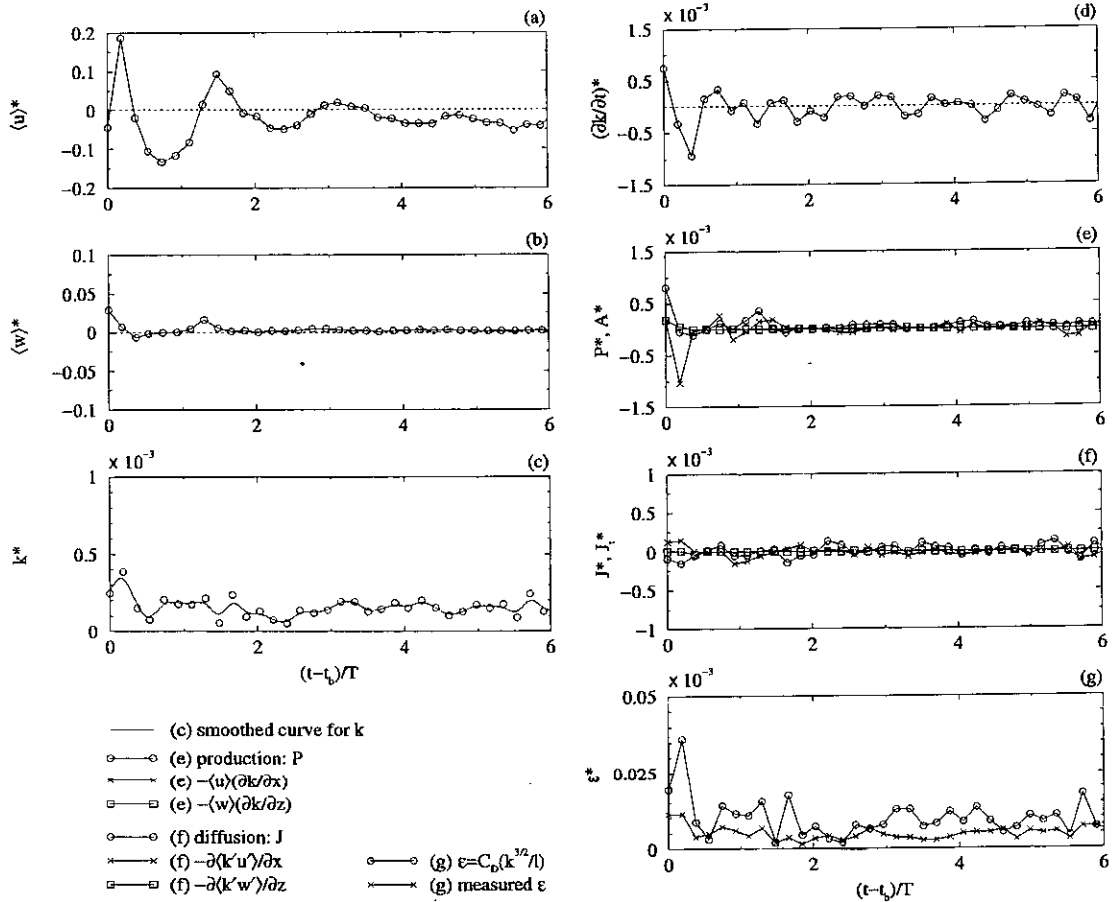


Figure 6.17: Similar to figure 6.14 but in the area $1.028 \leq (x - x_b)/h_b \leq 1.207$ and $-0.859 \leq z/h_b \leq -0.680$ (area IV of figure 6.13).

dissipation follow that of the predicted dissipation. These effects of the dissipation are also found in the results from the ISVA experiments which can be seen in the next chapter.

In the initial, or seaward, part of the transition zone (figures 6.16 and 6.17) the fluctuation of rate of change of k seems to be larger. The turbulent kinetic energy is, however, still quite small, of the same order of magnitude as that in the breaking-point location. Within this initial part of the transition zone the large fluctuation of $\partial k/\partial t$ appears during the first wave period. This effect is more obvious in the lower region (figure 6.17(d)). It can be seen that the horizontal

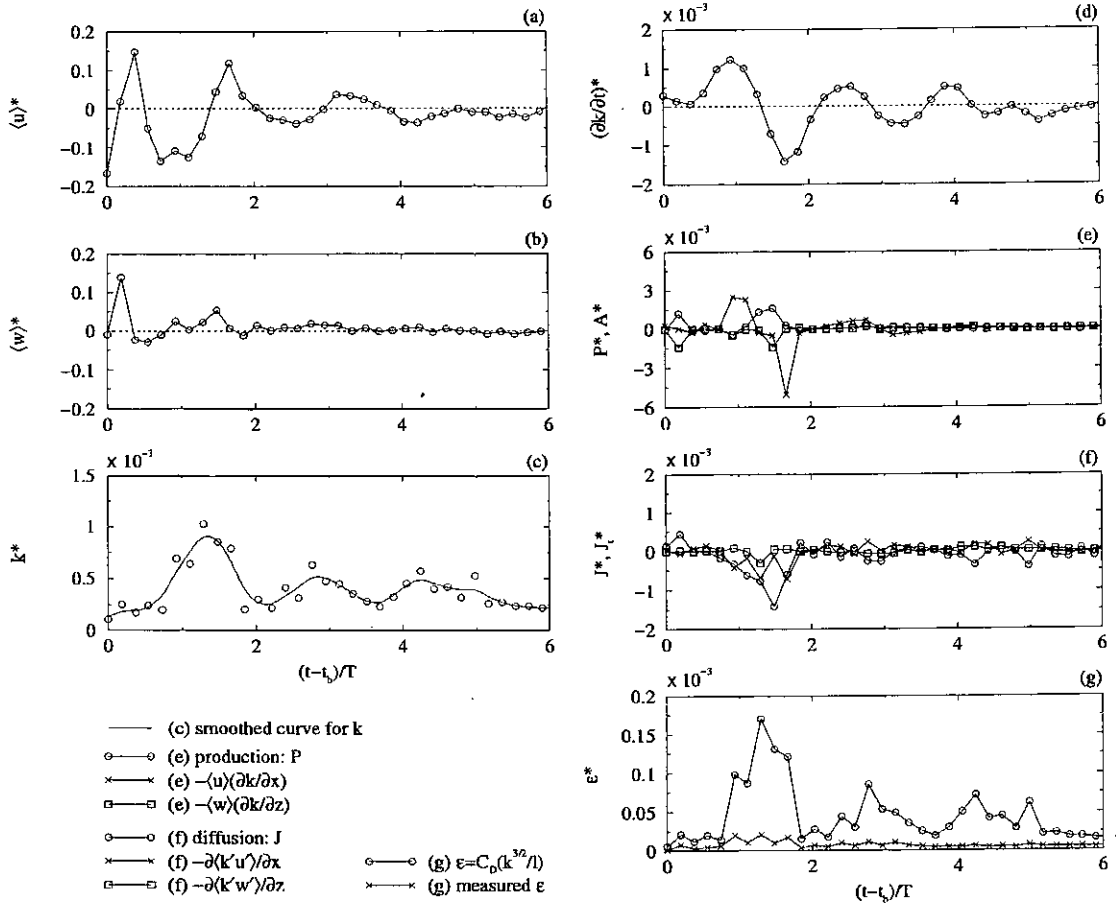


Figure 6.18: Similar to figure 6.14 but in the area $2.043 \leq (x - x_b)/h_b \leq 2.222$ and $-0.431 \leq z/h_b \leq -0.252$ (area V of figure 6.13).

advection and production are responsible for such large fluctuation of $\partial k/\partial t$ in the lower region. On the other hand, the turbulence production, advection and diffusion are the main mechanisms in the upper region (figures 6.16). After about two wave periods, after the wave breaks, none of the transport terms is dominant. These results are similar to those found in the area around the breaking point, as discussed above.

Moving onto the transition zone (figures 6.18 and 6.19), it is seen that the magnitude of k is greater than that in the previous two locations. In figure 6.18 the variation of k , as well as its time rate of change, seem to form a somewhat

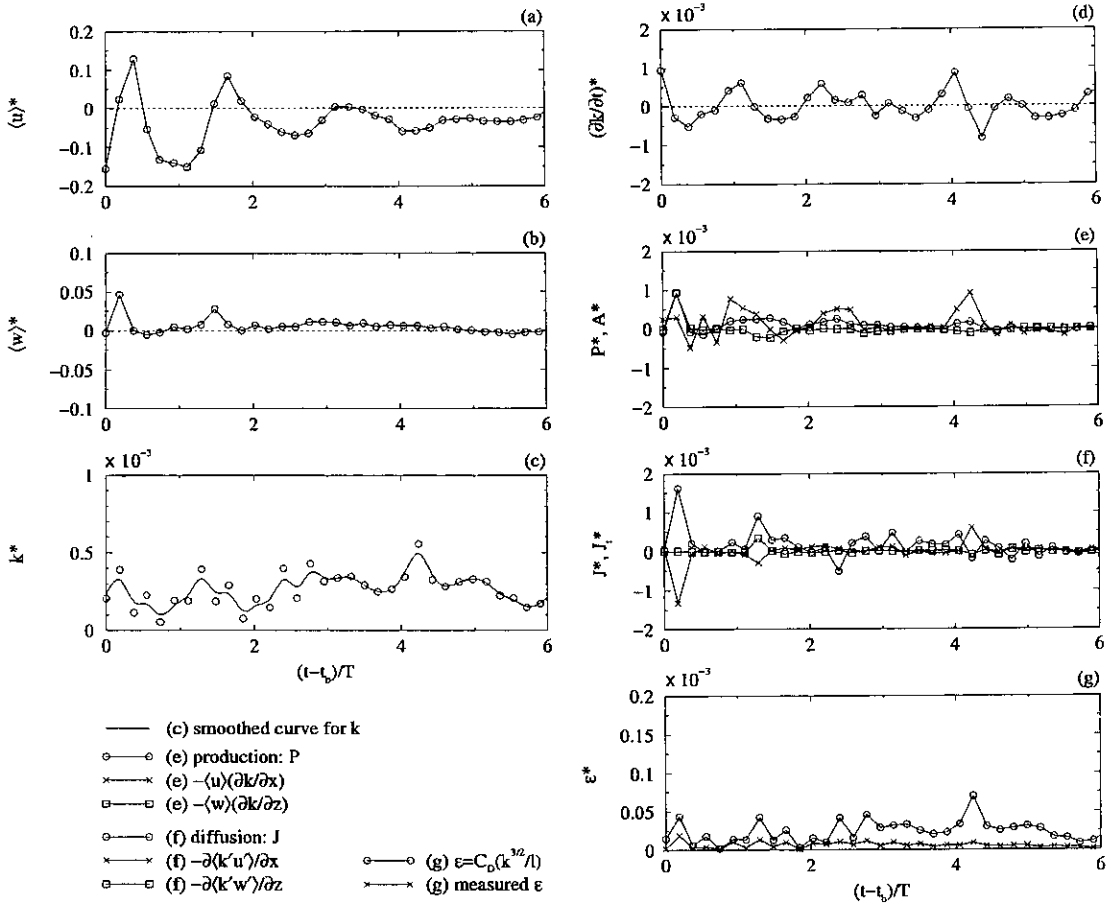


Figure 6.19: Similar to figure 6.14 but in the area $2.043 \leq (x - x_b)/h_b \leq 2.222$ and $-0.744 \leq z/h_b \leq -0.565$ (area VI of figure 6.13).

periodic pattern with a larger period than that of the wave. There is a time delay between the peaks of $\langle u \rangle$ and k . This can be explained by the fact that the turbulence generated in the surface roller is not transported into the region under investigation, which is located under the trough of the wave, until the flow reverses and the turbulence spreads and is convected into the region. This is supported by the results plotted in figure 6.18(e) where the dominant mechanisms are the turbulence production and horizontal advection. The horizontal advection is responsible for both the increase and decrease of the rate of change of k . In addition, the net diffusive transport, influenced mostly by the horizontal turbulent

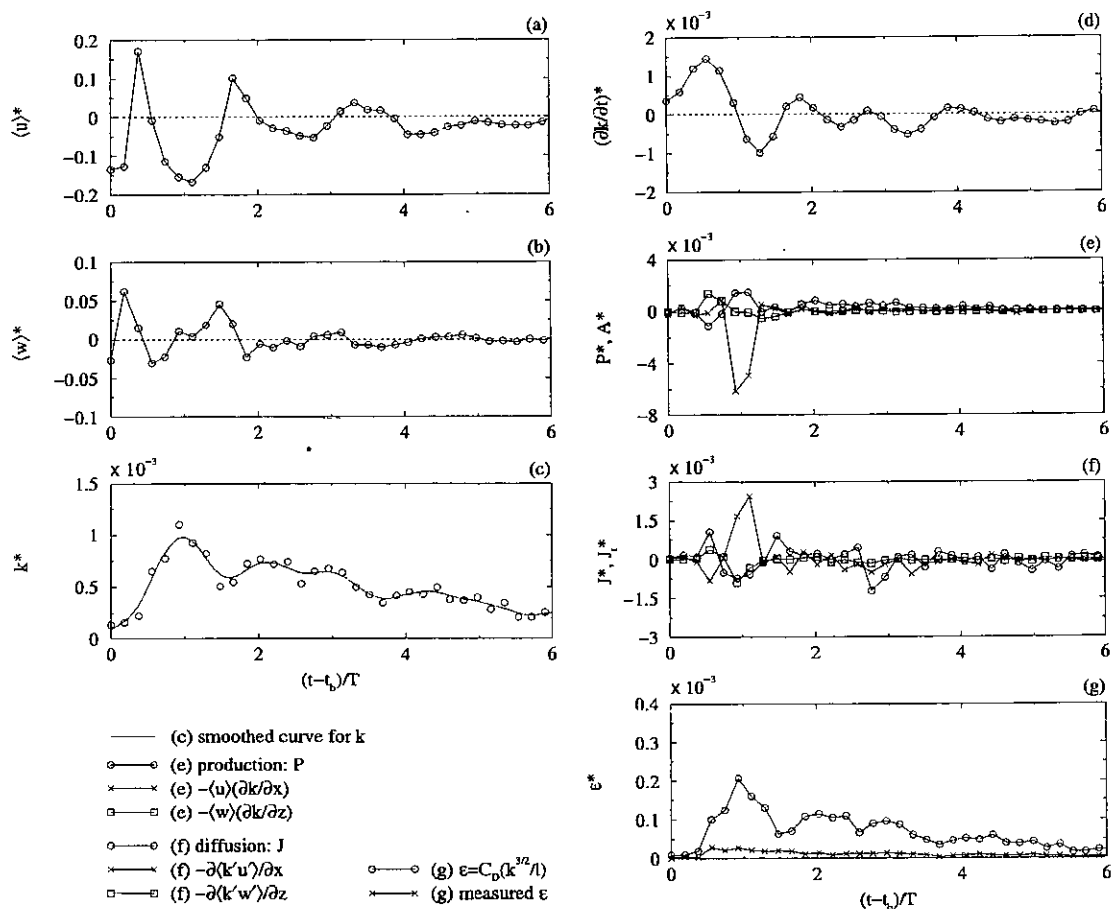


Figure 6.20: Similar to figure 6.14 but in the area $2.625 \leq (x - x_b)/h_b \leq 2.804$ and $-0.431 \leq z/h_b \leq -0.252$ (area VII of figure 6.13).

diffusion, is also responsible for the negative fluctuation of $\partial k / \partial t$. The dissipation rate in this location is one order of magnitude greater than that in the upstream locations but it is still much smaller than the rate of change of k . The damping in the fluctuation of $\partial k / \partial t$ occurs after two wave periods. This results from the vanishing effects of all of the transport terms except the dissipation.

In the lower region of the transition zone (figure 6.19) the periodic variation of k and its time rate of change is not observed. The magnitude of k is lower than in the upper region and is not correlated with the passage of the wave. There is a slight increase in the k value at about four wave periods after breaking.

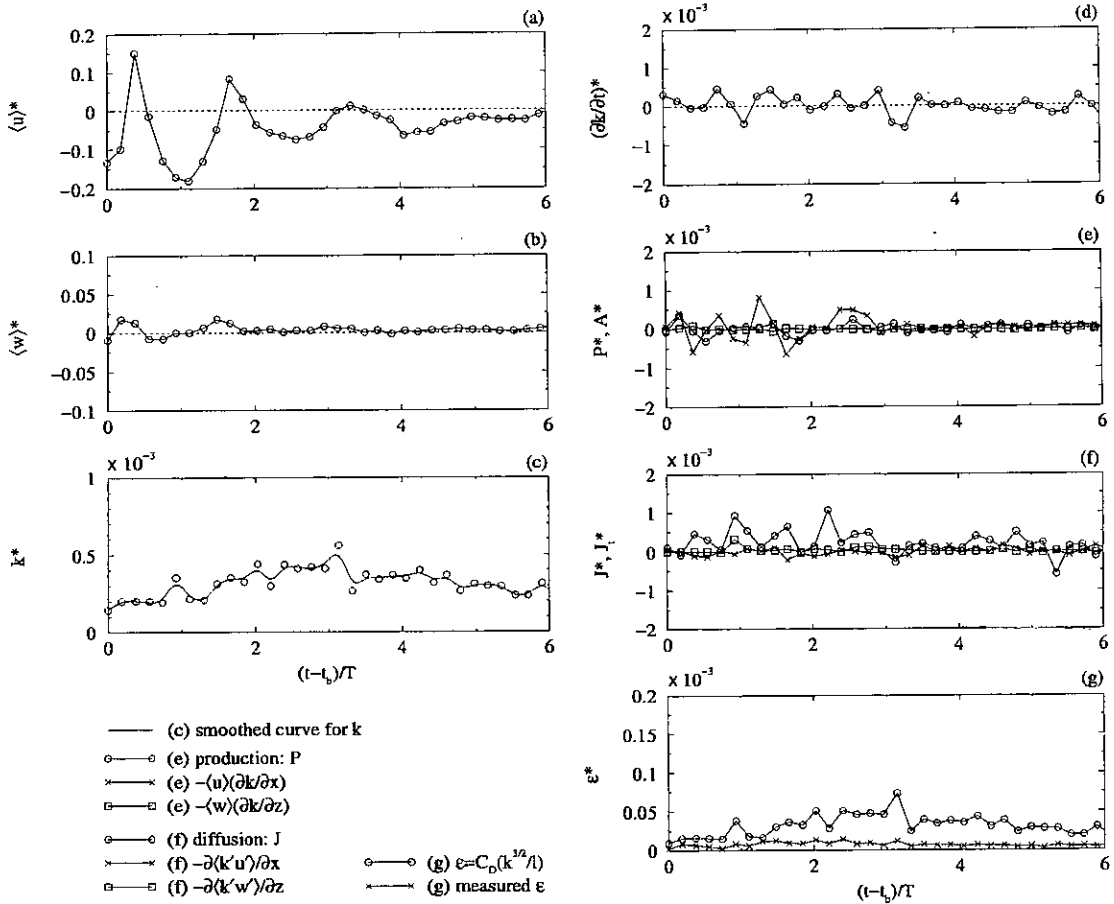


Figure 6.21: Similar to figure 6.14 but in the area $2.625 \leq (x - x_b) / h_b \leq 2.804$ and $-0.744 \leq z / h_b \leq -0.565$ (area VIII of figure 6.13).

Considering the plots of the transport terms, it is suggested that the horizontal advection is the main mechanism to such an increase in k , although during the first two wave periods after breaking, the production, advection and diffusion are the main mechanisms.

In the last location of investigation, which is further into the transition zone, the turbulence transport mechanisms are similar to those found in the previous location. In figure 6.20 the maximum value of k is of the same order of magnitude as that in the previous location, of the same vertical level. The periodic variation of $\partial k / \partial t$ is also observed, however, its damping effect seems to appear earlier and

the variation is smaller. The horizontal advection contributes to the decrease in the rate of change of k and is almost balanced by the horizontal diffusion. Again, after two wave periods, no turbulence transport mechanism is dominant causing the small variation of the $\partial k/\partial t$ term.

In the lower region (figure 6.21) of the last location a slight increase in the k value is also observed but it appears earlier than in the previous location. It can be explained by the fact that this location is closer to the region where strong turbulence is generated, therefore the maximum- k value in the upper region and the increase in the k value in the lower region should appear earlier than in the upstream location. The horizontal advection is found to be the main mechanism for the k -increment effect as it brings the high turbulent intensity into the upstream flow. However, almost all turbulence is dissipated before it reaches the location further upstream and this is why the lower amount of turbulent kinetic energy is observed there, as discussed earlier.

All of the results discussed above can not be readily compared with any of the published experiments. This is due to the fact that no turbulence transport investigation for the surf-zone single breaker has been reported. However, in the next chapter, the experiments were carried out for the train of breaking waves which have also been studied by some other researchers, although with different measuring techniques. Comparisons to the other work could then be made.

6.3 Summary of Chapter 6

In this chapter the experiments on a single plunging breaker carried out at UEDIN have been described. The PIV set-up and measurement procedure were explained at the beginning of the chapter, including the problems that occurred during the experiments. It was found that the main and unavoidable problem in using the

current PIV technique stems from the effect of breaking-wave generated air bubbles. Another problem was caused by the non-repeatability of the experiments. However, from the examination, the waves generated in the Green tank at UEDIN were reasonably repeatable.

After the description of the experimental set-up and procedure was given, the results were then presented and discussed. The presentation began with the series of maps of ensemble-averaged velocity, isovelocity contours, mean vorticity and turbulent intensity. The isovelocity contours are useful for an investigation of the transition from potential flow to rotational flow. It was found that the flow under the plunging breaker is irrotational until the wave overturns and impacts the frontal trough. A supporting result to this transition was found from the vorticity maps. A negative (clockwise) vorticity was observed and it was suggested that this was generated from the overturning jet. The vorticity dynamics were mainly caused by the advection which was correlated to the main flow. Results from the series of turbulent intensity maps support the knowledge that high-intensity turbulence is generated by the shear between the surface roller and water in the main flow. Additionally, the rotating plunger vortex is also suggested to be another source of turbulence generation.

Finally, the investigation of turbulence transport in the single plunging breaker was made. The time-history of all of the individual transport terms of the k -equation were plotted along with the time-history of the mean velocity components and turbulent kinetic energy. By this means, dominant transport mechanisms at different locations within the surf zone can be determined. It was found that in the breaking-point location and in the initial part of the transition zone, none of the transport terms were significant. This caused a small variation to the rate of change of turbulent kinetic energy. k in those locations was also very low

and nearly constant in time. Further in the transition zone, on the other hand, a larger variation of $\partial k/\partial t$ was observed. The turbulence production, advection and diffusion were the main mechanisms for the turbulence transport in the upper region which is located just under the wave trough. In the lower region of the transition zone the horizontal advection caused the increase in turbulent kinetic energy which appeared long after the wave had broken.

Chapter 7

Trains of Breaking Waves Experiments

This chapter discusses the experiments on trains of breaking waves which were carried out at ISVA. The experimental set-up is described and results are presented and discussed. As stated at the beginning of the previous chapter, the explanation of the experimental set-up concentrates mainly on the PIV systems and measurement procedures. Detailed descriptions of the PIV equipment and experimental facilities can be seen in chapters 3 and 4, respectively.

7.1 Experimental Set-up

The trains of breaking waves were produced in a large-scale wave flume (28 m) at ISVA. A regular wave train was generated by a piston-type wavemaker and sent towards a 1/13 beach. Two different types of breaking waves were generated; weak plunging breakers and spilling breakers. The summary of wave parameters can be seen in table 4.3. Both waves broke over a perspex beach which was used as a test section.

The experimental set-up, within the test section, is shown in figure 7.1. The PIV system developed at UEDIN was taken over to ISVA. Due to the fact that there is no optical axis from beneath the flume, the scanning beam system was set

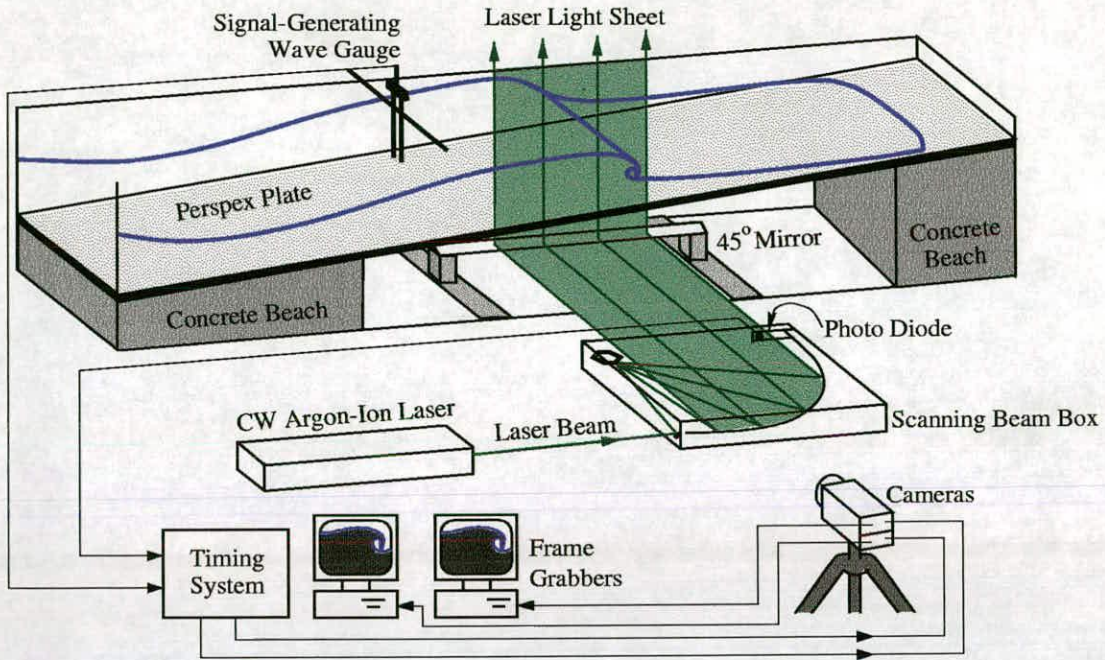


Figure 7.1: The PIV set-up for the experiments carried out at ISVA.

up horizontally and to the side of the flume. A laser light sheet, approximately 0.50 m wide, (generated by a CW Argon-Ion laser with an output power of up to 10 W) was then deflected vertically upwards into the flow by an under-water 45° mirror. This mirror was placed on the bottom, under the perspex beach, inside the tank.

Two CCD cameras (Pulnix TM-9701) and two frame grabbers were used as the imaging and recording system. In the tests the seeding particles used were conifer pollen. An image of a set of seeding particles was captured by one of the cameras, and at a very short time later ($\sim 5 - 6$ ms), another image of the same set of particles was captured by the other camera. The pair of images were then crosscorrelated to determine the mean particle displacements and hence the velocity vector in each interrogation area (32×32 pixels, or around 5×5 mm).

As can be seen from figure 4.3, the ISVA laboratory is very large and has many windows along its roof. Consequently, it is not dark enough to perform

PIV measurements, even with every light turned off. In order to make the measurement area as dark as possible, a “tent” was set up covering the test section of the flume. All of the PIV equipment that is shown in figure 7.1 was situated inside this tent.

Because it was not possible to generate signals from the ISVA wavemaker controller, a special procedure was performed in order to capture a pair of images at the same phase, in each wave cycle. This procedure involved constructing a specially designed signal-generating wave gauge (explained in section 4.3) and positioning it on top of the flume. When the peak of a wave crest travelled past and “touched” this wave gauge a signal was generated and sent to the timing system. In addition, in the scanning beam box a photo diode was attached to one end of the parabolic mirror, in order to detect the time when the laser beam was being swept into the flow. The photo-diode signal was also sent to the timing system. When the wave-gauge signal was synchronized with the photo-diode signal another signal was then sent to trigger the cameras. After locating this signal-generating wave gauge at different positions along the wave flume, covering one wave length, different phases of each wave cycle could be captured.

The PIV measurements were taken at 3 positions for both of the breaking wave types. For both wave types 16 phases within one wave period were recorded at each position. At each phase, images were captured from 60 successive waves. This means that for each breaking wave type 2880 pairs of images were taken. With this recording procedure, a phase-averaging technique was employed to calculate the mean and fluctuating velocity components in the post-processing data analysis (see section 5.2.2).

7.1.1 Problems with the Experiments

The problems that occurred in the trains of breaking waves experiments were caused by several effects. These are explained in the following.

Air Bubbles

The problem caused by wave-breaking generated air bubbles was similar to that which occurred in the previous experiments (see section 6.1.1). The velocity in the aerated region could not be measured. However, in this case only a small amount of air bubbles and seeding particles collected under the perspex beach. The section under the perspex beach, between the concrete beaches (see figure 7.1), was cleaned and filled up first with water, before filling the whole flume. Every connection and hole along the perspex beach, above this section, was then taped or plugged so that the air bubbles, generated by the breaking waves, and the seeding particles could not enter into the section and block the light sheet.

Wave Periodicity

In the previous experiments wave repeatability was examined. In the present experiments it is the periodicity of the breaking waves that is important because the

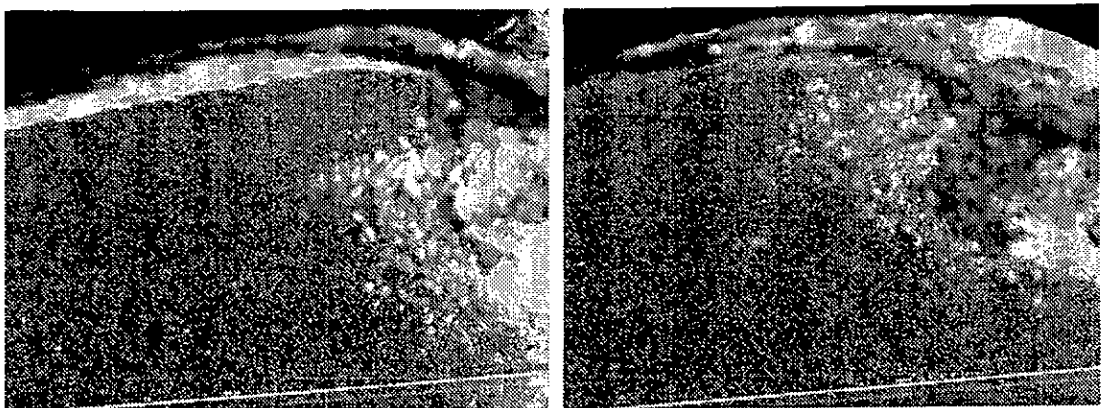


Figure 7.2: Two PIV images of the weak plunging breaker taken at the same position and phase ($(t - t_b)/T = 0.0625$) but from different cycles.

phase-averaging method was to be applied to the PIV data. Mean and turbulent quantities would differ from the true values if the phase between successive waves was not the same. The imperfection in the wave periodicity was affected by free second harmonic waves (see section 4.1.2). Although an attempt to reduce the free second harmonic waves was made by moving the piston with a non-sinusoidal motion, there were still occasions when the breaking point and wave period were not constant. The waves could also be affected by reflection. Figure 7.2 shows an example of two weak plunging breakers taken at the same position and supposedly the same phase. These two images were taken after the wave had broken. The plunger vortex, which contains air bubbles, can be observed. It can be seen that the horizontal position of the crest in each of the waves is not the same. If a wave was too different from the others, taken at the same phase, then its PIV images were not included in the analysis.

Other Problems

Apart from the major problems explained above there were also several other side problems which occurred during the experiments. One of these problems was unavoidable and concerned the 45° mirror; this mirror was submerged in the tank under the beach and was used to deflect the light sheet vertically upwards. Unfortunately, a signal-generating wave gauge had to be used at all times to trigger the cameras and this wave gauge created an electrical current in the water. This current then caused an electrolytic reaction which removed the silver coating on the mirror. Consequently, the mirror had to be replaced after a certain time and in doing this the whole flume needed to be emptied and refilled. Since the wave flume was large, this process took a long time.

Another problem was caused by the seeding. In a big wave flume it was more difficult to control seeding density and to ensure that the particles stayed within

the measurement region. After wave breaking, the particles were carried away from the light sheet due to the undertow effect and so a large amount of seeding was used at the beginning and also in between experiments. After a number of runs, the water eventually became “milky”, that is, there were too many particles in the flume and hence individual particles could not be easily identified. As a result, the flume was yet again emptied and refilled and the particles re-seeded.

7.2 Weak Plunging Breaker

In this section data from the train of weak plunging breaker experiments are presented. The maps of mean velocity, isovelocity contour, mean vorticity and turbulent intensity are shown in sections 7.2.1 – 7.2.4. These results are displayed in the same fashion as in the previous chapter. To reiterate, the maps in each figure are arranged into four rows (four phases) and three columns (three measurement positions). Instead of displaying all of the 16 measured phases, a sequence of 8 phases within one wave period, beginning at $(t - t_b)/T = 0.0625$, with an interval of 0.1250, is displayed for each quantity. The exception to this is for the isovelocity contours where there are only 4 phases in the sequence.

7.2.1 Velocity Vector Maps

Figures 7.3 and 7.4 show a sequence of phase-averaged velocity maps within one wave cycle of the weak plunging breaker. The three measurement positions cover approximately 50 cm: the breaking point, transition zone and the beginning of the inner surf-zone. Similar to the mean velocity vector maps shown in section 6.2.1, the velocity is normalised by C and the reference vector, shown at the corner of the map, is $0.5C$ where C is the speed of the wave crest at breaking ($C = 122$ cm/s).

Figure 7.3(a) shows the mean velocity fields at $(t - t_b)/T = 0.0625$. It is the

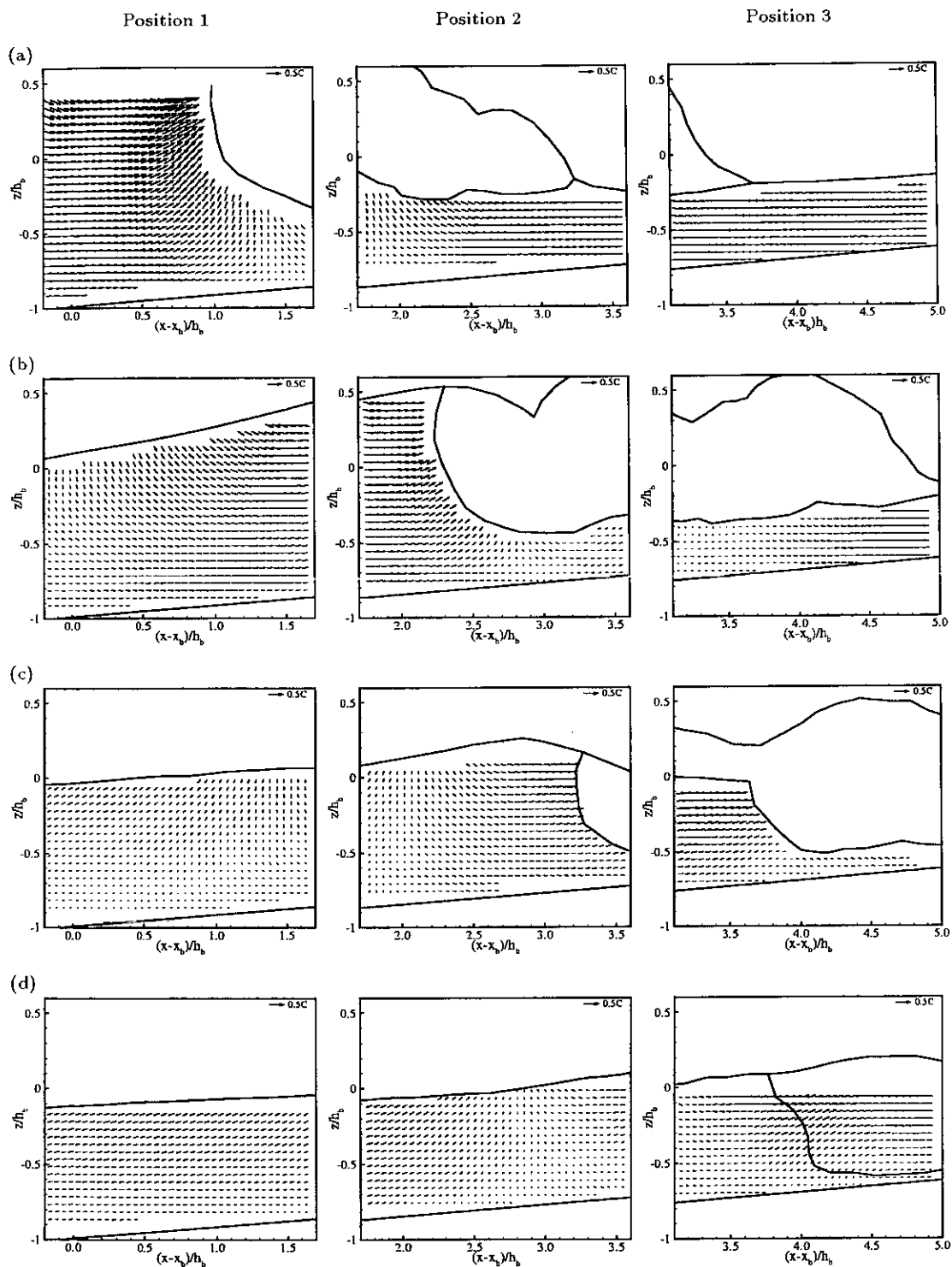


Figure 7.3: Mean velocity of the weak plunging breaker at $(t - t_b)/T =$ (a) 0.0625, (b) 0.1875, (c) 0.3125 and (d) 0.4375.

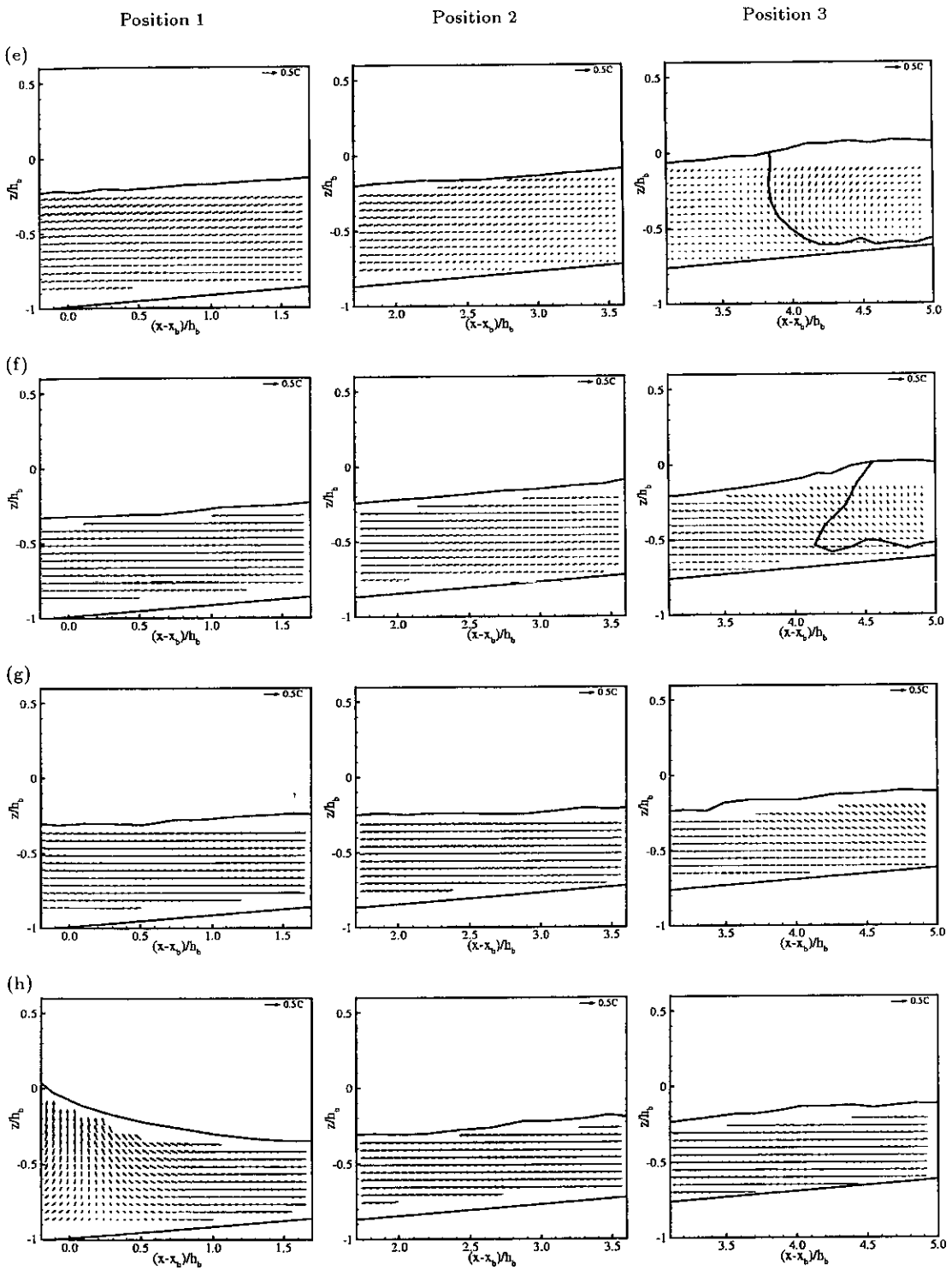


Figure 7.4: Mean velocity of the weak plunging breaker, continued from figure 7.3, at $(t - t_b)/T =$ (e) 0.5625, (f) 0.6875, (g) 0.8125 and (h) 0.9375.

phase at which the jet has impacted the frontal trough (appearing in position 1 and 2). The crest of the weak plunger is not included in the field of view but it can be seen that there is a strong forward movement ($\approx 0.5C$) behind the overturning jet. The backwash can be observed in position 3 which interacts with the incoming plunger causing a typical dividing region (zero horizontal velocity) under the wave trough.

By observing from the raw PIV images, at the time $(t - t_b)/T = 0.1875$ (corresponding to figure 7.3(b)), it is found that the overturning jet has impacted into the deeper region which almost touches the bottom. The water surface was splashed up by the impact of the jet and the surface roller was being formed in position 3. This time the wave crest can be seen in position 2 but the magnitude of the horizontal velocity just under the crest is only approximately $0.4C$.

In figure 7.3(c) the surface roller is formed and is moving onshore. The air bubbles generated from the overturning and jet-splash motion can be seen mostly in position 3. The generated air bubbles are so strong that they spread downwards until they reach the bottom. This is shown in position 3 where most of the region is dominated by the air bubbles. The flow in positions 1 and 2 at this phase begins to reverse.

The air bubbles still appear at the measurement times $(t - t_b)/T = 0.4375$, 0.5625 and 0.6875 , corresponding to figures 7.3(d), 7.4(e) and 7.4(f), respectively. However, an attempt to measure the velocity within the aerated region at those phases was made for the purpose of vorticity dynamics investigation which will be discussed in section 7.2.3. The difference between the kinematics of the main flow and that of the air bubbles can be determined from the vector plots. While the main flow has already reversed and is moving offshore, in position 1 and 2 of figure 7.4(e) and (f), the flow within the aerated region, in position 3 of the same

figures, seems to move upwards toward the free surface. This suggests the effect of the rising buoyant bubbles. Lin & Hwung [44] found that the rising bubbles interacted with the vortices and caused vortex stretching.

In figure 7.4(g) and (h) the air bubbles disappear from the measurement region and the flow continues to move offshore due to the backwash until the next wave arrives in position 1 of figure 7.4(h).

7.2.2 Isovelocity Contours

The transition from potential flow to rotational flow can be investigated with the isovelocity contour plots (as already explained in section 6.2.2). Figure 7.5 shows a sequence of these plots for the weak plunging breaker at four phases.

The interior domain of the flow, in position 1 and some part of position 2 of figure 7.5(a), is still potential although the overturning jet has already impacted onto the water surface at the front. Position 3, however, contains a complex pattern of the isolines of both velocity components which then suggests that the flow there is rotational. This result is different from what was found in the single plunging breaker experiments. Considering the isovelocity contours in position 3 of figure 6.7(a) where the backwash also occurs as in position 3 of figure 7.5(a), the flow in that position of the single plunging breaker is still potential whereas in the weak plunging breaker the flow is rotational. The rotational flow in position 3 of figure 7.5(a) is perhaps caused by the residual small-scale vortices and turbulence generated from the previous breaking wave.

In the next phase, figure 7.5(b), the orthogonality between the two different isolines can still be observed at the region around the overturning jet. However, the complex isovelocity contours under the jet-splash water surface in position 3 show that the flow is rotational there. The reason for this could be due to the interaction between the backwash, the surface roller and the bottom boundary

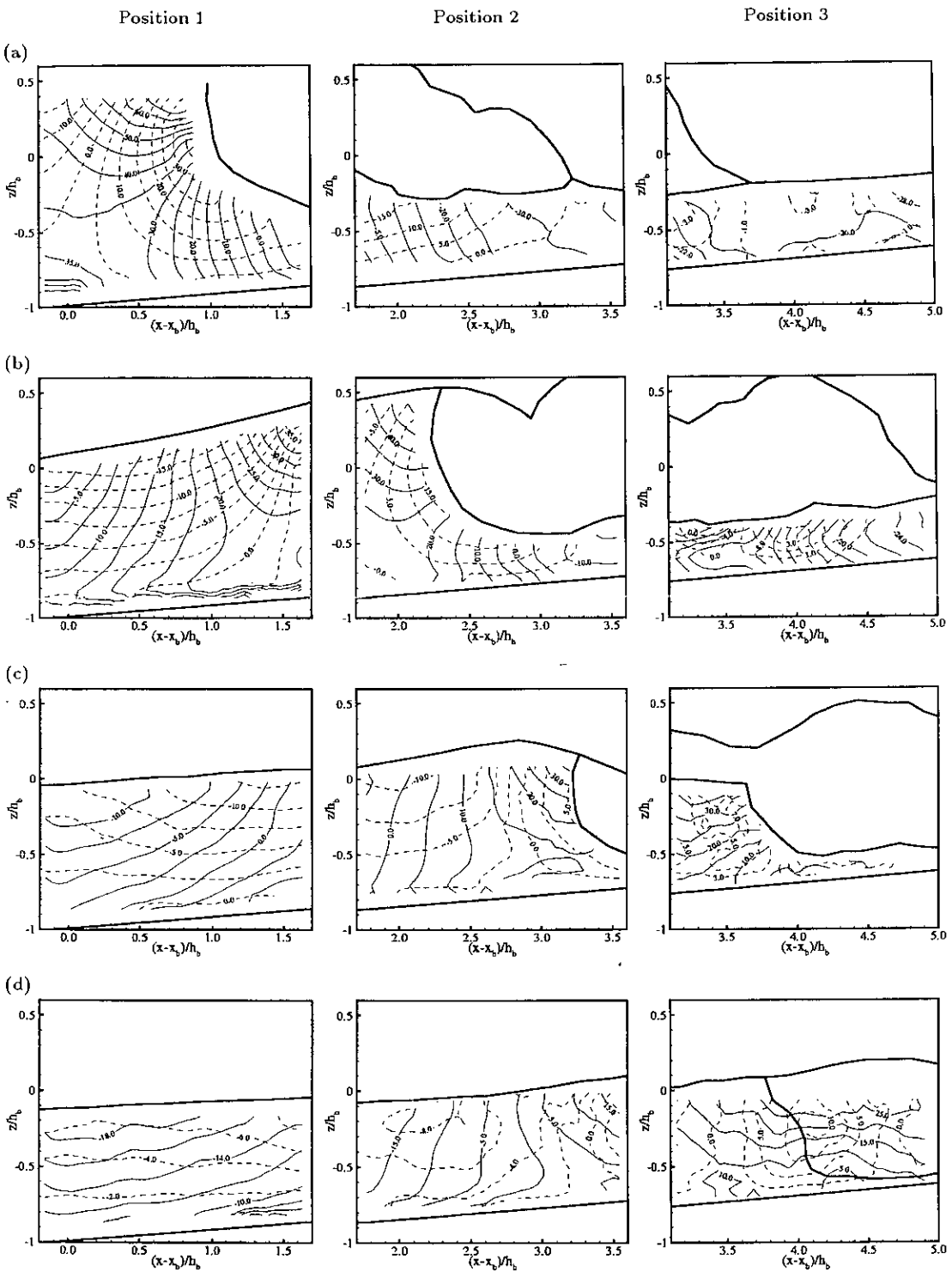


Figure 7.5: Isovelocity contours of the weak plunging breaker at $(t - t_b)/T =$ (a) 0.0625, (b) 0.1875, (c) 0.3125 and (d) 0.4375. The solid lines represent $\langle u \rangle$ and the dashed lines represent $\langle w \rangle$.

layer. Finally, in the last two phases, figure 7.5(c) and (d), it now becomes clear that the flow at these stages is completely rotational because no orthogonality between isolines could be observed.

7.2.3 Vorticity

The dynamics of breaker-generated vortices can be investigated using the contour plots of the calculated mean vorticity. These plots for the weak plunging breaker are shown in figures 7.6 and 7.7. The mean vorticity is normalised by $(C/h)_b$ and negative vortices appear in the blue-coloured region while the positive ones appear in the red-coloured region.

In figure 7.6(a) and (b) it can be seen that there are no significant vortices within the interior domain of the flow in position 1 and some part of position 2. This supports the results found in the previous section from the isovelocity contours that the flow at these phases are irrotational. There is, however, a negative vorticity which locates around the overturning jet in position 1 of figure 7.6(a). This vorticity is rotating in the same direction as the overturning jet. The maximum mean vorticity in that region is -12 s^{-1} which is roughly $-(C/h)_b$. This order of magnitude was also found in the vorticity generated around the overturning jet of the single plunging breaker (see section 6.2.3). Similar results were also found by Nadaoka *et al.* [54] and Chang & Liu [10].

Another negative vorticity can be observed in position 3 of figure 7.6(b) which locates beneath the jet-splash free surface. The maximum mean vorticity is -7.3 s^{-1} ($\approx -0.6(C/h)_b$). There is no coexistence between the negative vorticity and the positive vorticity found beneath the overturning jet in this case. The small-scale positive vortices are found along the free surface at the lee side of the wave crest. It was mentioned in section 6.2.3 that Lin & Liu [47] suggested that these positive vortices were generated within a thin boundary layer due to the

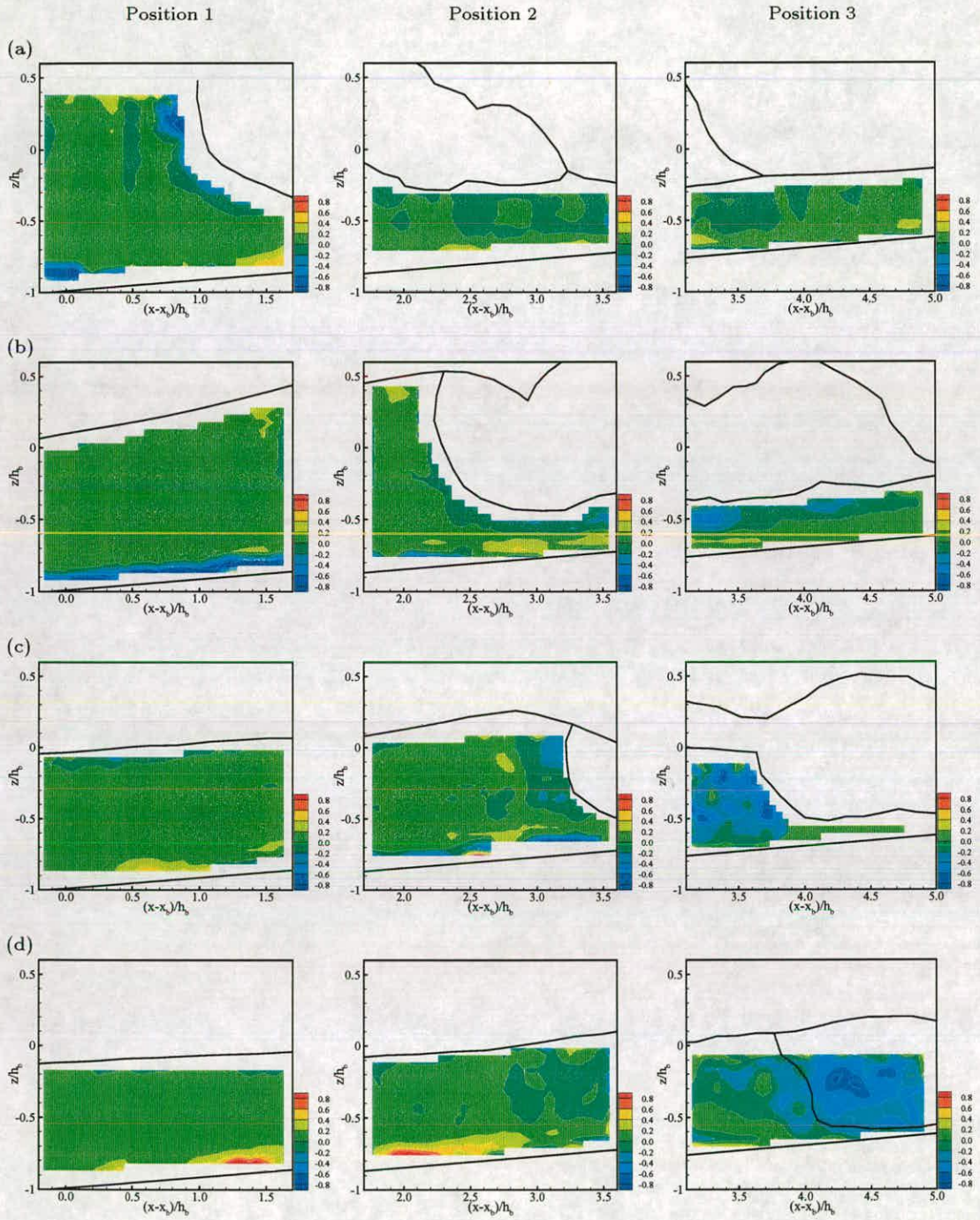


Figure 7.6: Mean vorticity of the weak plunging breaker at $(t - t_b)/T =$ (a) 0.0625, (b) 0.1875, (c) 0.3125 and (d) 0.4375.

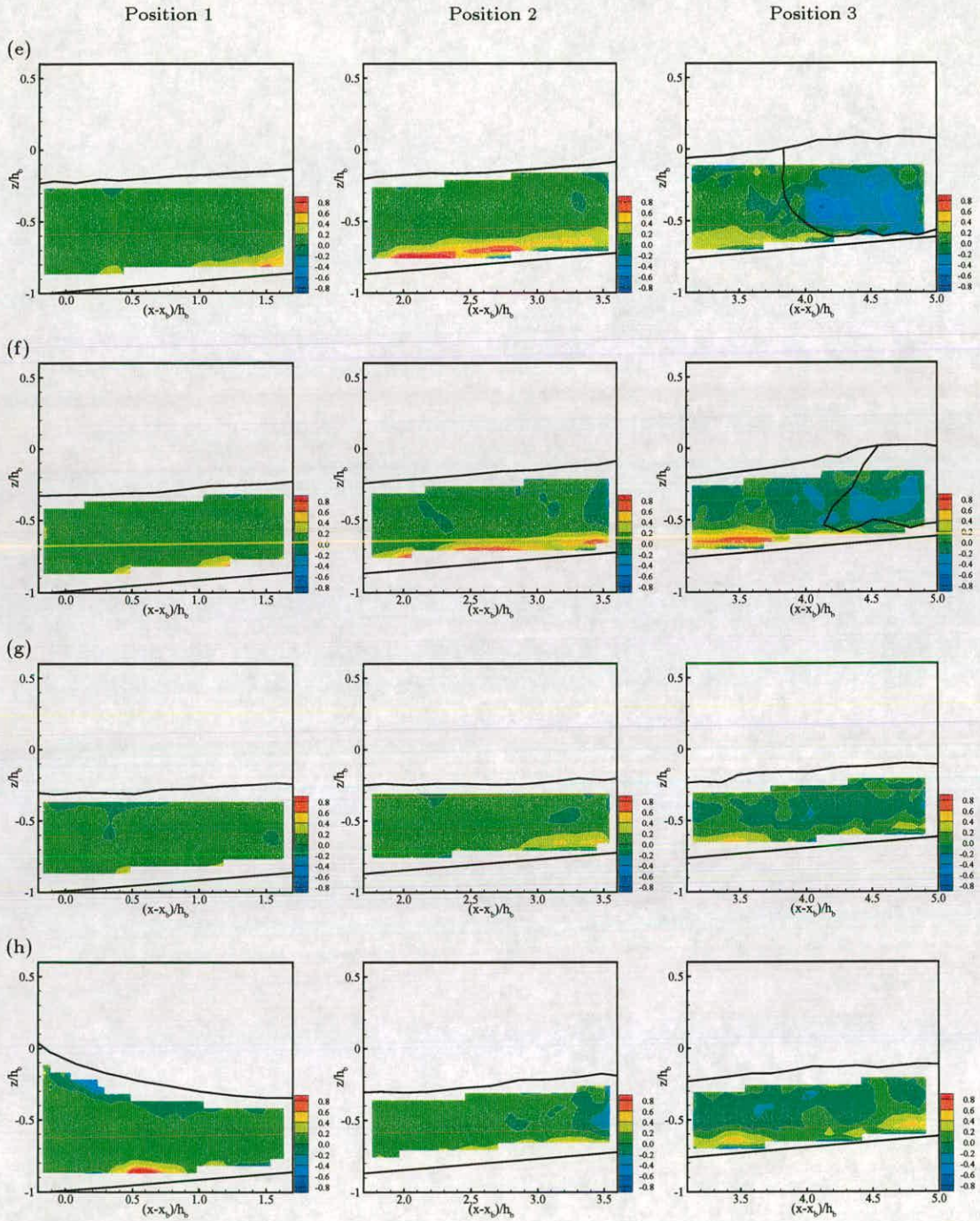


Figure 7.7: Mean vorticity of the weak plunging breaker, continued from figure 7.6, at $(t - t_b)/T =$ (e) 0.5625, (f) 0.6875, (g) 0.8125 and (h) 0.9375.

negative curvature of the free surface.

Moving onto figure 7.6(c), the overturning jet has passed position 2 leaving behind the generated air bubbles and the surface roller is formed in position 3. In position 2 the negative vorticity can be seen with its maximum value of -4 s^{-1} ($\approx -0.3(C/h)_b$). In position 3 where most of the region is dominated by the air bubbles, the maximum vorticity is found to be -12 s^{-1} ($\approx -(C/h)_b$) which is as strong as the negative vorticity generated around the overturning jet in position 1 of figure 7.6(a). This then suggests that the vorticity found in this position was perhaps the plunger vortex that was generated from the overturning jet, spread down into the interior domain of the flow. The complex contour pattern of the vortices in position 3 of figure 7.6(c) is perhaps due to the noise introduced from the velocity measurement in the air bubble region.

The plunger vortex can be seen within the aerated region in position 3 of figure 7.6(d). The maximum mean value is -11 s^{-1} ($\approx -0.9(C/h)_b$). The vortex is diffused into the main flow and becomes disordered, smaller in size and finally dissipates before the new breaking wave arrives. This can be explained by the gradual decrease in strength of the vortex as the wave progresses: the maximum mean vorticity are approximately $-0.6(C/h)_b$, $-0.46(C/h)_b$, $-0.24(C/h)_b$ and $-0.2(C/h)_b$ in figure 7.7(e), (f), (g) and (h), respectively.

Considering the sequence from figure 7.6(d) to figure 7.7(f), the “core” of the vortex appears on the left of its “tail” because the main flow starts to move backwards. However, the vortex seems to be moving shorewards with the surface bore. In figure 7.7(f) the tail of the vortex is pointing towards the free surface which is thought to be caused by the rising air bubbles. Positive vortices of smaller size can also be observed along the beach. These positive vortices are caused by the returning flow [47].

The main results obtained from this investigation imply that the majority of the vortices are mainly generated from the overturning jet and the air bubbles. The dynamics of the air bubbles affected the transport of the vortices and the rising of the buoyant bubbles causes the vortex stretching.

7.2.4 Turbulent Intensity

Figures 7.8 and 7.9 show a sequence of turbulent intensity maps. The turbulent intensity is normalised by C and the greater values appear towards the red-coloured region. The interval between contour levels is 0.01.

From figure 7.8(a) and (b) it can be seen that the highest turbulent intensity appears around the overturning jet and the surface roller. The maximum value of I in position 1 of figure 7.8(a) is found to be 25 cm/s which is approximately $0.2C$. The value then gradually decreases towards the bottom. The numerical model developed by Lin & Liu [47] has predicted that, in the plunging breaker, the turbulent intensity appears highest in the roller region (up to $\approx 0.6C$). Although measurement could not be made within this region, the measured patterns of turbulent intensity just outside this region matched the numerical simulation. The numerical results show that the intensity just outside the surface roller is around $0.2C - 0.3C$ which is close to that found in the current experiments.

As the wave propagates forward (figure 7.8(b)), the turbulent intensity decreases: its maximum value is about $0.14C$ around the crest and about $0.11C$ beneath the surface roller. The pattern of the turbulent intensity distribution is still similar to that in the previous phase. That is, the intensity gradually decreases towards the bottom and also decreases from the crest region towards the lee side of the wave. This is perhaps caused by the advection and diffusion effect that spreads the turbulence (which is generated and left over from the passing wave crest) downward and backward.

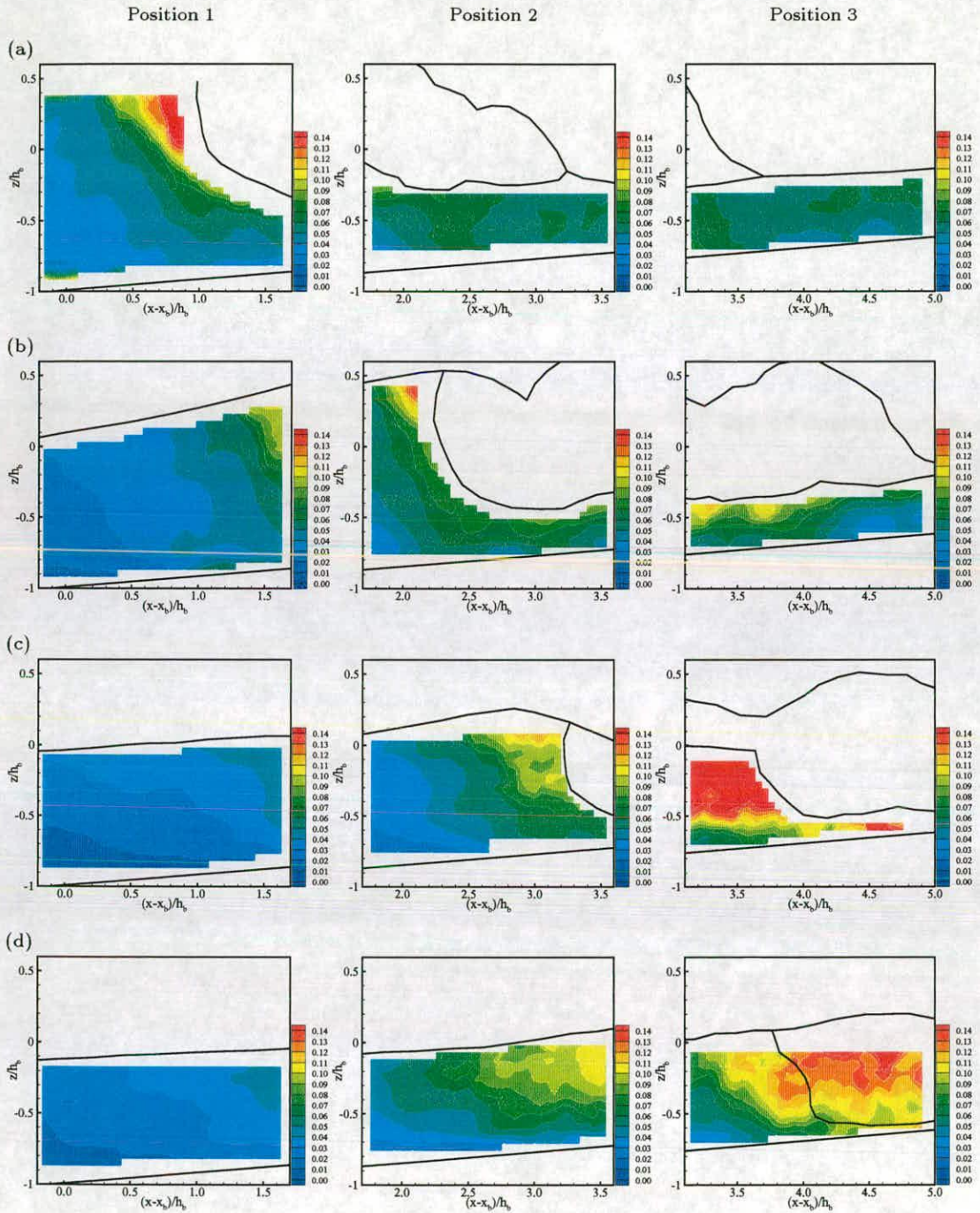


Figure 7.8: Turbulent intensity of the weak plunging breaker at $(t - t_b)/T =$ (a) 0.0625, (b) 0.1875, (c) 0.3125 and (d) 0.4375.

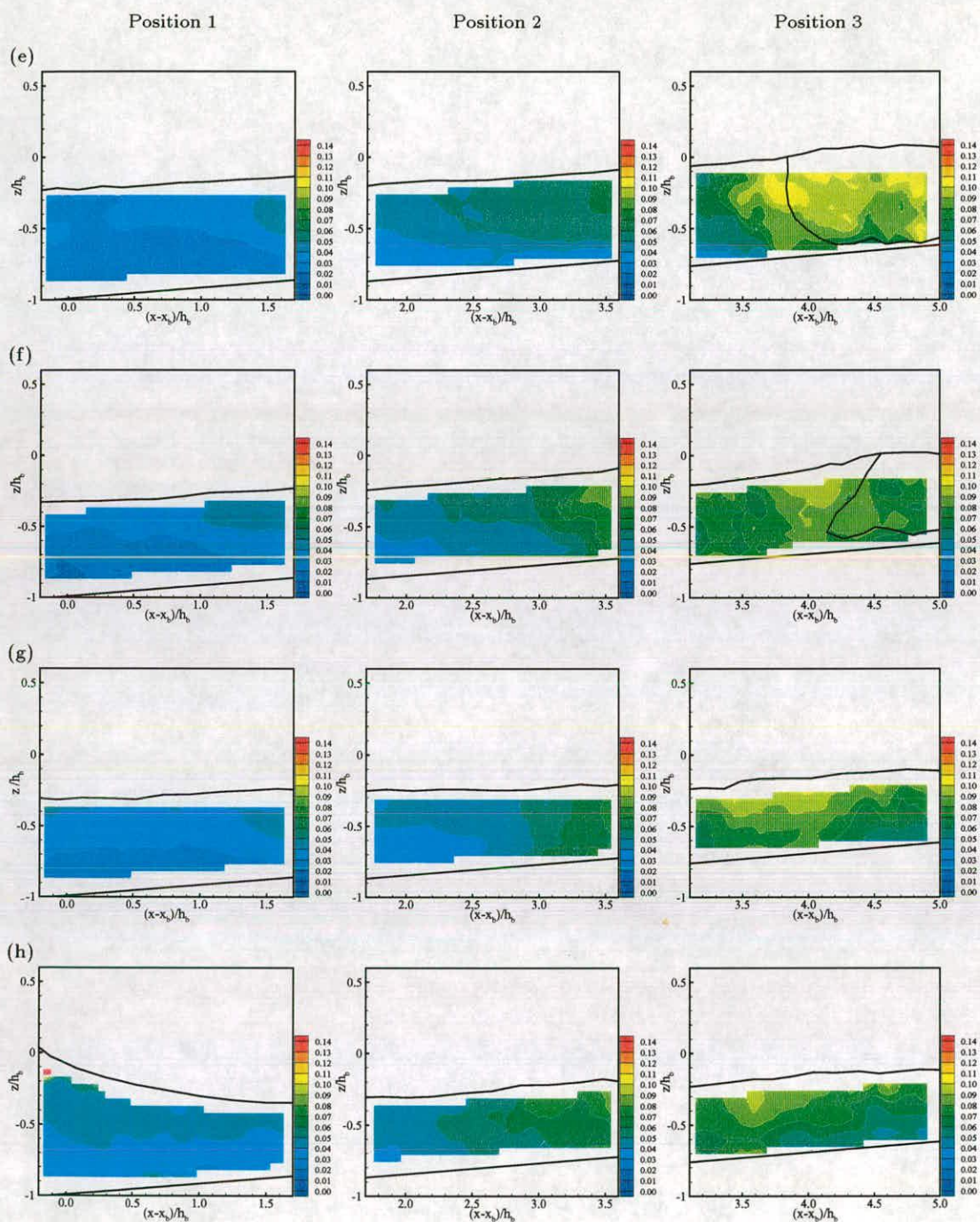


Figure 7.9: Turbulent Intensity of the weak plunging breaker, continued from figure 7.8, at $(t - t_b)/T =$ (e) 0.5625, (f) 0.6875, (g) 0.8125 and (h) 0.9375.

Figure 7.8(c) is the phase at which the air bubbles spread down to nearly touch the bottom. An attempt to measure the velocity in some part of the aerated region was made (see position 3). The maximum value of the turbulent intensity within such region is up to 27 cm/s ($\approx 0.23C$). The high intensity could be due to either the strong turbulence generated from the surface roller or the errors introduced from the velocity measurement. Because it is likely that the latter one is the main reason for the high measured turbulence, no interpretation of the results at this phase was made.

Moving on to the next phase, figure 7.8(d), when the surface roller has passed the measurement region and left behind the generated air bubbles, the maximum value of I is found to be 20 cm/s ($\approx 0.16C$) in position 3. The high intensity region seems to spread downward to the bottom. The turbulence, however, gradually decreases towards the offshore region.

Position 3 is where the high turbulent intensity appears, as it is the location where the air bubbles were generated and left behind from the passing surface roller. The maximum value of I gradually reduces as the wave progresses: $\approx 0.11C$, $0.10C$, $0.10C$ and $0.09C$ in figure 7.9(e), (f), (g) and (h), respectively. From figure 7.9(e) to (f) it can be seen that the turbulent intensity in position 2 seems to increase as the main flow is moving offshore. This is due to the advection of the turbulence from position 3 into position 2. Although there is residual small-scale turbulence ($\approx 0.05C$) left (see position 3 in figure 7.8(a)), most of the turbulence dissipates before the next breaker has arrived.

The main result obtained from these plots is that the turbulence is mostly generated in the overturning jet and the surface roller. Although no measurement was made in those regions to provide an evidence, the distribution pattern of the turbulent intensity outside the roller region seems to suggest the expectation. The

air bubbles generated from the breaking process caused the spread of turbulence which at some phases could reach the bottom. In the previous experiments on the single plunging breaker, the turbulence was also seen to spread downward but it did not reach the bottom. This is perhaps because the measurement region for the single plunger only covered the transition zone. If measurements were also made in the inner surf-zone, the same effect might be observed.

7.2.5 Turbulence Transport Mechanisms

In this section turbulence transport mechanisms in the weak plunging breaker are investigated. The results are calculated and presented in the same format as in section 6.2.5. That is, the phase-averaged velocity components, turbulent kinetic energy and all of the transport terms in the k -equation are calculated following the approaches that are explained in sections 5.2.2 and 5.2.3. Each of these calculated quantities are then averaged over a selected control volume and plotted as a function of time for one wave period. Here, 7 control-volume areas under the trough level of the wave are investigated. In the following, seven sets of graphs (corresponding to seven areas) are displayed and discussed. The selected control volumes, as shown in figure 7.10, cover the locations from around the breaking point to the inner surf-zone:

- Area I : upper region around the breaking point (results in figure 7.11)
- Area II : lower region around the breaking point (results in figure 7.12)
- Area III : upper region onshore from the breaking point (results in figure 7.13)
- Area IV : lower region onshore from the breaking point (results in figure 7.14)
- Area V : lower region in the initial transition zone (results in figure 7.15)
- Area VI : lower region in the transition zone (results in figure 7.16)
- Area VII : lower region in the inner surf-zone (results in figure 7.17).

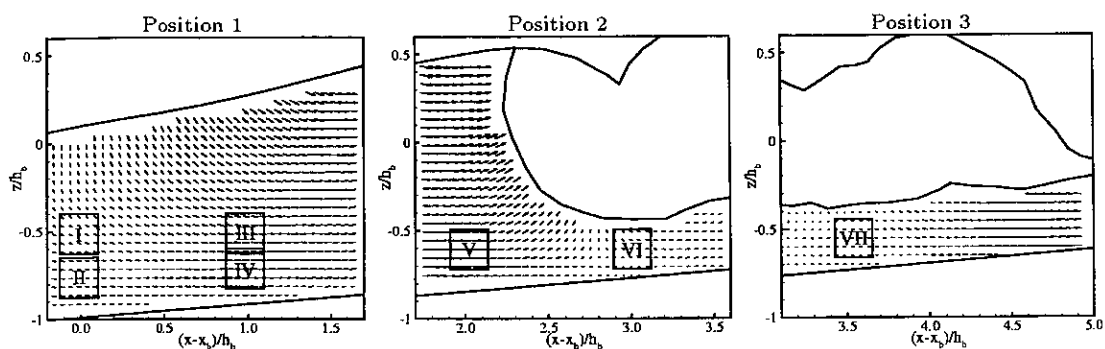


Figure 7.10: The control volumes for the weak plunging breaker in which the mean value of each term in the k -equation is calculated.

Discussions on Turbulence Transport in the Weak Plunging Breaker

The first investigation is made at the location around the breaking point (figures 7.11 and 7.12). It can be seen immediately that the turbulent kinetic energy is correlated to the passage of the wave, even in the lower region (figure 7.12). As explained in section 6.2.5, the passage or shape of the wave can be suggested from the temporal variation of the mean horizontal velocity component (graph (a)), rather than directly from the free-surface elevation. The LDA results of Ting & Kirby [79] and the numerical results of Lin & Liu [47] for a similar kind of waves have also shown this correlation. Lin & Liu [47] explained that the correlation between k and the passage of the wave, near the bottom for the plunging breaker, was caused by the penetration of turbulence into the deeper region. They found that this effect is in contrast to that in the spilling breaker [46]. However, the correlation is also found in the spilling breaker for the present study (see section 7.3.5). It is perhaps due to the fact that the wave parameters of the spilling breaker used here were not much different from that of the weak plunging breaker, as already mentioned in chapter 4.

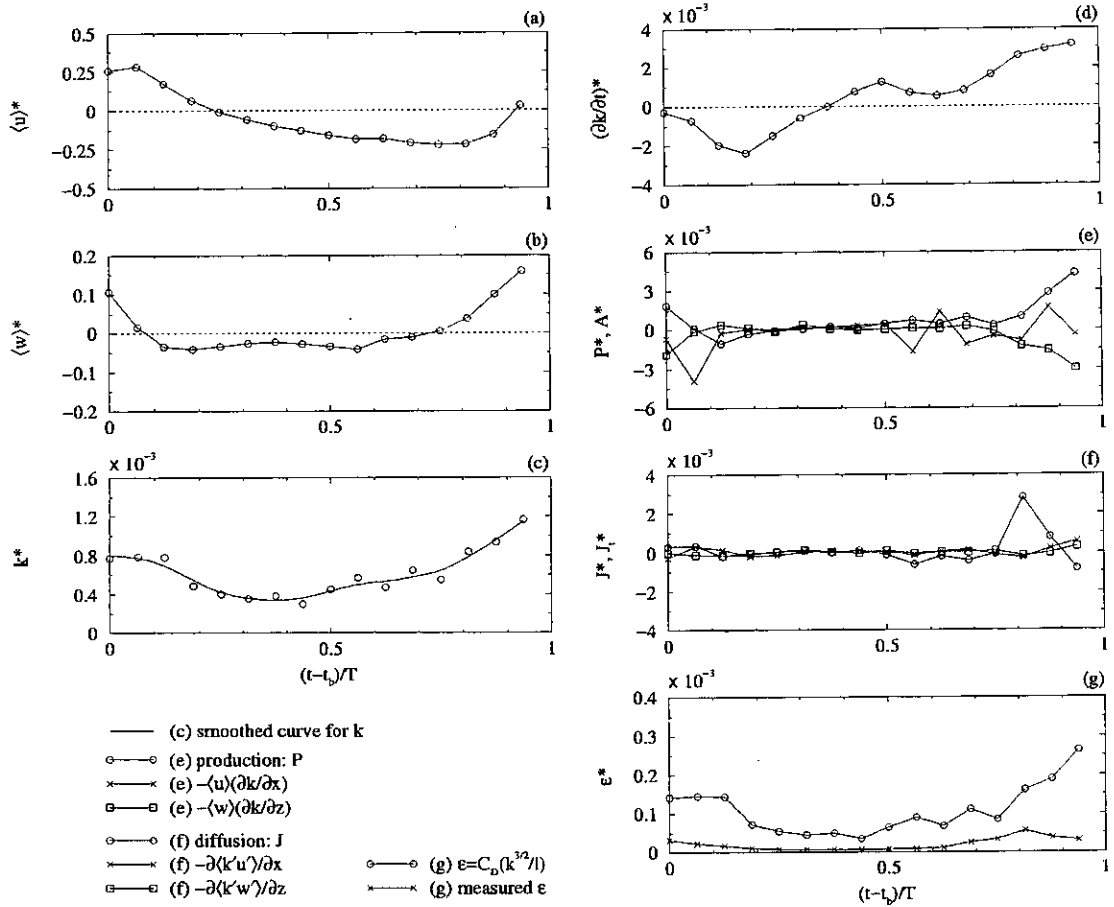


Figure 7.11: Mean velocities (a & b), turbulent kinetic energy (c) and turbulent transport terms (d – g) for k in equation (5.13), of the weak plunging breaker, calculated in the area $-0.112 \leq (x - x_b)/h_b \leq 0.087$ and $-0.615 \leq z/h_b \leq -0.416$ (area I of figure 7.10). The symbol * indicates normalised quantities: $\langle u \rangle$ and $\langle w \rangle$ are normalised by C , k by C^2 and all of the transport terms by C^2/T .

Another effect that can be seen from the turbulence investigation around the breaking point is that the turbulent kinetic energy increases towards the end of the wave period (see figure 7.11(c)). The increase in k also occurs in the lower region as can be seen in figure 7.12(c), however, with a smaller value. Considering the contour plots of turbulent intensity in figures 7.8 and 7.9, it can be seen that, within the breaking-point location, turbulent intensity is highly generated during the beginning of the wave period and its value then gradually decreases. After

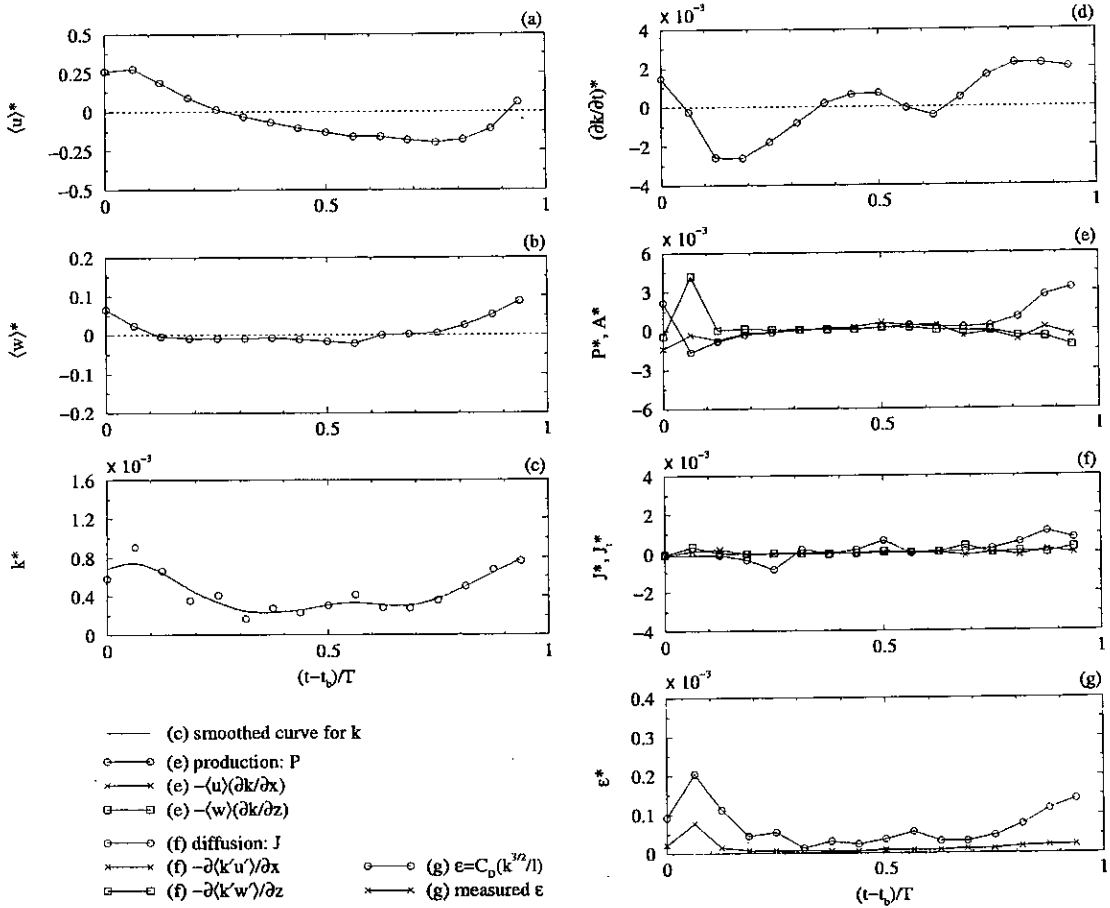


Figure 7.12: Similar to figure 7.11 but in the area $-0.112 \leq (x - x_b)/h_b \leq 0.087$ and $-0.864 \leq z/h_b \leq -0.665$ (area II of figure 7.10).

the flow reverses, the turbulent intensity in that location increases again. Judging from the contour plots, phase by phase, it looks as if the turbulence spreads and is advected into the upstream location by the main flow. Now, considering the time variation of the turbulence transport terms in figures 7.11(e) and 7.11(f), for the upper region, it is observed that the turbulence production is correlated with k and the passage of the wave. The horizontal advection is responsible for the reduction of the rate of change of k during the beginning of the wave period and for the increase in k towards the end of the period. Additionally, the production and diffusion are also important for the k -increment while vertical advection acts

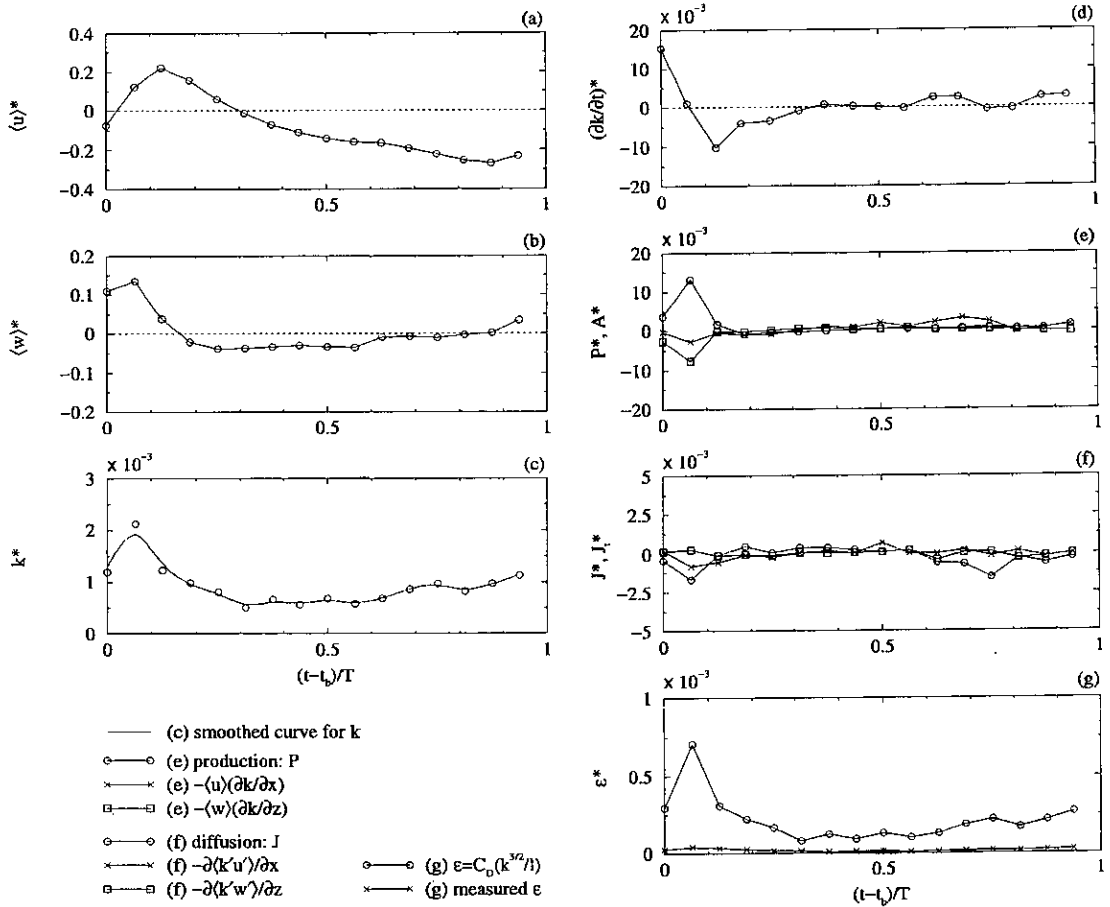


Figure 7.13: Similar to figure 7.11 but in the area $0.883 \leq (x - x_b)/h_b \leq 1.082$ and $-0.615 \leq z/h_b \leq -0.416$ (area III of figure 7.10).

to balance them.

In the lower region of the breaking-point location figures 7.12(e) and 7.12(f) reveal that production and vertical advection are the main mechanisms to the change of the turbulent kinetic energy during the passage of the wave front and the production is the only mechanism which contributes to the increase in k towards the end of the wave period. Advection and diffusion are not as significant as in the upper region which explains why a smaller increase in k is observed in the lower region.

It should be noted here again that the predicted dissipation is much smaller

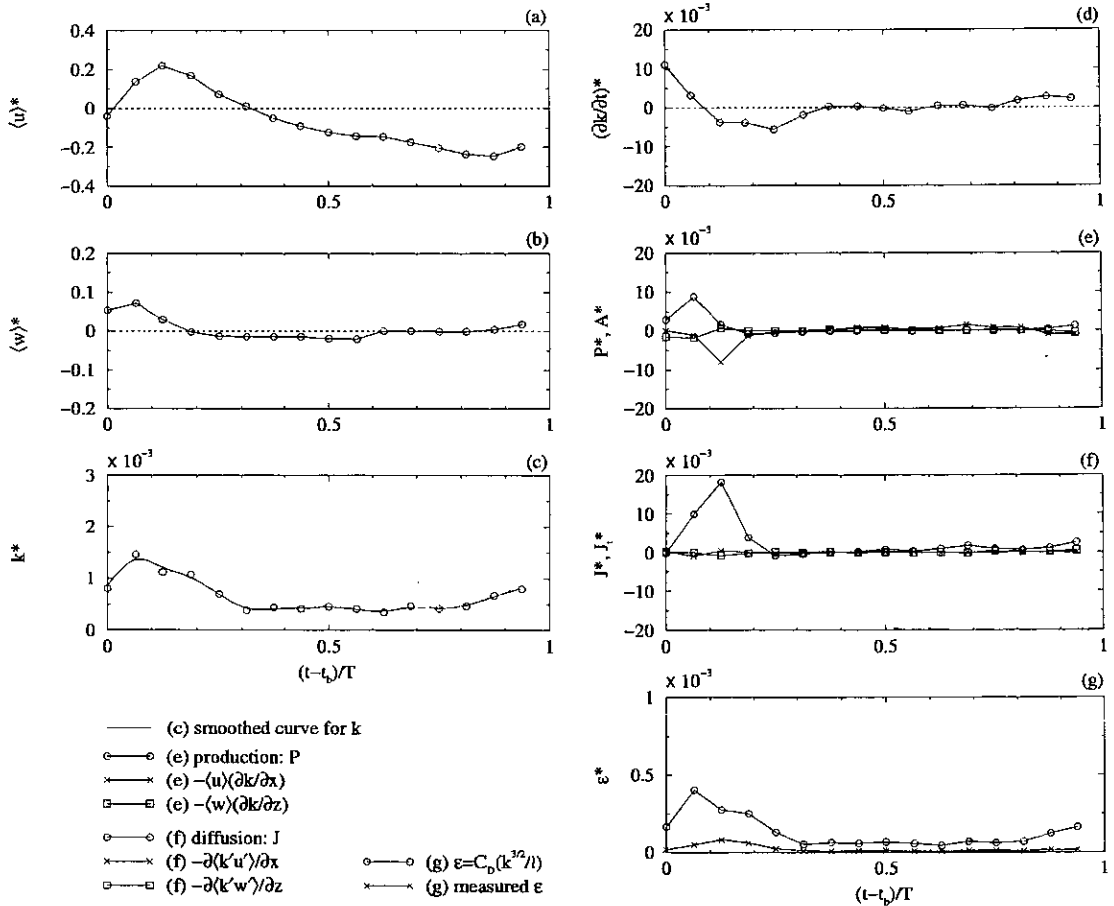


Figure 7.14: Similar to figure 7.11 but in the area $0.883 \leq (x - x_b)/h_b \leq 1.082$ and $-0.814 \leq z/h_b \leq -0.615$ (area IV of figure 7.10).

than the rate of change of k . Although the measured dissipation is even smaller, its trend mostly follows that of the predicted one. Full explanation to this can be seen in section 6.2.5 on page 122.

Moving on to the location just onshore (about 10 cm) from the breaking point (figures 7.13 and 7.14), turbulence mechanisms are different from the previous location. Turbulent kinetic energy and its transport mechanisms at this location are stronger, about two to three times those in the location around the breaking point. The correlation between the passage of the wave, k and the turbulence production can still be seen at both vertical levels. A small increase in k is

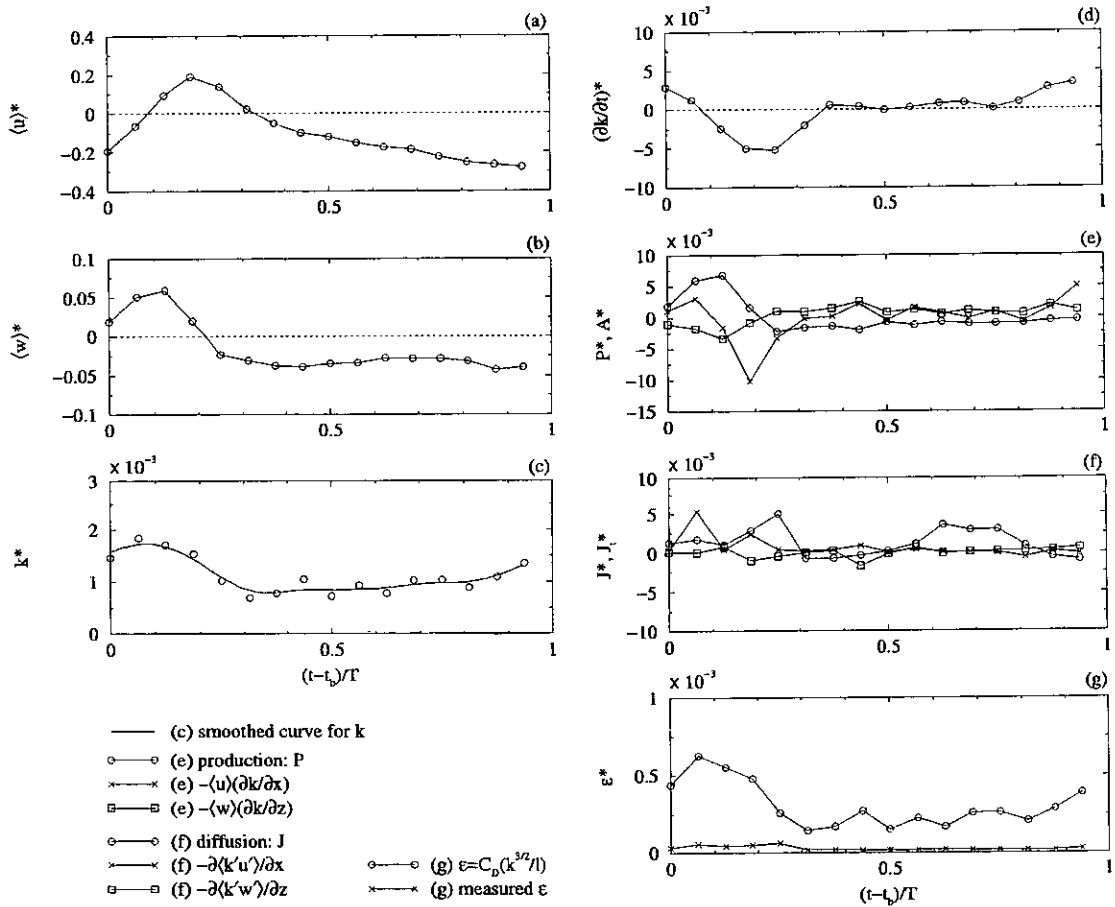


Figure 7.15: Similar to figure 7.11 but in the area $1.914 \leq (x - x_b) / h_b \leq 2.112$ and $-0.705 \leq z / h_b \leq -0.508$ (area V of figure 7.10).

observed but not as obvious as in the breaking-point location. This is due to the fact that no transport mechanism is effective after the passage of the wave front, regardless of vertical level. This effect also causes a small variation of $\partial k / \partial t$. In the upper region (figure 7.13) the turbulence production seems to be the main mechanism for an increase in k during the beginning of the wave period. Advection and diffusion act to reduce the turbulent kinetic energy in the upper region. On the other hand, the diffusive transport is the most important mechanism in the lower region (figure 7.14). This supports the suggestion of Lin & Liu [47], discussed earlier, that turbulence can penetrate into the deeper region

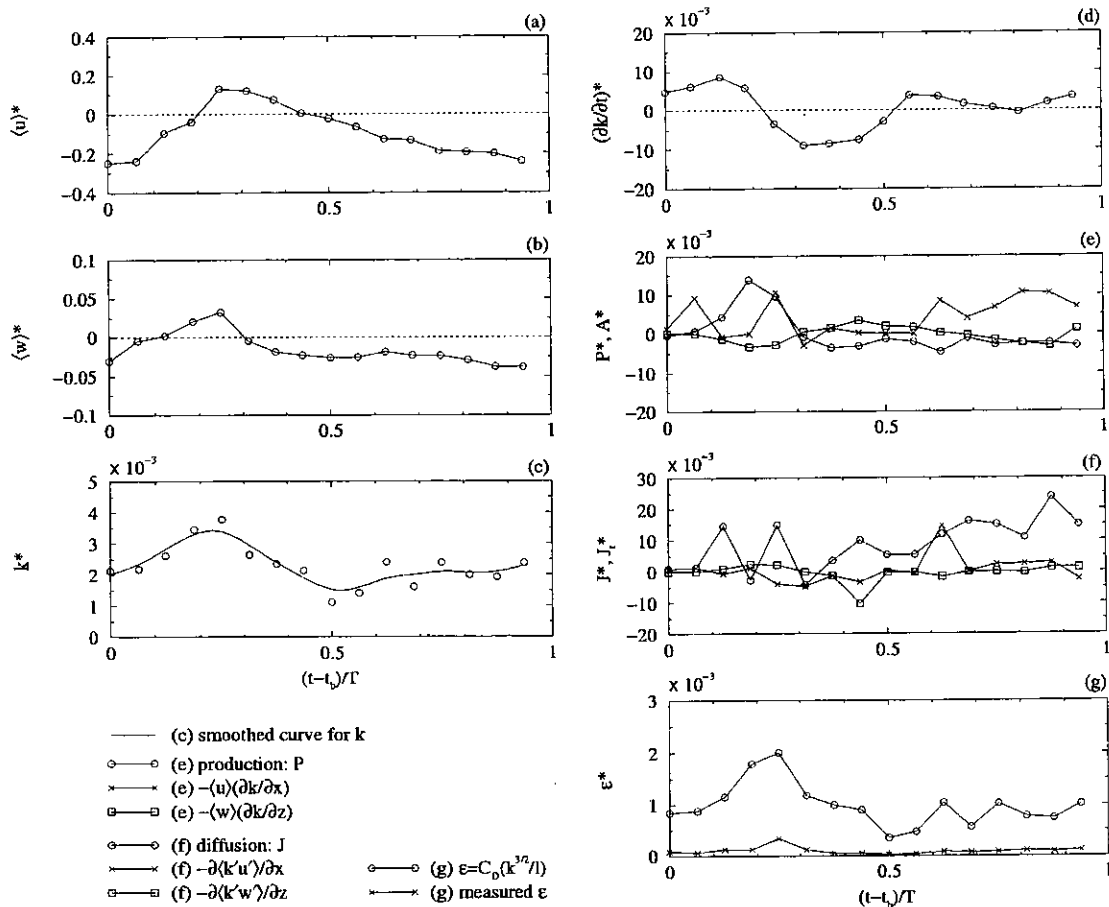


Figure 7.16: Similar to figure 7.11 but in the area $2.900 \leq (x - x_b)/h_b \leq 3.097$ and $-0.705 \leq z/h_b \leq -0.508$ (area VI of figure 7.10).

for the plunging breaker. The production also contributes to the high value of k but with smaller strength than in the upper region.

To avoid errors due to the air bubble effect, turbulence transport investigations have not been made within the aerated regions, although attempts were made to measure velocities within such regions. According to a small number of vector-grids outside the air bubble region (see figures 7.3 and 7.4), turbulence transport in the transition zone and the inner surf-zone, for the weak plunging breaker, is only investigated at one vertical level. This is referred to areas V, VI and VII, as indicated in figure 7.10; all of which locate close to the bottom.

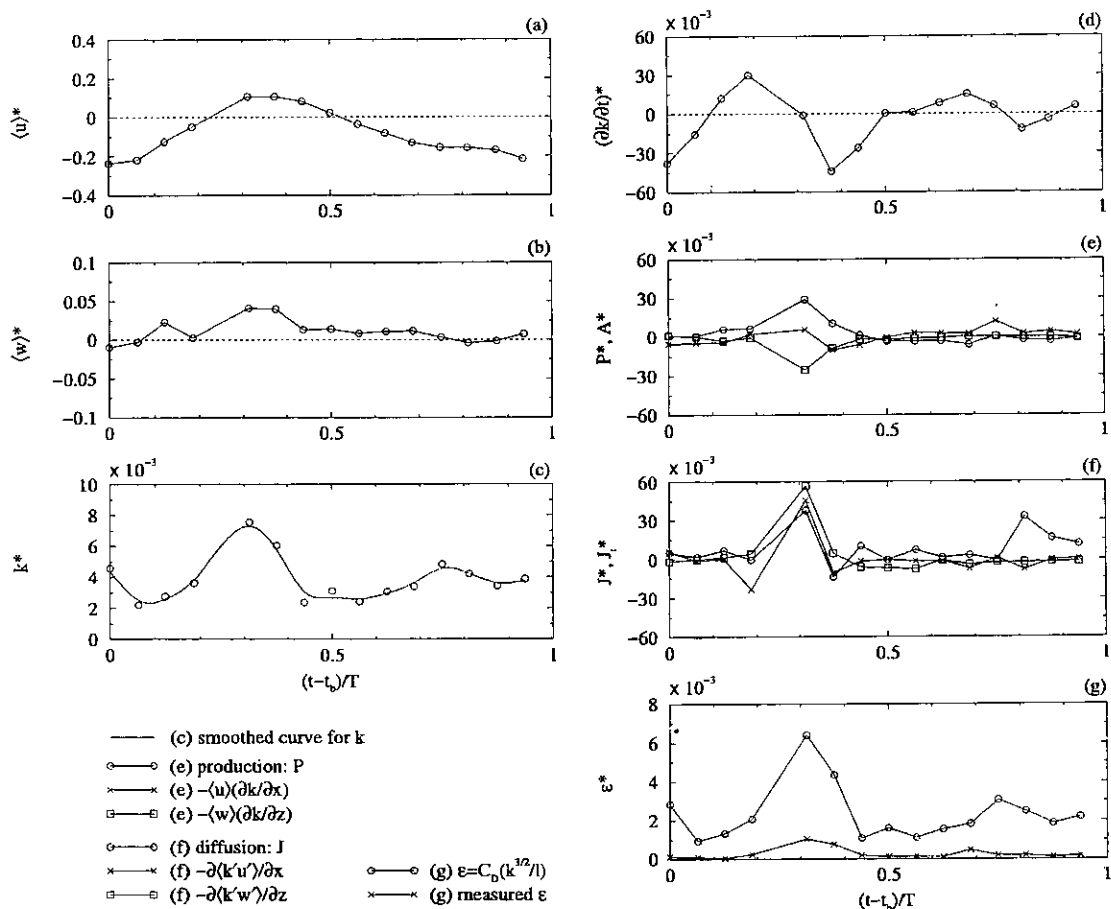


Figure 7.17: Similar to figure 7.11 but in the area $3.438 \leq (x - x_b)/h_b \leq 3.633$ and $-0.649 \leq z/h_b \leq -0.454$ (area VII of figure 7.10).

In the initial part of the transition zone figure 7.15 shows a typical correlation between the turbulent kinetic energy and mean velocity components. Turbulence production causes the high value of k during the passage of the wave front. Horizontal advection is responsible for the positive and negative rate of change of k . It also acts as a main mechanism for a slight increase in turbulent kinetic energy towards the end of the wave period. Diffusion as well as horizontal turbulent diffusion are also significant. However, they do not seem to correlate with any other transport terms or the rate of change of k .

Further in the transition zone of the weak plunging breaker (figure 7.16) al-

most all of the turbulence transport terms seem to vary randomly within one wave period. However, turbulence production and horizontal advection are found to be the mechanisms responsible for the rate of change of k . Diffusive transport at this location is stronger than in the upstream location, especially at the phases towards the end of the wave cycle. The diffusion and horizontal advection mechanisms contribute to the positive rate of change of k for the second half of the wave cycle.

The final investigation of turbulence transport in the weak plunging breaker is made in the inner surf-zone location (figure 7.17) which is about 35 cm away from the breaking point. In this location the strength of transport mechanism is about one order of magnitude greater than that in the breaking-point location and about three times that in the transition zone. The magnitude of turbulent kinetic energy is also higher and there are two peaks in its time variation within one wave cycle. The first peak seems to correlate with the turbulence production and all of the diffusion terms, even the vertical turbulent diffusion which has always been insignificant in the other zones. Vertical advection, however, acts to reduce the energy. The strong diffusion suggests that turbulence spreads downward from the surface roller into the deeper region close to the bottom. The second but smaller peak of k is due to the diffusion and a slight effect on the horizontal advection. No other transport mechanisms are significant after the passage of the wave front.

7.3 Spilling Breaker

Results from the train of spilling breakers experiments are presented in this section. The form of displaying the maps of wave and turbulent quantities is much the same as that used in the previous experiments. For each quantity a sequence of 8 phases within one wave period, beginning at $(t - t_b)/T = 0.0625$, with an interval of 0.1250, is displayed. Again, only 4 phases are displayed in the sequence of the isovelocity contours. There is missing data in position 3 at the times $(t - t_b)/T = 0.4375$, 0.5625 and 0.6875. This is due to the appearance of a high concentration of air bubbles during those phases. The presentation and discussion of these plots are given in sections 7.3.1 – 7.3.4.

7.3.1 Velocity Vector Maps

A sequence of phase-averaged velocity maps within one wave cycle of the spilling breaker is displayed in figures 7.18 and 7.19. The three measurement positions cover approximately 50 cm: the transition zone and the inner surf-zone. The velocity is normalised by C and the reference vector, shown at the corner of the map, is $0.5C$ where C is the speed of the wave crest at breaking ($C = 121$ cm/s).

Figure 7.18(a) shows the mean velocity field at $(t - t_b)/T = 0.0625$. The measurement region is dominated with the backwash and some of the air bubbles generated from the previous breaker still remain in position 3. In the next phase, figure 7.18(b), an overturning jet has arrived in position 1. By observing from the sequence of the raw PIV images, the jet is of smaller size than that in the plunging breaker, in the previous experiments. There is no obvious jet-splash motion in the spilling breaker: only the surface roller appears throughout the breaking process within the measurement region.

The typical dividing region (zero horizontal velocity region) due to the inter-

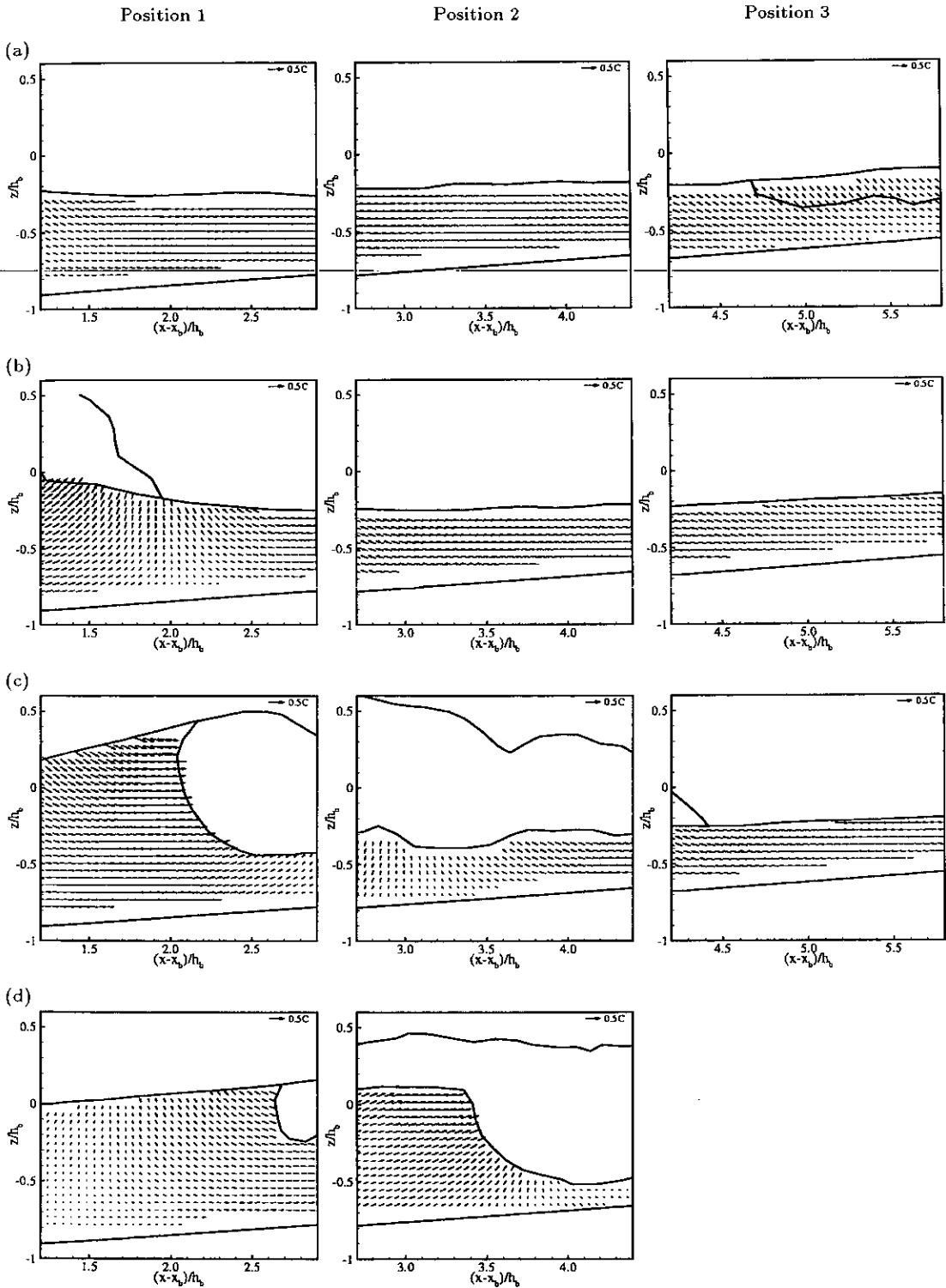


Figure 7.18: Mean velocity of the spilling breaker at $(t - t_b)/T =$ (a) 0.0625, (b) 0.1875, (c) 0.3125 and (d) 0.4375.

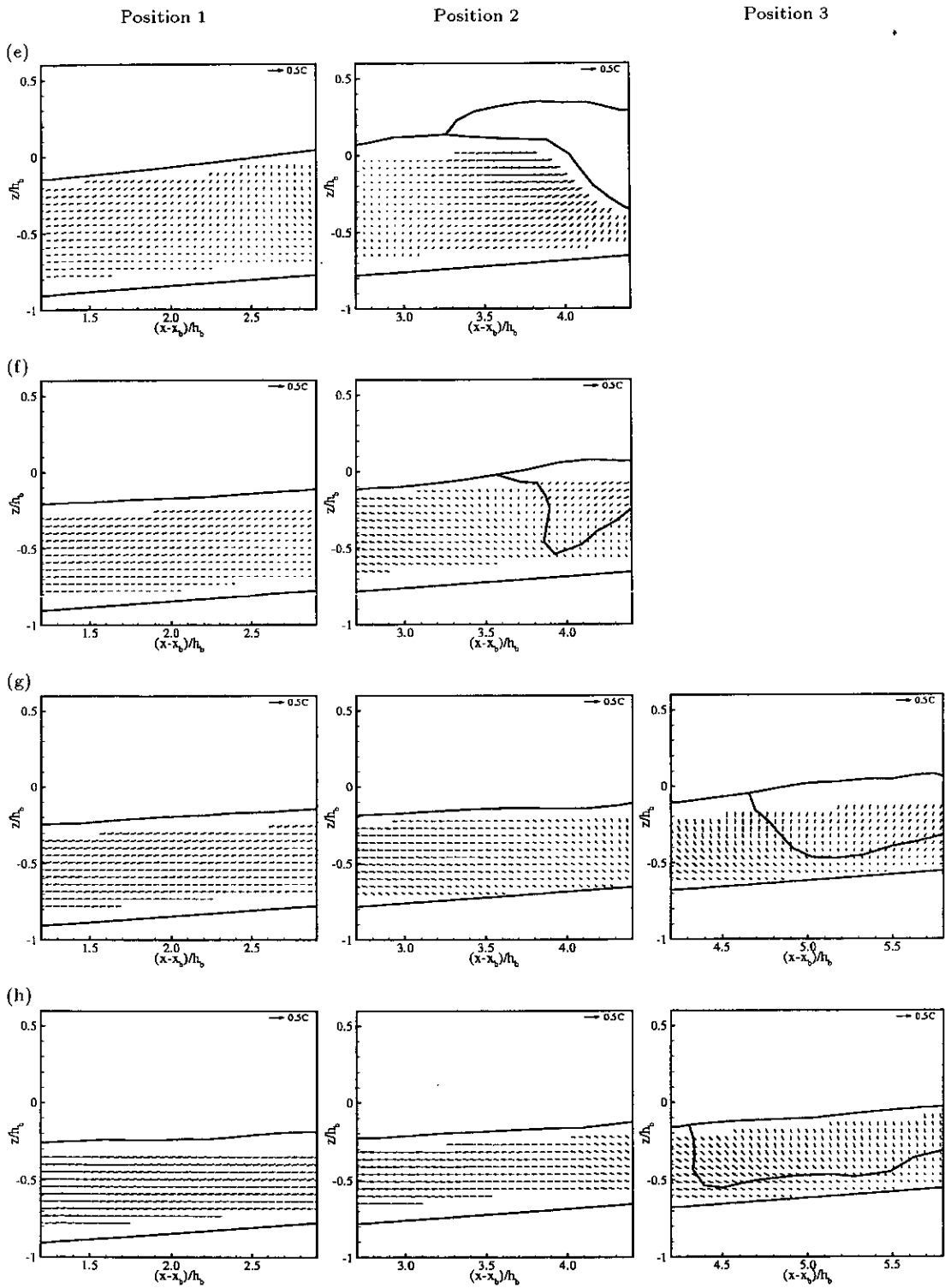


Figure 7.19: Mean velocity of the spilling breaker, continued from figure 7.18, at $(t - t_b)/T =$ (e) 0.5625, (f) 0.6875, (g) 0.8125 and (h) 0.9375.

action between the backwash and the incoming wave front can be seen under the trough in position 1 of figure 7.18(b) and under the surface roller in position 2 of figure 7.18(c) and (d). The maximum horizontal velocity around the crest region in position 1 of figure 7.18(c) is only around 50 cm/s which is roughly $0.41C$.

In figure 7.18(d) the surface bore was developed which nearly reaches the beach surface. Data in the region of high concentration of air bubbles is excluded as indicated in position 2. However, some bubbles that spread out backwards were included in the image for the PIV analysis. The small area containing these bubbles can be seen with the stronger forward movement ($\approx 0.33C$) compared to the neighbouring vectors. This high-concentration aerated region then propagates shoreward with the surface bore into position 3 which has to be excluded, in figure 7.18(d), 7.19(e) and (f), because the image analysis could not be made there. Once the bubble size became smaller in the subsequent phases, an attempt was then made to measure the velocity. This can be seen in position 3 of figure 7.19(g) and (h).

The flow begins to reverse at $(t - t_b)/T = 0.4375$ (figure 7.18(d)). In figure 7.19(f), although the main flow is now moving backward, the region which contains the air bubbles in position 2 seems to be moving forward as well as upwards to the free surface. This effect can also be seen in the next two phases where the large area of the air bubbles is in position 3. This result is similar to that found in the previous experiments. The upward and forward motion within the aerated region is due to the dynamics of the rising buoyant bubbles.

As mentioned earlier, the air bubbles still remain in the flow even until after the next wave has broken (see figure 7.18(a)). This result is different from what was found in the previous experiments where the air bubbles generated from the plunging breaker disappear before the next wave arrives.

7.3.2 Isovelocity Contours

To investigate the transition from potential flow to rotational flow under the spilling breaker, isovelocity contours were plotted at 4 phases and are shown in figure 7.20. In the contours, the solid lines represent the horizontal mean velocity components $\langle u \rangle$ and the dashed lines represent the vertical mean velocity components $\langle w \rangle$.

Figure 7.20(a) is when the backwash dominates the measurement region and the new wave has already broken outside it. The flow pattern in the backwash, especially in position 2 and 3, is rotational as the contour lines between different velocity components are not perpendicular. This is perhaps caused by the rotational flow due to the residual vortices and turbulence that are left from the previous breaking wave. This result agrees with that obtained from the vorticity and turbulent intensity plots which will be shown in the next sections. In position 1 it can be seen that there is a region where the flow is potential. This is the region where the flow starts to reverse and move forward due to the new incoming wave front.

In figure 7.20(b), although the overturning jet has impacted the frontal trough in position 1, the flow beneath it is potential. Most of position 2 and the whole of position 3 do not contain any orthogonal pattern of isolines which then suggests that rotational flow still remains within those regions. In the next phase, figure 7.20(c), the distribution pattern of the isovelocity contours implies that the flow in position 1 is irrotational but not in the area beneath the surface roller in positions 2 and 3. The local water depth in positions 2 and 3 at this phase is small so that the interaction between the backwash, the surface roller and the bottom boundary layer could have caused the rotational flow.

Once the wave crest has passed position 1 the rotational flow begins to form

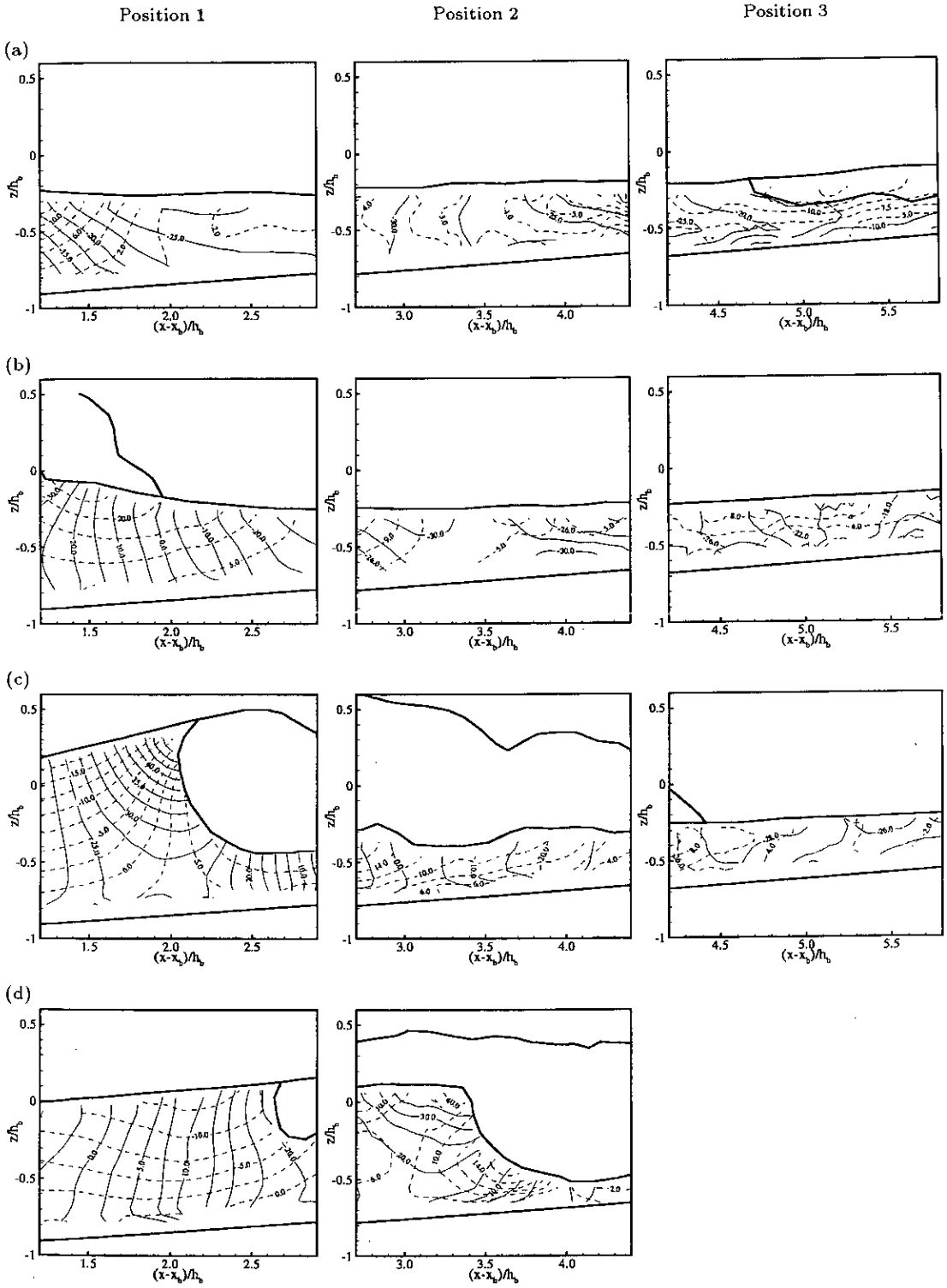


Figure 7.20: IsovLOCITY contours of the spilling breaker at $(t - t_b)/T =$ (a) 0.0625, (b) 0.1875, (c) 0.3125 and (d) 0.4375. The solid lines represent $\langle u \rangle$ and the dashed lines represent $\langle w \rangle$.

(see figure 7.20(d)) because the isolines start to deviate from the perpendicular pattern. The rotational flow is obvious in position 2. This is because of the complex dynamics of the air bubbles and turbulence generated from the surface roller.

7.3.3 Vorticity

The contour plots of mean vorticity within one wave period of the spilling breaker are displayed in figures 7.21 and 7.22. Similar to the vorticity contours of the previous experiments, the vorticity in these plots is normalised by $(C/h)_b$ and the contours of negative vorticity appear in the blue-coloured region while those of the positive one appear in the red-coloured region.

In figure 7.21(a) there are distinct negative vortices which mostly locate in position 3. The maximum value of these vortices is -4 s^{-1} which is approximately $-0.34(C/h)_b$. There is no significant vorticity in position 1 compared to the others. These results support the isovelocity contour plots in the previous section showing that the flow in position 2 and 3 at this phase is rotational. The negative vortices in position 3 are those generated from the previous spilling breaker and left behind even until now when the new wave has already broken.

In figure 7.21(b) the new spilling breaker front with the overturning jet has arrived in position 1. There is negative vorticity beneath the roller with a maximum value of -4 s^{-1} . The negative vorticity seems to be advected from position 3 into position 2 due to the backwash. The maximum value of the vorticity there is found to be -4.9 s^{-1} ($\approx -0.42(C/h)_b$) which is of the same order of magnitude as that beneath the surface roller. This shows that although the new spilling breaker has already arrived, the vorticity generated from the previous breaker is still “active” and not dissipated until the new surface roller takes place. This can be seen in figure 7.21(c) when there is no vorticity, of the same scale as in the

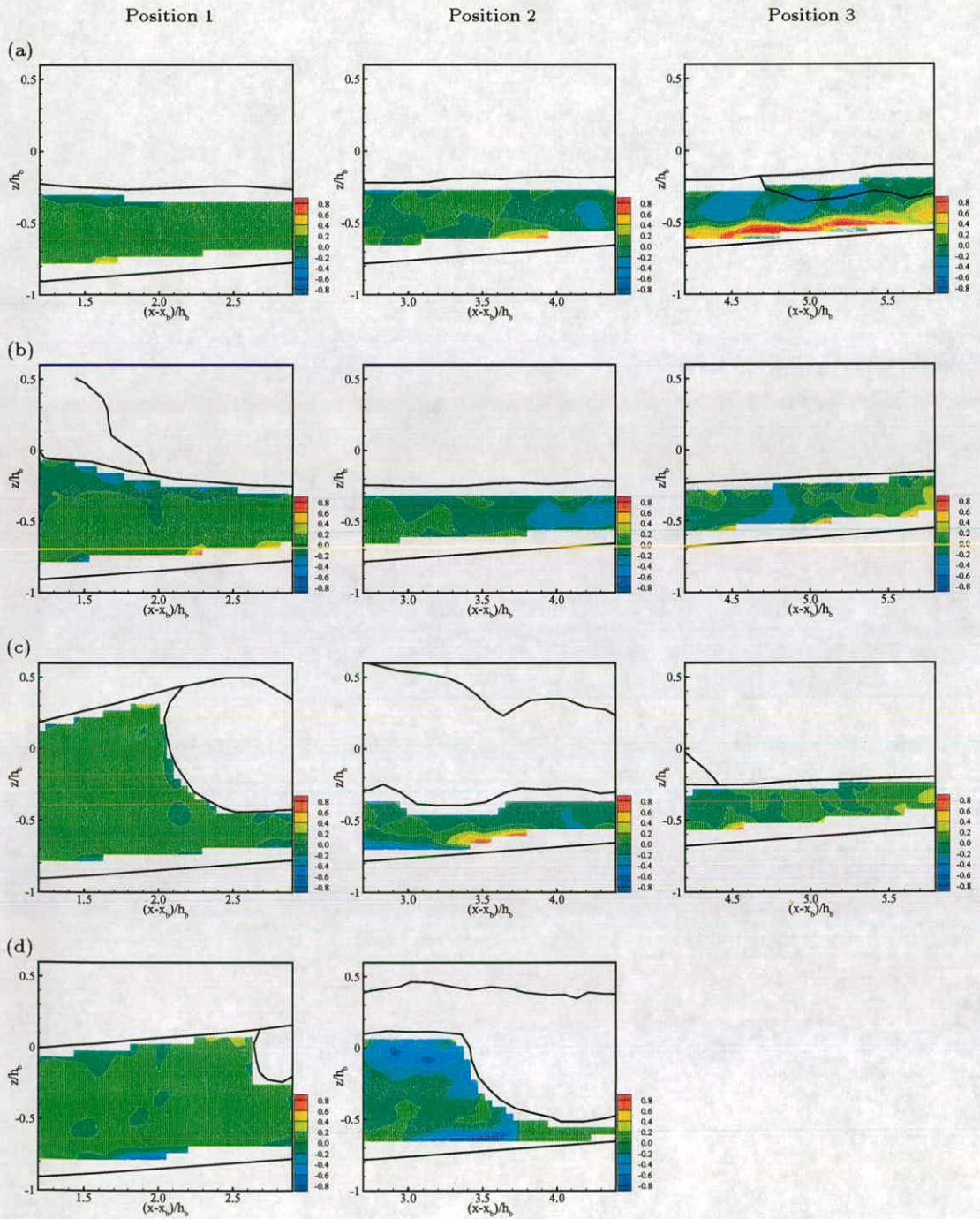


Figure 7.21: Mean vorticity of the spilling breaker at $(t - t_b)/T =$ (a) 0.0625, (b) 0.1875, (c) 0.3125 and (d) 0.4375.

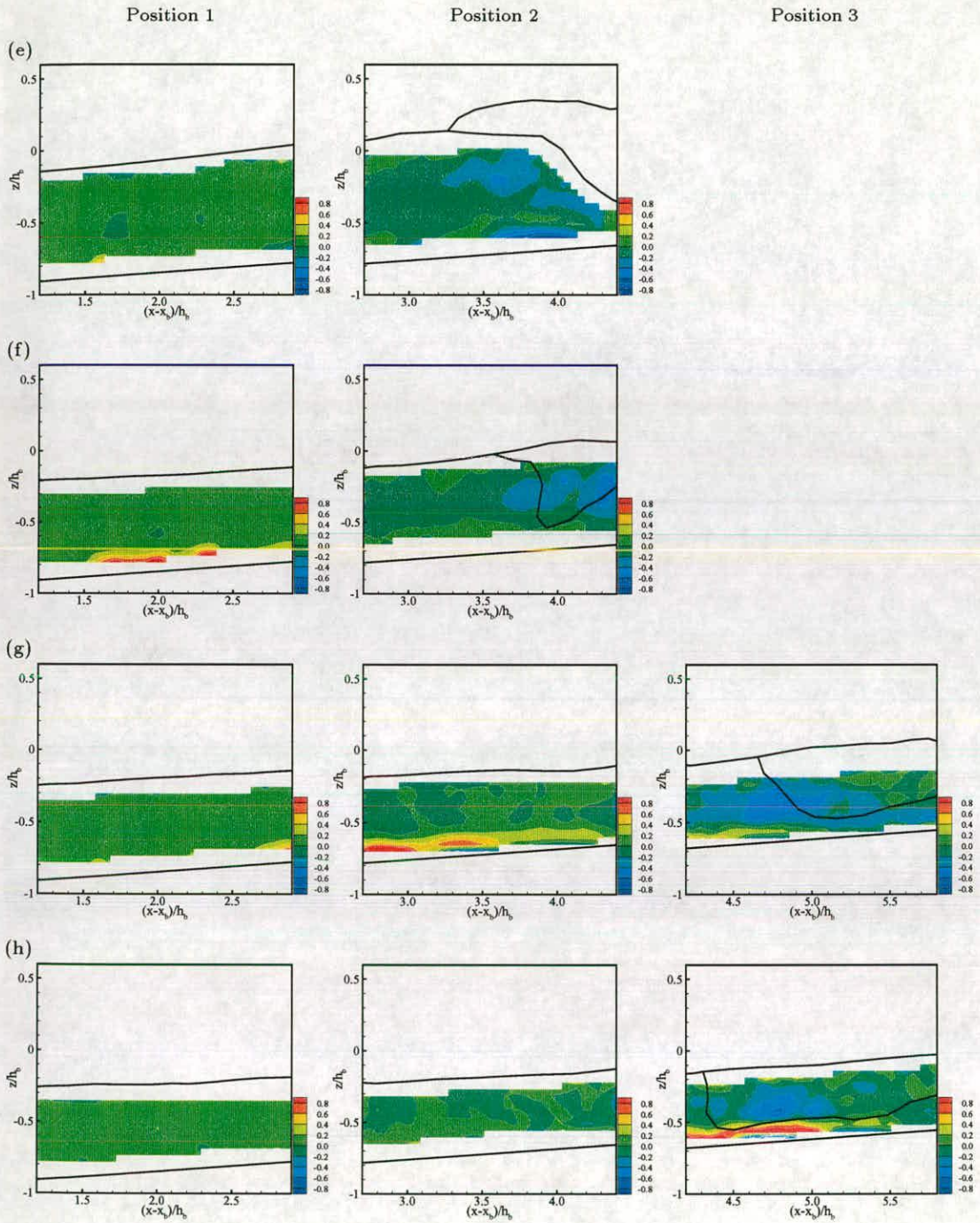


Figure 7.22: Mean vorticity of the spilling breaker, continued from figure 7.21, at $(t - t_b)/T =$ (e) 0.5625, (f) 0.6875, (g) 0.8125 and (h) 0.9375.

previous phase, left in the main flow in positions 2 and 3.

In position 1 of both figure 7.21(b) and (c) the interior domain of the flow contains no significant vorticity. This, then again, supports the result found in the previous section that the flow there is potential. The exception to this is, of course, within the region around the crest and the surface roller where positive and negative vortices are generated, respectively. The maximum value of the negative vorticity in position 1 of figure 7.21(c) is -5.3 s^{-1} ($\approx -0.45(C/h)_b$) which is not as large as that found around the overturning jet of the plunging breaker ($-(C/h)_b$; see section 7.2.3). This is perhaps due to the fact that the measurement region for the spilling breaker experiments does not cover the breaking position. The greater magnitude of the vorticity around the overturning jet of the plunging breaker was measured at the position close to the breaking point and at a very short time after breaking.

Moving on to the next phase, figure 7.21(d), when the surface bore is developed and nearly reaches the beach surface, the negative vorticity can be seen in position 2. The maximum value of this vorticity is -8s^{-1} ($\approx -0.69(C/h)_b$). This vorticity is thought to be part of the plunger vortex that is generated from the overturning jet, suggested from its rotational direction. The magnitude of this plunger vortex then becomes smaller as the wave progresses: the maximum values are approximately $-0.5(C/h)_b$ and $-0.34(C/h)_b$ in position 2 of figure 7.22(e) and (f), respectively.

Comparing the measured vorticity in this experiment with that in the previous experiment, it is found that the magnitude of the vorticity generated from the plunging breaker is greater than that generated from the spilling breaker. This supports the theoretical expectation as reviewed in section 2.4.

Once the size of the air bubbles become smaller and the analysis could be

made within the aerated region, more negative vortices are revealed in position 3 as seen in figure 7.22(g) and (h). These vortices are thought to be the new plunger vortices that are generated from the subsequent jet-splash motion, although this motion is not clearly observed from the raw PIV images. The maximum values of these vortices are approximately $-0.6(C/h)_b$ and $-0.69(C/h)_b$ in figure 7.22(g) and (h), respectively. These vortices then become weaker but still remain in the main flow until the surface roller of the new spilling breaker has arrived (see figure 7.21(a) and (b)), as already mentioned above.

7.3.4 Turbulent Intensity

A sequence of turbulent intensity contour plots within one wave cycle of the spilling breaker is shown in figures 7.23 and 7.24. The turbulent intensity is normalised by C and the greater values appear towards the red-coloured region.

Figure 7.23(a) shows the spatial distribution of the turbulent intensity at $(t - t_b)/T = 0.0625$, after the new wave has broken. The measurement positions are, however, dominated by the backwash. The turbulence generated from the previous wave still appears. The maximum values are found to be 11.6 cm/s ($\approx 0.09C$) and 13.3 cm/s ($\approx 0.11C$) in position 2 and 3, respectively. The intensity does not decrease much even when the new breaker has arrived into the measurement region in the next phase.

In position 1 of figure 7.23(b) the overturning jet has impacted the frontal trough and turbulence with the maximum intensity of around $0.08C$ is generated beneath it. The turbulence gradually decreases its intensity towards the bottom. The same order of magnitude of the turbulence generated from the previous breaker is also measured in positions 2 and 3.

As the wave propagates forward (figure 7.23(c)), the surface roller appears, mostly in positions 1 and 2, and the high intensity of turbulence is generated

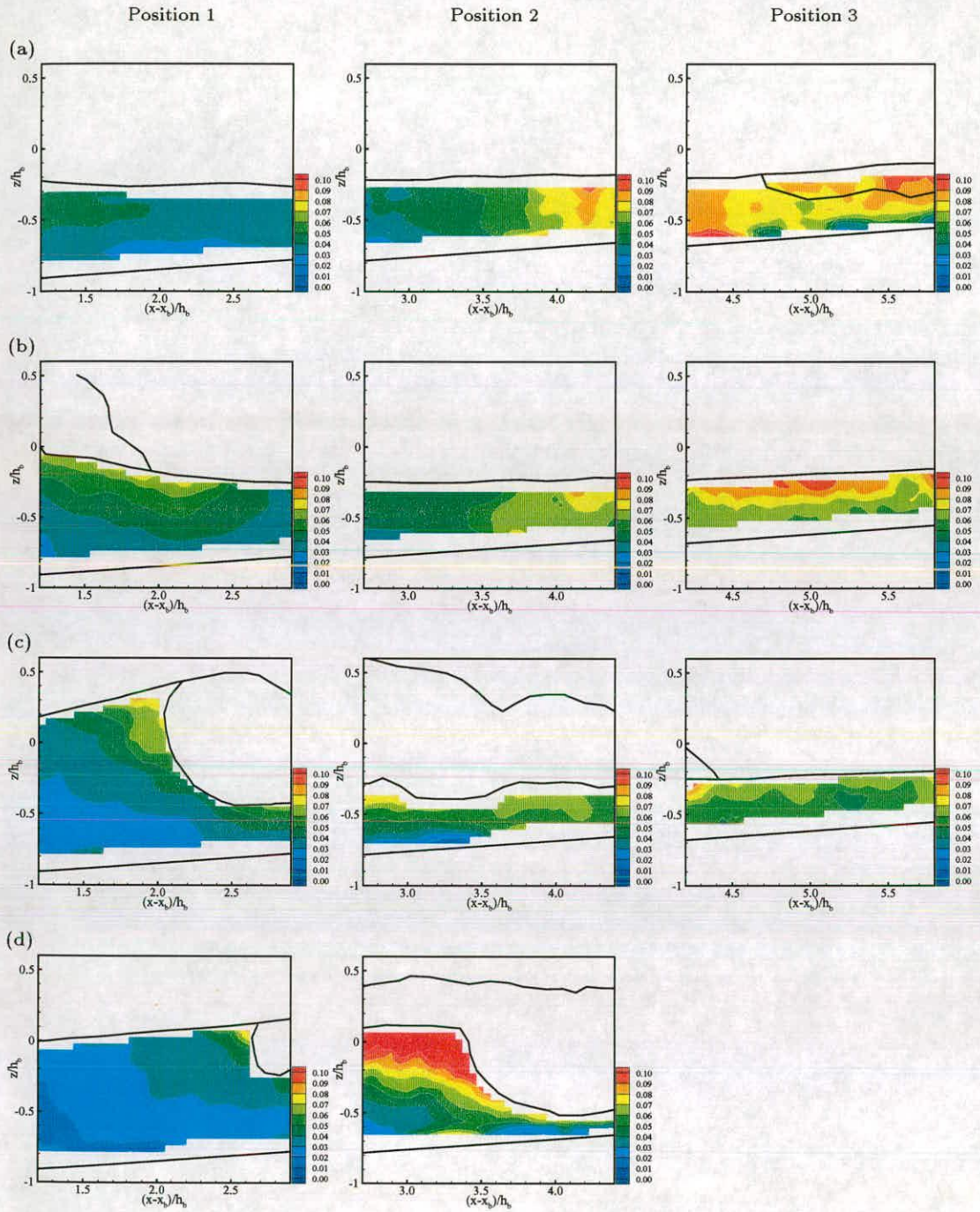


Figure 7.23: Turbulent intensity of the spilling breaker at $(t-t_b)/T =$ (a) 0.0625, (b) 0.1875, (c) 0.3125 and (d) 0.4375.

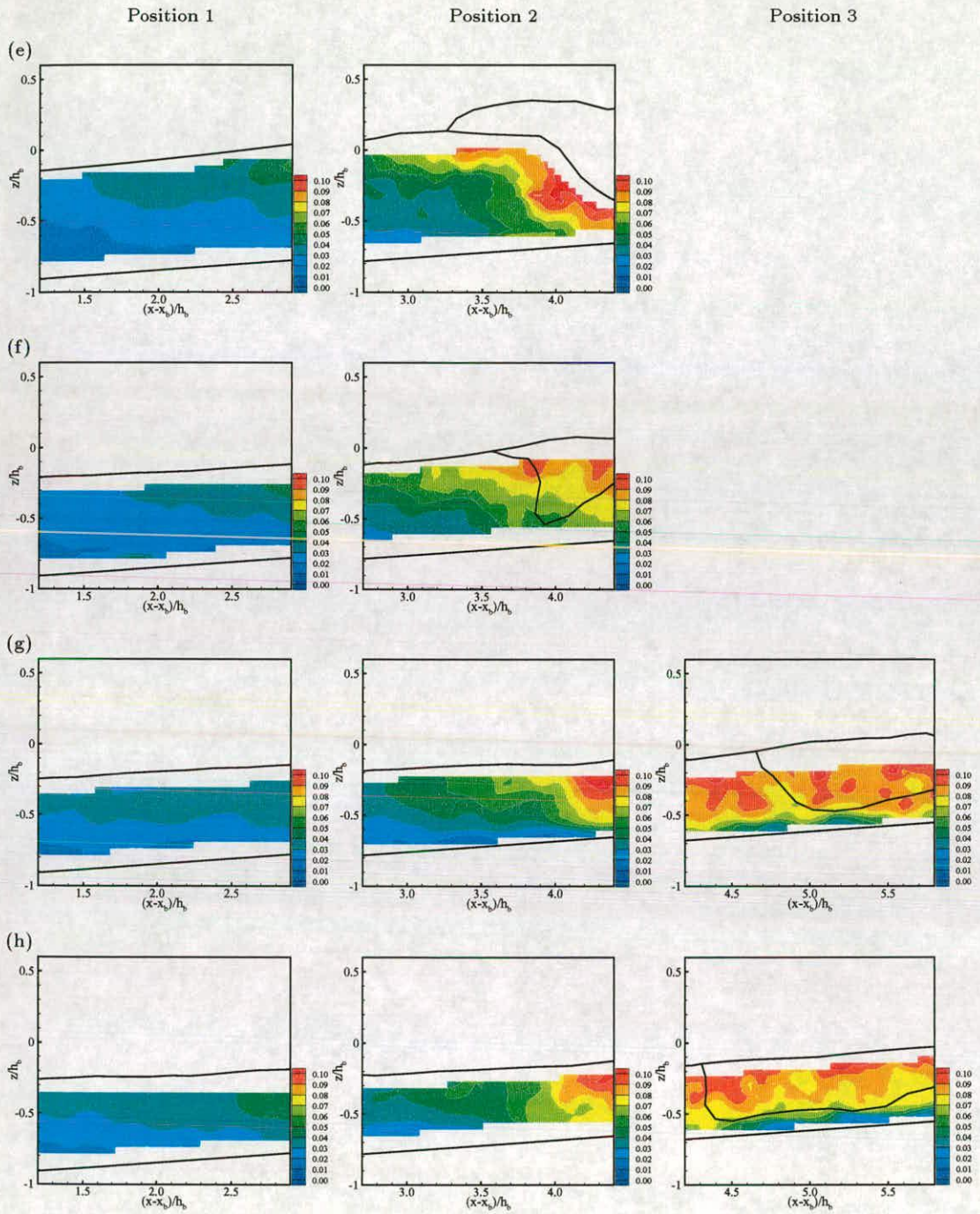


Figure 7.24: Turbulent intensity of the spilling breaker, continued from figure 7.23, at $(t - t_b)/T =$ (e) 0.5625, (f) 0.6875, (g) 0.8125 and (h) 0.9375.

around it. The maximum intensity at this phase is approximately $0.09C$ which is generated around the crest region behind the roller (in position 1) and approximately $0.08C$ beneath the roller (in position 2). The pattern of the turbulent intensity distribution of the spilling breaker is found to be similar to that of the plunging breaker. That is, the highest intensity appears around the overturning jet and the surface roller which gradually decreases in the deeper region towards the bottom and also decreases towards the lee side of the wave.

In the next phase, figure 7.23(d), the maximum value of turbulent intensity in position 1 is still the same order of magnitude as in the previous phase ($\approx 0.09C$) but the value decreases more rapidly towards the bottom and the lee side of the wave. In position 2 the maximum value increases up to 19.2 cm/s ($\approx 0.16C$). Most of the high intensity turbulence seems to be located in the air bubble region where an attempt was made to measure the velocity. The result at this phase is comparable to figure 7.8(c) of the plunging breaker when the air bubbles are also generated and spread down to nearly touch the bottom. However, the maximum value of the turbulence intensity generated from the plunging breaker is greater than that of the spilling breaker.

The high turbulent intensity region in position 2 of figure 7.23(d) then gradually decreases its maximum value as the wave progress: $\approx 0.11C$ and $0.09C$ in figure 7.24(e) and (f), respectively. In position 2 of figure 7.24(e) the high intensity region spreads downward and reaches the bottom. It is suggested that this is due to the spreading of the air bubbles as one can see that the high turbulent intensity mostly occurs around the indicated aerated region. Then in figure 7.24(f) the high intensity region seems to appear at the free surface when the air bubbles are rising upwards.

After the turbulent intensity in position 2 has decreased, its maximum value

then rises up again in the next phase (figure 7.24(g)) when the main flow is now moving offshore. This effect was observed before in the weak plunging breaker when it was suggested that the advection plays a major role in the increasing level of the turbulence in position 2.

The turbulent intensity can now be measured in position 3 at the last two phases of the sequence (figures 7.24(g) and (h)). The maximum values of the turbulent intensity at these phases are $\approx 0.10C$ and $0.11C$ respectively. The high intensity areas spread down to the bottom in figure 7.24(g) and then appear at the mid-depth in figure 7.24(h). Again, the rising buoyant bubbles are thought to affect the turbulence transport. The generated turbulence remains in the main flow and does not dissipate until the new surface roller has arrived and generates new turbulence. Therefore, the interaction of the turbulence generated between breakers may occur as suggested by Svendsen [72] (see section 2.5).

7.3.5 Turbulence Transport Mechanisms

The investigation of turbulence transport mechanisms in the spilling breaker is carried out in the same way as for the previous two waves (in sections 6.2.5 and 7.2.5). Figure 7.25 shows the velocity vector map indicating the locations of 5 control volumes selected for the investigation. Five sets of graphs (corresponding to five areas) are displayed and discussed in the following. The selected areas are:

- Area I : upper region onshore from the breaking point (results in figure 7.26)
- Area II : lower region onshore from the breaking point (results in figure 7.27)
- Area III : lower region in the transition zone (results in figure 7.28)
- Area IV : lower region in the inner surf-zone (results in figure 7.29)
- Area V : lower region further in the inner surf-zone (results in figure 7.30).

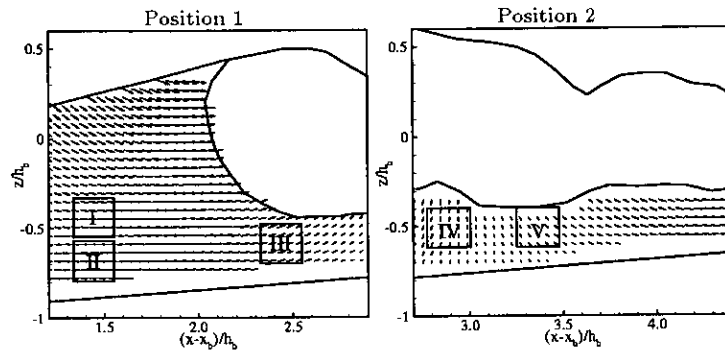


Figure 7.25: The control volumes for the spilling breaker in which the mean value of each term in the k -equation is calculated.

Discussions on Turbulence Transport in the Spilling Breaker

The first investigating location is at about 14 cm onshore from the breaking point (figures 7.26 and 7.27). Turbulent kinetic energy and its transport mechanisms are as strong as those in the weak plunging breaker investigated at the same location. Consider each transport terms; it is found that the mechanisms that drive the turbulence transport in the spilling breaker are very much similar to those found in the same location for the weak plunging breaker. The passage of the wave, turbulent kinetic energy and turbulence production are correlated. This correlation is also observed in the lower region as found in the weak plunging breaker. In the upper region (figure 7.26) the production is the main mechanism for an increase in k during the beginning of the wave period while advection acts to reduce it. After the passage of the wave front, no significant transport terms is found. This is why a small variation of $\partial k/\partial t$ is shown.

In the lower region (figure 7.27) the diffusive transport is more dominant which, again, suggests that turbulence can penetrate into the bottom region. The production is also responsible for the high value of k and the positive rate of change of k , however, its strength is smaller than in the upper region. These mechanisms are also found in the lower region of the same location for the weak

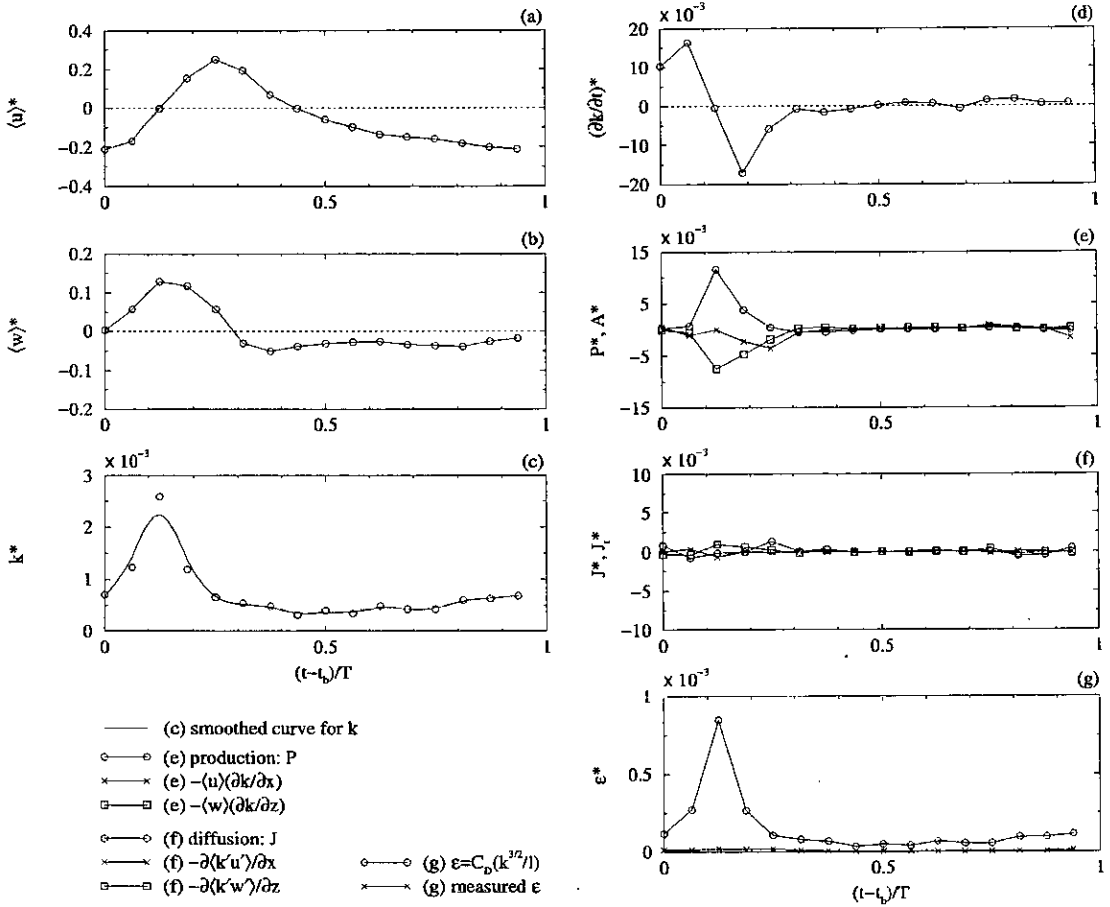


Figure 7.26: Mean velocities (a & b), turbulent kinetic energy (c) and turbulent transport terms (d – g) for k in equation (5.13), of the spilling breaker, calculated in the area $1.341 \leq (x - x_b)/h_b \leq 1.531$ and $-0.540 \leq z/h_b \leq -0.350$ (area I of figure 7.25). The symbol * indicates normalised quantities: $\langle u \rangle$ and $\langle w \rangle$ are normalised by C , k by C^2 and all of the transport terms by C^2/T .

plunging breaker (see figure 7.14).

With the same reason as given in section 7.2.5 only one vertical level is investigated in the transition zone and the inner surf-zone. In the transition zone of the spilling breaker (figure 7.28) it can be seen that the turbulence transport mechanisms are much similar to those in the upstream location (figure 7.26). The turbulence production is, again, a dominant feature for the increased rate of change of turbulent kinetic energy, while the advection is responsible for the

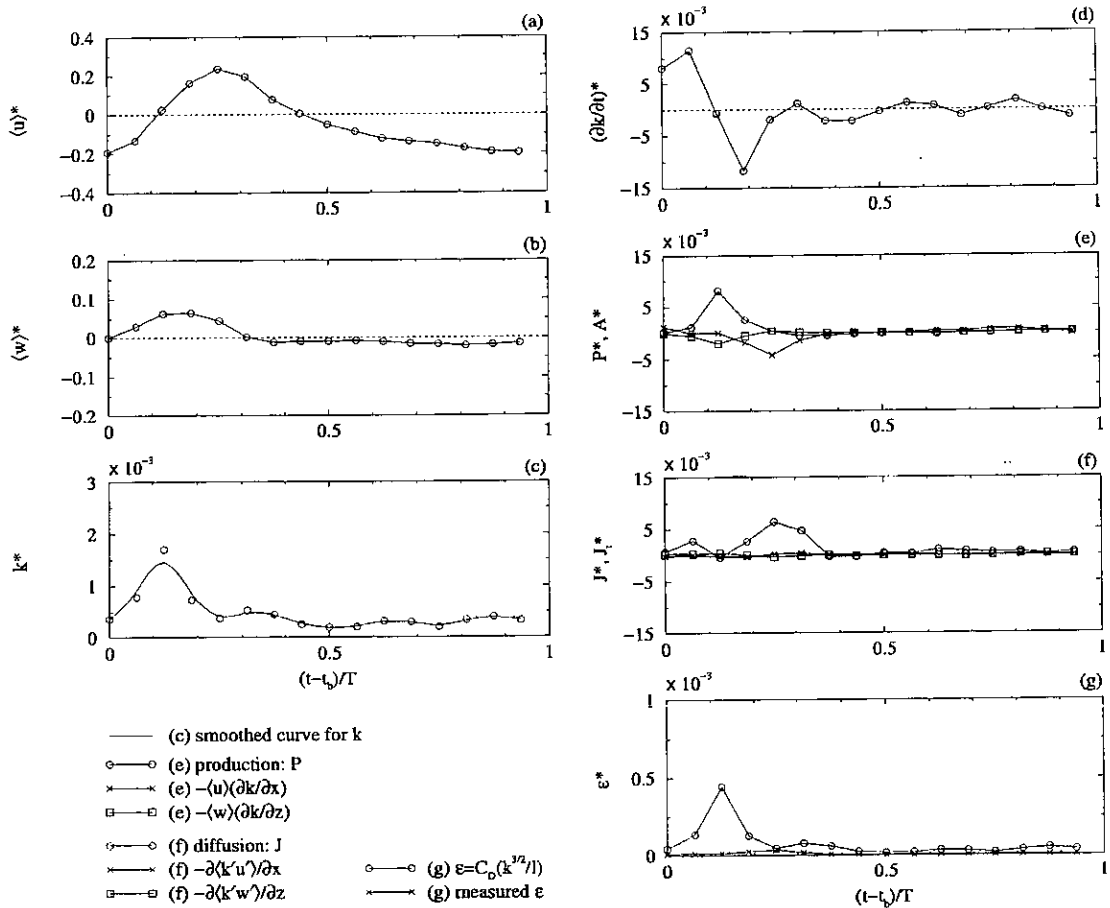


Figure 7.27: Similar to figure 7.26 but in the area $1.341 \leq (x - x_b)/h_b \leq 1.531$ and $-0.778 \leq z/h_b \leq -0.588$ (area II of figure 7.25).

decrease of $\partial k / \partial t$. After the passing of the wave front, none of the turbulence transport terms are significant, leaving a low value of k and a small variation of its time rate of change in the investigating region. The similarity of the wave patterns and turbulence transport mechanisms at different zones suggests a so-called quasi-steady state of the spilling breaker. Ting & Kirby [80] and Lin & Liu [46] also observed the similar turbulence transport processes and the similar flow characteristics between different surf-zone locations for the spilling breaker. This can be seen from the results of the present study (from figures 7.26 to 7.30) that the forms of variation of the mean velocity components, k and its time rate

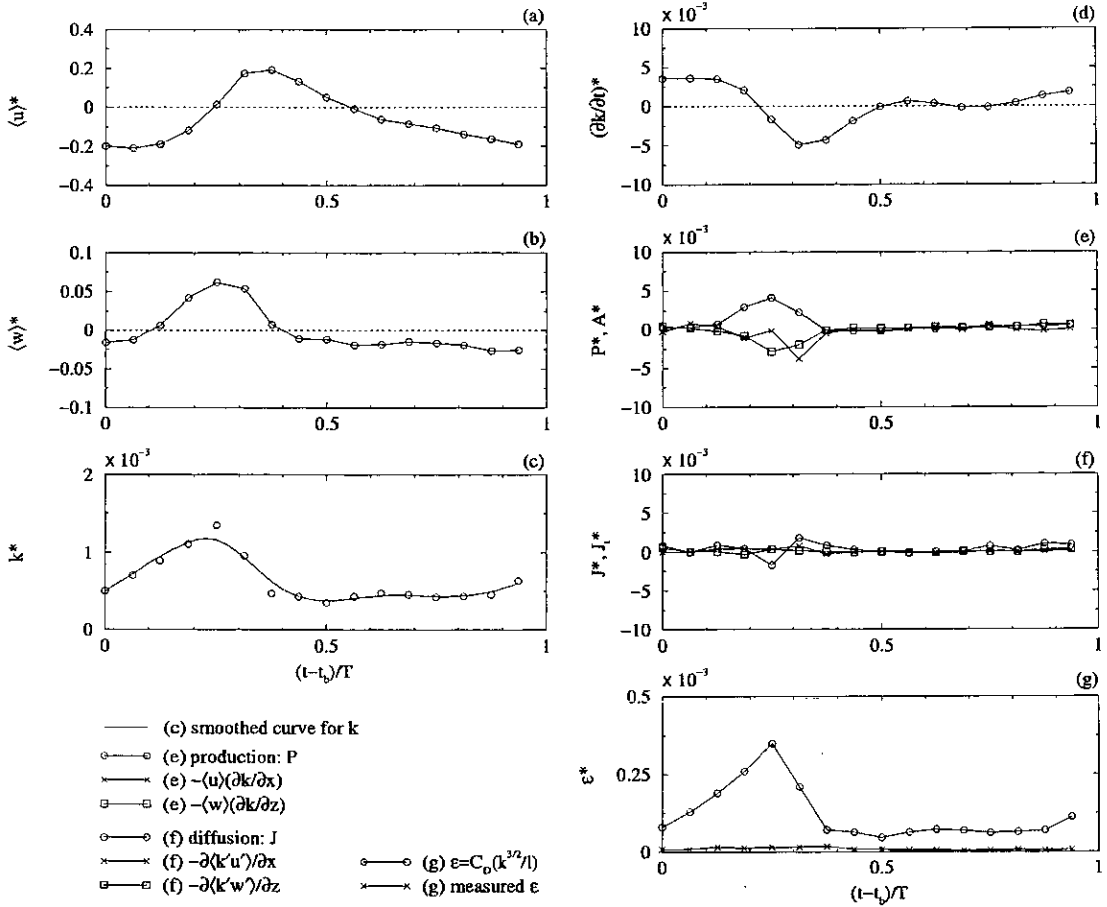


Figure 7.28: Similar to figure 7.26 but in the area $2.339 \leq (x - x_b)/h_b \leq 2.530$ and $-0.683 \leq z/h_b \leq -0.492$ (area III of figure 7.25).

of change are the same throughout the surf-zone region. The only differences are their magnitudes and the phase at which their peaks occur.

Moving into the inner surf-zone (figure 7.29), the production is still active but not as strong as the vertical advection. This result is also found in Ting & Kirby [80] who suggested that the fluctuations in $\partial k / \partial t$ are produced by convection of turbulence structure past the LDA probe (or past the investigating region in this case) as turbulent kinetic energy spreads downward. At the same time when vertical advection occurs, the diffusion also contributes to change the turbulent kinetic energy. The vertical advection acts to reduce the energy while

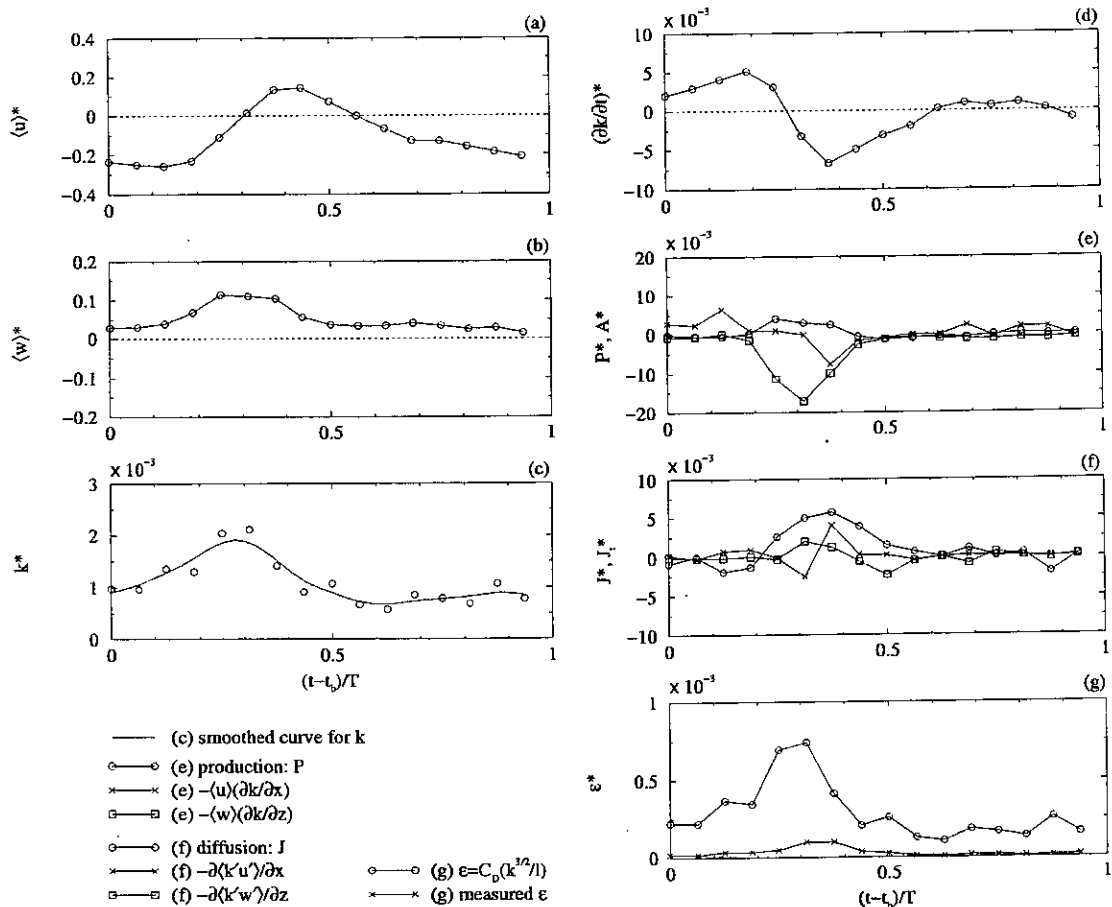


Figure 7.29: Similar to figure 7.26 but in the area $2.800 \leq (x - x_b)/h_b \leq 2.989$ and $-0.603 \leq z/h_b \leq -0.413$ (area IV of figure 7.25).

the diffusion acts to increase it.

Similar turbulence transport processes to the above are also found in the last investigating location which is further into the inner surf-zone (figure 7.30). The transport mechanisms are, however, stronger than in the previous location. This, again, supports the knowledge that the spilling breaker is a quasi-steady wave. It can be seen that the production and diffusion are responsible for the increased rate of change of k , while at the same duration of time, within one wave cycle, the vertical advection is responsible for the decrease. It should be noted that the similarity of the transport processes at different locations in the surf zone is not

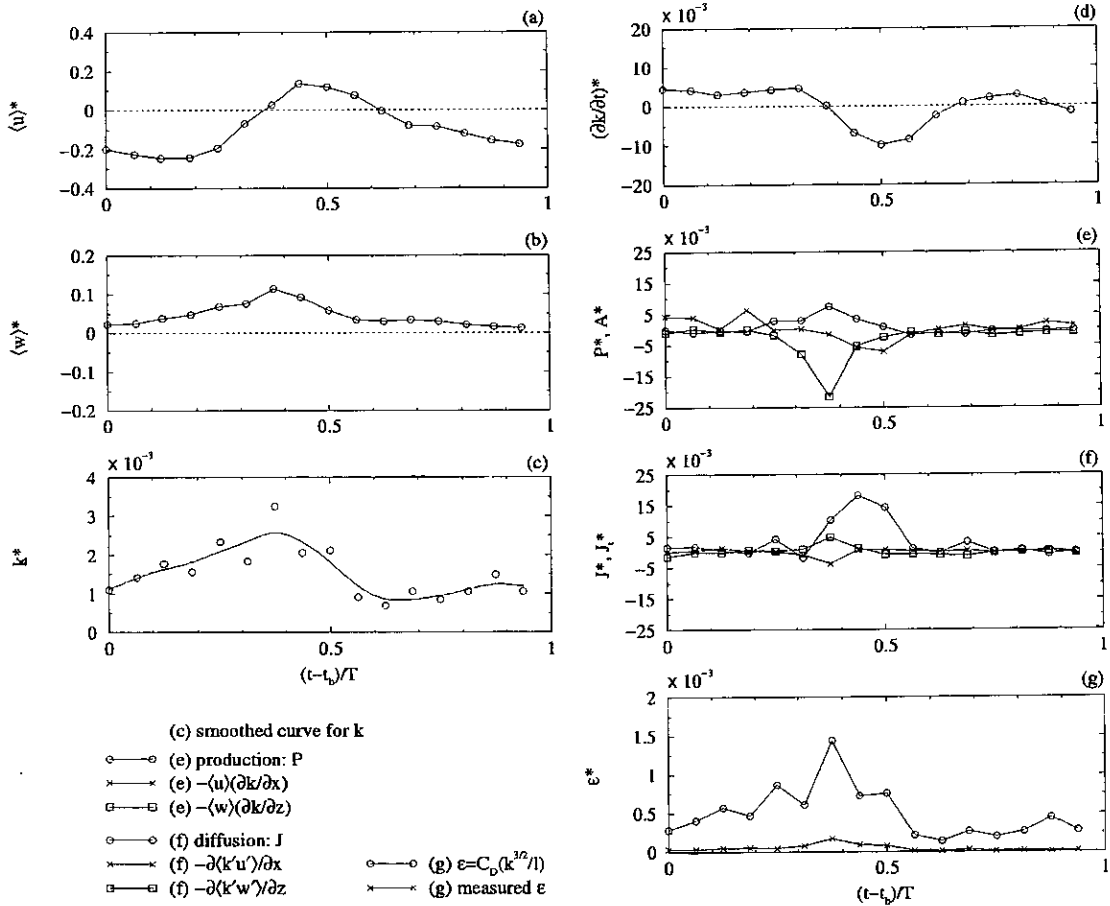


Figure 7.30: Similar to figure 7.26 but in the area $3.275 \leq (x - x_b)/h_b \leq 3.465$ and $-0.603 \leq z/h_b \leq -0.413$ (area V of figure 7.25).

found for the weak plunging breaker.

7.4 Summary of Chapter 7

This chapter described the experiments on the trains of surf-zone breaking waves carried out at ISVA. Two breaking-wave types were studied: weak plunging breakers and spilling breakers. At the beginning of the chapter the PIV set-up and measurement procedure were explained along with the problems that occurred during the experiments. As also found in the single breaker experiments performed at UEDIN, breaking-wave generated air bubbles were the main problems

for the current PIV technique. Velocities could not be measured within the aerated region limiting the knowledge of turbulence generation and transport mechanisms. Another problem stemmed from the non-periodicity between successive waves. This could give errors to the mean and turbulent quantities when calculating with the phase-averaging method.

After the experimental description was given, the results were then displayed and discussed. The form of result presentation used in this chapter was the same as that used in the previous chapter. For each type of wave, the series of maps of phase-averaged velocity, isovelocity contours, mean vorticity and turbulent intensity were shown. Turbulence transport investigation was also made for both weak plunging and spilling breakers, using the same method as for the single breaker discussed in the previous chapter.

For the weak plunging breaker, strong generated air bubbles were observed which at some phases could reach the bottom. The velocity vector plots revealed the difference between flow kinematics inside and outside the aerated region. The effect of the rising buoyant bubbles was found. The isovelocity contours not only showed the transition from potential flow to rotational flow but also indicated the residual vortices and turbulence generated from the previous breaker. This effect was not found in the single plunging breaker. The vorticity contour maps gave a supporting knowledge that vortices were mainly generated from the overturning jet. The dynamics of the air bubbles affected that of the vortices. Finally, the spatial distribution of the turbulent intensity suggested that strong turbulence is generated in the overturning jet and the surface roller. The air bubbles also play a major part for the spread of turbulence towards the bottom.

Turbulence transport mechanisms at different locations within the surf zone for the weak plunging breaker are different. At every location, however, there

existed a correlation between the passage of the wave, turbulent kinetic energy and turbulence production. The increase in turbulent kinetic energy was found in the location around the breaking point. The main mechanism to this effect was suggested to be the horizontal advection. This result was also found in the single plunging breaker although the increase in k appeared long after the wave broke. Just onshore from the breaking point, the production is the main mechanism for an increase in k in the upper region where the diffusion is important in the lower region. In the transition zone, the production and horizontal advection are dominant. Diffusive transport is more effective in this zone. The stronger transport mechanisms, especially the diffusion, were found in the inner surf-zone, even when the investigation was made close to the bottom. This suggested that for the plunging breaker, turbulence could penetrate into deeper region to the bottom.

For the spilling breaker, the similar effect due to the rising buoyant air bubbles was also found. The strength of vortices and turbulence generated from the spilling breaker were smaller than those generated from the plunging breaker. The isovelocity contours as well as vorticity and turbulent intensity maps showed the residual vortices and turbulence which were generated from the previous wave and their existence was found to be longer than in the plunging breaker. However, it might be due to the fact that the wave period of the spilling breaker was shorter than that of the plunging breaker. Also, the region where this effect occurred was further towards the inner surf-zone where no measurement was done for the weak plunging breaker. Although, the suggestion that the spilling-breaker generated turbulence which remains in the flow and does not dissipate until the new wave arrives agrees with some other researcher's work [80], it needs to be carefully considered in these experiments.

Another different mechanism between the plunging and spilling breakers was found from the turbulence transport investigation. However, there was a similarity of the transport mechanisms between the two different breaker types at the location just onshore from the breaking point. There the production and advection are dominant in the upper region while the diffusive transport is important in the lower region. The transport mechanisms in the spilling breaker did not change much when moving into the transition zone and into the inner surf-zone. The only differences were the strength of the mechanisms and the phase at which their peaks occurred. The strength of the production, advection (especially vertical advection) and diffusion is higher in the inner surf-zone than in the transition zone. The similarity in the turbulence transport processes as well as in the wave and turbulence characteristics at different surf-zone locations for the spilling breaker suggested the quasi-steady state of the wave. This effect was not found in the plunging breaker.

Chapter 8

Comparison with Numerical Results

This chapter shows the comparison between the experimental and numerical results. The comparison was only made with the results obtained from the single plunging breaker experiments, which were conducted at UEDIN (see chapter 6). An introduction is first given which shows features of this comparison that make it different from previous work. A brief description of the numerical model and input conditions for the model are then given. Finally, the comparisons are made and discussed.

8.1 Introduction

In the past, many attempts have been made to numerically simulate breaking waves and compare the results with experiments [46, 47, 68]. Of these studies, only a few have included comparisons between numerically predicted and measured flow fields, for example Skyner [68]. In that paper, Skyner used the PIV technique to measure the kinematics of a deep-water breaking wave and compared them with the numerical results from a Boundary-Integral Method. However, this comparison was not made after the wave had broken. Additionally, the experimental and numerical conditions were not completely matched. That is, the

geometry of the numerical and physical wave tanks were not the same and the motion of the numerical and physical wavemakers were not identical.

An attempt to numerically simulate surf-zone breakers, including after breaking, was made by Lin & Liu [46, 47]. They compared their numerical results with the measurements of Ting & Kirby [79, 80]. However, again, the numerical and experimental conditions were not matched, as explained above. Furthermore, no full-field flow comparisons were performed.

In this study the comparisons between numerically predicted and measured surf-zone single plunging breaker kinematics are performed under the following conditions:

1. Experimental and numerical conditions are matched exactly. That is, the geometry of the numerical and physical wave flumes are the same and the motion of the numerical and physical wavemakers are identical.
2. Full flow fields are compared.
3. The flow after breaking is compared.

The author believes that very few, if any, previous studies have satisfied two out of three of the above conditions and, to the author's knowledge, no previous studies have fulfilled all three.

8.2 Numerical Model

For the numerical investigation of surf-zone plunging breaker mechanics a numerical model has been developed by Dr. Erik Christensen, at DHI Water and Environment, Denmark. In the following, a brief description of the numerical model is given, based on Emarat *et al.* [21].

The objective of the numerical model is to find the solution of the general Navier-Stokes equations under specified conditions. The model used in this study is an improved version of the model described in Christensen [12]. In that model a *surface markers* method was used to determine the position of the free surface. Unfortunately, this does not conserve mass when the waves break. For this study Dr. Erik Christensen has implemented a Volume of Fluid (VOF) method, based on the model of Mayer *et al.* [48]. The model of Mayer *et al.* is a finite volume model for non-orthogonal multi-block grids. No turbulence model has been included in Dr. Christensen's (VOF) method.

At the left boundary of the domain for the numerical model the velocities found by another numerical model are specified as the input conditions. This is explained in the following subsection.

8.2.1 Input Conditions

The numerical model described above has the advantages that it solves the full Navier-Stokes equations and it can go beyond breaking. However, it is not easy to match the input conditions in this model to the input conditions in the experiments. That is, it is not easy to incorporate a wavemaker into this model. Consequently, a Boundary-Integral Method (BIM), developed at Edinburgh by Dr. David Forehand, was used to produce input conditions for the Navier-Stokes solver.

BIMs are numerical methods for modelling nonlinear free-surface potential flows. In brief, the BIM used here employs explicit second-order time-stepping together with cubic variation of the complex potential and a five-point numerical differentiation scheme. In addition, the BIM uses dynamic time-stepping as well as cubic spline smoothing and regriding of the free-surface. Wavemakers can be easily incorporated into BIMs but BIMs cannot go beyond breaking. In order

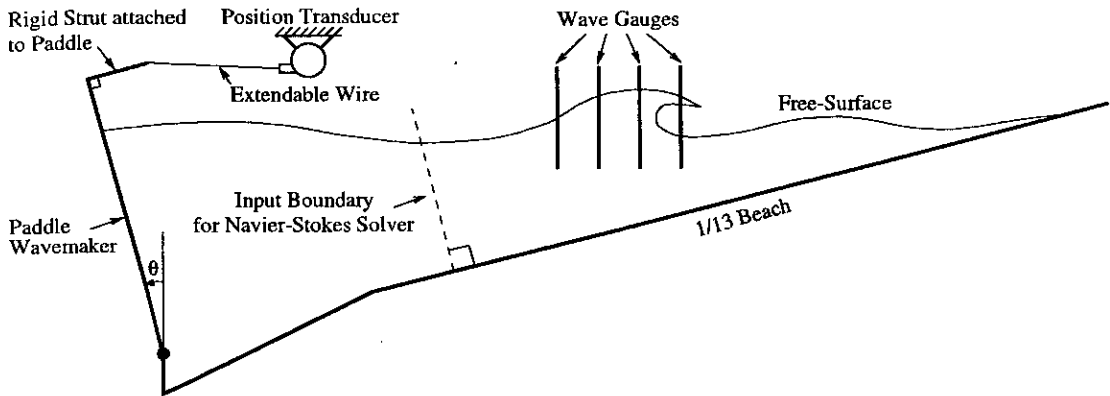


Figure 8.1: Experimental set-up to record wavemaker angle (θ) and free-surface elevation.

to overcome this problem, a small amount of smoothing was used to suppress breaking. A detailed explanation of this BIM, as well as others, can be seen in Forehand [25].

To reproduce the wavemaker motion in the BIM, a small experiment was set up (see figure 8.1). In the experiment, waves were generated by the paddle wavemaker under exactly the same condition as in the PIV experiments explained in Chapter 6. A position transducer was used to obtain the wavemaker angle as a function of time. The position transducer was a very accurate potentiometer whose output voltage was linearly dependent on the extension of the wire connecting it to the paddle. The output signal was sampled at 16 Hz by the wavemaker controller at the same time as the wave was being generated. After calibration, the extension of the wire could be obtained from the output voltage. Then a time series of the wavemaker angle could be calculated from that of the wire extension by using some trigonometry.

In Addition to recording the wavemaker angle, wave gauges were used to measure the free-surface elevation as a function of time at different positions down the wave flume. The free-surface elevation measurements provided a useful check on whether the BIM data could be used.

Once the exact motion of the paddle wavemaker as well as the exact geometry of the wave flume and beach were reproduced in the BIM, velocities could be calculated along a line perpendicular to the beach and near to the toe of the slope (the dashed line in figure 8.1). These velocities are the input conditions for the Navier-Stokes solver.

8.3 The Comparisons

8.3.1 Free-Surface Elevation

The first comparison to be made is that of the free-surface elevations. As mentioned before, this comparison is done in order to indicate whether the BIM can be used to produce good input conditions for the Navier-Stokes solver.

Figure 8.2 shows the free-surface elevations measured in the experiments and the free-surface elevations generated from the BIM and Navier-Stokes solver, at 5 positions along the flume. These positions correspond to $(x - x_b)/h_b = -5.26, -3.51, -1.75, 0$ and 1.75 . The horizontal axis of each graph indicates the time from the initiation of the wave paddle motion. The time when the free-surface elevation is highest corresponds to the time when the wave is focused (see chapter 4 for a detailed explanation of the generation of the single plunging breaker by a focused wave). Therefore, at $(x - x_b)/h_b = 0$, the time when the highest peak in the free-surface elevation appears is the time when the wave breaks.

It can be seen that there is excellent agreement between the measured and numerical free-surface elevations. The profiles of the numerical results agree well with that of the measured results except for a small time-lag, which is evident during the focusing of the wave, and which is most noticeable at the locations offshore of the breaking point. In addition, the maximum height of the free-surface is slightly overpredicted by the BIM and hence by the Navier-Stokes

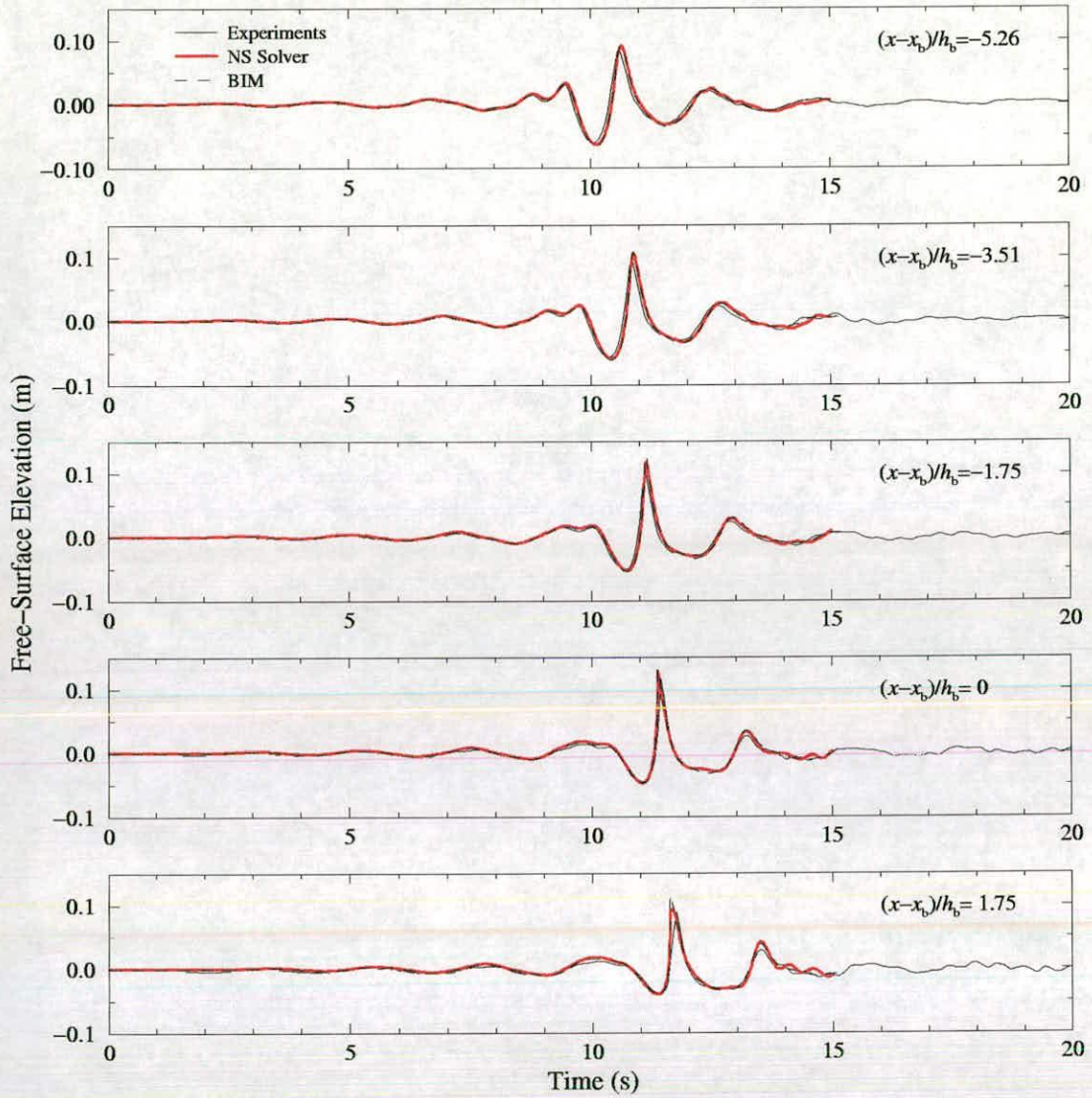


Figure 8.2: Free-surface elevations of the plunging breaker from the experiments, BIM and Navier-Stokes solver.

solver. However, in general, very good agreement can be seen at every location along the beach and throughout the breaking process, even at, and after, breaking. This leads to the conclusion that the BIM can be used to generate good input conditions for the Navier-Stokes solver.

8.3.2 Velocity Vector Maps

Because the Navier-Stokes equations are solved on a fixed grid, the calculated velocities are then generated on a grid similar to the PIV data. Therefore, this is ideal for making a comparison between the numerical and measured flow fields. A typical way of displaying a flow field is by plotting the spatial distribution of the velocity, in other words, a velocity vector map. In order to make an immediate comparison between the results from the two approaches, the PIV velocity vector map is plotted overlapping the numerical velocity vector map. These plots are shown in figures 8.3 and 8.4, where the numerical velocities are in black and the PIV velocities in red. The plots start from the time when the wave breaks, $(t - t_b)/T = 0$, to $(t - t_b)/T = 1.287$, with an interval of 0.184. The reference vector of each result, shown at the corner of each graph, is half of the crest speed measured at breaking (80 cm/s).

It should be pointed out here that the numerical velocity vectors are not calculated at exactly the same x & z positions as the PIV velocity vectors. This is due to the fact that the grid alignments are different. That is, in the computational domain of the numerical model the grid is tangential to and normal to the beach, whereas the PIV grid is horizontal and vertical. In addition, the numerical and PIV grid-spacings are not the same. However, the velocity vectors of both approaches are plotted with respect to the same x & z references.

Consider the first plot in figure 8.3, which is the velocity vector map at breaking. A good comparison can be seen. The trends of the numerical velocities are very much consistent with those of the PIV velocities. As mentioned in Chapter 6, the crest of the wave was not included in the measurement region, therefore comparison around the crest could not be made. The numerical results show that, at breaking ($(t - t_b)/T = 0$), the maximum horizontal velocity in the crest region

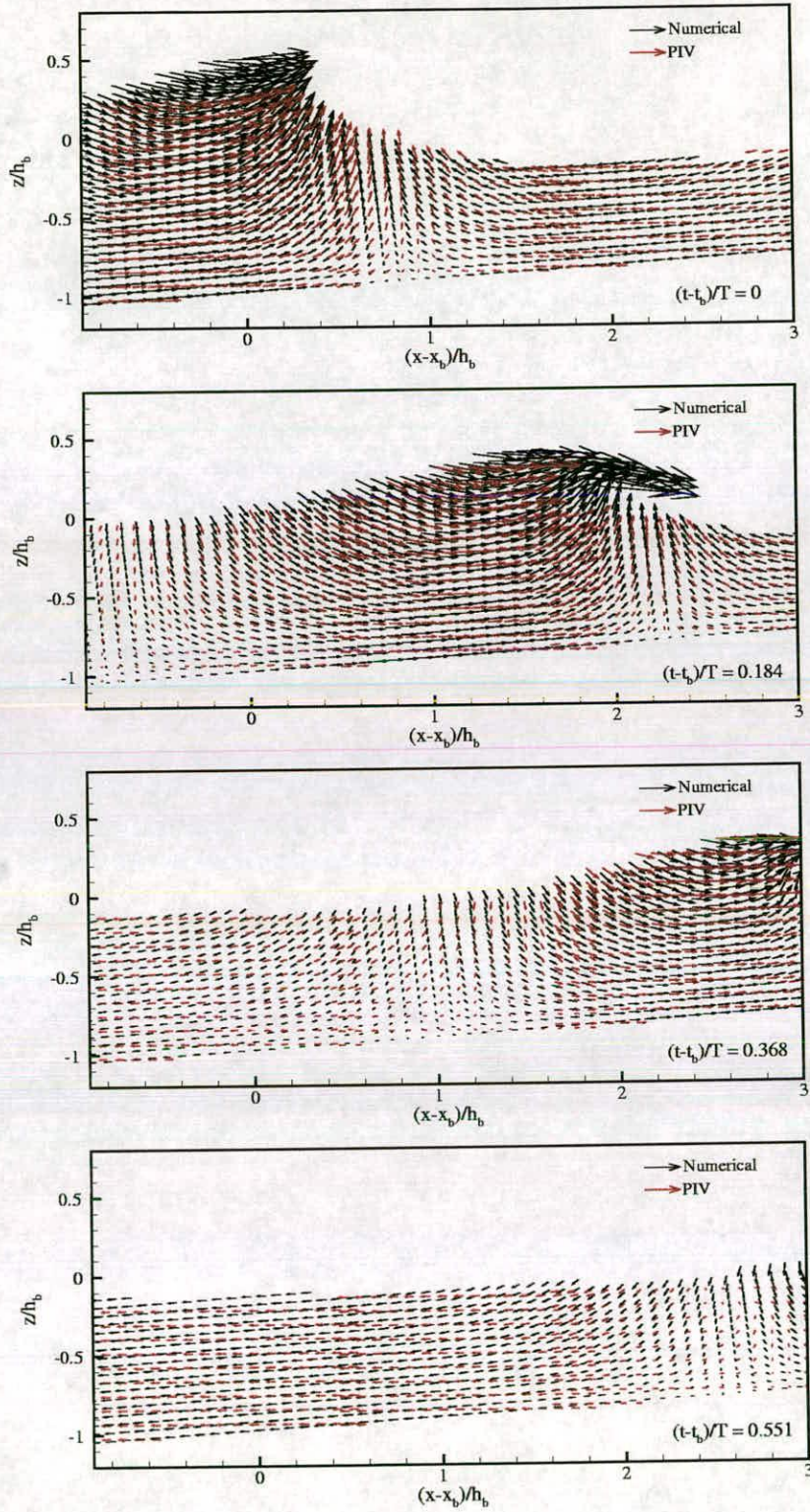


Figure 8.3: Comparisons between the numerical and PIV vector maps of the plunging breaker at $(t - t_b)/T = 0, 0.184, 0.368$ and 0.551 .

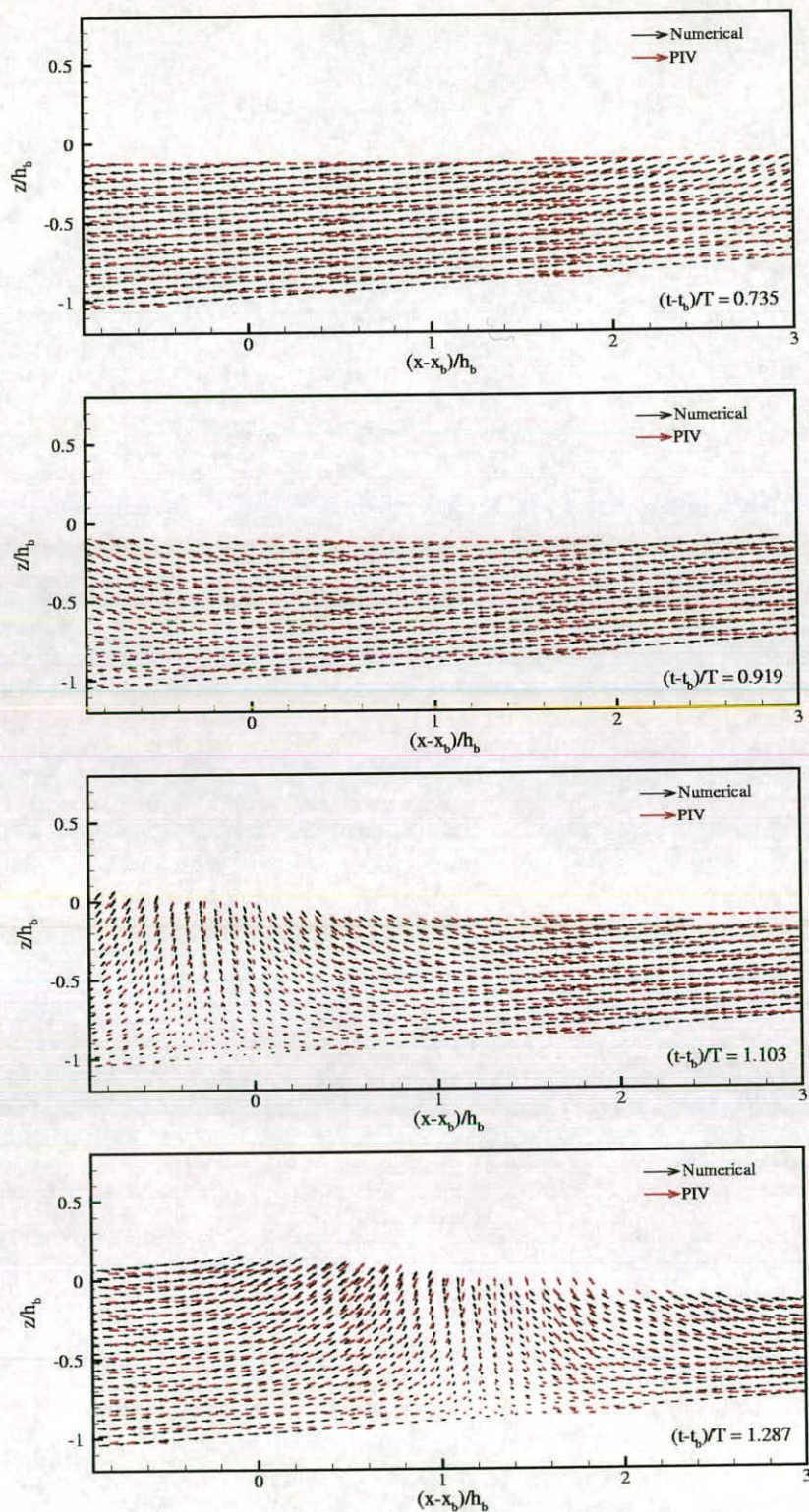


Figure 8.4: Continuing from figure 8.3: at $(t - t_b)/T = 0.735, 0.919, 1.103$ and 1.287 .

is about 146 cm/s, which is around $0.91C$, where C is the crest speed measured using two wave gauges.

In the next phase ($(t - t_b)/T = 0.184$) the crest of the wave is overturning onto the frontal trough. It can be seen that PIV data is missing in the overturning region due to the appearance of trapped air and air bubbles, which are being generated. However, the numerical model has no problems with the above effect and it reveals that the maximum horizontal velocity in the area around the overturning tip is about 203 cm/s or $1.27C$. The trends and magnitudes of the numerical and measured velocities in the interior domain of the flow compare very well.

In the following map ($(t - t_b)/T = 0.368$) of figure 8.3 it can be seen that there is an area where the PIV velocity vectors are not consistent with the numerical velocity vectors. This area is located near the free surface at the right-hand end of the map. In fact it is the area where the air bubbles generated from the overturning wave appear (see position 3 of figure 6.4(c)). Therefore, the PIV velocities in that area are likely to contain errors due to the air-bubble effects. This is why the comparison is not good in this region. Outside the air-bubble region, the comparison is better.

The air bubbles are seen to penetrate into a deeper region in the next phase ($(t - t_b)/t = 0.551$). Again, the presence of these air bubbles explains the discrepancies between the measured and numerical velocities in a region which is roughly within the area $2.0 \leq (x - x_b)/h_b \leq 3.0$. Outside this area, the trend of the numerical flow, which is now reversing offshore, follows that of the measured one.

In figure 8.4 very good comparison can be seen at every phase. The air bubbles have moved away from the measurement region. No obvious discrepancies

between the velocity vectors from the two different approaches can be seen.

In conclusion, the numerical and experimental velocity vector fields agree quite well throughout the breaking process. The discrepancies can be found mostly in the regions where the air bubbles appear.

8.3.3 Velocity-Magnitude Contours

Another way to give an immediate picture of how well the numerical and experimental flow fields compare is by displaying contour plots of the velocity magnitude. These plots are shown in figure 8.5 to figure 8.8. Contours of higher velocity magnitude appear towards the red-coloured region while those of smaller magnitude appear towards the blue-coloured region. Velocity vector maps are also shown overlapping the velocity-magnitude contours. Each figure displays 2 pairs (corresponding to two phases) of contour plots. In each pair the numerical result is shown above the PIV result. The magnitude of the reference vector shown at the corner of each plot is half of the crest speed measured at the breaking point.

Figure 8.5 shows the velocity-magnitude contour plots at breaking, $(t - t_b)/T = 0$, and at $(t - t_b)/T = 0.184$. It can be seen immediately that there is excellent agreement between the numerical and measured velocity distribution of the plunging breaker. Also from the figure, regions of overlapping PIV data, due to the different positions of the camera, can quite clearly be seen. Despite these regions of overlapping data the contour lines are fairly smooth, from which it can be concluded that there is good repeatability of the single plunging breaker in the “Green” tank at UEDIN.

In figure 8.6 the velocity-magnitude distribution in the PIV plot at $(t - t_b)/T = 0.368$ seems to deviate from that in the numerical plot, especially in the region close to the free-surface, at the right-hand end of the plot. However, it can be observed that the comparison is good outside this region. As already explained

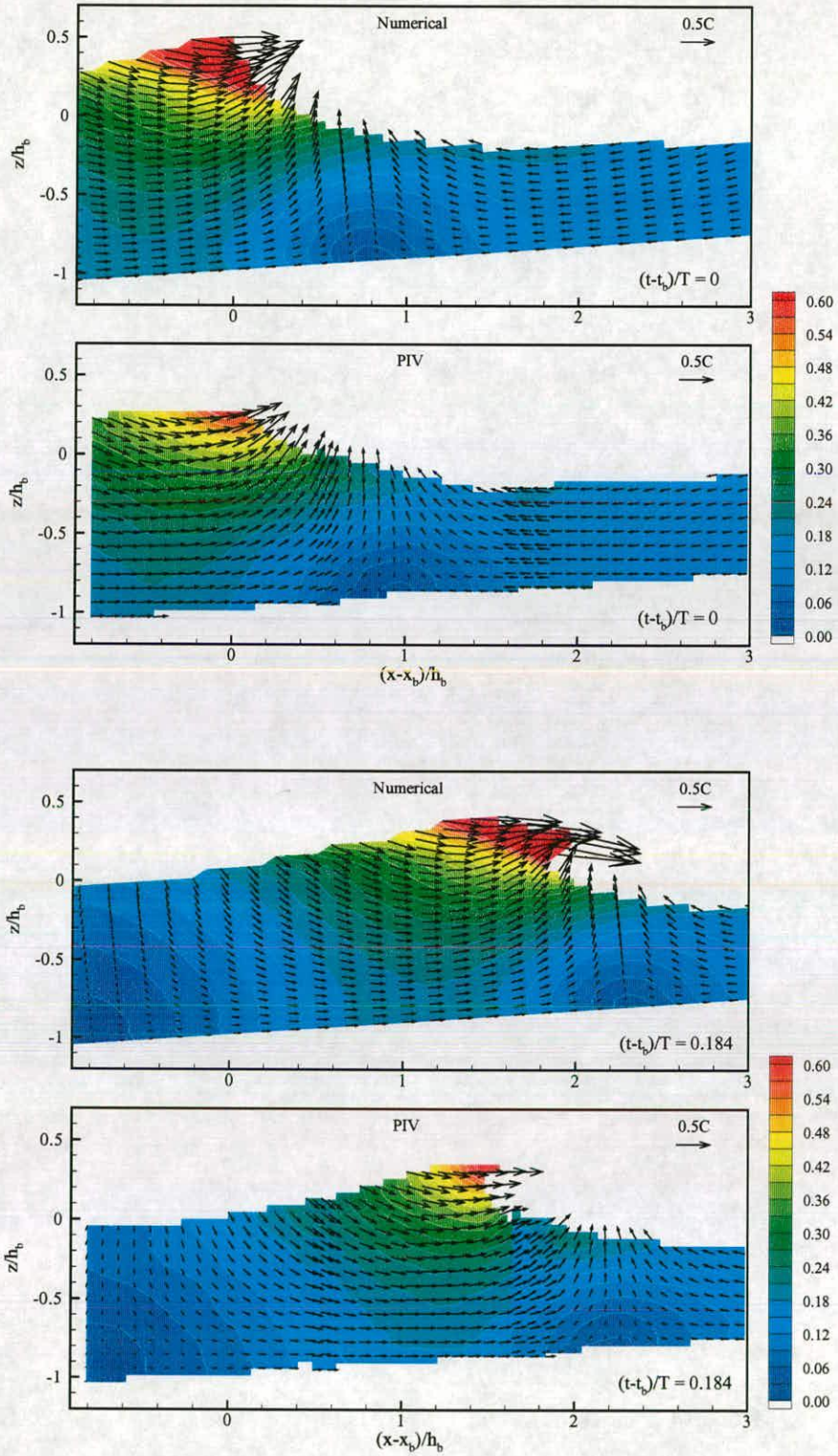


Figure 8.5: Comparisons between the numerical and PIV results for the plunging breaker at $(t - t_b)/T = 0$ and 0.184. Velocity vector maps are shown overlapping velocity-magnitude contours.

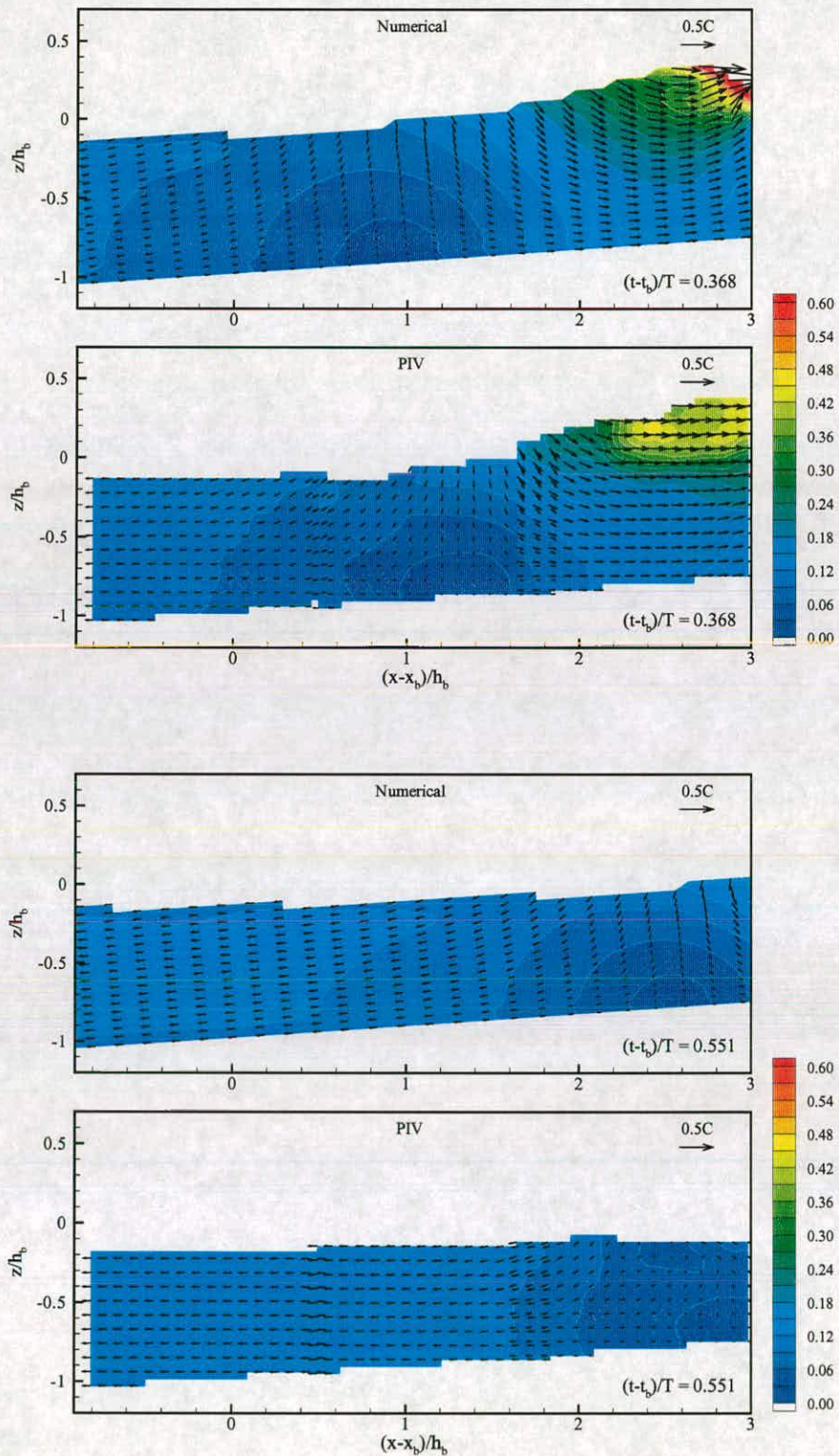


Figure 8.6: Continuing from figure 8.5: at $(t - t_b)/T = 0.368$ and 0.551.

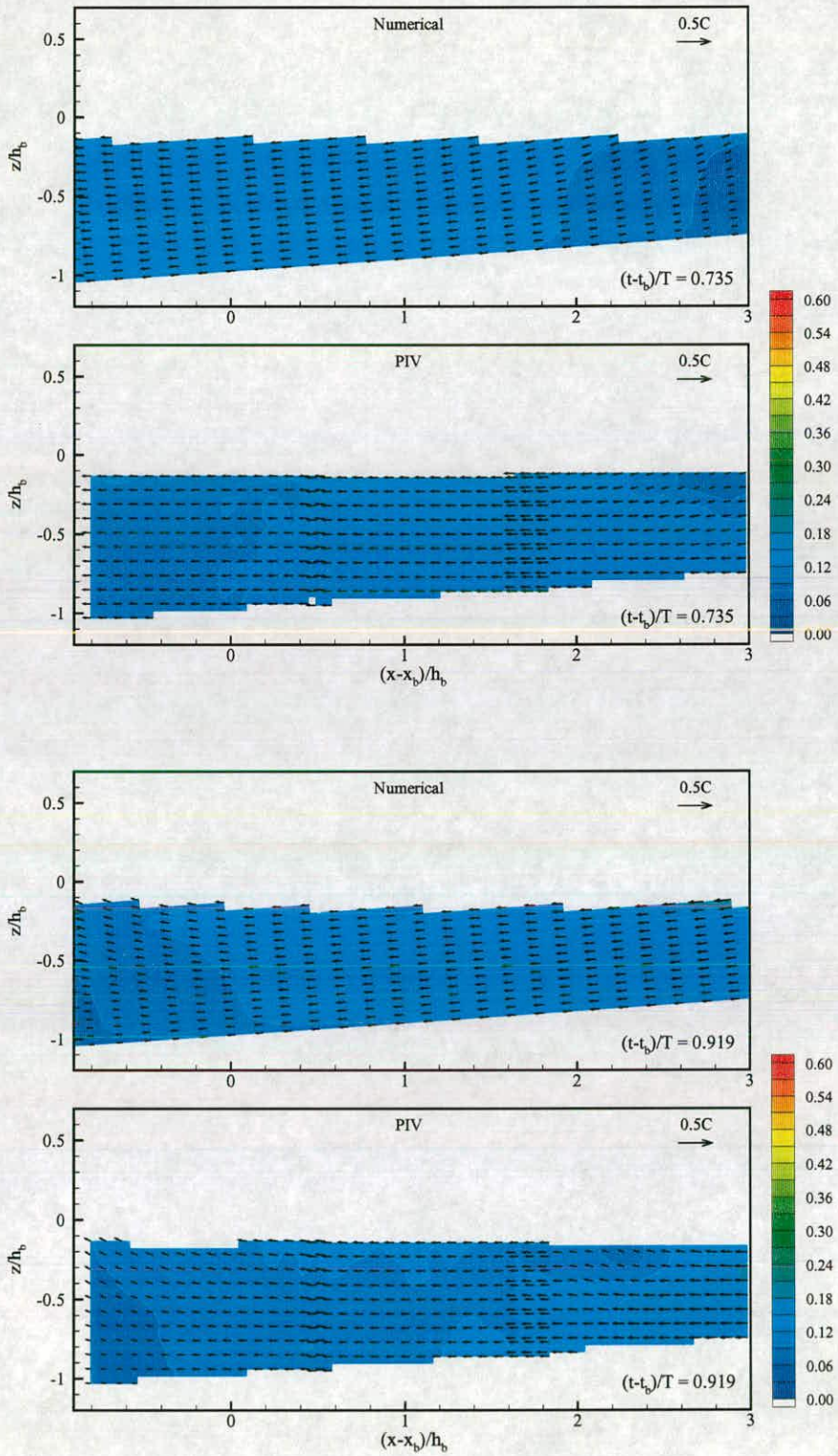


Figure 8.7: Continuing from figure 8.6: at $(t - t_b)/T = 0.735$ and 0.919.

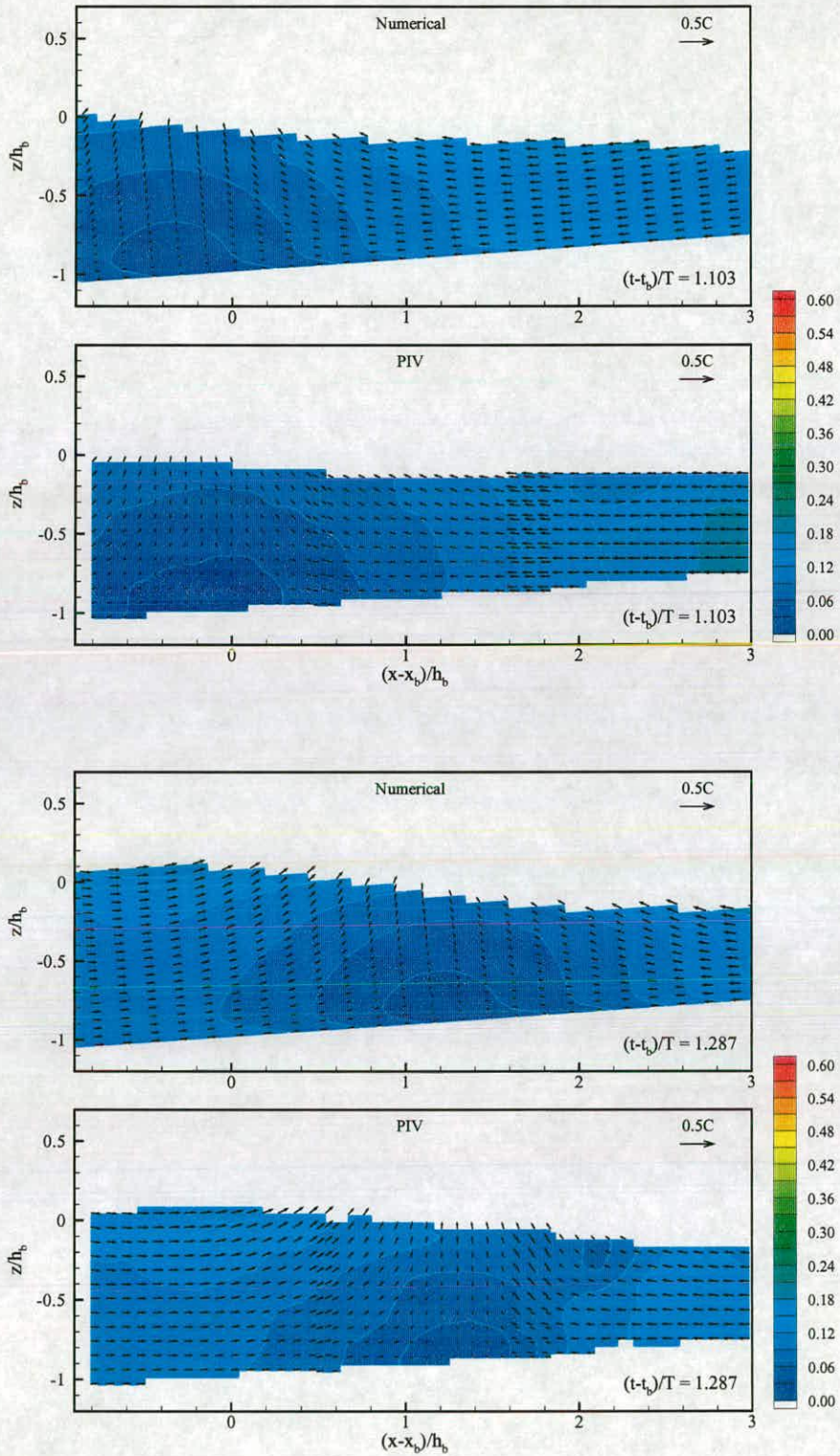


Figure 8.8: Continuing from figure 8.7: at $(t - t_b)/T = 1.103$ and 1.287 .

in the previous subsection, this deviation appears to be due to errors in the PIV velocities caused by air-bubble effects. It can perhaps also be suggested that the deviation is due to the fact that the numerical model does not deal with turbulence which are generated in the aerated region. These deviations are more obvious in the contour plots than in the vector maps. Similar discrepancies between the contour plots of the numerically predicted and experimental velocity-magnitudes can also be seen in the next two phases (at $(t - t_b)/T = 0.551$ in figure 8.6 and at $(t - t_b)/T = 0.735$ in figure 8.7). These discrepancies mostly appear at the right-hand end of the plot, where the generated air bubbles occur. After that the contour plots of the two approaches seem to agree quite well (see figure 8.8).

8.4 Summary of Chapter 8

In this chapter the results obtained from the single plunging breaker experiments, performed at UEDIN, were compared against the results predicted by a numerical model. This work was carried out as part of the SASME project. The (hybrid) numerical model and input conditions were described first and then the experimental and numerical results were compared and discussed.

The numerical model is based on a Navier-Stokes solver using the Volume of Fluid (VOF) method. However, the input conditions for this model were produced by a Boundary-Integral Method (BIM). This was due to the fact that the wavemaker motion could not be easily incorporated into the Navier-Stokes solver. The exact motion of the wavemaker and the exact geometry of the wave flume were duplicated in the BIM. Velocities along a line perpendicular to the beach and near to the toe of the slope were calculated by the BIM and then used as the input conditions for the Navier-Stokes solver.

Initially, comparisons were made of free-surface elevation time series at dif-

ferent positions along the beach. Very good agreement was found between the free-surface elevations measured using the wave gauges and those calculated from the BIM, as well as from the Navier-Stokes solver, even at and after breaking. This suggests that the BIM can be used successfully to produce input conditions for the Navier-Stokes solver.

To compare measured flow fields against numerically predicted flow fields, PIV velocity vector maps were displayed overlapping numerically predicted velocity vector maps. In addition, velocity-magnitude contour plots of both approaches were also compared. In general, the numerical results agreed very well with the PIV results. However, some discrepancies were found, and these occurred mostly in areas where there were breaker-generated air bubbles. It is suggested that these discrepancies are due to errors in the PIV data caused by air-bubble effects, but they are perhaps also due to breaker-generated turbulence which was not dealt with in the numerical model.

Chapter 9

Conclusions & Further Work

In this final chapter a summary of the features of the present study is given. Then, conclusions to the findings of the experiments, which have fulfilled the aim of this thesis (see section 1.1), are presented. Finally, suggestions for further work are made.

9.1 Conclusions

The Particle Image Velocimetry technique was used to obtain full-field instantaneous velocity data of surf-zone breaking waves at different positions along the beach. The breaker types studied here included the single plunging breaker and the train of periodic waves: weak plunging breakers and spilling breakers. The PIV data was post-processed to extract mean and turbulent quantities, allowing the investigation of wave kinematics, vorticity dynamics, turbulent structures and turbulence transport mechanisms, to be made. The conclusions to the main aspects and findings of the study are as follows.

Particle Image Velocimetry

It has been shown that it is possible to use PIV to obtain velocity fields of surf-zone breaking waves. PIV has a unique advantage over other non-intrusive velocimetry techniques, in that it provides the instantaneous spatial structure of

the flow. This is useful for the determination of the vorticity and the turbulent structures, which are important in surf-zone breaking waves. Although care has been taken throughout the measuring process in order to obtain accurate results, there are still shortcomings in the technique. Among these shortcomings, such as the limitation on spatial and temporal resolution, the main problem which limits the efficiency of PIV, when applied to breaking wave studies, is the presence of air bubbles. However, despite these shortcomings, PIV can still be effectively used to achieve the aims of this thesis.

Surf-Zone Breaker Kinematics and Vorticity

Spatial distributions of velocity and vorticity under breaking waves on beaches were obtained from PIV data. A number of velocity vector maps and vorticity contour plots were shown for all three breaker types. In the single plunging breaker, where the investigation was made in the outer surf-zone, clockwise and counter-clockwise vortices were observed at the initial stage of breaking under the overturning point. The dynamics of the clockwise vorticity generated from the overturning jet was suggested to be correlated with the main flow. In the periodic waves, where the investigation was made both in the outer and inner surf-zone, the transport of vorticity was not only affected by the main flow but also, and mostly, by the dynamics of breaker-generated air bubbles. The strength of vortices generated in the spilling breaker is, however, smaller than that in the plunging breaker.

Turbulent Structures under Surf-Zone Breakers

To investigate the transition from irrotational to rotational or fully turbulent flow, a series of isovelocity contours was plotted for all three breaking waves. In all types of breaker, the flow remains irrotational until the wave overturns

and impacts the water surface in front. The flow beneath the surface roller becomes rotational whereas the flow behind the wave front still remains essentially potential, at least until turbulence is advected into it. Under the train of breaking waves, the isovelocity contours also suggested the existence of residual vortices and/or turbulence which were generated from the previous breaker. This was not found in the single breaker experiments.

A series of turbulent intensity distributions for all breaker types was also plotted. It was found that the turbulence generated by the single breaking wave and that generated by the periodic breaking waves were not exactly the same. In the single plunging breaker high turbulent intensity was found between the surface roller and the water in the main flow. The area of high-intensity turbulence was found to be correlated with the area where the rotating plunger vortex appeared.

Under the breaking of the periodic waves the turbulent-intensity contour plots suggested that strong turbulence was generated in the overturning jet and in the surface roller. In both breaker types there was a downward spread of turbulence after the passage of the wave. At some phases it was seen to spread down to the bottom. It was thought to be affected by the air bubbles. Again, the strength of the turbulence generated from the plunging breaker was greater than that generated from the spilling breaker. Another difference found between different breaker types was the dissipation rate of the turbulence. The spilling-breaker generated turbulence does not dissipate until the new wave arrives, whereas the turbulence in the plunging breaker dissipates before the new wave breaks. Although this agrees with other results in the literature, it needs to be kept in mind that the wave period of the spilling breaker used here is shorter than that of the plunging breaker.

Turbulence Transport Mechanisms in the Surf Zone

The mechanisms of turbulence transport under different types of surf-zone breaking waves were investigated from the PIV data using the turbulent energy equation (the k -equation). In the single plunging breaker experiments the levels of the turbulence transport mechanisms were found to be much less than those in the train of breaking waves experiments. This is due to the fact that in the single plunging breaker experiments measurements were only carried out in the initial, or seaward, part of the outer surf-zone. The outer surf-zone is also called the transition zone. Despite these low levels of the turbulence transport mechanisms it was still possible to conclude that in the upper region (the region just below the free-surface) of the shoreward part of the measurement region the main turbulence transport mechanisms were production, advection and diffusion.

In the train of breaking waves experiments the correlation between the passage of wave and the turbulent kinetic energy was more obvious than in the single plunging breaker experiments. For the weak plunging breaker the dominant mechanisms just onshore from the breaking point were production in the upper region and diffusion in the lower region. Then, moving further into the outer surf-zone and into the inner surf-zone the dominant mechanisms in the lower region were production, diffusion and horizontal advection and these became stronger as the shore was approached.

For the spilling breaker the dominant mechanisms just onshore from the breaking point were production and advection in the upper region and diffusion in the lower region. Then, moving further into the outer surf-zone and into the inner surf-zone the dominant mechanisms in the lower region were production, advection and diffusion and these became stronger as the shore was approached.

Comparison with Numerical Model

The work in chapter 8 was carried out as part of a European project in which the author has participated. PIV data obtained from the UEDIN experiments was compared against the results from a numerical model. The numerical model was a hybrid numerical model which consisted of a Boundary-Integral Method (BIM) and a Volume of Fluid (VOF) method. The BIM was used to produce input conditions for the VOF method. Two main aspects can be concluded from the comparison:

- In general, excellent agreement was found between the numerical and experimental results for the single plunging breaker.
- The discrepancies that did occur were found mainly in the aerated regions. These discrepancies were attributed to either the effects of the air bubbles or to the fact that no turbulence model was included in the numerical method.

It should be pointed out that the author believes that this comparison represents the first time that all three of the following criteria have been met:

1. Numerical and experimental conditions matched exactly.
2. Full flow fields compared.
3. The flow after breaking compared.

9.2 Suggestions for Further Work

Two aspects of the present study which could lead on to further work are the Particle Image Velocimetry technique and the study of turbulence in surf-zone breaking waves.

The PIV Technique

To the author's knowledge there have not been experiments done to measure the three-dimensional velocity flow under surf-zone breaking waves. If the out-of-plane velocity component could be measured simultaneously with the other two in-plane components, full, and more accurate, information on breaker-generated turbulence could be obtained. 3-D PIV has been an on-going and quickly developing research project. In fact, it has already been extensively used in other areas of fluid dynamics. Two main techniques that have been used are Stereo PIV and Dual-plane PIV (see Raffel *et al.* [62]).

It has been mentioned that breaker-generated air bubbles are one of the biggest problems for current PIV systems. It has also been shown in the literature review that the kinematics in the air-bubble region of breaking waves could be measured by using fluorescent seeding particles [39, 44]. However, no turbulence information was made from those measurements. This suggests that the next step could be to measure the velocity of the water and air-bubble flows at the same time in order to reveal more insight into the source of turbulence in breaking waves. Some commercial systems have already been developed to obtain the above quantities.

Development of the PIV technique mostly depends on advances in CCD camera and computer technology. The higher frame rate and resolution of the latest cameras, along with faster computers and the larger size of memory, means that better temporal and spatial resolution of the results can be obtained.

Turbulence in Surf-Zone Breaking Waves

Making measurements over a wider range of breaker types and beach slopes could be an extension to this work. The conclusions made earlier were based on weak

plunging and spilling breakers, whose wave parameters/characteristics were not very different. If a greater range of different kinds of waves were studied, the difference in the turbulent structures and transport mechanisms between various types of breaker in the surf zone could be revealed more comprehensively.

Another interesting piece of work that could be done to study surf-zone breaking waves is to investigate the interaction between externally (or breaker) generated turbulence and bottom-boundary generated turbulence. A few researchers have been working on this, but they have used non-intrusive velocimetry techniques other than PIV. Recently, Kozakiewicz *et al.* [43] have revealed the effect of externally generated turbulence on the bottom boundary layer by using the LDA technique. However, the external turbulence was artificially generated by a series of grids, not by a breaking wave. If PIV with a much larger magnification was available, velocity distribution and perhaps the turbulent structures inside the surf-zone boundary layer could be obtained.

In addition to the above suggestions, one other thing that could be done as an extension to this study is to compare the experiments with a numerical model in which turbulence is dealt with, such as by including the k - ϵ equations in the model. This kind of numerical model has already been developed, such as in Lin & Liu [46, 47]. However, in those studies no comparison was made between experimental and numerical vorticity and turbulence fields for surf-zone breaking waves.

Appendix A

List of Publications

The papers that have been and are going to be published as well as those presented at workshops and conferences during the course of the author's PhD are shown as follows.

Review Papers

1. C. A. Greated and N. Emarat. Optical studies of wave kinematics. In *Advances in Coastal and Ocean Eng.* (ed. P. L.-F. Liu), volume 6, pages 185–223. World Scientific, 2000.
2. E. D. Christensen, D. J. Walstra, and N. Emarat. Vertical variation of flow structures in the surf zone. To appear in a special issue of *Coastal Eng.* under topic “Surf and Swash Zone Mechanics”.

Workshop and Conference Proceedings

1. N. Emarat and C. A. Greated. Turbulence study in breaking waves on a beach using PIV. In *Proc. 3rd Int. Workshop on Particle Image Velocimetry*, pages 427–432, Santa Barbara, California, 16–18 September 1999.
2. N. Emarat, E. D. Christensen, and D. I. M. Forehand. A study of plunging breaker mechanics by PIV measurements and a Navier-Stokes solver. To

Appendix A — List of Publications

appear in *Proc. 27th Int. Conf. Coastal Eng. (ICCE 2000)*, Sydney, Australia, 16–21 July 2000.

Other Relevant Abstracts

1. N. Emarat and C. A. Greated. *Breaking waves over beaches*. Scottish Fluid Mechanics Meeting, University of Dundee, UK, 28 May 1997.
2. N. Emarat and C. A. Greated. *PIV experiments on post-breaking turbulence*. MAST-III SASME Midterm Workshop, Delft, The Netherlands, 3–4 May, 1999.
3. N. Emarat, D. I. M. Forehand, E. D. Christensen, and C. A. Greated *Modelling of plunging breaker mechanics*. MAST-III SASME Midterm Workshop, Delft, The Netherlands, 3–4 May, 1999.

Appendix B

List of Symbols

$\langle \rangle$	indicates averaging operator
'	indicates turbulent fluctuation
b	indicates breaking point
c	indicates deep-water
a	wave amplitude
$A(x, y)$	autocorrelation function
C	wave-crest speed
C_D	empirical constant
$C(x, y)$	crosscorrelation function
d	still water depth
e	amplitude of piston translation
f	wave frequency
g	acceleration due to gravity
h	mean water depth
H	wave height
H_2	second order Stokes wave height
H_{22}	free second harmonic wave height
I	turbulent intensity
$I(x, y)$	intensity distribution function in an interrogation area
k	wave number
k	turbulent kinetic energy
ℓ	turbulent length scale
L	wave length
m	beach slope
n	wave front index
N	number of repeated experiments
N	number of wave cycles
p	pressure
s	slope factor in a wave spectrum

Appendix B — List of Symbols

s_{ij}	fluctuating rate of strain
S_{ij}	mean rate of strain
t	time
t_0	time of the first exposure
Δt	time between illuminations
T	wave period
\vec{u}	velocity vector
u	x -component velocity
v	y -component velocity
w	z -component velocity
x	horizontal direction/axis
y	transverse horizontal direction/axis
z	vertical direction/axis
A	advection of turbulent kinetic energy
\mathcal{J}	diffusive transport of turbulent kinetic energy
\mathcal{J}_p	pressure diffusive transport
\mathcal{J}_t	turbulent diffusive transport
\mathcal{P}	production of turbulent kinetic energy

Greek Symbols

α	beach slope
α_{22}	phase angle between main wave and free second harmonic wave
β	angle between a beach and a horizontal bottom
β_{22}	phase angle between two components of the piston motion
ϵ	dissipation of turbulent kinetic energy
ϵ_{thresh}	threshold used in the vector validation algorithm
η	free-surface elevation/displacement
λ	smoothing parameter used in a cubic smoothing spline
μ	dynamic viscosity
ν	kinematic viscosity
ν_t	eddy viscosity
ξ	surf similarity parameter
$\xi(t)$	piston wave generator translation function
ρ	fluid density
σ_k	empirical diffusion constant
σ_s	smoothing factor used in the vector interpolation algorithm
ϕ	wave phase
ω	wave angular frequency
ω_y	vorticity component along the y -axis
$\vec{\omega}$	vorticity vector

Abbreviations

CCD	charge coupled device
CW	continuous wave
DPIV	digital particle image velocimetry
FT	Fourier Transformation
FFT	fast Fourier Transformation
FLV	fibre-optic laser Doppler velocimeter
H	horizontal direction
IA	interrogation area
ISVA	Institut for Strømningsmekanik og Vandresurser (Department of Hydrodynamics and Water Resources), Technical University of Denmark
LDA	laser Doppler anemometry
LDV	laser Doppler velocimetry
MWL	mean water level
PIV	particle image velocimetry
PTV	particle tracking velocimetry
SASME	Surf and Swash Zone Mechanics (the EU-sponsored project)
SWL	still water level
S/N	signal to noise ratio
UEDIN	The University of Edinburgh
V	vertical direction
rms	root mean square

Bibliography

- [1] R. J. Adrian. Image shifting technique to resolve directional ambiguity in double-pulsed velocimetry. *Appl. Optics*, 25(21):3855–3858, 1986.
- [2] R. J. Adrian. Particle-imaging techniques for experimental fluid mechanics. *Ann. Rev. Fluid Mech.*, 23:261–304, 1991.
- [3] R. J. Adrian. Dynamic ranges of velocity and spatial resolution of particle image velocimetry. *Meas. Sci. Technol.*, 8(12):1393–1398, 1997.
- [4] D. R. Basco. A qualitative description of wave breaking. *J. Waterway, Port, Coastal and Ocean Eng.*, ASCE, 111(2):171–188, 1985.
- [5] J. A. Battjes. Surf similarity. In *Proc. 14th Int. Conf. Coastal Eng.*, volume 1, pages 466–480, 1974.
- [6] J. A. Battjes. Surf-zone dynamics. *Ann. Rev. Fluid Mech.*, 20:257–293, 1988.
- [7] J. Buhr Hansen and I. A. Svendsen. Laboratory generation of waves of constant form. In *Proc. 14th Int. Conf. Coastal Eng.*, volume 1, pages 321–339, 1974.
- [8] K.-A. Chang and P. L.-F. Liu. Measurement of breaking waves using particle image velocimetry. In *Proc. 25th Int. Conf. Coastal Eng.*, volume 1, pages 527–536, 1996.
- [9] K.-A. Chang and P. L.-F. Liu. Velocity, acceleration and vorticity under a breaking waves. *Phys. Fluids*, 10(1):327–329, 1998.

Bibliography

- [10] K.-A. Chang and P. L.-F. Liu. Experimental investigation of turbulence generated by breaking waves in water of intermediate depth. *Phys. Fluids*, 11(11):3390–3400, 1999.
- [11] E. D. Christensen. DHI Water and Environment. Private communication, 1997.
- [12] E. D. Christensen. Turbulence in breaking waves: A numerical investigation. Series Paper No. 67, ISVA, Tech. Univ. Denmark, 1998. 141 pages.
- [13] J. A. Cosgrove. The University of Edinburgh. Private communication, 1998.
- [14] D. T. Cox, N. Kobayashi, and A. Okayasu. Bottom shear stress in the surf zone. *J. Geophys. Res.*, 101(C6):14337–14348, 1996.
- [15] D. Dabiri and M. Gharib. Experimental investigation of the vorticity generation within a spilling water wave. *J. Fluid Mech.*, 330:113–139, 1997.
- [16] R. G. Dean and R. A. Dalrymple. *Water wave mechanics for engineers and scientists*, volume 2 of *Advanced Series on Ocean Eng.* World Scientific, 1991.
- [17] T. P. Dewhurst. *Multiple CCD Array Digital Particle Image Velocimetry*. PhD thesis, The University of Edinburgh, 1998.
- [18] F. Durst. *Principles and Practice of Laser-Doppler Anemometry*. Academic Press, London, 2nd edition, 1981.
- [19] H. C. Earnshaw. *A Study of Flow over a Rippled Bed using Particle Image Velocimetry*. PhD thesis, The University of Edinburgh, 1997.
- [20] W. J. Easson, T. Bruce, C. Gray, C. A. Greated, D. R. McCluskey, and D. J. Skyner. *Particle Image Velocimetry*. Course Note, The University of Edinburgh.

Bibliography

- [21] N. Emarat, E. D. Christensen, and D. I. M. Forehand. A study of plunging breaker mechanics by PIV measurements and a Navier-Stokes solver. Abstract for the *27th Int. Conf. Coastal Eng. (ICCE)*, Sydney, Australia, 16–21 July 2000.
- [22] N. Emarat and C. A. Greated. Turbulence study in breaking waves on a beach using PIV. In *Proc. 3rd Int. Workshop on Particle Image Velocimetry*, pages 427–432, Santa Barbara, California, 16–18 September 1999.
- [23] J. D. Entwistle. *Digital Particle Image Velocimetry Applied to a Flow Through a Duct*. PhD thesis, The University of Edinburgh, 1999.
- [24] M. Eskholm, P. Prescott, and J. Buhr Hansen. *Users manual for ISVA wave generation programme*. ISVA, Tech. Univ. Denmark, 22 July 1993.
- [25] D. I. M. Forehand. *Numerical Prediction of Free-Surface Flows Caused by Body/Fluid Interaction*. PhD thesis, The University of Edinburgh, 1998.
- [26] J. Fredsøe and R. Deigaard. *Mechanics of Coastal Sediment Transport*, volume 3 of *Advanced Series on Ocean Eng.* World Scientific, 1992.
- [27] C. J. Galvin. Breaker type classification on three laboratory beaches. *J. Geophys. Res.*, 73(12):3651–3659, 1968.
- [28] R. J. Goldstein, editor. *Fluid Mechanics Measurements*. Taylor & Francis, Washington D. C., 2nd edition, 1996.
- [29] C. Gray. *The Development of Particle Image Velocimetry for Water Wave Studies*. PhD thesis, The University of Edinburgh, 1989.
- [30] C. Gray and T. Bruce. The application of Particle Image Velocimetry (PIV) to offshore engineering. In *Proc. 5th Int. Offshore and Polar Eng. Conf.*, volume 3, pages 701–708, The Hague, The Netherlands, 11–16 June 1995.

Bibliography

- [31] C. Gray, C. A. Greated, D. R. McCluskey, and W. J. Easson. An analysis of the scanning beam PIV illumination system. *Meas. Sci. Technol.*, 2(8):717–724, 1991.
- [32] C. A. Greated and N. Emarat. Optical studies of wave kinematics. In P. L.-F. Liu, editor, *Advances in Coastal and Ocean Eng.*, volume 6, pages 185–223. World Scientific, 2000.
- [33] C. A. Greated, D. J. Skyner, and T. Bruce. Particle Image Velocimetry (PIV) in the coastal engineering laboratory. In *Proc. 23rd Int. Conf. Coastal Eng.*, volume 1, pages 212–225, 1992.
- [34] D. B. Hann. The University of Edinburgh. Private communication, 1998.
- [35] T. R. Haydon. *Turbulence and Vorticity Generated by Breaking Waves*. PhD thesis, The University of Edinburgh, 1998.
- [36] T. R. Haydon, D. B. Hann, P. Davies, C. A. Greated, and T. C. D. Barnes. Turbulence structures in the surf zone. In *Proc. 25th Int. Conf. Coastal Eng.*, volume 1, pages 214–220, 1996.
- [37] J. O. Hinze. *Turbulence: An introduction to its mechanism and theory*. McGraw-Hill, New York, 1959.
- [38] H. Huang, D. Dabiri, and M. Gharib. On errors of digital particle image velocimetry. *Meas. Sci. Technol.*, 8(12):1427–1440, 1997.
- [39] P. C. M. Jansen. Laboratory observations of the kinematics in the aerated region of breaking waves. *Coastal Eng.*, 9(5):453–477, 1986.
- [40] R. D. Keane and R. J. Adrian. Optimization of particle image velocimeters: I. Double pulsed systems. *Meas. Sci. Technol.*, 1(11):1202–1215, 1990.
- [41] R. D. Keane and R. J. Adrian. Optimization of particle image velocimeters: II. Multiple pulsed systems. *Meas. Sci. Technol.*, 2(10):963–974, 1991.

Bibliography

- [42] R. D. Keane and R. J. Adrian. Theory of cross-correlation analysis of PIV images. *Appl. Sci. Res.*, 49(3):191–215, 1992.
- [43] A. Kozakiewicz, B. M. Sumer, J. Fredsøe, R. Deigaard, and N.-S. Cheng. Effect of externally generated turbulence on wave boundary layer. Progress Report No. 77, ISVA, Tech. Univ. Denmark, 1998.
- [44] C. Lin and H. H. Hwung. External and internal flow fields of plunging breakers. *Exps. Fluids*, 12(4–5):229–237, 1992.
- [45] J. C. Lin and D. Rockwell. Evolution of a quasi-steady breaking wave. *J. Fluid Mech.*, 302:29–44, 1995.
- [46] P. Lin and P. L.-F. Liu. A numerical study of breaking waves in the surf zone. *J. Fluid Mech.*, 359:239–264, 1998.
- [47] P. Lin and P. L.-F. Liu. Turbulence transport, vorticity dynamics, and solute mixing under plunging breaking waves in surf zone. *J. Geophys. Res.*, 103(C8):15677–15694, 1998.
- [48] S. Mayer, A. Garapon, and L. S. Sørensen. A fractional step method for unsteady free-surface flow with applications to non-linear wave dynamics. *Int. J. for Numerical Methods in Fluids*, 28(2):293–315, 1998.
- [49] J. McCowan. On the highest wave of permanent type. *Philos. Mag. J. Sci.*, 38, 1894.
- [50] C. D. Meinhart, A. K. Prasad, and R. J. Adrian. Parallel digital processor system for particle image velocimetry. In *6th Int. Symp. on Applications of Laser Techniques to Fluid Mech.*, pages 30.1.1–30.1.5, Lisbon, Portugal, 20–30 July 1992.
- [51] A. Melling. Tracer particles and seeding for particle image velocimetry. *Meas. Sci. Technol.*, 8(12):1406–1416, 1997.

Bibliography

- [52] I. G. Morrison. *The Hydrodynamic Performance of an Oscillating Water Column Wave Energy Converter*. PhD thesis, The University of Edinburgh, 1995.
- [53] W. Munk and M. Wimbush. A rule of thumb for wave breaking over sloping beaches. *Oceanology*, 6:56–59, 1969.
- [54] K. Nadaoka, M. Hino, and Y. Koyano. Structure of the turbulent flow field under breaking waves in the surf zone. *J. Fluid Mech.*, 204:359–387, 1989.
- [55] C. Pedersen, R. Deigaard, and J. Sutherland. Turbulence measurements under broken waves. Progress Report No. 74, ISVA, Tech. Univ. Denmark, 1993. pages 81–97.
- [56] D. H. Peregrine. Breaking waves on beaches. *Ann. Rev. Fluid Mech.*, 15:149–178, 1983.
- [57] M. Perlin, J. He, and L. P. Bernal. An experimental study of deep water plunging breakers. *Phys. Fluids*, 8(9):2365–2374, 1996.
- [58] C. J. D. Pickering and N. A. Halliwell. Particle image velocimetry: a new field measurement technique. In P. H. Richards, editor, *Optical Measurements in Fluid Mechanics*, number 77 in Inst. Phys. Conf. Series, pages 147–152. Adam Hilger Ltd, Bristol, 1985.
- [59] J. Pullen. *Particle Image Velocimetry Applied to Waves with Surface Active Films*. PhD thesis, The University of Edinburgh, 1999.
- [60] P. A. Quinn. *Breaking Waves on Beaches*. PhD thesis, The University of Edinburgh, 1995.
- [61] P. A. Quinn, D. J. Skyner, C. Gray, C. A. Greated, and W. J. Easson. A critical analysis of the particle image velocimetry technique as applied to waves. In F. T. M. Nieuwstadt, editor, *Flow Visualization and Image*

Bibliography

- Analysis*, volume 14 of *Fluid Mechanics and Its Applications*, pages 227–245. Kluwer Academic Publishers, Dordrecht, 1993.
- [62] M. Raffel, C. Willert, and J. Kompenhans. *Particle Image Velocimetry: A Practical Guide*. Springer-Verlag, Berlin and Heidelberg, 1998.
- [63] R. J. Rapp and W. K. Melville. Laboratory measurements of deep-water breaking waves. *Phil. Trans. R. Soc. Lond.*, A 331(1622):735–800, 1990.
- [64] W. Rodi. *Turbulence Models and Their Application in Hydraulics: A state-of-the-art review*. IAHR Monograph Series. A. A. Balkema Publishers, The Netherlands, 3rd edition, 1993.
- [65] D. Rogers and G. Bolton King. *Wave generation using Ocean and wave: version 3.61*. Users Manual. Edinburgh Designs Ltd, Edinburgh, Scotland, UK, March 1997.
- [66] T. Sawaragi, editor. *Coastal Engineering - Waves, Beaches, Wave-Structure Interactions*, volume 78 of *Developments in Geotechnical Engineering*. Elsevier, Amsterdam, 1995.
- [67] D. J. Skyner. *The Mechanics of Extreme Water Waves*. PhD thesis, The University of Edinburgh, 1992.
- [68] D. J. Skyner. A comparison of numerical predictions and experimental measurements of the internal kinematics of a deep-water plunging wave. *J. Fluid Mech.*, 315:51–64, 1996.
- [69] M. Stanislas, J. Kompenhans, and J. Westerweel. *Particle Image Velocimetry*. Kluwer Academic Publishers, 2000.
- [70] M. J. F. Stive. Velocity and pressure field of spilling breakers. In *Proc. 17th Int. Conf. Coastal Eng.*, volume 1, pages 547–566, Sydney, 1980.

Bibliography

- [71] B. M. Sumer. ISVA, Tech. Univ. Denmark. Private communication, 1998.
- [72] I. A. Svendsen. Analysis of surf zone turbulence. *J. Geophys. Res.*, 92(C5):5115–5124, 1987.
- [73] I. A. Svendsen and J. Buhr Hansen. Deformation up to breaking of periodic waves on a beach. In *Proc. 15th Int. Conf. Coastal Eng.*, volume 1, pages 477–496, 1976.
- [74] I. A. Svendsen and I. G. Jonsson. *Hydrodynamics of Coastal Regions*. Den Private Ingeniørfond, Tech. Univ. Denmark, 1976.
- [75] I. A. Svendsen, P. Å. Madsen, and J. Buhr Hansen. Wave characteristics in the surf zone. In *Proc. 16th Int. Conf. Coastal Eng.*, volume 1, pages 520–539, Hamburg, 1978.
- [76] I. A. Svendsen and U. Putrevu. Surf-zone hydrodynamics. In P. L.-F. Liu, editor, *Advances in Coastal and Ocean Eng.*, volume 2, pages 1–78. World Scientific, 1996.
- [77] H. Tennekes and J. L. Lumley. *A First Course in Turbulence*. The MIT Press, USA, 1972.
- [78] F. C. K. Ting and J. T. Kirby. Observation of undertow and turbulence in a laboratory surf zone. *Coastal Eng.*, 24(1-2):51–80, 1994.
- [79] F. C. K. Ting and J. T. Kirby. Dynamics of surf-zone turbulence in a strong plunging breaker. *Coastal Eng.*, 24(3-4):177–204, 1995.
- [80] F. C. K. Ting and J. T. Kirby. Dynamics of surf-zone turbulence in a spilling breaker. *Coastal Eng.*, 27(3-4):131–160, 1996.
- [81] D. J. Tritton. *Physical Fluid Dynamics*. Oxford University Press, 2nd edition, 1988.

Bibliography

- [82] J. Wang. *Oscillatory Flows Round Combinations of Cylinders*. PhD thesis, The University of Edinburgh, 1999.
- [83] B. M. Watraswicz and M. J. Rudd. *Laser Doppler Measurements*. Butterworths, London, 1st edition, 1976.
- [84] J. Westerweel. Fundamentals of digital particle image velocimetry. *Meas. Sci. Technol.*, 8(12):1379–1392, 1997.
- [85] J. Westerweel, D. Dabiri, and M. Gharib. The effect of a discrete window offset on the accuracy of cross-correlation analysis of digital PIV recordings. *Exps. Fluids*, 23(1):20–28, 1997.
- [86] C. E. Willert and M. Gharib. Digital particle image velocimetry. *Exps. Fluids*, 10(4):181–193, 1991.